A Twist in Strong-Field Physics: Structured, Ultrafast Optical and Extreme Ultraviolet Waveforms with Tailored Spin and Orbital Angular Momentum

by

Kevin M. Dorney

M.S., Wright State University, 2014

B.S. (Chemistry), Wright State University, 2012

B.S. (Biology), Wright State University, 2012

A thesis submitted to the

Faculty of the Graduate School of the

University of Colorado in partial fulfillment

of the requirements for the degree of

Doctor of Philosophy

Program in Chemical Physics

2019

This thesis entitled:
A Twist in Strong-Field Physics: Structured, Ultrafast Optical and Extreme Ultraviolet Waveforms with Tailored Spin and Orbital Angular Momentum
written by Kevin M. Dorney
has been approved for the Program in Chemical Physics

Margaret M. Murnane

Henry C. Kapteyn

Date

The final copy of this thesis has been examined by the signatories, and we find that both the content and the form meet acceptable presentation standards of scholarly work in the above mentioned discipline.

Dorney, Kevin M. (Ph.D., Chemical Physics)

A Twist in Strong-Field Physics: Structured, Ultrafast Optical and Extreme Ultraviolet Waveforms with Tailored Spin and Orbital Angular Momentum

Thesis directed by Professors Margaret M. Murnane and Henry C. Kapteyn

Structured light, which is composed of custom-tailored light waves possessing nontrivial intensity, polarization, and phase, has emerged in recent decades as a powerful tool for probing and controlling light-matter interactions, with wide-reaching applications in fields ranging from microscopy, to scientific/industrial imaging, lithography, and even to forensic science. In particular, structured light possessing optical angular momentum can exhibit both spin and orbital flavors related to the polarization and topological phase structure of light, respectively. This new ability to sculpt light into complex optical patterns has proven to be particularly beneficial for telecommunications, quantum computing, chiral sensing, and super-resolution imaging, to name a few. By connecting principles of generating and controlling structured light with the extreme nonlinear process of high-harmonic generation, this thesis details how exquisite control can be attained over extreme ultraviolet attosecond light waves—in some cases rivaling and even surpassing the intricate structures so readily obtained at visible wavelengths.

Using novel optical control schemes, I first show that the ellipticity of attosecond pulse trains produced via high-harmonic generation can be actively controlled in real time, yielding attosecond pulses with a custom-tunable polarization state. These concepts are then taken a step further by adding controllable amounts of orbital angular momentum to the visible driving lasers, which yields full control over the polarization, divergence, and topological charge of short-wavelength, coherent light pulses. The use of spin-orbit driving beams provides unprecedented control over the emitted high-harmonics, allowing for the generation of, for example, spatially isolated short-wavelength vortex beams—and attosecond pulses—of pure circular polarization. Then in a final, beautiful result, I show experimentally that by driving the high harmonic upconversion process with a time-delayed pair of optical vortex beams, it is possible to create an entirely new property of propagating waveforms, that possess a self-torque. This novel property of light is manifested in extreme ultraviolet beams that exhibit a rapid, attosecond variation of their orbital angular momentum,

which spans an entire octave of topological charges. In the future, these sculpted attosecond waveforms with designer spin and orbital angular momentum can serve as the basis for applying structured light waves to solving grand challenge problems in chemistry and physics, while also making it possible to tailor light-matter interactions on nanometer spatial and attosecond temporal scales.

Dedication

In the words of my old stomping grounds in Ohio, this one's for all y'all. All y'all friends, family, collaborators, fellow laser-(and non-laser-)dungeon dwellers, and nearly equally broke roommates over the years for, in one way or another, making this all possible.

Acknowledgements

Earning a PhD is certainly no easy or even moderate task, and the successful completion of a PhD cannot be accomplished based on the efforts of one individual. Throughout the ups and downs, lefts and right, occasional diagonalizations and renormalizations, the folks listed below have been unwavering in their support of me and my goals, and no matter how many pages I use, I cannot express my gratitude enough. Hopefully, what is written below will serve as a good start to thanking everyone who has helped me along the way.

- To Prof. Margaret Murnane and Prof. Henry Kapteyn. For not only being the best advisors that a young scientist could ask for, but for also being incredible mentors and even better human beings.

- To my mentors in the KM Group, both past and present, and in particular Dr. Daniel Adams, Dr. Seth Cousin, Dr. Franklin Dollar, Dr. Jennifer Ellis, Dr. Daniel Hickstein, Dr. Chris Mancuso, Dr. Bill Peters, Dr. Tenio Popmintchev. I cannot thank y'all enough for teaching me the ways of physics and ultrafast lasers, and for putting up with a near infinite amount of uninformed questions over the years.

- To the past and current members of PT1; Nathan Brooks, Prof. Franklin Dollar, Dr. Jennifer Ellis, Dr. Tingting Fan, Dr. Hickstein, and Quynh Nguyen. I don't think I could've found a happier, more motivated set of individuals that call laser dungeons their home.

- To my labmates and fellow dungeon dwellers in the KM Group, both past and present; Dr. Begoña Abad-Mayor, Charles Bevis, David Couch, Yuka Esashi, Travis Frazier, Dr. Ben Galloway, Christian Gentry, Maithreyi Gopalakrishnan, Guan Gui, Peter Johnson, Robert Karl, Joshua Knobloch, Dr. Chen-Ting Liao, Drew Morrill, Dr. Christina Porter, Dr. Elisabeth Shanblatt, Dr. Phoebe Tengdin, Bin Wang, and Dr. Dmitriy Zusin.

- To some seriously talented and kind undergraduate students: Johnathan Nesper, Sanjana Paul, and Dylan Zollinger. In particular, Laura Wooldridge for putting up with late nights, heavy vacuum chambers, and the author's taste in music after the hours of 2200 during the construction of the 3D VMI.
- To some of the best collaborators, both near and abroad, that anyone could ask for; Prof. Jan Chaloupka, Prof. Charles Durfee, Prof. Maciej Lewenstein, Prof. Win Li, Prof. Dejan Milošević, Prof. Xiao Min-Tong, Dr. Emilio Pisanty, Dr. Justin M. Shaw, and Prof. Stefan Witte. Particularly, Laura Rego, Prof. Luis Plaja, Antonio Picón, Julio San Román, and Carlos Hernández-García. We've had a lot of fun spinning and twisting the physics of strong-field optical science.
- To the staff of the JILA instrument shop; Todd Asnicar, Hans Green, Kim Hagen, Blaine Horner, Kyle Thatcher, James Uhrich, Calvin Harris, and the late Tracy Keep. Somehow y'all, have perfected the art of working miracles every day, while also being incredibly kind and patient, even when dealing with the author of this thesis.
- To the JILA electronics shop; Terry Brown, James Fung-A-Fat, Christopher Ho, and Carl Sauer for continuing the JILA tradition of incredibly supportive and kind people.
- To the JILA computing team, particularly J. R. Raith and Jim McKown for putting up with my terrible Google searches and teaching me to not fear the Matrix behind the screen.
- To the wonderful staff of the JILA Keck laboratory, particularly Dave Alchenberger and Mark Carter for doing what seems impossible to me every day.
- To Steven Burrows and Julie Phillips; for teaching me how to draw pretty pictures in 3D space and write, respectively.
- To the rest of the amazing support staff at JILA that work so hard to continually make it one of the best places on Earth to work.
- To the incredibly patient and kind staff at KMLabs, particularly Dr. Sterling Backus, Dr. Michael Gerrity, Dr. Daisy Raymondson, and Dr. Seth Cousin, who appears again as he had the unfortunate experience of being "bugged" by the author first in the research group, and now at KMLabs.

- To Prof. Neils Damrauer and Prof. Jun Ye, for serving on my thesis committee and for their help and advice throughout my years at CU and JILA.
- To Dr. David Dolson, Dr. Peter Lauf, and Dr. Ioana Pavel-Sizemore at Wright State University for encouraging me to pursue a PhD, which is still one of the best decisions I've ever made.
- To Michael Ortiz and James Smith. I don't think I could've asked for better graduate school mates, scientists, or friends.
- To an unbelievable set of friends, both in Colorado and back home in the fields of Ohio for helping me to realize that the most important things in life are the bonds we make with each other.
- To the best family anyone could be luckily enough to be a part of; mom, dad, Eric, Kyra, Barb, Janet, John, and Karl. "Chuck", you're little "Itsy bit", finally grew up.
- To Trisha Brockman, for reasons so numerous that it would require a second thesis to list them all. You have no idea how much of this, and so much else, would not be possible without you.
- And finally, to the Ironman Triathlon; for teaching me that no matter how much I learn, or how smart I think I am, I am still capable of doing incredibly stupid things.

Contents

Chapter

Appendix

Tables

Table

Figures

Figure

List of Abbreviations

APT(s)	Attosecond pulse train(s)
ATI	Above threshold ionization
BBO	Beta barium borate – A common nonlinear crystal used to perform wave-mixing in the ultraviolet to infrared spectral regions.
BHHG	Bicircular high-harmonic generation – A method for producing circularly and elliptically polarized light in the EUV and soft x-ray light regimes
BPS	Beam pointing stabilization
CCD	Charge-coupled device – A type of light sensor in digital cameras, telescopes, and even supermarket barcode scanners
CoM	Center of mass
CPA	Chirped pulse amplification
CW	Continous wave
DPSS	Diode-pumped solid-state – A descriptor for lasers possessing a solid-state gain medium, which is optically pumped via light emitting diodes.
FROG	Frequency-resolved optical gating – A robust method for characterizing the temporal and spectral profiles of an ultrashort laser pulse, minus a constant phase here and there.
EUV	Extreme ultraviolet (light)

EUV-MCD	Extreme-ultraviolet magnetic circular dichroism – An optical property of ferromagnetic materials that manifests as a dichoric absorption of the different helicities of circularly polarized light.
eV	Electron volt – Unit of energy, 1 eV $\approx 1.602 \times 10^{-19}$ J
FWHM	Full width at half maximum
GB	Gigabyte
GS	Gerchberg-Saxton – A type of iterative phase retrieval algorithm
HHG	High-harmonic generation – A method for producing coherent, laser-like EUV and soft x-ray light
IAP	Isolated attosecond pulse
IR	Infrared (light)
JILA	The institute formerly known as the Joint Institute for Laboratory Astrophysics
LCP	Left-circular polarization
MCD	Magnetic circular dichroism
OAM	Orbital angular momentum
OPA	Optical parametric amplifier
RAM	Random access memory
RCP	Right circular polarization
SAM	Spin angular momentum
Self-AM	Self-amplitude modulation – A process by which a sufficiently intense laser pulse can alter its own amplitude via the non-linear optical Kerr effect
SFA	Strong-field approximation – A theoretical tool for investigating strong-field phenomena
SFA+	Improved strong-field approximation – An improved version of the SFA, which takes into account several aspects that are neglected in the traditional SFA
SFI	Strong field ionization
SHG	Second harmonic generation

SLM	Spatial light modulator – A device for controlling the spectral phase of a light beam as a function of spatial extent of the same beam, typically via computer-generated interference patterns
SPM	Self-phase modulation – A process by which a laser pulse may self-induce a variation of its instantaneous frequency via the non-linear response of a medium
SPP	Spiral phase plate – An optic that has a spiral-staircase-like pattern on one face, so that the height of the optic increases in (typically) discrete amounts.
STSM	Semiclassical three step model – A model for the single-atom physics of high-harmonic generation, which treats the quantum electron dynamics of the up-conversion process in a straightforward, classical manner
Ti:sapph	Titanium sapphire – The workhorse laser crystal of ultrafast, high powered laser amplifiers
TSM	Thin slab model – An approximation used in SFA simulations of HHG driven in a medium that is ”thin” compared to the Rayleigh length of the focused laser beam
UV	Ultraviolet (light)

Outline

The new research outlined in this thesis is described in three major sections, that summarize my thesis work as a member of the Kapteyn-Murnane group (KM group) at JILA.

- Chapter 3 is adapted from a publication titled “Helicity-selective enhancement and polarization control of attosecond waveforms driven by bichromatic circularly polarized laser fields” [1], which details how conventional optics typically employed to manipulate visible laser light can be used to control the polarization of light in the extreme-ultraviolet regime. Additional details are presented in Appendix A.

- Chapter 4 is based on a publication titled “Controlling the polarization and vortex charge of attosecond high-harmonic beams via simultaneous spin—orbit momentum conservation” [2] and describes how exquisite control over the angular momentum of attosecond pulses of extreme-ultraviolet light can be attained by exploiting spin-constrained energy conservation in the highly nonlinear process of high-harmonic generation. Additional information can be found in Appendix B.

- The inspiration for Chapter 5 is manifested from a paper titled “Light with a self-torque: extreme-ultraviolet beams with time-varying orbital angular momentum” [3], which chronicles how an entirely new property of light is both theoretically predicted and experimentally verified, leading to attosecond “whirlwinds” in the extreme ultraviolet regime. Extended details are given in Appendix C.

The Introduction (Chapter 1) attempts to provide the foundation for why we should care about ultrafast processes (Section 1.1.1), why light is an ideal probe of this ultrafast and ultrasmall quantum world (Section 1.1.2), the methods that yield light with properties to perform this task (Section 1.1.3), and how light can actually be used to control the very things we wish to probe (Section 1.1.4). With a proper appreciation of how light can be tailored to observe and control ultrafast processes, I introduce the concept of "structured" light (Section 1.2)—in particular focusing on light fields with structured polarization (Section 1.2.1) and azimuthal phase (Section 1.2.2)—and how the unique properties of structured light yield a much richer picture of the physics of our world. Finally, I finish with a brief overview of high-harmonic generation (Section 1.3), as well as the production (Section 1.3.1) and control (Section 1.3.2) of extreme ultraviolet and attosecond pulses possessing optical spin (Section 1.3.3) and orbital angular momenta (Section 1.3.4). With this motivation, Chapter 2 then gives a broad overview of the experimental setups and techniques employed to conduct the work presented below. After the stage is finally set, the three main acts mentioned above will follow, and finally I conclude this story with some final remarks, future perspectives and anticipated extensions of the techniques described in this thesis.

Additional works

I note that additional contributions in related fields that are not included in this thesis are listed below.

- A manuscript describing "Ultrafast, strong-field photoemission dynamics of ligand-free metallic nanoparticles" is currently in preparation and will be featured in the thesis of Quynh Nguyen of the KM Group.
- A complete account of "Spatially resolved, hyperspectral magnetic imaging using a mutually coherent, phase-locked, table-top high-harmonic source" is currently in preparation and will make an appearance in the thesis of Nathan Brooks of the KM Group.
- "Conservation of torus-knot angular momentum in high-order harmonic generation" by Emilio Pisanty et al [4] provides a beautiful and complete description of the conservation of optical angular momentum during the high-harmonic generation process.
- "Ptychographic amplitude and phase reconstruction of bichromatic vortex beams" by Yuka Esashi of the KM group [5] details how a coherent diffractive imaging technique, ptychography, can be utilized

to reconstruct complex, ultrafast optical wavefronts with high resolution.

- The generation and characterization of extreme-ultraviolet radiation with a spatially varying polarization is described in “High Harmonics with Spatially Varying Ellipticity”, which was spearheaded by Jennifer Ellis during her research in the KM group [6].

- “Phase matching of noncollinear sum and difference frequency high harmonic generation above and below the critical ionization level” also by Jennifer Ellis et al. [7] provides a thorough account of phase-matching effects in high-harmonic generation performed in a noncollinear geometry.

- The sister process of high-harmonic generation, strong-field ionization, with ultrafast, two-color, circularly polarized laser fields is described in wonderful detail in the thesis of Chris Mancuso of the KM Group [8]. Several of the publications described in Ref. [8] have a direct relation to the content of Chapter 3.

  - A detailed analysis of the photoelectron energy spectrum and how it can be precisely controlled by varying the relative intensities of the two-color laser field is given in “Controlling electron-ion rescattering in two-color circularly polarized femtosecond laser fields” [9].

  - A more intimate look at the kinetic energy spectrum of the recolliding electrons (which can be the same electrons that lead to high-harmonic generation) in strong-field ionization with two-color circularly polarized light pulses can be found in “Controlling nonsequential double ionization in two-color circularly polarized femtosecond laser fields” [9].

  - A rather curious finding of an enhancement in the ionization rate of counter- vs. co-rotating configurations of the same two-color laser field is described in “Observation of ionization enhancement in two-color circularly polarized laser fields” [10].

- A complete description of the generation of soft x-ray circularly polarized high harmonics and their utility for performing x-ray magnetic circular dichroism measurements on iron-gadolinium films is presented in the paper “Bright circularly polarized soft X-ray high harmonics for X-ray magnetic circular dichroism”, which appeared in the thesis work of Tingting Fan of the KM Group. [11].

  - I am currently preparing related work on Cooper-minimum-induced spectrotemporal effects in circularly polarized high-harmonic generation with 800 nm and 2000 nm laser fields.

➢ A detailed account of the first generation of spatially isolated, circularly polarized high harmonics is given in “Non-collinear generation of angularly isolated circularly polarized high harmonics” [12]. which was based on experiments and theory developed as a collaboration between the KM and Becker groups at JILA.

Brief Notes on Style and Organization of This Story

Regarding the presentation and style of this thesis—.

- First, the elephant in the room[1] ; the excessive use of “we”. We’re going to hear this pronoun a lot, and it has absolutely everything to do with the fact that science is very, very, very, rarely performed and advanced by the efforts of a sole “I”. Even in such rare cases, the sole “I’s” whom have contributed to science have only been able to do so because of the collective efforts of hundreds, if not thousands of individuals that came before them and laid the foundations supporting their original ideas. So consider the excessive us of “we” as a reoccurring tip of the hat to everyone, both past and present, who has helped make this work, and related works, possible.

- High-harmonic generation is an emerging quantum light source that is impacting light science, as well as enabling new measurement capabilities for quantum dynamics. Many publications and prior theses describe the early history and emerging applications, with much promise going forward. Thus, I will not be comprehensive in my references or explanations of high-harmonic generation (owing to the many, many geometries and schemes for producing coherent EUV and x-ray light via HHG), but every effort will be made to give a generalized, but also accurate, account of HHG, as well as the specific aspects of this now broad and impactful light-science technique as it pertains to the work in this thesis.

[1] Pardon the English idiom here. The meaning of this saying can probably best be summed up by a single word from the Kilivila language—*mokita*—roughly meaning “the truth we all know, but agree not to speak about”.

- The manuscripts which serve as the bulk of this thesis were written in “letter”-style format, with the intention of landing in venues with a diverse readership and thus many of the ensuing discussions are presented in a qualitative fashion, yet the results are rigorously quantitative. This style of story-telling comes along with a heavy reliance on the literature, but has the benefit of being far more welcoming than more mathematical discussions.

Copyright

Prologue

”I thought you said you wanted to be successful?”. He said, ”I Do.”.

He said, ”When you want to succeed, as bad as you wanna breathe, then you’ll be successful.”

Now, I don’t know how many of y’all have asthma here today, but if you’ve ever had an asthma attack before... You short of breathe... You wheezin’... Huuuuhhh... Huuuuhhhh... The only thing you tryin’ to do, is get some air. You don’t care about no basketball game. You don’t care about what’s on TV. You don’t care about nobody calling you. You don’t care about a party. The only thing you care about when you’re tryin’ to breathe is to get some fresh air. THAT’S IT! And when you get to the point where all you want to do is be successful, as bad as you wanna breathe, then you’ll be successful.

I’m here to tell you number 1, that most of you say you want to be successful, but you don’t want it bad. You just kinda want it. You don’t want it badder than you wanna party. You don’t want it as much as you want to be cool. Hell, most of you don’t want success as much as you wanna sleep! Some of you love sleep, more than you love success. And I’m here to tell you today that if you’re going to be successful, you’re going to have to be willing to give up SLEEP.

–Eric Thomas

Chapter 1

Introduction

1.1 Motivation

Throughout recorded history, nature has shown time and time again that just when we think we've got it figured out, some new phenomenon, obstacle, or process emerges that changes how we think about and understand the natural world. Luckily, nature's desire to keep its secrets has been equally matched by our curiosity, leading to the continual pursuit for a "complete" understanding of our world. Of all the tools available to us for teasing out the intricate chemistries and physics that underly the world around us, the use of light has arguably been one of our most powerful capabilities. Whether we're turning on a flashlight to light up a dark environment or shining some of the world's brightest x-rays on chocolate to figure out why it goes "bad" [13], nearly all of us have, in one way or another, used light and its interaction with matter to gain a greater understanding of our world.

The utility of light to illuminate the physical world has been historically paralleled by an interest in our ability to control light itself; either for simply controlling light to illuminate the dark, or for controlling the light-matter interaction. Although control over light-matter interactions is fairly new terminology in comparison to the length of recorded history, several accounts show that our ancestors in ancient Greece, Rome, Alexandria, Mesopotamia, and Tenochtitlan understood the importance of these concepts. "Burning" lenses appear in many classical Greek texts, nanoparticle-containing solutions color the famous Roman Lycurgus Cup, and near-perfect condition mirrors have even been unearthed in the tombs of Egyptian rulers [14]. Fast-forwarding a few millennia, we now find ourselves in an optical wonderland where light waves can be twisted, spun, bent, and slowed down or sped up, seemingly at will. Advanced materials with negative refractive indices—termed metamaterials—can bend light rays around an object, effectively making "invisibility cloaks" more than just science fiction [15, 16]. Literal tractor beams can be realized by tightly focusing laser light, which allow for unprecedented control of particles [17], atoms and molecules [18], proteins, DNA, viruses [19], and even cells [20]. Specifically modified light beams (i.e., "structured" light) can be generated and manipulated at will, which can be used to manipulate objects [21, 22], encode quantum computers [23], transfer information at unprecedented speeds [24], and yield some of the highest resolution images of biological structures [25]. Along with the explosion of applications exploiting optical control, so to has our ability to control light itself, as some manor of optical control is now achievable from x-ray to radio frequency regimes. This has sparked a revolution in "structured" light fields [26], with the goal of tailored light beams to exert specific control of material systems.

The research described in this thesis starts where the sidewalk ends, exploring the new frontier of complete control of ultrafast visible and extreme ultraviolet (EUV) waveforms. Specifically, it details how control over high-intensity, ultrafast light pulses in the visible can be used for controlling attosecond pulses (1 as = 10^{-18} s) of EUV light produced via high-harmonic generation (HHG). As we journey through the work presented below, we'll encounter a variety of unique visible and EUV light waves comprising flowers, doughnuts, and even croissants. These exotic light forms are ideally suited for both improving existing spectroscopic methodologies, and opening new avenues for optically controlling and observing nature's fastest processes.

1.1.1 Life in the Ultrafast Lane

No PhD thesis in ultrafast laser physics would be complete without a brief attempt at justifying why we should care about natural processes that happen on timescales on the order of billionths (10^{-9}) to quintillionths (10^{-18}) of a second, and for good reason. Why should we care about such things? Life, for the most part, is fairly macroscopic and humans can only process stimuli on the order of a few milliseconds, so what could there be to benefit from learning about aspects of nature beyond our sensory limits? Of course, the answer is well-known thanks to a few millennia-worth of scientific thought and discovery; as we look closer at our surroundings, life is made up of increasing smaller and faster “bits” and it is the collective action of these “bits” that make up our every day experiences. Even the biological actions involved in reading and seeing the words on this page exhibit this very behavior [27]. The words are sighted and read in, causing a myriad of neurological processes, themselves controlled by neurons that fire impulses at a rate of ∼15-40 Hz (∼67-25 ms periods). These impulses trigger cellular function and trafficking of vesicles, which traverse mm–μm distances in just a few milliseconds. These vesicles—from a few microns to hundreds of nanometers big themselves—contain chemical mediators composed of amino acids, nucleic acids, and polysaccharides, which travel at near diffusion-limited rates to molecular-specific target sites of cellular machinery. The interactions of the individual macromolecular potentials occur over Van der Waals distances (i.e., angstroms to nanometers), and the potentials themselves are set by the atoms and electrons making up the receptor and mediator, which ”move” on picosecond (atoms) to attosecond (electrons) timescales. Finally, this spatiotemporal journey, which traverses over 11 orders of spatial and 15 orders of temporal magnitude, results in a coherent reading of this excessively long paragraph.

This picture of tiny quantum actors banding together to create the macroscopic physical phenomena of the universe is more than just philosophy, and appears now to just be the way nature goes about its business. Photosynthesis relies on photoexcitation and charge transfer via absorbing pigments, meaning the absorption and subsequent trafficking of photo-induced charge must occur on picosecond times scales or shorter [28]. Absorption of infrared light by CO_2 in the atmosphere results in molecular vibrations with periods of ∼14 fs [29], a time so short that ∼72 trillion of these vibrations occur in the time we blink. The saturation velocity of electrons in state-of-the-art 5-nm transistors is $\sim 10^8$cm/s [30], indicating that an electron crossing through the gate would do so in a time of ∼500 ps. Even looking at your reflection in a mirror involves ultrafast dynamics; the reflection we see is generated by optically driven currents on the mirror surface, and these currents oscillate at the plasma frequency of the material. For a common mirror material such as aluminum, the plasma frequency is around 12-15 eV (depending on purity and underlying structure of the aluminum), which means it takes ∼100 as for the electrons to respond to incident optical field and reflect it [31]. Phase-change materials—which act as memory materials by treating different phases of the material as ’0’ and ’1’ bits—common to USB flash drives and formattable compact-discs can be ”written” by subjecting a laser beam onto the material, which triggers a phase change occurring on picosecond timescales [32]. In fact, this benchmark is already being surpassed by optically-driven magnetic memory devices, which can exhibit phase transitions on the order of a few 10s of femtoseconds [33, 34]. The resistivity of gold, which forms the connections between transistor chips on many of our electrical devices, is on the order of 20 nΩ-m, meaning that it takes about 2 attoseconds for gold to develop Ohm's Law-type behavior [31]. Clearly, many aspects of the natural and technological wonders that surround are daily lives are rooted in fundamental physical processes that take place on ephemeral time and equally imperceptible length scales.

So far, we've got an idea that life is fast, and that these fast processes give rise to the macroscopic phenomena we experience every day. However, this does very little to justify why we should care about nature being so fast and small. Luckily, this answer is straightforward as well; by fully studying and understanding these intricate processes, we can determine how nature is so good at—well, being nature—and with this knowledge we can begin to exploit nature for the benefit of all species on our planet. The efficiency of state-of-the-art solar-cell materials hovers somewhere around 25-45% (commercial units are a bit lower at ∼22%), and much current research is focused on unraveling a similar light-harvesting energy process—namely, electron/charge transport in photosynthesis—to increase solar cell efficiency[1] . Transition state theory, which describes at a basic level how chemical reactants are transformed into products, predicts that transition-state complexes break up during a single vibrational period, which requires few-to-sub femtosecond timing resolution to elucidate the intricate dynamics during chemical transformation (not to mention, needing to disentangle what parts actually form the excited complex). Carbonic anhydrase, the main reason our pH and fluid levels in the body stay balanced, is one of the fastest enzymes, with a reaction rate of $\sim 10^6$ molecules catalyzed per second [27]. Considering diffusion-limited shuttling of carbonic acid (HCO_3^-), this indicates that the entire reaction must take place on few nanosecond, to picosecond time scales, with the breaking and rearranging of bonds occurring on femtosecond time scales. If we can resolve these ultrafast, nanoscopic dynamics and develop a complete picture of how nature accomplishes such tasks, we can then start fiddling with the "knobs" of nature to create exciting and crucial technologies that can solve problems such as renewable energy, custom chemical synthesis, and perhaps even petaHertz electronics driven by laser fields.

[1] We must be careful with our comparisons here. Photosynthesis as a whole, is woefully inefficient, as plants only absorb a finite fraction of solar light. However, the electron/charge transport chain, is incredibly efficient

As such, ultrafast spectroscopies, metrologies, and imaging modalities (not to mention the light sources that drive them) are all needed in order to answer the remaining riddles of the physical world.

1.1.2 Light as an Ideal Observer of the Ultrafast, Ultrasmall, and Ultracomplex

Our story so far is the following; life emerges from ultrafast phenomena occurring over ridiculously small length scales, and often in complex environments. In order to understand these processes, we need some sort of probe that is fast enough, specific enough, and can give enough resolution to achieve the dream of scientists for millennia; watching physical processes take place in real time and space. Out of all the tools that we have at our disposal for elucidating life's mysteries, light is perhaps the most ideally suited to accomplish all of these tasks[2] . The reasons for this can quickly pile up to become more numerous the page count of this thesis, but all can be boiled down to the basic physical quantities of a light wave; the wavelength, λ, the associated period, T, of the light-wave oscillation, the amplitude or "strength" of the wave, and the associated spectral, spatial, and temporal phases. The wavelength, along with its associated spectral phase, largely determines how light will interact with the environment (e.g., absorption, scattering, reflection, diffraction, etc.), while the optical period sets the speed limit for what we can observe, and the amplitude determines what type of interactions we may have access to. The wavelength also determines the maximum resolution we can expect to attain by using light to image physical systems, which manifests in the Abbe formula that determines the smallest size object we can resolve with conventional optical systems, $d = \lambda/(2nsin\theta)$ [14]. As a final bonus, the bosonic nature of photons means that we can squeeze large amounts of them into finite spectral, spatial, and temporal windows, which it vital for obtaining signals from weakly interacting systems.

However, light as we find it in nature is far from the ideal observer we require it to be. Naturally produced light occurs primarily through thermal or chemical reactions, which emit wavetrains in a typically *incoherent* fashion. In plain terms, this means that the light emitted from natural sources does not possess a consistent and predictable spatiotemporal structure, owing to the finite nature of the excited states that

[2] Of course, spectroscopic and imaging techniques using particle-based sources (e.g., electrons, neutrons, etc.) have their own advantages and can yield, in some cases, more information than light itself. However, that discussion is for a different thesis than the one at hand.

produce natural light[3]. In order to exploit the properties of light to observe the ultrafast, ultrasmall, and ultracomplex, we need *coherent* sources of light with reproducible and predictable waveforms that lead to reproducible and predictable interactions with matter.

1.1.3 Coherent Light, Lasers, and Ultrafast Optical "Pancakes"

The early days of optical research on methods of producing coherent light were rather simple; poke a set of small holes or slits in a material, those holes/slits will act as secondary sources of an incoming light source and, due to their finite size, will create spatially coherent light at the output. Such schemes were pioneered by folks like Newton, Young, Fresnel, and countless others [14]. These methods provided the spatial coherence necessary for observing interference effects and, to date, still allow straightforward tests of the spatial coherence of a light wave or beam. However, producing temporally coherent light is a much more daunting task, owing to the fast oscillation period of the light. The recipe for producing temporally coherent light took a bit longer to figure out, but the basic framework was laid out in Einstein's work on absorption and emission of light quanta[4]. However, actually producing temporally coherent light was much harder than envisioned in the early 1900s, and it wasn't fully realized in the optical regime until the invention of the laser in 1960 [35]. With the advent of the laser, spatially and temporally coherent light could be produced in the laboratory, which finally provided the high-quality waveforms needed to harness the power of light as an ideal probe of nature's most intricate processes. However, the high-quality of the produced light led to a quick realization; a high temporal coherence demands a low *spectral* coherence, which translates to highly monochromatic sources. Conversely, a low(er) temporal coherence is characteristic of a waveform possessing many frequencies, and thus low spectral coherence. Practically, this admittedly overly-simplified view is one source of the schism between frequency-domain and time-domain experiments. High resolution in the frequency domain gives an accurate picture of the wavelength-dependence of light-matter interactions and requires light with a high temporal coherence, while high resolution in the time domain gives us the molecular movies we've dreamed of for centuries, but blurs the "colors" of the movie, so to speak (i.e., the

[3] To appreciate this, consider the average filament-based light bulb. Thermal excitation via Ohmic heating causes the filament to glow and emit light, which itself is the result of electronic decays from thermally excited states to ground states. These states have ∼ns lifetimes, meaning the structure of the emitted wave is only coherent on the same temporal window.

[4] Interestingly enough, this same paper also provided the framework for quantized momentum conservation in absorption and emission processes, which is the basis for techniques such as laser-atom cooling and optical trapping.

spectral resolution is reduced). Unfortunately, Heisenberg showed us that both can't be obtained at the same time, and for the sake of brevity (for a change), we'll keep our focus on the production of light of the former, which brings us into the realm of pulsed lasers. Fortunately, as my colleagues have recently shown [36, 37], high-harmonic light has analogies with squeezed light, enabling exquisite advanced spectroscopies that can achieve temporal resolution of 10 attosecond lifetimes, while preserving sufficient energy resolution 100meV to allow state- and band-specific measurements. Thus, by harnessing the temporal structure of HHG and its perfect synchronization to the laser field, the limits imposed by a simple analysis of the Heisenberg Uncertainly Principle has been far surpassed.

Interestingly enough, the first laser produced by Maiman in 1960 [35] was actually a pulsed laser, in that it did not emit a continuous wave (CW) of light, but rather emitted light "pancakes" composed of temporally confined photon bunches. At first glance this appeared to provide the necessary ultrafast "strobe lights" required to capture physical dynamics in real time; however, particulars of the first ruby laser resulted in an unstable *train* of pulses, which rendered them fairly useless for time-resolved studies. In order to obtain a stable train of light "pancakes", it was quickly realized that one would need to precisely control the frequencies of the participating cavity modes, *as well as* their corresponding spectral phases (in fact, this is also needed for stable, monochromatic radiation from CW lasers, such as the popular He-Ne laser). This realization ignited interest in "mode-locked" lasers—so named because their cavity modes were "locked" to a set of certain frequencies and phases—and within a few short years, stable, reproducible pulses were obtained from lasers of all types (e.g., CO_2, ruby, HeNe, dye lasers, etc.)[5] [38]. Work continued on this trajectory for a few decades, resulting in numerous strategies and schemes for creating mode-locked lasers [39] that could produce shorter and shorter pulses. The most rapid progress was made in realm of dye laser technology, where the "colliding pulse" geometry (combined with proper negative dispersion in the laser cavity) could bestow sub-30 fs pulses [40] onto the scientific world. These pulses were certainly fast enough to resolve nature's fastest dynamics, even if the lasers themselves were quite complicated. Just as dye lasers were approaching near single-cycle optical pulses, an unexpected result in 1991 out of the group of Wilson Sibbet at St. Andrews University showed a relatively new laser material, titanium-doped sapphire

[5] For a wonderful account of the early history of mode-locking, the distracted reader is referred to Ref. [38].

(Ti:sapph), could be self-mode-locked, resulting a stable train of pulses lasting for just 60 fs [41]. The robust and straightforward nature of the self-mode-locking process—combined with the compactness and relative simplicity of solid-state laser design—stimulated an avalanche of momentum in generating ultrafast pulses from Ti:sapph lasers, and before the turn of the recent millennium, pulses lasting less than 10 fs were produced directly from Ti:sapph lasers around the world [42–44]. With a variety of short pulse lasers available at hand, researchers now had the recipe, to produce the world's fastest strobe lights, which paved the way for obtaining molecular movies of chemical and physical dynamics in a continually growing number of complex systems.

1.1.4 Light as a an Ideal Director of the Ultrafast, Ultrasmall, and Ultracomplex

Nearly as soon as Maiman and others demonstrated that stable laser operation could be achieved in a variety of gain media, researchers also began contemplating the use of coherent laser light to not only observe nature, but also control the light-matter interaction (aptly named "coherent control"). Although quite broad in context now, the basic tenants of coherent control involve tailoring the phase (either spatial, temporal, spectral) of a fully coherent light source, such that it acts in a particular fashion on matter, which in turn would yield control over the ensuing dynamics. Such a "quantum director" would allow us to steer the electronic and structural behaviors of matter, solely by precisely controlling the degrees of freedom of the laser light. Although elaborate schemes for laser-based coherent control exist in a variety of physical fields and are too numerous to name here, in the context of strong-field, ultrafast physics, we find ourselves primarily concerned with the control over—you guessed it—ultrafast nuclear and electronic processes (i.e., chemical reactions, and charge/spin transport). The natural choice for controlling such processes are the high-powered amplifiers and attosecond light sources we met in the last section; high-intensity optical fields can compete with Coulombic binding potentials, while attosecond pulses via HHG (Section 1.3) provide sufficiently fast temporal resolution to capture the ensuing dynamics. In particular, this marriage of a subfemtosecond light pulse and its femtosecond optical generator has resulted in elegant demonstrations of active control of molecular dynamics [45, 46], charge migration [47], electronic dynamics [48–50], and ultrafast nanoscale phenomena [51].

1.2 Structured Light: Optical Spinors, Singularities, Vortices, and the Angular Momentum of Light

Before we get our feet wet in the realm of sculpted, attosecond, high-harmonic waveforms, we must first get a firm grasp of how structured light is generated and controlled in the visible regime. Structure is a pretty odd thing to talk about when it comes to light, but just as we describe the structure of matter in terms of bond lengths and angles, lattice "constants", and quantized energy levels, so too can we speak of the structure of light in terms of the parameters that define it. In the context of the work here, we are mostly concerned with the structure of coherent laser light, which can be adequately described by a product of a Gaussian wavepacket in time and a Gaussian amplitude distribution in the transverse plane[6]. For simplicity, we assume our laser is operating in the lowest-order, transverse spatial mode (much like the oscillator and amplifier employed in this work) and that the temporal duration of the Gaussian wavepacket is much larger than its optical period.

The complex amplitude of a coherent, collimated Gaussian laser beam (see Figure 1.1) propagating in time can be described—in the cylindrical coordinate system—via

$$\begin{aligned} E(\rho, z, t; k_0) = E_0 \frac{w_0}{w(z)} & e^{\left[\frac{\rho^2}{w^2(z)}\right]} e^{i\left[\frac{k_0\rho^2}{2R(z)} - \Phi_G(z)\right]} \\ \times & e^{-\frac{(t-t_0)}{\tau^2}} e^{-i(t-t_0)\omega_0} \\ \times & \begin{pmatrix} \rho\cos\phi \\ \rho\sin\phi \end{pmatrix} \end{aligned} \tag{1.1}$$

where we have explicitly included the vector nature of the light-wave oscillation with the final term. In the above, E_0 is the amplitude of the beam, w_0 is the beam waist radius (defined as *radius* of the beam at the $1/e^2$ intensity points) at $z = 0$, $w(z)$ describes the increase in w as the beam propagates, k_0 is the wavenumber ($k_0 = 2\pi/\lambda_0$) of the pulse with carrier frequency ω_0, $R(z)$ is the radius of curvature of the spatial wavefronts, and $\Phi_G(z)$ is the so-called Gouy phase[7]. Physically, E_0 is the "strength" of the laser field, the first exponential term and its prefactor describe the spatial extent of the beam, the complex, spatial exponential describes the evolution of the wavefront during propagation, and the remaining exponentials

[6] The many benefits of a using a Gaussian basis when describing coherent light can be summed up quite nicely; they have "well-behaved" Fourier transforms.

[7] An intuitive description of the Gouy phase can be obtained via simple ray tracing arguments. See Ref. [52] for details.

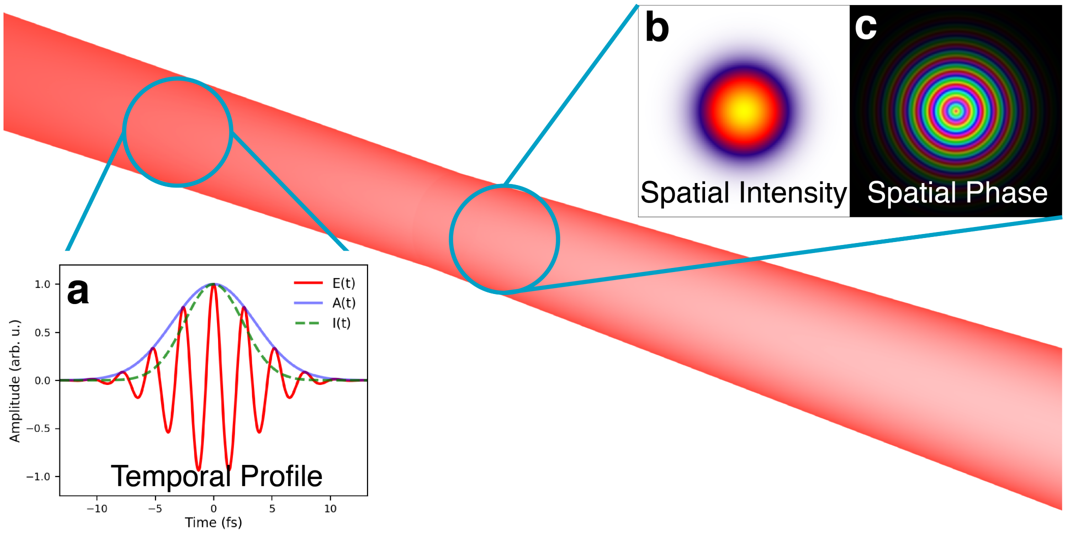

Figure 1.1: **General schematic of a Gaussian laser beam.** The common Gaussian laser beam is fundamentally composed of spatial and temporal parts. **a** The temporal part is composed of a product of a carrier wave (here, the carrier wave (red line) and has a frequency, $\omega_0 = 790nm$), with a Gaussian temporal amplitude (blue line). Additionally, the intensity envelope of the pulse is shown (green dashed-lines), which is much narrower than the amplitude envelope. **b** The spatial amplitude of a Gaussian beam resembles a bright, circular structure that falls off exponentially as we move to the beam edges. *c* The spatial structure also has an imaginary component associated with the phase of the beam, which under typical conditions exhibits a radially symmetric profile.

describe the duration of the pulse as well as its carrier frequency. Many of these quantities can be further described via a physically convenient relation, the confocal parameter b,

$$b = \frac{2\pi w_0^2}{\lambda} = 2z_R \tag{1.2}$$

where z_R is the Rayleigh length of the beam, and translates to the distance, z, that it takes for beam to double in transverse,spatial extent. These terms relate the parameters of Equation 1.1 to physically measurable—and controllable—quantities of laser radiation

$$w(z) = w_0\sqrt{1 + \left(\frac{z}{z_R}\right)^2} \tag{1.3}$$

$$R(z) = z\left[1 + \left(\frac{z_R}{z}\right)^2\right] \tag{1.4}$$

$$\Phi_G(z) = \arctan\left(\frac{z}{z_R}\right). \tag{1.5}$$

These fundamental quantities can completely describe the propagation of "well-behaved" light beams, and the aforementioned parameters can be manipulated in some way to structure a laser-like light beam.

In these works, and throughout the literature, we refer to structured light as coherent radiation with a manufactured polarization, intensity, and/or phase. The polarization—which is the familiar "wiggling" of the electric field—can be accounted for with a convenient formalism based on Jones Calculus. By isolating the carrier wave, grouping the spatial phase and amplitudes, and considering we're working at the beam's waist (i.e., $z = 0$), we can recast Equation 1.1 in a more convenient from,

$$E(\rho, t) = E_0(\rho)e^{-i(t-t_0)\omega_0} \tag{1.6}$$

with $E(\rho)$ being the spatially dependent, complex amplitude. We can further decompose Equation 1.6 into two transverse Cartesian vectors, as Cartesian unit vectors tend to be more similar to the wiggling ropes of our youth

$$E_0(\rho) = \begin{bmatrix} E_0(x)e^{i\varphi_x} \\ E_0(y)e^{i\varphi_y} \end{bmatrix}. \tag{1.7}$$

This not only provides a computationally friendly formalism for computing the polarization distribution of a propagating laser wave, as properties of matrix algebra can reduce complicated equations to a single eigenvalue operation (much like the propagation of Gaussian beams via Fourier methods). Physically, it provides the comfort of a 2D transverse coordinate system, while also resulting in a more intuitive picture of polarization and how it evolves; simply "tug" on the components given in Equation 1.7, and their superposition yields the instantaneous polarization state. This also provides a natural extension to time-dependent polarization, which is the basis of the polarization-gating technique for producing IAPs [53, 54]. In practice, polarization of ultrafast, high-powered laser beams are controlled by employing thin birefringent crystals (i.e., waveplates) that possess crystal axes with unequal dispersion relations. When cut and polished just right, a controllable amount of phase can be added to each component in Equation 1.7, allowing for precise control over the light beam's polarization. As a side note, this phase modulation can be performed without altering the other phases in Equation 1.1 (aside from a spatially uniform spectral phase acquired on passing through the crystal), which is convenient for generated highly structured optical waveforms.

1.2.1 Optical Spinors: Helical Field Lines and The Spin Angular Momentum of Light

Since ultrashort, coherent laser beams carry energy and propagate in space, they must also possess some form of optical momentum. Termed *radiation pressure*, the optical, linear momentum of light can be exploited to exquisitely control light-matter interactions, and serves as the basis for techniques such as optical tweezers [17, 20, 21] and laser-mediated atom trapping/cooling [55–57]. At the turn of the 20$^{\text{th}}$ century, very precise measurements of the linear momentum of light [58–60] showed that indeed light could impart an *optical force*. At nearly the same time, John Poynting was having a field day with the mathematical description of the energy flow of light, and in 1909 "suggested" that light with two orthogonal, oscillating components (i.e., non-zero components of Equation 1.6) forms a spiraling cylinder as it propagates, and thus should exhibit an angular momentum as well [61]. This relatively new angular momentum was termed *spin angular momentum* (SAM), in analogy with the spinning nature of the propagating electric field lines. Thanks to careful work by Richard Beth in 1936 [62], we now know that the SAM of light, on the photon level, is quantized in units of $\hbar$ such that the SAM, S_z, is equal to $\pm\hbar$ [62], where left-circularly polarized (LCP) light is carries a SAM of $-\hbar$, and right-circular polarization (RCP) carries SAM of $\hbar$ (in the literature, SAM is often designated with a lower-case sigma, $\sigma_{+1,-1}$). The quantized nature of photonic SAM can be related to the near continuous range of the polarization states of light (e.g., linear, elliptical, LCP/RCP, and everything between), by considering all polarizations of coherent light as being composed of a superposition of LCP and RCP waves with relative amplitudes and phases, as RCP/LCP waves are themselves the corresponding optical eigenstates for the SAM operator. For monochromatic beams, this leads to a fairly boring variety of Lissajous profiles in the transverse plane; monochromatic, homogenous beams are either linearly or elliptically polarized. Despite the apparent simplicity of polarized monochromatic radiation, this realization formed the foundations of optical dichroism, which is perhaps one of the most powerful methods for discriminating chiral dynamics in complex environments. When combined with the recent advances of ultrashort laser pulses, the polarization of light can also be used to impulsively align molecules [63], providing exquisite control of the light-matter interaction in photochemical dynamics.

So far we've kept things relatively simple by only considering the transverse nature of homogeneously

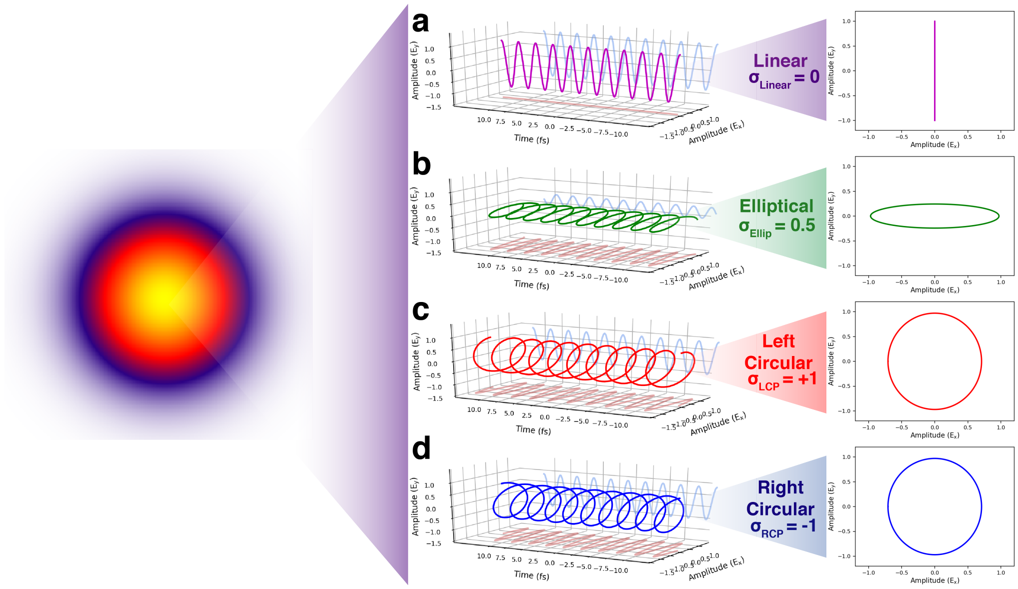

Figure 1.2: **General overview of common SAM states in laser waveforms.** Although a Gaussian laser beam has a uniform transverse intensity profile, the underlying temporal waveforms can possess a range of different amounts of optical SAM, which imparts to the laser beam the unique polarization states. Here, some common polarization states are sketched out in a spatiotemporal landscape, while Lissajous curves of the electric field in the transverse plane are given in the right most column. The polarization states shown are **a** linear, *b* elliptical, **c** left-circular polarization, and **d** right-circular polarization. Note that we have shown the x,y components of the fields, which themselves represent the orthogonal bases used in the Jones calculus formalism of polarization (Equation 1.6). Also note that the *expectation* values of each field's SAM are given as well.

polarized light waves. However, SAM requires that the light wave propagate, which means our picture of flat field lines on a plane is missing a big part of the physical picture. In our current picture, the polarization of a light beam is given by points of linear or elliptical polarization on a 2D plane, but in reality (i.e., 3D) these points are actually threads of constant polarization that can exhibit a complex, 3D spatial structure. These threads, in the context of optical SAM and polarization, form *polarization singularities* that may be either purely linearly or circularly polarized, and provide the separation between regions of elliptical polarization in the light beam. This aspect was first discussed by Nye in early 1980s [64, 65], yet the realization of generating and controlling, complex, structured, *vectoral* light beams was not obtained until just a few decades ago [26]. Such beams fall under the general class of light beams with structured polarization, and are described by a complex distribution of polarization vectors at any instance in time (i.e., a slice in the transverse plane). One example of such a beam is the so-called "bicircular field", which is composed of two circularly polarized, ultrafast laser beams with a non-degenerate frequency (see Figure 1.3). Such a beam exhibits exotic Lissajous profiles of the electric field lines that depend on the relative frequencies and amplitudes of the constituent waveforms, and clear singularities can be observed in their transverse profiles. More exotic polarization structures can be obtained via inhomogenous phase elements (e.g., s-wave and q-plates [66, 67]), which can yield optical "doughnuts" with radial or azimuthal polarization. Although we are just beginning to scratch the surface of the exotic, spatial polarizations of cylindrical vector beams, they offer enormous potential [26, 66]. In the context of strong-field physics and attosecond science, spatially defined polarization fields would give unprecedented control over the HHG upconversion process, which could be used to generate uniquely structured attosecond pulses, as well as precisely guiding the recollision of liberated electronic wavepackets in molecular self-imaging.

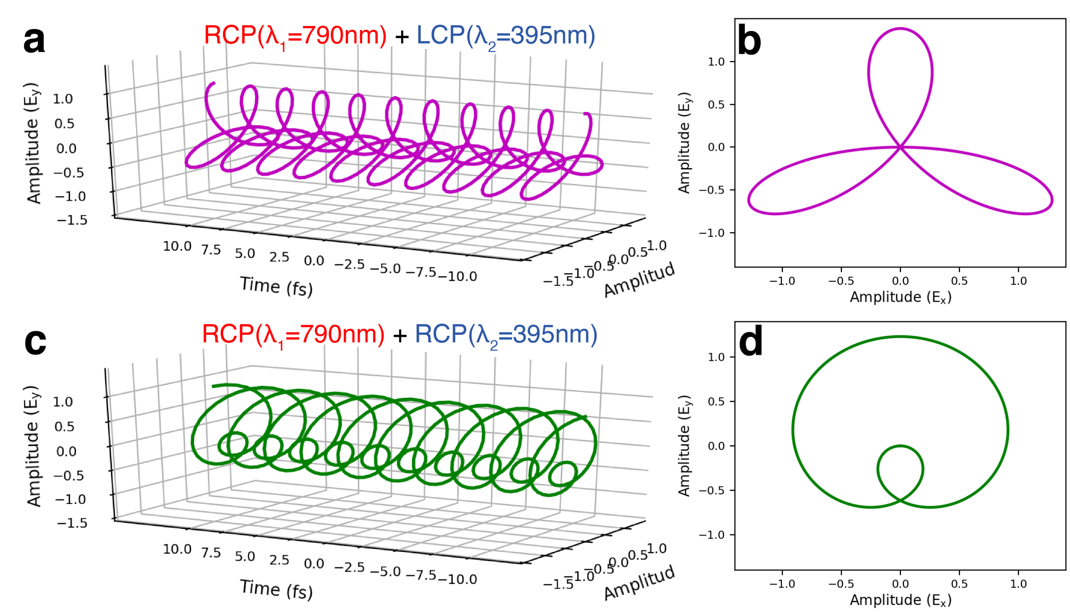

Figure 1.3: **Comparison of mixed optical fields composed of circularly polarized fields with non-degenerate frequencies—the bicircular field.** When two circularly polarized optical fields, but with non-degenerate frequencies, are superposed the result is a unique waveform with non-trivial polarization structure. Here, two configurations of the bicircular field are shown, which are synthesized from a fundamental wave ($\lambda_1 = 790$nm) and its second harmonic ($\lambda_2 = 395$nm). **a** When the two constituent waveforms possess opposite SAM (i.e., they are "counter-rotating"), a "trefoil" optical wave is generated and contains a polarization singularity at center. This more easily exemplified in the Lissajous figure shown in **b**. If the fields possess the same SAM, the bicircular field is said to be "co-rotating" **c**, resulting in a very different Lissajous profile **d**.

1.2.2 Optical Whirlwinds: Twisted Photons, Vortices and The Orbital Angular Momentum of Light

The first notion of an additional component comprising the angular momentum of light can be traced back to Charles *Galton* Darwin[8] whom suggested that momentum conservation in high-order, optical transitions (e.g., quadruple and octupole) required an optical counterpart possessing orbital angular momentum (OAM) in quantized units of $\hbar$ [68]. However, it took nearly 60 years before it was realized how coherent light beams could be produced with quantized amounts of OAM. Although optical vortices had been discussed and observed for several decades [22, 64, 65], the key contribution of Allen and coworkers in 1992 was connecting an azimuthally varying, quantized phase, $e^{i\ell\phi}$, to photonic energy flow. This implied a quantized, optical OAM given in units $\ell\hbar$, where ℓ is the standard OAM quantum number [69]. Such beams are characterized by the presence of a phase singularity (typically located on the beam axis), which is characterized by a rapidly varying azimuthal phase structure resulting in a point of zero intensity in the transverse plane (see Figure 1.4b). Aside from demonstrating that an azimuthally varying phase front possesses OAM, the seminal work by Allen showed that these *optical vortex* beams were natural solutions of the Helmholtz equation in a cylindrically symmetric coordinate system, suggesting that they could be generated, propagated, and even controlled. Figure 1.4 shows the first realization of generating an OAM beam using a cylindrical-lens mode-converter. These beams were found to be described a product of the Gaussian beams of Section 1.2 and an amplitude distribution described in terms of Laguerre polynomials. Such Laguerre-Gaussian (LG) beams, satisfy the following spatiotemporal amplitude distribution

$$
\begin{aligned}
LG_{\ell,p}\left(\rho,\phi,z;k_0\right) = E_0\frac{w_0}{w(z)}\left(\frac{\sqrt{2}\rho}{w(z)}\right)^{|\ell|} L_p^{|\ell|}\left(\frac{2\rho^2}{w^2(z)}\right)& \\
\times e^{\left[-\frac{\rho^2}{w^2(z)}\right]} e^{\left[i\ell\phi + i\frac{k_0\rho^2}{2R(z)} + i\Phi_G(z)\right]}& \\
\times e^{-\frac{(t-t_0)}{\tau^2}} e^{-i(t-t_0)\omega_0}& \\
\times \begin{pmatrix}\rho\cos\phi \\ \rho\sin\phi\end{pmatrix},&
\end{aligned}
\tag{1.8}
$$

where the indices $\ell = 0, \pm1, \pm2, ...$ and $p = 0, 1, 2, ...$, which must be integers, describe the quantized degree of azimuthal phase variation (commonly referred to as the ”topological charge” of the beam) and number

[8] No, not the Darwin of naturalistic notoriety. Although, Charles G. Darwin was his grandson.

of non-axial radial nodes in the beam, and $L_p^{|\ell|}$ are the associated Laguerre polynomials [70]. This key result not only showed that all helically phased light beams possessed OAM, but that such beams could be generated in the laboratory. Moreover, the paraxial nature of these beams provided a clean separation of SAM and OAM, suggesting that SAM and OAM could be controlled independently. Moreover, the helically phased wavefronts suggested a spiraled flow of photon momentum, and thus an optical torque, which was demonstrated via the rotation of suspended cylindrical lenses [69].

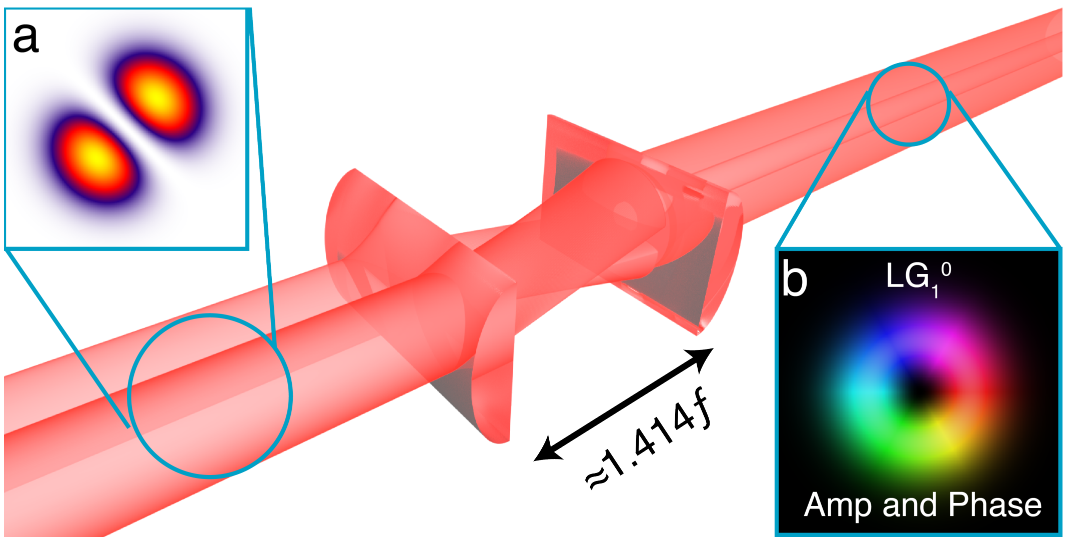

Figure 1.4: **Schematic showing the original method used to produce an optical OAM laser beam via a cylindrical-lens mode-converter.** The first method of producing a laser beam possessing OAM—and satisfying Equation 1.7—employed a cylindrical-lens mode-converter to synthesize an $\ell = 1$ LG beam from a uniquely structured Gaussian beam. **a** When a Hermite-Gaussian beam impinges on a separated pair of cylindrical lens (which are separated by $\sqrt{2}f$, with f being the common focal length of the two lenses), the input beam in transform into an OAM beam **b** possessing a "doughnut"-like amplitude distribution and an azimuthally varying phase. In **b**, the amplitude of the OAM beam us represented in brightness, while the phase is represented in false rainbow colors.

With the introduction of a new, controllable degree of optical freedom, many research and industry groups began to explore the generation and application of optical vortices in light-matter interactions. Although first obtained using cylindrical lens mode converters, there now exists a variety of methodologies for importing azimuthal phase fronts to laser beams (e.g., spiral phase plates (SPPs), q-plates, spatial light modulators (SLMs), forked diffraction gratings, etc. See Refs. [23, 24, 26, 67, 70] for extensive surveys). With OAM beams in hand, the applications quickly became apparent, largely owing to the lack of restriction on the absolute value of the OAM in a beam can carry. Since the photonic momentum is quantized in $\ell\hbar$ per photon, and ℓ can take on any positive or negative whole integer, theoretically, arbitrary amounts of OAM could be imparted to a light beam, and possibly transferred to material systems. This was shown just three years after the initial demonstration of OAM beams [71], which opened the door for microparticle rotation, manipulation, and trapping with OAM beams [21]. The rise of quantum computing and logic sparked its own surge of interest in designing and manipulating OAM beams, as the large state space available in an OAM beam could in principle yield much more efficient quantum computations and logic protocols, as paralleled operations would no longer be restricted to the superpositions of a two-state basis set (i.e., SAM states) [23, 72]. This unique property of OAM beams also has merits in optical communication protocols, and large amounts of data can be multiplexed into an OAM beam carrying a superposition of topological chargers [73]. Reading the information simply require a mode analyzer, and impressively fast data transfer rates, in atmosphere, have already been achieved [24]. OAM beams have also made their way into biological and chemical fields, the unique phase and amplitude profiles of OAM beams can be manipulated to yield superresolution images of complex biological structures via a stimulated-emission-depletion optical excitation in laser-based microscopies (STED microscopy) [74]. Finally, we note a unique property of beams possessing SAM and OAM; they form mixed eigenstates of the L_z and S_z operators, which couples their SAM and OAM [75, 76]. These exotic light beams create unique optical field topologies, allowing for literal optical knots to be tied, which themselves are formed of the same singular threads discussed in Section 1.2.1. This leads to complex, topological optical structures that have great promise for quantum logical applications, as well as generating custom light fields with unique symmetries [26, 75, 76].

In the context of atomic and optical physics, the helical momentum flow of OAM beams was largely applied to inducing quantized rotations in atomic clouds of Bose-Einstein condensates, allowing for fundamental studies of many particle interactions to be studied [77, 78]. Interestingly, a good deal of the curiosity and interest in OAM beams has been due to similar thoughts by Darwin in his 1932 paper; the presence of OAM in a light beam should enable access to optically forbidden transitions, such as quadruples, otcupoles, and direct spin-flips. This sparked numerous theoretical [79–81] and experimental [82, 83] inquiries into the nature of the OAM in a beam (i.e., extrinsic vs. intrinsic [84]), and how it may be transferred to material systems [85, 86]. Although great progress has been made, the original ideas of Darwin—and the hopes of others working in OAM light-matter interactions—were quickly dashed away when it was realized that detectable signals of unique optical transitions mediated by OAM beams were near impossible to detect, requiring elaborate geometries [83] to extract the transfer of OAM to bound electrons. The difficulty can be summed up quite nicely with the help of our friend Heisenberg. Just like linear momentum, there exists another uncertainty relationship for angular momentum and angular position,

$$\Delta\ell\Delta\phi \geq 1/2. \tag{1.9}$$

Physically, this means that if we place an atom or molecule in an OAM beam, we have then localized its wavefunction somewhere along the azimuth, which yields a fairly high precision for position and thus a low precision for measuring the OAM-mediated interaction. As such, the discrete nature of photonic OAM is lost on the particle, and coherent optical excitation does not need to conserve OAM (and it doesn't). Put another way, if a molecule is much smaller than the beam itself *and* it is located far from the singularity, the molecule is largely unaware of the varying azimuthal phase and the molecules responds solely to the SAM of the light field (since SAM is always an intrinsic property of coherent light beams).

Despite this "nail in the coffin", recent progress in extreme nonlinear optics and solid-state physics have shown new capabilities of OAM beams, as well as unique applications that can exploit the OAM in vortex beams to induce novel excitations of matter. A large body of work has focused on the interaction of X-ray OAM beams with magnetic systems [87–89], with a particular emphasis on magnetic vortices and skyrmions [90], which have promise in magnetic memory devices [91]. Also, a paralleled interested in semiconductor excitations with OAM beams has resulted in several theoretical investigations into OAM-mediated light-matter interactions [92–94]. Moreover, recent theoretical predictions have shown x-ray OAM beams could exhibit enhanced dichroism at the L absorption edges, allowing for separation of charge and orbital contributions to the angular momentum dynamics of spin systems [95]. In the realm of attosecond science, OAM beams can also serve as a unique probe of photoionization dynamics, allowing for attosecond time delays to be obtained with sub-wavelength spatial resolution [96]. Although these exotic applications have yet to be demonstrated experimentally, the advent of high-harmonic sources capable of producing attosecond, EUV light containing OAM [2, 97–103], as well as free-electron laser sources of x-ray OAM beams [104, 105], has provided unique optical vortex beams that could, and likely will, lead to realization of these exotic spectroscopic and metrology modalities.

1.3 Nature's Most Exotic Light Source; High-Harmonic Generation, Attosecond Light Waves, and Twisted Beams of EUV Light

Now that we've spent some time to get a firm grasp on the nature of structured light and its angular momentum properties, we can finally begin our journey as to how structured, visible light can used to create structured attosecond, EUV light via the highly non-linear and non-perturbative[9] upconversion process of high-harmonic generation. We've already dropped hints alluding to the field-driven nature of HHG in the previous sections, and this will (and does) serve as the central theme not only here, but also throughout the works described in this thesis. The field-driven nature of HHG is inherently quantum-mechanical [106], but many of fundamental aspects can be nicely summed up in a semiclassical, three-step model (STSM) [106–108]; a strong-laser field liberates an electronic wavepacket from an atomic or molecular ground state, and this wavepacket emerges into the continuum with zero momentum (i.e., note that this implies the ionization is a tunneling event, as multiphoton excitation would leave the electron with some finite momentum upon entering the continuum). Once freed of its atomic prison, this wavepacket is accelerated by the external laser field, and over the course of half an optical cycle (or more), it may finally recollide with the its parent ion, and in the process emit a high-frequency photon. When this process is performed under proper conditions such that the harmonic emission is *phase matched*, a bright, comb-like spectrum of high-harmonics are produced, which themselves exhibit full spatial and temporal coherence, that extends into the EUV [109, 110] and soft x-ray [111–116] spectral regions. The fully coherent nature of these beams—as well as their high frequency and sub-femtosecond pulse durations—makes them invaluable tools for investigating the extremely fast, extremely complex, and extremely small dynamics of our world.

[9] We should note that "non-perturbative" in the context of nonlinear optics and HHG refers to the non-perturbative scaling of the spectral intensity of the high-harmonics, and not the discrete quantum channels composed of photons that give rise to harmonic frequencies in traditional nonlinear optics.

1.3.1 A Brief History of Strong-Field Physics and High Harmonic Generation

The discovery, understanding and development of high harmonics as a new strong-field response of matter to light, and as a new quantum light source, took the marriage of atomic, optical, quantum, laser, nonlinear and strong-field science. Interestingly, the basic tenants of the semiclassical STSM were well known by the photoionization community just shortly after the invention of the laser. The advent of powerful, coherent light sources initially sparked questions related to the tunneling process in oscillating electrical fields (sometimes referred to as AC fields, inspired from electronics), and the work of Keldysh was the first breakthrough by providing a “static” approximation to AC tunneling in long wavelength fields [117]. Additionally, this seminal work also provided an *adiabaticity* coefficient that defined the range of laser and ionized target parameters for which a tunneling approximation would be valid,

$$\gamma = \sqrt{\frac{I_p}{2U_p}}. \tag{1.10}$$

Here, I_p is the ionization potential of the irradiated target, and U_p is the cycle-averaged, kinetic energy of the electron in the field (i.e., Ponderomotive potential, $U_p = e^2 E_0^2/(4m_e\omega_0^2)$). This relatively compact equation has a classical interpretation as the tunneling ”time” of the electron divided by the optical cycle of the laser field. This simple relation—although derived in hydrogen with a pretty stiff approximation of the electric field—would initiate the (theoretical) birth of strong-field physics, and provide the foundation for the modern theories of strong-field photoionization (i.e., step 1 in the STSM).

Over the next decade or so, Keldysh’s theory was refined [118–121] and experimental progress was made on detecting multiphoton and tunneling ionization processes in laser-irradiated atoms and molecules, more or less agreeing with the ionization rates inspired by Keldysh theory. However, a surprising result out of Saclay in 1979 showed that just as bound electrons can absorb multiple photons on the way out of their atomic potentials, so too could the liberated electrons [122]. This process, *Above Threshold Ionization* (ATI), involved free-free transitions between continuum states modified by the vector potential of the laser field (often referred to as “laser-dressed states”), and manifest as discrete peaks of excess energy in the photoelectron energy spectrum[10] . This initial report, and several subsequent studies [123, 124], showed

[10] The analogy with the discrete, comb-like nature of HHG spectra is glaringly obvious, which is the reason we often refer to ATI and HHG as “sister” processes.

that the laser potential could no longer be considered as a minor perturbation to the electronic dynamics in strong-field photoionization, which upgraded our current model of strong-field physics to the non-perturbative regime.

With the ingredients for the first two steps in hand, all that had to be done was consider the possibly of recollision of the electron with its host atom. While great theoretical strides in describing the ATI process were being made [108, 125, 126], the first reports of multiple harmonic conversion in rare gases began to surface in the late 1980s [127–129]. Certainly the production of EUV light from visible laser sources was exciting in itself, but the spark that lit the HHG fire was the presence of a spectral plateau observed in [128], as this was in drastic disagreement with perturbative non-linear optical processes. While Kuchiev had a very nice theoretical description of a nanoscale dipole antenna, that combined many key concepts, work by Kulander and his group at LLNL were first to implement a full quantum model of the HHG process that described this (and many other) unique features of high-harmonic spectra [106]. Later, the ideas behind the quantum-mechanical model were adapted to the classical STSM of HHG [107], which is summarized in Figure 1.5. These experimental demonstrations, along with the proper theoretical tools to describe the findings, triggered an explosion of research into strong-field optical physics, and in particular HHG, and true to its name the ultrafast community kept pace. Interestingly, in HHG the transition from the continuum back to the ground state is a dipole transition—thus, the process must be phase matched to generate a good spatially coherent beam, and also to achieve good conversion efficiency from laser light to EUV light. The first complete picture of the time-dependent phase-matching dynamics of the upconversion process were laid out for the EUV region by 1998 [113, 130–132], and by 2014 phase-matching in the soft x-ray region was fully understood [133–137]. This lead to the generation of bright, spatially and temporally coherent, EUV [110, 114] and soft x-ray [133–137] laser-like beams from university-scale laser sources.

Around the same time that laboratory HHG sources were coming online in the mid-1990s to early 2000s, theoretical developments based on a path integral formalism to the HHG process [138, 139], coupled with optical Fourier synthesis methods [140] lead to the notation that the spectral plateau in HHG spectra possess the necessary amplitudes and, if phase-locked, should support attosecond pulses [141]. This generated much excitement in the strong-field community, leading to first demonstration of an attosecond

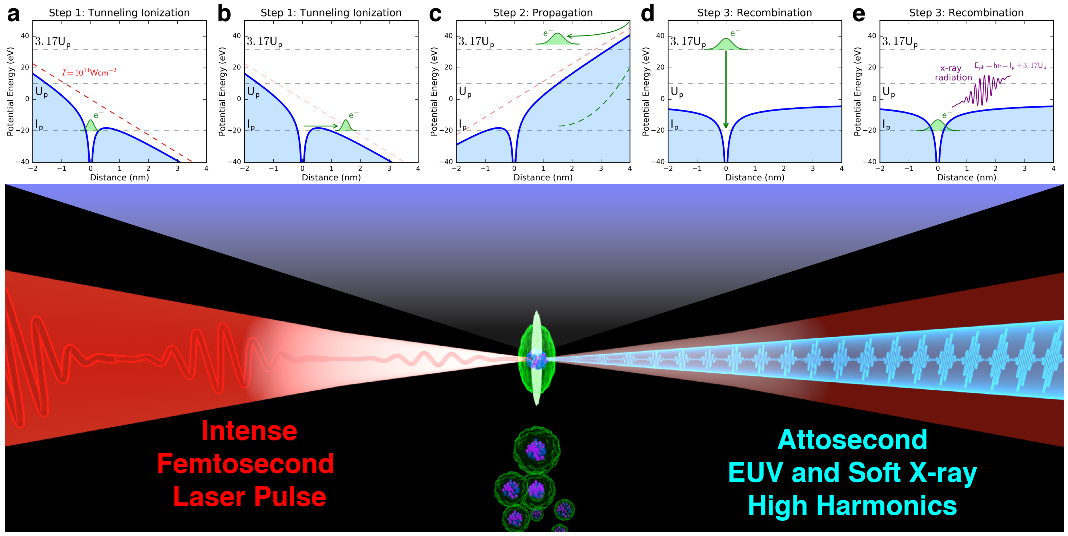

Figure 1.5: **Schematic showing the conversion of a intense, femtosecond, IR laser pulse into coherent, attosecond, EUV and soft x-ray light via high-harmonic generation.** In HHG performed in atomic gases, an intense, femtosecond laser pulse interacts with atoms of a noble gas to produce coherent, laser-like EUV and soft x-ray light. The microscopic mechanism can be, under certain conditions, mostly recaptured by invoking a semiclassical three-step model (STSM) (upper insets); **a-b** first, an electron wavepacket in a ground state is tunnel ionized via an intense, external laser field, **c** then the freed electron wavepacket is propagated in the laser field and upon reversal of the field amplitude the wavepacket may find itself in the vicinity of its parent ion **d**, after which it may recombine and in doing so emit a high-harmonic photon, with a maximum energy equal to the gained energy in the field (the ponderomotive potential, U_p) minus the energy of the ground state (i.e., the ionization potential, I_p). Note that in this tightly focused geometry, only partial phase matching is possible due to many uncompensated relative phase shifts in the transverse and longitudinal directions.

pulse train (APT) produced via HHG in 2001 [142]. Interestingly, the exact same year saw the birth of isolated attosecond pulses (IAPs), which were produced by few-cycle laser pulse to drive the HHG process, such that only one(ish) cycle contributes to the high-harmonic emission, and this was the methodology first used to produce IAPs [143], as predicted many years earlier [144]. Subsequent follow up work showed that single-cycle IAPs could be produced [53]. The confirmation that attoseocond pulses could be obtained from HHG-based sources birthed the attosecond revolution in optical physics, and forms the basis for observing the fastest dynamical processes in nature. Now, the choice of which set of attosecond light sources to use is a question of the dynamics. Is the driving laser period much longer than the dynamics? Then APTs are your friends [36, 37, 145]. If we are interested in impulsive, yet long lived dynamics, then IAPs are the name of the game.

Thanks to many years of development and countless players in the game, HHG has matured to a reliable, table-top source of attosecond, EUV and soft x-ray light with the only apparent limitations being that of the driving lasers themselves. This has resulted in wide-spread of the principles of attosecond physics and HHG-based light sources across numerous scientific disciplines, and properly accounting for all of these would only serve to increase the curb weight of this tome. Thus, the interested reader is referred to several wonderful review articles that detail the history and various methods of generating coherent EUV light via HHG-type processes, as well as the varied and exotic applications of these unique quantum light sources [146–152].

1.3.2 Taking Control of High-Harmonic Generation; Sculpting Attosecond, EUV Waveforms via Optically Controlled, Quantum, Electron Dynamics

Over the past several decades, EUV and attosecond light sources based on HHG have revolutionized ultrafast chemistry and physics, allowing us to resolve nature's fastest, most intricate dynamics. These generational efforts have resulted in a mature knowledge of the upconversion processes, and a general qualitative picture can be formed; the entirety of the HHG process is driven by a coherent, external laser field, which itself can control the electron dynamics and they in turn yield control over the emitted radiation. This idea of optically based, coherent control of EUV and soft x-ray light was already known in the early days of HHG, and can be most readily described within the path integral formalism laid out by Lewenstein and others [138, 139, 153, 154]. Unlike the classical STSM [107], the Lewenstein model, which works in the strong-field approximation (SFA)[11] , fully accounts for the presence of a coherent light field driving the HHG process, leading to a single equation for the atomic dipole moment (and thus the radiation field via a Fourier

[11] The basic tenants of the SFA are the following; minimal depletion of the ground state, a "long" laser wavelength, and that the continuum dynamics are determined solely by the laser field and not the ion

transform)

$$\vec{\mu}(t) = i\int_0^t dt' \int d^3p E_0 \cos(\omega t')$$
$$\times \vec{d}\left(\vec{p} - \vec{A}(t')\right)$$
$$\times e^{[iS(\vec{p},t,t')]} \tag{1.11}$$
$$\times \vec{d}\left(\vec{p} - \vec{A}(t)\right) *$$
$$+c.c.$$

where we have introduced as new conserved quantity, termed the *canonical momentum* ($\vec{p} = \vec{v} + \vec{A}(t)$), t' is the time at the instant of ionization while t is the time the wavepacket returns to the ionized target, $\vec{d}(\vec{v})$ is the transition probability from the bound electronic state of the target to the laser-dressed continuum state with momentum $\vec{p}$ (known as generally as *Volkov states*), while $\vec{d}(\vec{v})*$ is the complex conjugate and describes the recombination probability, and $\vec{A}(t)$ is the vector potential of the oscillating electric field with amplitude and phase at the moment of ionization of $E_0 cos(\omega t')$. The only other suspicious-looking term in Equation 1.10 is $S(\vec{p}, t, t')$, which is known as the semi-classical action. The action, S, is itself given be a second integral over the time the electron spends in the continuum

$$S(\vec{p}, t, t') = \int_{t'}^{t} dt'' \left[\frac{\left(\vec{p} - \vec{A}(t'')\right)^2}{2} + I_p \right]. \tag{1.12}$$

This final piece of the Lewenstein model recaptures the same physics described in the classical picture [107]; however, we know have an explicit expression relating the properties of the driving laser field, namely it's amplitude and phase, to the nonlinear dipole moment produced in HHG, and thus a handle for how to start sculpting the emitted high harmonics. It's worth noting at this point that Equations 1.10 and 1.11 provide a single-atom picture of the HHG process, and as such they neglect propagation to the detector. The importance of including propagation was well known at the time (in fact, the same authors suggested using medium effects to obtain APTs a few years later [141]); however, the computational cost of Equations 1.10 and 1.11 is already quite high[12] (it is a five-dimensional integral in space *and* time). Moreover, the macroscopic aspects of HHG were not well understood at the time, not to mention efficient methods for calculating the

[12] A variety of methods exists to ease this burden, with many also handling corrections for aspects left out of the Lewenstein model (e.g., Coulombic effects).

propagation of the harmonics to the detector [155]—and these are not the only reasons. Nonetheless, the Lewenstein model gives us an accurate theoretical framework, while also providing the recipe for structuring and controlling the HHG process and thus the ensuing emitted high-harmonic waveforms. Fundamentally, this theoretical tool kit provides a clear route for mapping properties of coherent visible radiation into the EUV and beyond.

1.3.3 A New Spin on High-Harmonic Generation; Optical SAM in HHG

Almost immediately after the discovery of HHG [127, 128], initial attempts were made at producing elliptically polarized EUV light via the use of elliptically polarized driving lasers [156, 157]. However, the recollision-based nature of HHG resulted in a significant reduction in the emitted harmonic flux, as the electron wavepackets simply "missed" their parent ions. Interestingly, an early scheme using a two-color laser field with independently variable polarization was employed to drive the HHG process [158] and likely produce elliptically polarized harmonics; however, there was no polarization analysis and instead the report focused on efficiencies and cutoffs. A few theoretical papers appeared at the turn of the millennium [159, 160] that focused on bicircular-driven HHG (BHHG), which suggested such a scheme would not only produce elliptically polarized high-harmonics, but also yield an underlying APT with "unusual" polarization properties [160]. These APTs were unusual in that the harmonics were highly elliptically polarized in the frequency domain, their underlying APTs were composed of short, *linearly* polarized bursts, each offset by a transverse angle determined by the ratio of the driving field frequencies. Despite the unique capabilities afforded by such a source, effort in producing coherent, circularly polarized EUV light quickly faded within the attosecond and HHG communities.

Fast forwarding 15 years, a series of papers revisited the two-color scheme in the context of HHG, showing that indeed optical SAM could be imparted into EUV waveforms [161–163]. Aside from confirming the highly elliptical polarization of the EUV waveforms and their potential for element-resolved dichroic spectroscopies, these works strongly supported the idea that the emission of high-harmonics in BHHG could be viewed as progressing through quantum channels that themselves are described via the absorption of discrete numbers of photons from each field [11, 161, 164], provided that energy and momentum conservation rules were upheld. We'll get an intimate tour of these conservation rules in Chapter 3, but in essence the introduction of SAM in the upconversion process constrains the momentum conservation rules, which themselves constrain the allowed quantum paths leading to bright harmonic emission. The primary feature of these constrained conservation rules is the presence of gaps in the BHHG spectrum, which are the manifestation of suppressed emission of harmonics generated by spin-forbidden quantum paths (i.e., paths that involve an equal number absorbed photons). For the typical case of a biciruclar field composed of a fundamental laser field and its second harmonic, the resulting spectral structure is a series of oppositely circularly polarized harmonics "doublets", while the temporal structure is that of the "trefoil", both of which are the direct result of the 3-fold symmetry of the biciruclar laser field.

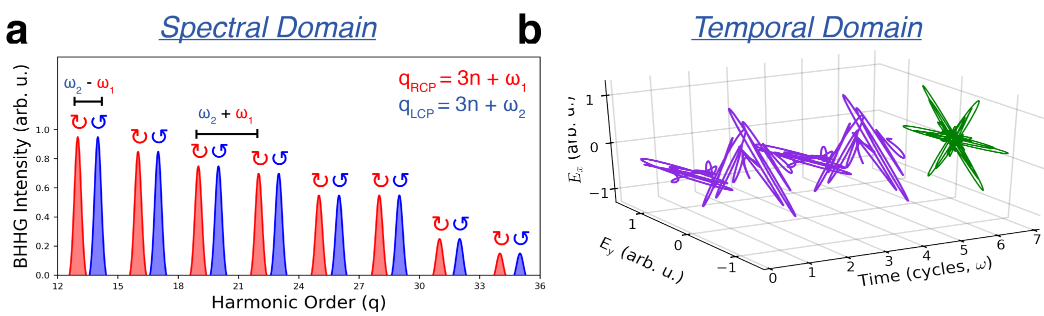

Figure 1.6: **Bicircular high-harmonic spectra and attosecond pulses trains when driven with a frequency-commensurate bicircular field.** **a** When HHG is driven with a counter-rotating bicircular field composed of a fundamental and its second harmonic, the HHG spectrum exhibits a characteristic intensity pattern, consisting of high-harmonic doublets of opposite circular polarizations spaced by a single missing harmonic order. The harmonics within each doublet are copolarized with the constituents of the driving bicircular laser field, such that the lower (higher) frequency harmonic in each doublet has the same helicity as the lower (higher) frequency component of the bicircular field. **b** The unique spectral structure inherent to BHHG results in a non-trivial structure of the underlying APTs, which (is this case) possess a series of linearly polarized harmonic bursts that are rotated from one another in the polarization plane. The angle of rotation between successive bursts is determine by the symmetry of the bicircular laser field and for the 3-fold symmetric bicircular field considered here results in a rotation of 120 degrees between the peak each burst.

These initial results provided the foundations for producing, tailored, polarization-sculpted EUV and attosecond waveforms, simply by constraining the HHG process with properties of the driving laser fields. These constraints provided a unique mapping of optical SAM to EUV wavelengths, and helped to propel angular momentum generation and control to the forefront of attosecond science. Building off these results, bright, cicularly polarized, soft x-ray high-harmonics have been produced from mid-IR drivers [11], spatially isolated APTs of LCP and RCP polarization have been generated via a noncollinear geometry employing frequency-degenerate, circularly polarized laser pulses [7, 12], circularly polarized IAPs, with controllable polarization, can be produced from few-cycle drivers [165], and even the unique spectral features themselves can be used to as markers for chiral detection and dynamics [166–168]. Many other unique applications of EUV beams obtained via BHHG, as well as the first method demonstrating active control of the underlying APTs, are described in Chapter 3.

1.3.4 High-Harmonic Generation with a Twist; Production of Coherent EUV and Attosecond Vortex Beams Possessing OAM

Much the same as the total angular momentum of light can be cleanly separated into SAM and OAM, the initial efforts of introducing SAM and OAM in HHG were largely removed from one another. The resistance to introducing OAM into existing HHG schemes likely stemmed from a multitude of studies on frequency conversion of OAM beams in the visible regime. The nonlinear interaction resulted in degraded beam profiles and subsequently lower quality modes for the upconverted vortex beams, and if the OAM had trouble surviving a two-photon process, how could it survive the highly nonlinear process of HHG? The initial report by Zürch in 2012 [97] also seemed to verify this; a visible optical vortex with a topological charge of $\ell_1 = 1$ yielded high harmonics with *the same* topological charge (e.g., $\ell_q = \ell_1 = 1$). Since theory and experiments predicted integer scaling of the OAM with the harmonic order, the strange results were attributed to impure driving modes and spatiotemporal aspects associated with an azimuthal phase delay across the beam profile [169]. Thankfully, hope was not lost and only a year later, a rigorous theoretical model based on the SFA showed that indeed the harmonics should have possessed an integer topological charge equal to the harmonic order multiplied by the OAM content of the driving laser waveform [99], and that under appropriate conditions the azimuthal phase would survive propagation in the nonlinear medium. Subsequent experimental confirmation followed a year after that [98], and an elegant study in 2016 showed that not only did OAM-driven HHG lead to a spectrum of high-harmonic "donuts", but the spatiotemporal nature of azimuthally phase beams yielded helical attosecond pulse trains in the domain [100], which incidentally was predicted a year before [170]. Over the last few years, several other theoretical

[171, 172] and experimental schemes [101, 102] have explored OAM-driven HHG, with attempts being aimed primarily at controlling the OAM spectrum of the emitted harmonics. Thus, just as the discovery of laser modes possessing OAM in 1992 [69] added a new degree of freedom for producing structured light, so to did OAM emerge in HHG as yet another "knob" for producing and controlling unique forms of structured, EUV and attosecond waveforms.

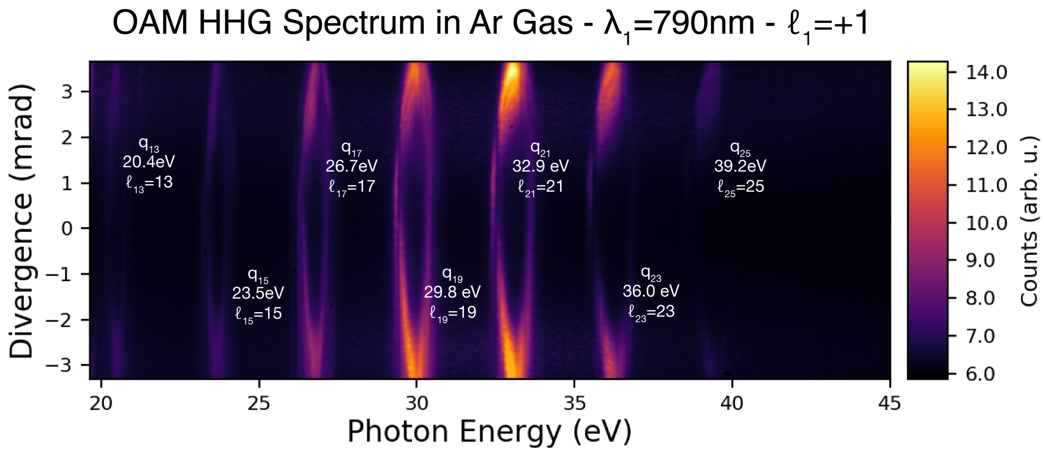

Figure 1.7: **Experimental high-harmonic spectrum generated in Ar gas with a driving laser possessing an OAM value of $\ell = +1$.** When HHG is driven by a laser waveform possessing OAM, the emitted high-harmonics retain the "doughnut" shaped structure of the driving laser, even in the far-field. Momentum conservation demands that the emitted harmonics possess an OAM of $\ell_q = q\ell_1$, leading to extremely high OAM charges in the emitted harmonics. Also, the effects of decreasing wavelength and increasing OAM result in all harmonics possessing similar divergences, as observed in the above spectrum.

1.4 Conclusion and The Winding, Twisting Road Ahead

And that, friends, is where the sidewalk ends. Angular momentum control and generation in attosecond science is a relatively new sub-discipline, and as such the field is actively evolving, even as these pages are being written and read. The role of the work in this thesis is to not only extend the methods of angular momentum control in HHG, but also provide a unique marriage of the segmented fields of SAM and OAM-based high-harmonic sources. In all of the work that follows, a central idea will continually re-emerge out of the darkness; EUV and attosecond waveforms can be controlled in real time via the angular momentum of optical waveforms, yielding some of the most exquisite control over the waveforms of EUV beams and attosecond light pulses. Much like the early days of HHG and ultrafast lasers that required concrete demonstrations of the production and control of light's properties before these sources could become useful, the work in this thesis is aimed at how we can create complex, structured and coherent light waves that will form the basis of advanced spectroscopies, metrologies, and imaging modalities that exploit the unique properties afforded by the angular momentum of light. So, let's go for a spin[13] .

[13] Every single ounce of the pun is intended here.

Chapter 2

Experimental Scheme and Approach for Generating Sculpted Extreme Ultraviolet, Attosecond Light Pulses

Research is soup, and I am a fork. –Despite his best wishes, the author

2.1 Experimental Overview and Design

The suspiciously chronological nature of the three works detailed in this thesis provides an added benefit here, in that most of the experiments performed can be described with a few common "pieces"; despite the fact that different physical phenomena are observed and investigated in each chapter. The most prominent stars of the show are the regenerative Ti:sapph amplifier (9 mJ, 40 fs, 1 kHz, KMLabs Wyvern HE [173, 174], Section 2.2) and the bicircular HHG beamline (Section 2.3) and, as is customary, we introduce them first. Section 2.4 describes a suite of optical characterization techniques, ranging from spatially resolved wavefront measurements of visible OAM beams (Section2.4.1), to frequency resolved optical gating (FROG) measurements of the amplified laser pulses (Section 2.4.2), and EUV magnetic circular dichroism (EUV-MCD) spectroscopy is employed to verify the high circularity of the SAM-OAM harmonics produced in Chapter 4 (Section 2.4.3). Below, we take a tour of these techniques, with explicit intent of not rehashing what is already described perfectly well in the available literature. Thus, we shall not encounter an excessive amount of equations and diatribe, but instead take a surface approach; techniques will be described in broad, but practical strokes (since each chapter will provide a more specific account of the methods), equations will be given only when they can directly contribute to the discussion at hand, and an attempt will be made to connect the concepts found in classrooms and textbooks to the tinkering that is done the lab.

2.2 Femtosecond, High-Peak Intensity Laser System

High-harmonic generation is bit greedy. Even under the most optimal conditions, the ”currency” exchange rate (i.e., the trading of UV/visible/IR/mid-IR photons for high-frequency ones) required to produced coherent EUV and soft x-ray light is pretty dismal, with optimal conversion efficiencies (i.e., $\mathrm{n_{UV,Vis,IR}}/\mathrm{n_{HHG}}$, with n_i being the number of photons) floating some where around 10^{-4} to 10^{-6}. Fundamentally, this indicates that an excessive amount of driving laser photons is needed for the upconversion process, which brings us into the realm high-peak-power lasers[1] . To date, the most successful and widely used method for producing high-peak-power pulses is chirped pulse amplification (CPA), pioneered by Donna Strickland and Gerard Mourou in 1985 [175, 176]. In CPA, a low-intensity, ultrafast, broadband “seed” pulse (typically produced via a passively mode-locked oscillator) is first stretched in time by forcing the individual colors in the seed pulse to take ray paths that depend upon their color. The stretched seed is then amplified inside the laser amplifier cavity, and—after a few round trips—is recompressed by undoing the initial stretching action in (usually) a similar fashion, finally yielding an ultrashort pulse with a high peak power, on the order of terawatts. Such pulses when focused can easily reach intensities of $10^{13} - 10^{15}$ W/cm^2, which is more than enough for generating high-harmonics. In order to produce such high-peak-power pulses, we need a source for the seed pulses (Section 2.2.1) and a suitable laser amplifier (Section 2.2.2), along with the associated pump lasers. Although a complete description of ultrafast laser physics is beyond the scope of this thesis (and the patience of the author), the curious reader is referred to Chapter 5 of a wonderful PhD thesis by Ihar Shchatsinin [177] for the intricate details of ultrafast light pulses and amplifiers, a review article in the late 1990s provides a thorough overview of the practical aspects of high-power ultrafast amplifiers [178], and Rick Trebino’s tome on FROG [179] is an excellent starting point for the physics of ultrashort laser pulses.

2.2.1 Ultrafast Kerr-Lens Mode-Locked Oscillator System

The standard approach for seeding high-peak-power amplifiers is to employ a passively mode-locked oscillator. In this work, a Kerr-lens Ti:sapph oscillator (∼10-20 nJ, <12 fs, 80 MHz, KMLabs Griffin) is used

[1] This glosses over many elegant HHG setups that don’t require high-peak-power laser sources (i.e., cavity-assisted HHG, HHG in tight focusing geometries, etc.), but a full discussion is beyond the scope of this thesis.

as the amplifier front-end, with >99% up-time in mode-locked operation. Briefly, the oscillator is pumped with a diode-pumped solid-state (DPSS), frequency-doubled, neodymium:vanadate (Nd:VO_4) laser that lases in a continuous-wave (CW) fashion[2]. In this particular oscillator, mode-locking is initiated by exploiting the optical Kerr effect in a Ti:sapph crystal medium to transition—on the course of a few milliseconds—from an unstable CW lasing state to a stable mode-locked state. In the lab, this transition is best observed using an optical spectrometer in conjunction with a fast photodiode, with which a MHz-frequency pulse train emerges just before the onset of a dramatic spectral broadening. Although Kerr-lens mode-locking in a Ti:sapph oscillator was discovered less than 30 years ago [41], until recently, a unified picture of the exact mechanism of Kerr-lens mode-locking was out of reach—owing to the stochastic nature of initiating the mode-locking process, and the need to record spectra at 10's of MHz frame rates. Fortunately, recent experimental results [180] have provided the necessary observations to unite many theoretical and experimental observations into a unique, stochastic, spectrotemporal movie of the birth of femtosecond pulses in Kerr-lens mode-locked oscillators (see Figure 2.1).

In order to get to the femtosecond domain, we require a large bandwidth in the frequency domain. Such a large bandwidth is obtained via the optical Kerr effect, discovered nearly 150 years ago [181], which is a spatiotemporal modification of the dielectric function of a material in the presence of an external electric field,

$$n(\vec{r}, t) = n_0 + n_2 I(\vec{r}, t). \tag{2.1}$$

Here, n_0 is the static refractive index of the medium, I is the electric field intensity, n_2 is the non-linear part of the refractive index, and we have written explicitly the dependence of these quantities on space and time. This spatiotemporal modification to the refractive index results in a (nearly) simultaneous effect—self-phase modulation, SPM—, which acts on the pulse via the n_2 term. This results in a temporal variation of the frequency content of the pulse, which itself occurs via picosecond fluctuations in the pulse phase,

$$\phi(\vec{r}, t) = w_0 t - k_0(\vec{r}) z = w_0 t - \frac{2\pi L}{\lambda_0} n\left[I(\vec{r}, t)\right] L \tag{2.2}$$

$$\omega(\vec{r}, t) = \frac{d\phi(\vec{r}, t)}{dt} = \omega_0 - \frac{2\pi L}{\lambda_0} \frac{dn\left[I(\vec{r}, t)\right]}{dt} \tag{2.3}$$

[2] Although we typically refer to such laser sources as ”continuous wave”, the wave itself is never continuous. Continuous and plane waves extend infinitely in time, and at one point or another we had to turn the laser on.

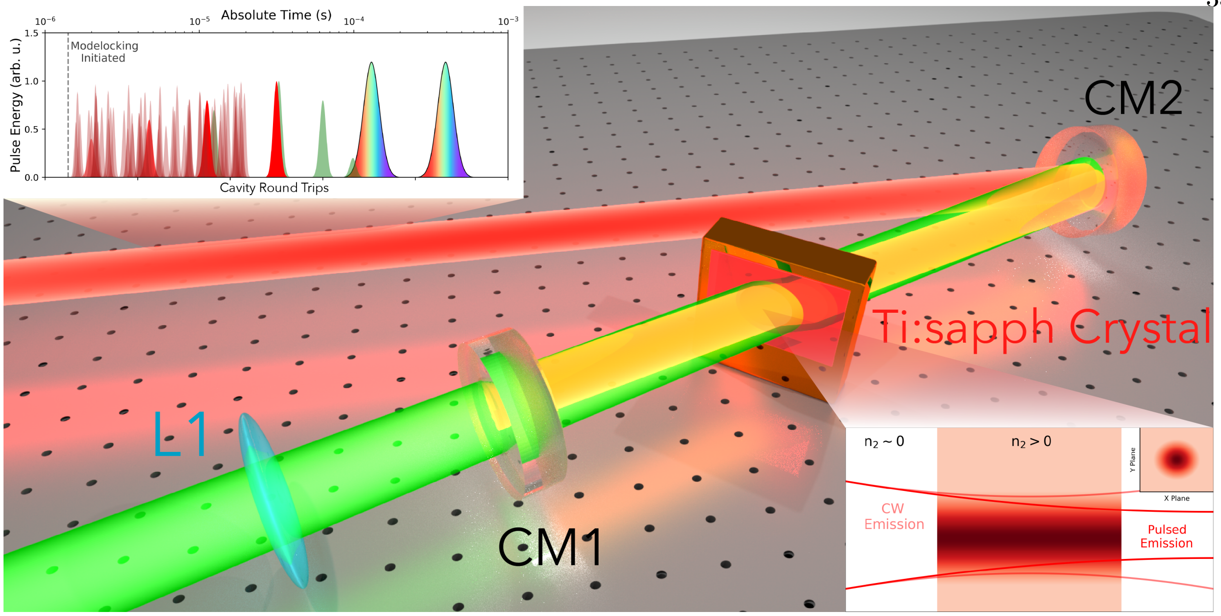

Figure 2.1: **Femtosecond pulse production via Kerr-lens mode-locking in a Ti:sapph. oscillator** In a typical Ti:sapph oscillator—here, showing the minimal components of a pump laser (green), lens (L1), curved cavity mirrors (CM1 and CM2), and a copper-mounted Ti:sapph crystal—the Kerr optical effect is utilized to passively mode-lock the oscillator, effectively changing it from a CW laser, to a pulsed one. **Upper-left inset**, Mode-locking is initiated by a small "kick" of a prism or cavity end-mirror (grey-dashed line in upper left inset), which induces stochastic, picosecond fluctuations (light-red pulses) in the laser output. Eventually, one of these fluctuations has the "right" set of cavity modes and begins to build up amplitude (dark-red pulses). Eventually, the pulse amplitude becomes large enough to induce self-actions (i.e., SPM, and self-AM), which broadens the spectrum and creates a stable train of femtosecond pulses (rainbow-colored pulses). Sometimes, a neighboring set of cavity modes can beat together with the dominant fluctuation (light-green pulses), which induces femtosecond structure in the dominate fluctuation, and seeds the mode-locking process. The entire mode-locking process happens over the course of a millisecond or so, seeming nearly instantaneous in the lab. **Lower-right inset**, The temporal dynamics in Kerr-lens mode-locking occur simultaneously with non-linear spatial effects, which leads to a lensing-type action in the Ti:sapph medium. This lensing increases the intensity, up to a point, which is then stabilized by extraction of power out of the gain medium via the Kerr-activated, dominant fluctuation. Note that the Snell shift of the Ti:sapph-produced beam and the pump laser are different in the Ti:sapph crystal, leading to slight angular displacements of the two beams.

where $\phi(\vec{r},t)$ is the instantaneous phase of the pulse, $\omega(\vec{r},t)$ (ω_0) is the instantaneous (central) frequency of the pulse, $k_0(\vec{r})$ is the pulse wave number ($k_0 = 2\pi/\lambda_0$), L is the length the pulse propagates in the crystal[3], and we again have retained the spatiotemporal dependence of the necessary quantities. As we transition into a mode-locked regime (typically initiated by "bumping" a prism or mirror), random, picosecond fluctuations via neighboring cavity modes interact to form an intense-enough femtosecond variation in the pulse intensity, which triggers spectral broadening via Equation 2.3. The spectral broadening is further reinforced by the

[3] We only consider the crystal length since the pulse intensities are far too low to generate nonlinear effects in air.

spatial dependence of the optical Kerr effect, which essentially sets the intensity-threshold necessary for stable mode-locked operation via self-amplitude modulation (self-AM). The self-AM effect is mediated by placing the crystal just after the focus of pump laser, which not only increases the intensity in the Ti:sapph medium, but also reduces the pump mode size. The reduced size of the pump mode in the crystal favors pulsed operation, while concurrently suppressing CW lasing. Compression of the subsequent broadband pulses is then achieved by using a prism pair to impart negative group velocity dispersion to the propagating beam.

With a qualitative, but complete, spatiotemporal picture of the Kerr-lens mode-locking process, we can begin to make sense of how this it typically done in the lab. After getting an oscillator lasing in CW state, a curved mirror is typically translated along the propagation direction of the CW mode, resulting in the focus of the CW laser beam being slightly beyond the face of the Ti:sapph crystal. This sets the cavity arrangement to favor mode-locked operation[4] , which can be confirmed via an elongated spatial profile of the CW mode at the output coupler. Mode-locked operation is initiated via the motorized movement of one of the dispersion-compensating prisms or by tapping one of the non-curved oscillator mirrors. This initial disturbance induces variations in the allowed cavity modes (via the cavity length), and these variations are the source of the picosecond fluctuations that eventually become the femtosecond pulse (Figure 2.1 upper-left inset).

Finally, we include below some tidbits that the author has found useful for obtaining a stable, broadband, femtosecond seed pulse for amplification. Using the techniques below, the oscillator employed in this work would routinely operate in mode-locked operation for weeks at a time, with the only maintenance being slight translations of the dispersive prisms and semi-monthly cleanly of the Ti:saphh crystal.

- In-line cooling of oscillator is a must for stable operation, and the optimal configuration was found to be: chilled-water circulator (Cold, out) → Ti:sapph crystal → oscillator optical board → pump laser → chilled-water circulator (Hot, return).

- Despite enclosing the entire oscillator, dust and contamination are always present in configurable

[4] Put another way, we ”misalign” a perfectly good CW laser, and the Kerr lens ”realigns” it to favor mode-locked operation.

systems. Placing a small, DC, brushless computer fan directly in the oscillator (the author's favorite is the APO0512MX-J90 manufactured by ADDA Corp., Ltd) can mitigate accumulation of dust on optics, while negligibly effecting air flow and vibrational dynamics (verified by a consistent shot-to-shot stability of <1% RMS while running).

- Placing a fast photodiode directly at the crystal is critical to providing active feedback, as the Kerr effect is initiated in the crystal.
- Nearly all oscillator woes can be attributed to contamination of optics or long-term drifts in alignment. The latter can typically be corrected via slight adjustments to the *flat* cavity end-mirrors. Curved mirrors should be moved as a last resort.

2.2.2 High-Gain, High-Power, Single-Stage Regenerative Ti:sapph Amplifier

The subsequent amplification of the femtoseconds pulses we obtained in the past section is, conceptually, refreshingly simple as compared to the complex spatiotemporal dynamics underlying Kerr lens mode-locking. Once we have our ultrashort pulses, the next step is to increase their peak intensity via the CPA process [175, 176]. In CPA, a broadband, ultrashort laser pulse is controllably stretched in time—a process called "chirping", with a direct relation to audible frequencies, and first developed in the radio and microwave regime—via a dispersive element (e.g., fiber, grating, prism), amplified in a suitable laser medium, and then recompressed via a second dispersive element at the exit. This scheme can be achieved in a variety of optical arrangements, with the most common configurations for Ti:sapph amplifiers being the multipass and regenerative types. In this thesis, a regenerative amplifier was employed (Figure 2.2), which employs a common-path-type design for the optical cavity, and modulated optical materials are utilized to control the number of round trips each pulse takes within the cavity. However, it's worth noting that a mutli-pass laser amplifier can offer several advantages over the regenerative-type used in this work, for example, shorter pulse durations (sub-25 fs, FWHM) and broader bandwidths (>40 nm, FWHM) [178, 182, 183].

The ultrashort pulses (12 fs, $\sim$10 nJ, 84 MHz) produced from the oscillator are directed into a common-path, double-pass grating stretcher, which temporally chirps the pulses to $\sim$100 ps in duration. A single

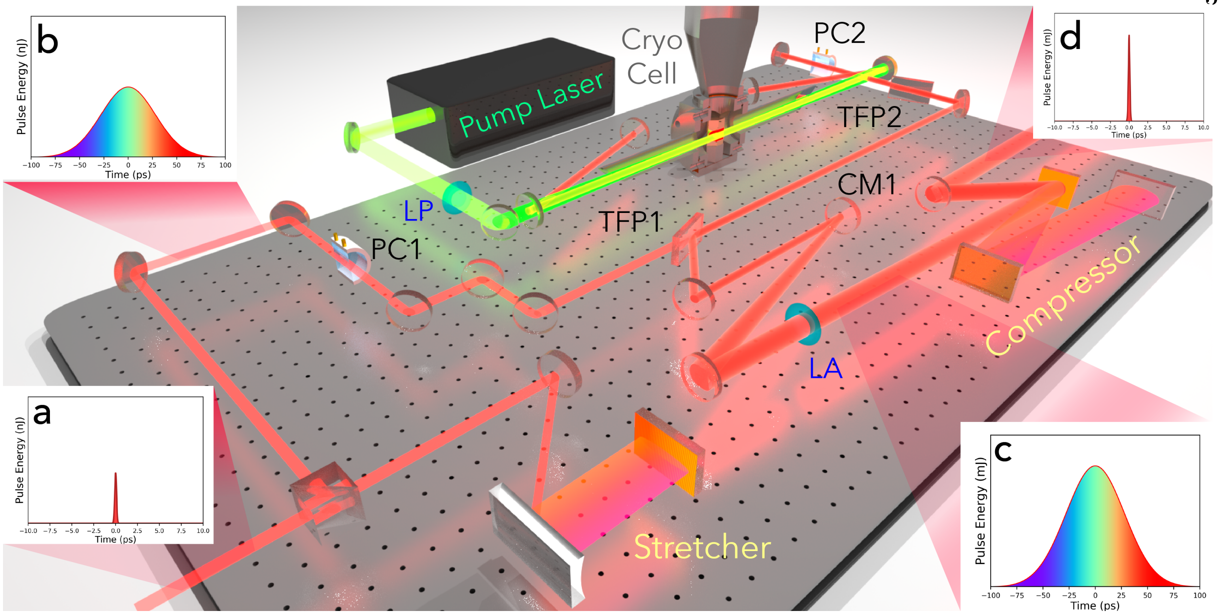

Figure 2.2: **Optical layout of the Wyvern HE, a high-power, single-stage, regenerative amplifier.** The amplifier is the standard regenerative design, composed of a grating-based stretcher, a common-path amplifier cavity, a mirror-lens telescope, and a grating-based compressor, and is pumped via a high-power, ns ND:YLF laser system (Coherent, Evolution). **a**, Seed pulses from the oscillator (12 fs, ∼8-10 nJ, 84 MHz) are passed into a grating based stretcher, causing it to stretch in time. **b**, The action of the stretcher results in a modified pulse train (∼100 ps, ∼7-9 nJ, 84 MHz), of which only one pulse from the train is injected into the cavity via the combined action of a Pockels cell (PC1) and a thin-film polarizer (TFP1). This also has the combined effect of reducing the initial 84 MHz pulse train, to a 1 kHz pulse train. A second Pockels cell and thin-film-polarizer pair (PC2, and TFP2, respectively) control the number of round trips in the cavity, and the pulses themselves are amplified in a cryo-cooled Ti:sapph module, which reduces effects of thermal lensing, increases the single-pass gain, and increases thermal conductivity (preventing temperature gradients), among other benefits. After ejection from the cavity, the amplified pulse is then reflected off of TFP1, passes through a curved-mirror-lens tele-periscope (CM1 and LA, respectively). The lens, LA, also helps to correct astigmatism introduced by the cryo-cell Brewster windows, and the off-axis reflection on CM1. **c** The amplified, stretched pulse (15 mJ, ∼100 ps, 1 kHz) is then sent into a grating-based compressor, which compresses the pulses to near transform limit, resulting in, **d**, femtosecond, high-peak-power pulses (∼40 fs, 9 mJ, 1 kHz) at the output. For simplicity, only the basic optics and components of the amplifier are shown.

pulse out of the stretched pulse train is extracted via a pre-cavity Pockels cell, and this seed pulse is injected into the amplifier cavity. The seed pulse is amplified in a second Ti:sapph crystal—pumped by a frequency-doubled Nd:yttrium lithium fluoride (Nd:YLF) DPSS laser (Coherent, Evolution)—by recirculating the pulse along the same beam path for a number of round trips. The exact number of round trips, and thus the gain, is controlled via a second, intracavity Pockels cell[5] , which operates as a nanosecond waveplate for ejecting

[5] The use of dual Pockels cells is two-fold; two Pockels cell allow for precise control of the timing window for injection/ejection of pulses from the laser cavity, while also increasing the pulse contrast—a not-so-straightforward thing for high-gain amplifiers.

the pulse into and out of the laser cavity. Once freed of the cavity, the stretched, amplified pulse (~100 ps, ~15 mJ, 1 kHz) is passed through a tele-periscope to increase the mode size (~11 mm, $1/e^2$ diameter) and impart a bit of divergence to the amplified beam[6] . Finally, the beam is passed through a pair of diffraction gratings that temporally compress the pulse to near transform limit, yielding ultrafast, high-power, IR laser pulses ($\lambda_0 \sim 790$ nm, $\Delta\lambda = 25$ nm (FWHM), $\tau = 40$ fs (FWHM), 9 mJ, 1 kHz) for driving HHG.

2.3 Beamline for Bicircular-Driven High-Harmonic Generation with Gaussian and Optical Vortex Beams

The entirety of the work contained within this thesis makes use of a fairly common set of optical elements, which can all be grouped under the common theme of "high-harmonic generation with non-identical pulses". This rather vague terminology can be distilled down to the Mach-Zehnder-type interferometer, in which a single beam is spilt into two spatially isolated arms, the beams are manipulated in some way, and then later recombined at the interferometer's exit. The spatial separation of the beam paths is key to the work detailed below, as we often have to manipulate the properties of the driving laser fields (i.e., intensity, SAM, OAM, mode size, etc.), independently of one another[7] . As we'll see a bit later down the road, this independent control of the beam properties in each arm is crucial for realizing the generation of light possessing an optical self-torque (see Chapter 5).

In the general setup (Figure 2.3), the full output of the Ti:sapph amplifier (see Section 2.2.2 above) is directed onto an amplitude-splitting beamsplitter, with a power-branching ratio of 60/40 (Chapters 4 and 5) or 70/30 (Chapter 3). The more intense arm of the interferometer is usually directed into a β-barium borate (BBO) nonlinear crystal to produce the 2^{nd} harmonic, centered at ~395 nm (Chapters 3 and 4), or the BBO is simply removed (Chapter 5). The power in each arm is controlled via a set of wire-grid polarizer-half-waveplate pairs, and the resulting polarization of each arm is controlled by an additional set of half-waveplate and quarter-waveplate pairs, yielding either circularly polarized driving beams (Chapters 3 and 4) or their linearly polarized counterparts (see Chapter 5). The two beams are recombined at the

[6] This bit of trickery is to avoid B-integral effects for the high-power pulses used in this work.

[7] Sometimes, this can be done to both beams at the same time. See [184] and [6] for two unique methods that achieve SAM control over both driving beams, simultaneously.

interferometer exit, and spatiotemporal overlap at focus is achieved by employing separate lenses in each arm (spatial overlap) and a high-resolution delay stage (Newport, XPS160S) in one arm (temporal overlap). The use of independent lenses and adjustable apertures in each arm of the two-pulse beamline allows for precise mode matching of both beams at focus, ensuring a more uniform field for driving the HHG process.

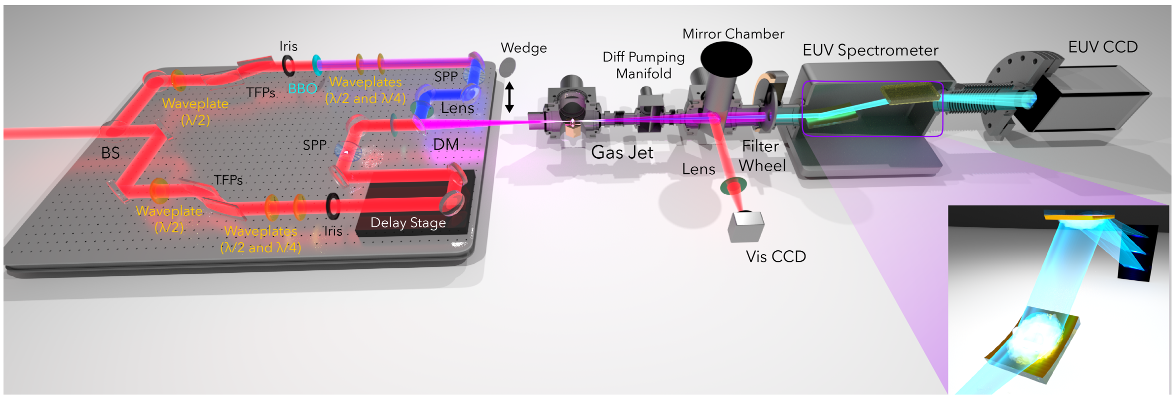

Figure 2.3: **General beamline and components for bicircular- and two-pulse-driven HHG.** The bicircular and two-pulse beamline is constructed from a Mach-Zehnder-type interferometer, which allwos for precise manipulation of the visible driving lasers, and thus the emitted high harmonics. The full output of the Ti:sapph amplifier is passed into a beamsplitter (BS), which spatially separates the beam. A suite of optics (see text for details) is placed in each arm to control the intensity, SAM, and/or OAM of the individual beams, and the beams are then recombined at the interferometer exit by a dichroic mirror (DM). The beams are then focused onto a supersonic expansion of noble gas in a custom gas jet, which generates EUV light via the HHG process. The co-propagating driving and EUV beams pass through a differential pumping manifold, and then a mirror chamber which can be used to re-image the driving laser for beam diagnostics—which are especially important for HHG performed with structured driving beams. A custom-made filter wheel is used to insert different metal foil filters into the beams, which serve to reject the intense driving laser while passing the EUV light, as well as serve an rough spectral markers for calibrating the EUV spectrometer. The emitted harmonics are then dispersed via an EUV spectrometer (shown above is the spectrometer used in Chapters 4 and 5), and the resulting spectrum is imaged with an EUV CCD camera (Andor, Newton 940). **Lower-right inset** No matter which spectrometer is deployed, the EUV beams are dispersed such that spectral information is obtained in one dimension, while spatial information is preserved in the other. This principle is demonstrated in the inset for the self-torqued beams obtained in Chapter 5.

Aside from these similarities, each experiment detailed below uses a slightly different configuration of the bicircular beamline. In Chapter 4, a unique optical element—the spiral phase plate, SPP (HoloOr, 16 steps per phase ramp)—is inserted into each arm in order to impart integer amounts of OAM to each beam[8]. The operating principle of an SPP is refreshingly intuitive [70]; simply exploit the natural optical dispersion

[8] The use of thin SPPs was preferred over other OAM generation methods (e.g., spatial light modulators (SLMs), diffractive optics, etc.) due to their relative ease-of-use, high damage threshold, and low dispersion.

of a transmissive material to induce an azimuthally-dependent group delay to the propagating beam. For the SPPs used in these works, the azimuthal group delay is imparted via segmented, triangular steps with each with a height, $h = \ell\lambda/16(n-1)$, where ℓ is the desired topological charge and n is the material dispersion at the design-wavelength, λ. Each step in the staircase is etched into fused-silica substrates, and a final anti-reflective coating is applied to each face. In Chapter 5, the SPPs remain while we remove the BBO (and the associated high-reflectivity coated mirrors) and the quarter waveplates to generate frequency-degenerate, linearly polarized vortex driving pulses.

In order to obtain a stable beamline, minimize pulse dispersion, and relative CEP fluctuations, thin optics are used where ever possible, with the same optical thickness for each transmissive component in each arm and the entire beamline is enclosed in an air-tight box to remove air currents. Also, a in-house beam pointing stabilization (BPS) system [185] is employed to maintain accurate alignment of the amplified beam into the interferometer. This system is comprised of two piezo-actuated mirror mounts (Thorlabs, POLARIS-K1S2P), a pair of charge-coupled device (CCD) cameras (Mightex, CGE-B013-U), and an in-house-written computer program. In essence, the use of two cameras and two detectors allows for precise control of both the position and propagation angle of the beam, *at all points in space*[9] . In our implementation, the leak through of the final turning mirror into the bicircular beamline is passed into a focusing lens, the converging beam is then split with a beamsplitter and one detector measures the beam at focus, while another measures the beam some distance after the focus. In order to ensure long term stability, the first piezo mirror is placed directly before the compressor *inside the amplifier*, and the second piezo mirror is placed just before the last turning mirror prior to interferometer's entrance. As crazy as it seems to have a potentially "wandering" beam pointing going into the compressor, we have not observed any detrimental effects on beam mode quality or output pulse duration while the BPS system is activated.

Under the above configuration, we routinely experienced continuous spatiotemporal overlap of the two beams at focus for periods exceeding 96 hours of constant run time. In fact, recalibration of the BPS system is only required when altering the optics of the BPS system itself, or in the semi-annual destruction and subsequent reincarnation of this beamline.

[9] An excellent description of the basic operating principles of such a BPS system, as well as pros and cons, is given in the thesis of Matthew Seaberg [185]

2.3.1 Generation and Detection of Twisted Extreme Ultraviolet Beams via SAM/OAM HHG

Extreme ultraviolet beams—and attosecond pulses—with controllable amounts of SAM and/or OAM are produced by driving the HHG process with the above-mentioned configurations of the two-color SAM/OAM beamline (see Section 2.3 above). In the context of these works, we will always employ a supersonic expansion of a noble gas (i.e., He or Ar) as the HHG medium, and our source of the supersonic expansion is a home-made gas jet, composed of a thin, quartz capillary (inner diameter of 100-150 μm) carefully epoxied into a drilled Swagelok®cap[10] . The gas jet is then enclosed in a 6-way Kwik-Flange™ bulkhead, and mounted onto a two-axis translation stage. A "wedding-cake"-style pumping aperture (i.e., a cylindrical tube with segmented steps of increasing inner diameter) is placed immediately after the gas jet, followed by a second differential pumping stage, which is also movable in both transverse dimensions. Both the interaction chamber and the differential pumping stage are pumped via high-capacity roots or scroll-type vacuum pumps (Pfeiffer, Adixen ACP40 for Ar studies, Aglient IDP-15 for He studies), which significantly reduces reabsorption of the emitted harmonics. Upon exiting the differential pumping aperture, a filter-wheel housing is used for inserting various thin metal foils into the beam line for blocking the residual driving laser and performing energy calibrations of the spectrometer system.

The emitted high harmonics are then collected using one of two different spectrometer systems. Chapter 3 employs the use of an aberration-corrected, variable line-spaced (VLS), concave EUV grating (Hitachi, 001-0266), which has the benefit of being able to spectrally disperse and focus the harmonics with a single optic. However, the popularity of this particular grating (along with its associated cost) resulted in the use of a different spectrometer system for Chapters 4 and 5. In these later chapters, we deploy a (slightly) bulkier spectrometer composed of a cylindrical mirror and a flat, VLS grating (Hettrick Scientific, ES-XUV™). Despite their different designs, both spectrometers accomplish the very same thing; collapse the HHG beam spatially in one dimension, while spectrally dispersing the high-harmonics in the orthogonal dimension. The resulting spatiospectral HHG spectra are then imaged using an EUV CCD camera (Andor, Newton 940, 512

[10] Although this seems like a rather sloppy way of going about things, we routinely observed better fluxes and spatial modes of the high harmonics from in-house-built gas jets as compared to commercially available jets.

x 2,048 pixels, 13.5 μm pitch), and all harmonic spectra are corrected for transmission of the EUV beamline (e.g., by using published transmission and reflection spectra from the Center for X-ray Optics online database), as well as the frequency-dependent response of the CCD sensor. In order to observe the spatial mode of the SAM-OAM EUV vortex beams in Chapter 4, the detector is translated to ~8 cm beyond the flat-field focus of the spectrometer, which results in only a minor reduction in spectral resolution.

2.4 Optical Characterization of Visible and Extreme Ultraviolet Light Beams

The generation of the unique, twisted attosecond light waves described in the following chapters necessitates the use of ”high-quality”, high-power, ultrafast pulses for driving the HHG upconversion process. Depending on the particular experiment at play, ”high-quality” can refer to highly pure states of circularly (Chapters 3 and 4) or linearly (Chapter 5) polarized light, highly uniform and circular beam modes, and low-dispersion and near-transform-limited pulse durations, to name a few. In particular, the experiments involving the use of vortex driving beams require extremely pure Gaussian modes, which maximizes the conversion of the input mode into the desired LG_ℓ^0 mode, as well as the quality of the LG_ℓ^0 mode. This can have profound effects on the emitted OAM high-harmonics, as any spatial inhomogenieties in the driving beam will be amplified in the high harmonic beam profiles. In order to ensure high quality pulses for producing high quality harmonics, we employ a suite of optical characterization techniques[11] ranging from simple measurements of beam mode sizes for high-resolution reconstructions of the ultrafast, visible driving wavefronts (Section 2.4.1), temporal characterization of amplified pulses via frequency-resolved optical gating (FROG, Section 2.4.2), as well as characterization of the ellipticity of high-harmonics generated with the bicircular field (Section 2.4.3).

2.4.1 High-Resolution Wavefront Characterization of Ultrafast, Vortex Light Beams

The wavefront of an intense, ultrafast pulse can undergo significant distortions during propagation, leading to a complex phase front that may no longer be uniform in space or time. In the context of HHG, such distortions can be detrimental for not only the production of bright, coherent EUV light, but also for the

[11] This is, of course, a fairly limited sampling of techniques used in the day-to-day running of the lab; however, those described below proved to be most crucial for the success of the works contained within this thesis.

subsequent deployment of the emitted harmonics in spectroscopies, metrologies, and imaging applications. The ramifications of wavefront distortions on the emitted harmonics has been well-known since the early days of HHG, and now—thanks to recent technological developments—we are able to verify these effects by measuring the wavefronts of both the low-frequency driving beams and their high-harmonic counterparts. To date, the most popular wavefront sensing devices, in both frequency regimes, are those based on the Hartmann/Shack-Hartmann design [186–188]. In a Hartmann-type (Shack-Hartmann-type) device, an image of the point-like diffraction of an incoming light beam when passing through a micro-aperture (or micro-lens) array is recorded, and the wavefront is then reconstructed by fitting the recorded diffraction pattern to (typically) a family of Zernike polynomials[12]. Such devices are robust, commercially available, routinely operate in single-shot mode at kHz repetition rates, and, in most situations, yield highly accurate results.

Unfortunately, the use of high-intensity optical fields in HHG returns the typically routine Hartmann (Shack-Hartmann) technique to the realm of the non-trivial, as high intensities necessitate small-ish focal spots ($w_{1/e^2} \sim 10 - 200\ \mu$m), which themselves are usually much below the size of the individual apertures (lenslets)[13], resulting in poor-quality of the reconstructed wavefronts. In the EUV regime, life is further complicated by the lack of refractive optics, but rapid progress is being made on this front as EUV Hartmann masks are becoming more available and routine to fabricate [189–193]. In order to circumvent the limited resolution of Shack-Hartmann-type wavefront sensors, we simply throw away the micro-array and use the raw beam intensity profile as imaged by the CCD. By recording beam intensities at multiple image planes throughout the Rayleigh range of the focused beam, we can reconstruct the spatial wavefront of the driving pulse using a common phase-retrieval algorithm—the Gerchberg-Saxton (GS) algorithm [194, 195]—, which yields the complex amplitude of the beam with a resolution limited only by the camera pixel size. This technique is ideal not only for the Gaussian beams of Chapter 3, but also for the complex OAM beams utilized in Chapters 4 and 5.

The operating principle of the GS algorithm is refreshingly simple for non-mathematicians like the author. In its most basic form, the GS algorithm retrieves the phase of a pair of mathematical distributions

[12] The use of Zernike polynomials is a matter of convenience; wavefront aberrations have a surprisingly similar mathematical description when compared to Zernike polynomials, which facilitates their use in the reconstruction.

[13] For a semi-anecdotal account of the initial efforts in fabricating Shack-Hartmann lenslet arrays, the distracted reader is referred to Ref. [188].

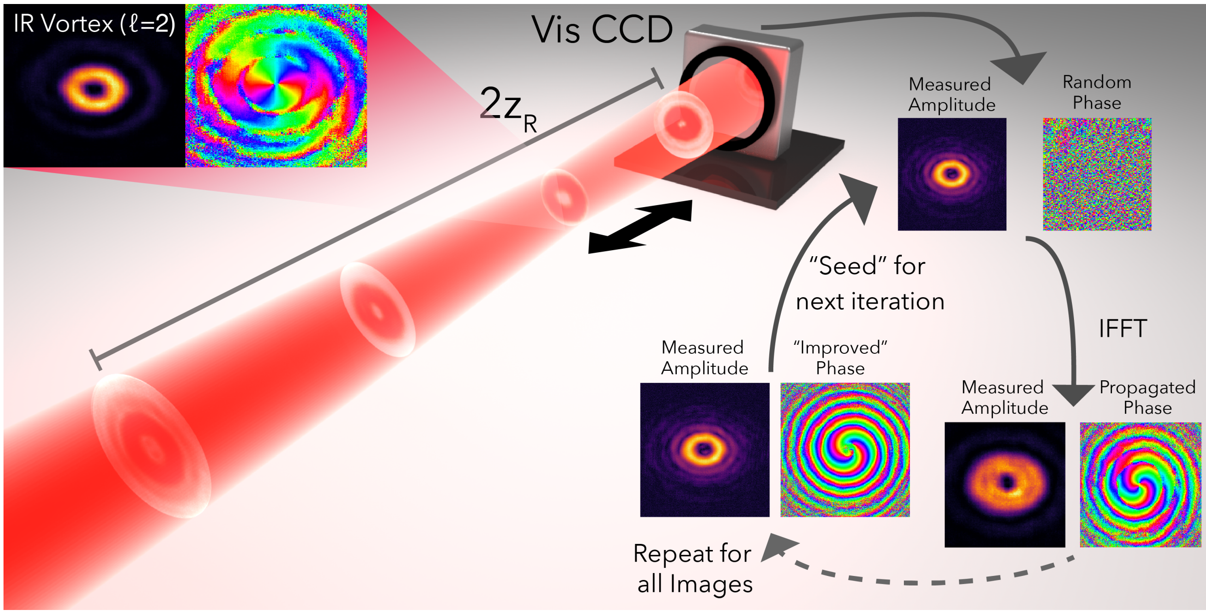

Figure 2.4: **Implementation of the Gerchberg-Saxton phase-retrieval algorithm for high-resolution, wavefront characterization of optical vortex beams.** The characterization of the wavefronts of the visible, vortex beams is performed by first obtaining measurements of the beam profile, then passing the beam profiles into a GS algorithm to retrieve the spatial phase. First, a CCD camera on a moveable translation stage records images of the beam intensity at several image planes (shown above as white cutouts in the beam) over a propagation distance of $2z_R$. The background-subtracted images are then passed into a modified GS algorithm (lower-right inset) to obtain the spatial phase. The GS algorithm is initiated with the measured amplitude at the first image plane, multiplied with a random phase. This complex beam is then propagated to the next image plane, and the propagated amplitude is thrown away while the propagated phase is retained. This is repeated for all recorded images, yielding an "improved" guess for the phase to seed the next iteration of the GS algorithm. The entire process is repeated for up to 1,000 iterations, or until the error between the reconstructed beams and the measured beams reaches a global minimum. When complete, we can obtain a high-resolution image of the complex beam amplitude at focus (**upper-left inset**), which is typically too small to be properly imaged using traditional Shack-Hartmann wavefront sensors. Not that intensity rings observed in the beam profile images in the lower-right inset are consequences of the use of diffractive optical elements to impart the OAM to the beam. At focus; however, a highly pure OAM beam is obtained (upper-left inset).

that are related via some propagating function, provided we also know the locations of the planes containing the distributions. Translating this into the optical domain, the GS algorithm can reconstruct the phase of a propagating light wave from only two inputs; a set of measured beam amplitudes (i.e., mathematical distributions) and the corresponding locations where the images were measured (i.e. plane locations). The GS algorithm then recovers the spatial phase of the sampled light beam by performing via an iterative Fourier transform process (see Fig. 2.4). It's worth noting that since this algorithm works via propagation functions, in the ideal case there is a set of measurements performed in the near-field, and another set performed in the far-field. In practice, we have found that sampling the visible driving beams over a range $\pm 2z_R$ is sufficient to yield highly accurate reconstructions.

In our implementation of the GS algorithm for reconstructing twisted wavefronts, which is based upon related works in the literature [196, 197], we first record the beam intensity profile with a CCD camera (Mightex, BTE-B013-U, 2.2 μm pixel pitch) at no less than 10 image plane locations that are evenly spaced about the focal point of a converging optical system over the range of $\pm 2z_R$. The background-subtracted images and their corresponding locations are then fed into the GS algorithm. The algorithm first applies a random phase to the first image, and this image is propagated to the next image plane. The propagated amplitude at this new plane is replaced with the observed amplitude, while the phase information is retained. This process is repeated for all recorded images in the stack, and after which the final retrieved electric field is used as the seed for the next iteration. This process is repeated for up to 1,000 total iterations, or until a global minimization of the per-pixel error between the retrieved and measured beams is obtained. In order to prevent stagnation of the GS algorithm for OAM beams, we seed the algorithm with a small, random "kick" of azimuthal phase every 10 iterations, to the tune of $\ell = \pm 1/2$. Using this approach, we can reconstruct the wavefront of complex, twisted light beams, of both pure and non-integer OAM modes, with a high resolution in under 5 minutes on a personal laptop computer.

2.4.2 Temporal Characterization of Ultrafast, Infrared Pulses for High-Harmonic Generation

Equally important to the 2D spatial evolution of the phase of ultrafast, high-powered laser pulses is the evolution of the spectral phase—and the subsequent effects induced on the complex amplitude of the pulse—on the exit from the amplifier to its destination in a number of beamlines. The desire to obtain the full, temporal electric field waveform has resulted in a nearly uncountable number of techniques (and for some reason, an equally uncountable amount of cute, animal-based acronyms) that in one way or another, can reconstruct the temporal electric field with a high accuracy and precision. The most popular and straightforward of these techniques is the frequency-resolved optical gating method (FROG) pioneered by Rick Trebino and Dan Kane in early 1990s [179, 198]. The operating principle behind the most basic implementation of FROG is to spectrally resolve the intensity of a near-instantaneous, nonlinear optical signal as a function of temporal delay between two (nearly) identical pulse pairs. The optical toolkit of nonlinear interactions available for intense pulses is quite large, but in our case we resort to the method most suitable for the bicircular experiments described the coming chapters; second harmonic generation (SHG)-FROG.

As FROG is a now routine technique with an equally countless number of technical references describing its underlying theory and implementation in the lab (Rick's book [179] is a wonderful place to start for both of these aspects), we will not attempt to simply reword what is already written quite well in other places. However, reports of SHG-FROG measurements of spatially structured light beams is surprisingly scarce, likely owing to the complex spatiotemporal phase associated with helical wavefronts. In essence, the main crux is that the topological phase leads to an azimuthally dependent phase delay of the pulse at each point in space, which means that in order to fully reconstruct the temporal electric field, we must perform FROG measurements at each point in space. This has led to a number of novel adaptations of the SHG-FROG technique, with most simply performing FROG in conjunction with a wavefront sensor [199–203] (e.g., Shack-Hartmann, see Section 2.4.1 above). Luckily for us, the use of long pulses renders the associated spatiotemporal effects negligible. As a confirmation of this, we present in Figure **??** the obtained FROG traces for both a reference Gaussian beam, and an OAM beam with the same frequency, but a topological charge of $\ell = 1$. As can be seen from these back-to-back measurements, the presence of OAM results in very little observed differences, although we do note that the SHG conversion efficiency is reduced from the Gaussian case, which is expected based on previous results of nonlinear frequency conversion employing OAM beams (see Ref. [204] and references therein).

2.4.3 Extreme-Ultraviolet Magnetic Circular Dichroism Measurements (EUV-MCD)

Extreme ultraviolet beams possessing SAM are particularly tricky to quantify, as the usual methods of characterizing the ellipticity of optical waveforms via polarization rotators and filters simply does not work in the EUV (refractive indices are already near unity, and natural birefringence is a rarely observed phenomenon in the EUV and soft x-ray regions of the spectrum). As such, we are forced to use more elaborate techniques, primarily based upon the dichroic absorption of materials. The most popular dichroic interactions for measuring the ellipticity of EUV beams is to employ either helicity-selective photoionization [205–207], polarimetry [165, 208], or the EUV/soft x-ray magnetic circular dichroism (EUV-MCD and XMCD, respectively) effect [11, 162, 209, 210]. Of course, it wouldn't be worth listing a bunch of different polarization characterization methods if we didn't compare and contrast their pros and cons. Polarimetry is by far the most straightforward, but this involves several bounces off of metallic mirrors [165, 208], which for sources that aren't the size of small towns results in dramatically reduced flux. Moreover, this method cannot discriminate unpolarized light from polarized light, and fully polarized light is almost never emitted in an extreme nonlinear process like HHG. Helicity-selective photoionization processes [205–207] are attractive as they do not require any assumptions of the polarization of the interrogated light wave, but such methods operate on a much narrower energy range, and weak photoionization signals require extremely long run times. Measurements based on the EUV-MCD and XMCD effect are quick, straightforward, and can be performed with relatively low-intensity EUV [162, 209, 210] and soft x-ray pulses [11]; however, these measurements are also constrained by a limited energy range for the MCD effect, difficulty in producing high-quality samples, and an absolute value for the ellipticity of light can only be obtained by a reference to existing measurements. Despite these difficulties, we opt to exploit the EUV-MCD effect, as the infrastructure and the necessary sample-making gurus are in close proximity to the lab spaces where this thesis work was performed. Moreover, the results described in Chapter 4 do not require an absolute value of the ellipticity of the emitted high harmonics.

In the EUV-MCD effect, the dichroic absorption of elliptically polarized light is measured for different macroscopic magnetizations of a magnetic thin film, and the resulting transmitted EUV light is spectrally dispersed and recorded with an EUV-sensitive imaging device[14] . The dichroic absorption is described via a magneto-optical correction to the absorpitive part of the refractive index, $\Im[\mathrm{n}] = \beta \pm \Delta\beta$, where β is the magneto-optical (MO) constant for a particular material, and $\Delta\beta$ describes the helicity-dependent modification to the MO constant. In order to extract the $\Delta\beta$ term, absorption spectra are taken for different macroscopic magnetizations of the thin-film sample. For perfectly circularly polarized light, the transmitted

[14] A notable exception is when EUV MCD is performed in a spatially resolved fashion, as in Ref. [6].

intensity of a single harmonic is given by,

$$I_{q,up} = I_0 e^{2k_q \Delta\beta_q L} \tag{2.4}$$

$$I_{q,down} = I_0 e^{-2k_q \Delta\beta_q L}. \tag{2.5}$$

where, $I_{q,[up,down]}$ is the transmitted intensity of the q^{th} harmonic for different magnetization vectors of the thin film and k_q is its associated wavevector ($k_q = 2\pi c/\lambda_q$), and L is the path length of the sample. With transmitted intensities in hand for each magnetization direction, we can then compute their normalized ratio (i.e., the MCD asymmetry, A), which gives a direct relation to the $\Delta\beta$ parameter,

$$A = \frac{(I_{q,up} - I_{q,down})}{(I_{q,up} + I_{q,down})} = tanh\left(2k_q \Delta\beta L\right). \tag{2.6}$$

With asymmetries in hand, we can invert Equation 2.3 to obtain the $\Delta\beta$ term, which can be compared to literature values—themselves being calculated from experimental data obtained at synchrotron sources with highly pure polarization [209, 211]. Finally, we can derive an ellipticity for each harmonic order, q, that contributes to the MCD effect.

So far, we've kept this discussion pretty general, which doesn't do a whole lot for us if we want to pull this off in the lab. Right away, we find ourselves restricted to performing measurements at the more EUV-friendly magnetic M and N absorption edges, as the L absorption edges are currently beyond stable, bright, keV-range table-top HHG systems[15] . Unfortunately, this significantly reduces the magnitude of the MCD effect, necessitating the use of bright, highly circular high harmonics to achieve detectable experimental signals. Along these lines, M edge spectroscopy demands high-quality samples, especially to prevent effects from oxidation and thermal heating. For the elemental thin-film samples used in Chapter 4, we orient the magnetic sample—in practice, a 10-20 nm layer of Fe, Ni, Co, or a mixture thereof deposited on a 200-nm-thick Al foil, then capped with a few nm of Cu or Ta—at 45° with respect to the propagation vector of the EUV light. This angle is chosen due to an armistice between maximizing the MCD effect (via the angle of the sample, and the sample path length), providing a flexible experimental geometry, and the use of samples that require in-plane magnetization. The samples themselves are held by a machined iron rod, which is

[15] Although, rapid progress is being made on this front. High-energy, mid-IR laser systems based on optical-parametric CPA (OPCPA) are nearing commercial availability, which will facilitate deployment of keV high-harmonic sources around the globe.

magnetized via an external, home-built electromagnet. By placing a magnetic “sink” (i.e., a small piece of iron with a 45° miter cut) on the opposite side of the sample, we can achieve in-plane magnetic fields up to $\sim$100 mT, which is more than enough to fully magnetize thin films composed of elements from the 3d and 5f blocks.

Chapter 3

All Optical Control of the Polarization of Attosecond Pulse Trains in Bicircular High-Harmonic Generation

This chapter is adapted, with permission, from:

- K. M. Dorney, J. L. Ellis, C. Hernández-García, D. D. Hickstein, C. A. Mancuso, N. Brooks, T. Fan, G. Fan, D. Zusin, C. Gentry, P. Grychtol, H. C. Kapteyn, and M. M. Murnane. Helicity-Selective Enhancement and Polarization Control of Attosecond High Harmonic Waveforms Driven by Bichromatic Circularly Polarized Laser Fields. *Phys. Rev. Lett.*, 119 (6), **2017**, 45–47. DOI: 10.1103/PhysRevLett.119.063201

3.1 Chapter Overview

This chapter takes us on a journey that details a straight-forward, all-optical control of the polarization of APTs produced when HHG is driven with a bicircular driving laser field. Almost immediately after the re-discovery of "circularly polarized"[1] HHG driven with a two-color laser field where the constituents (typically) possess opposite circular polarizations, it was realized that the resulting APTs were predominately linearly polarized. By employing a straight-forward technique inspired by the photoelectron recollision control detailed in [212] and [9], we show how the polarization of the APTs in bicircular-driven HHG can be precisely controlled simply by varying the relative intensity of the two laser fields comprising the bicircular field. By altering the relatively intensity, the propensity rules governing HHG can be tuned to favor production of either LCP or RCP high-harmonics. In a Fourier picture, control over the power

[1] In theory, the harmonics should be as circularly polarized as the two drivers; however, effects from depolarization can also be present, which reduces the circularity of the high harmonics.

spectrum of RCP and LCP harmonics results in the tuning of the polarization of the APTs. We employ advanced numerical simulations within the framework of the SFA+, including propagation, of the HHG upconversion process, which are utilized to inform the degree of ellipticity control afforded by tuning the properties of the driving laser waveform. The results open a relatively straight-forward route to produced elliptically polarized APTs without the complication of a non-collinear geometry [7, 12, 213] or the use of elaborate field-gating techniques. The results of this chapter will provide for light sources that will aide in increasing signals in EUV chiral spectroscopies, as well as opening an additional route to generate circularly polarized IAPs.

3.2 Introduction

3.2.1 Polarization Control in HHG

Shortly after the experimental realization of HHG [127, 128], it was quickly realized that the re-collision nature of HHG precluded the emission of circularly polarized high-harmonics, as the HHG yield drops exponentially as the ellipticity of the driving laser waveform is varied away from linear polarization. In addition to this limitation, the short-wavelength nature of the emitted high-harmonics precludes the use of conventional polarization optics—as birefringence is negligible or non-existent in this wavelength regime—, which results in elaborate optical setups known as EUV phase-shifters to control the polarization of EUV and soft x-ray light[2] . As such, we must resort to controlling the quantum processes leading to the emission of high-harmonics in order to harness the polarization of EUV light.

Interestingly, polarization control in HHG was actually realized a just under a decade after the discovery of HHG itself [158]; however, the polarization of the emitted harmonics was not characterized at the time. Although the polarization state was not quantified, this initial work inspired several theoretical works describing HHG driven by a bicircular field [159, 160], but the HHG community seemed to have missed this initial excitement. Fast-forwarding nearly 20 years, the use of a two-color driving laser field to control the polarization of HHG was independently re-discovered [161–163], and characterization of the emitted EUV

[2] The issue here is that multiple bounces off of carefully arranged mirrors results in a dramatic reduction in the flux of the short-wavelength light, which is detrimental to EUV and soft x-ray sources that are not the size of small towns.

harmonics showed that indeed the harmonics were highly elliptically polarized. Although the harmonics were shown to be highly elliptically polarized in the frequency domain [11, 162, 164], the nature of bicircular-driven HHG resulted in APTs that were predominately linearly polarized [145]. This precludes the study of chiral dynamics occurring faster than the harmonic pulse width via BHHG, as if a single burst was isolated from the APT, it would be linearly polarized [214]. These works, along with the realization that the underlying ATPs were predominately linearly polarized, sparked a revolution in polarization control in attosecond science, as circularly polarized, short-wavelength light allows for interrogation of element-specific, ultrafast chiral dynamics in material, molecular, and atomic systems. As such, numerous schemes have been proposed to control the polarization of HHG-based APTs, ranging from the exploitation of single-emitter effects in HHG [215, 216], or tailoring the macroscopic HHG response (e.g., phase matching) to yield elliptically polarized APTs [184, 217].

3.2.2 HHG Driven with an Ultrafast, Bicircular Laser Field

In what follows, we will take a predominantly photon-oriented picture of describing the BHHG upconversion process. This is of course an interpretation of a highly dynamcal and non-perturbative process, but has the benfit of being very physically insightful. For a detailed account of the unique, quantum features that are not captured by a simple photon model, the interested reader is referred to the PhD thesis of Emilio Pisanty [218]. The use of bicircular driving laser waveforms for the upconversion process restricts the conservation rules governing high-harmonic emission [219], as we must now consider the conservation of photon SAM, along with the usual energy and parity constraints. For the case of pure circular polarization of the bicircular driving field, the HHG conservation rules determining the emission of a particular harmonic, q, are modified such that,

$$\sigma_q = n_1\sigma_1 + n_2\sigma_2 \tag{3.1}$$

$$n_2 = n_1 - \sigma_q\sigma_1 \tag{3.2}$$

$$q\omega_1 = \omega_q = n_1\omega_1 + n_2\omega_2 \tag{3.3}$$

where σ_i is the SAM of the harmonic and bicircular fields, $n_{1,2}$ is the number of photons absorbed from each driver, and ω_i is the frequency of the harmonic and bicircular fields. These conservation rules manifest in a unique HHG spectrum comprised of high-harmonic "doublets" of opposite circular polarization, with a missing interstitial harmonic that is spin-forbidden [1, 162, 219, 220]. The harmonics within each doublet are themselves elliptically polarized, where the $3n{+}\omega_1$ harmonics co-rotate with the lower frequency component of the bicircular waveform, and the $3n{+}\omega_2$ harmonics co-rotate with the higher frequency counterpart. The degree of suppression of the interstitial harmonic serves as a powerful experimental handle for optimizing the circularity of the emitted high-harmonics, while also serving as a unique spectroscopic signature that is indicative of the overall symmetry of the HHG system. For instance, the emergence of the spin-forbidden harmonics can be used as a chiral discriminator [166, 167, 221] or for unraveling dynamical symmetry breaking and depolarization during the HHG upconversion process [207, 222]. The overall 3-fold symmetry is a direct result of the combined symmetry of the nonlinear medium and the driving field, which serves the basis for BHHG-based spectroscopies of chiral structures and dynamics [168, 221, 223].

In the time domain, the presence of phase-locked harmonics of alternating helicities but equal amplitudes results in a train of linearly polarized APTs [159, 160, 162, 224] where each attosecond burst is rotated in the polarization plane by an angle that depends on the central frequencies of the bicircular laser field [145, 159, 160, 162, 184, 224]. It is this unique spectrotemporal coupling in BHHG that forms the basis for controlling the polarization of the underlying APTs; if the spectral symmetry of a BHHG spectrum can be broken, not only are elliptical APTs naturally produced, but the harmonics themselves retain their elliptical polarizations. This relatively simple concept has sparked a resurgence in polarization control in BHHG, leading to numerous theoretical predictions [215, 216, 225] and experimental demonstrations [1, 226–228] for obtaining chiral HHG spectra when driving with a bicircular laser field[3] . Along with this renaissance, an equally explosive effort has manifested with an intent set on explaining the relative intensity of $3n{+}\omega_1$ and $3n{+}\omega_2$ harmonics in BHHG [1, 164, 215, 216, 225, 226, 229–231]. For the truly curious, the doctoral thesis of Emilio Pisanty [218] provides an excellent discussion of the mechanisms at play in BHHG and how they relate to the observed harmonic intensity ratios.

[3] Although other methods exist for producing circularly polarized APTs without relying on the generation of a chiral HHG spectrum [6, 12, 165, 213], for the purposes of this discussion, we restrict ourselves to HHG driven with a bicircular field.

3.3 Experimental

The HHG process is driven with a bicircular laser field composed of the fundamental (λ_1=790nm, σ_1=+1, RCP) and second harmonic (λ_2=395nm, σ_2=-1, LCP) of an ultrafast Ti:sapphire amplifier (8.5 mJ, 45 fs, 1 kHz, KMLabs Wyvern HE). The full output of the amplifier is sent into a Mach-Zehnder-type interferometer, which spatially separates the beams and allows for independent control of the power and polarization in each arm. A large portion (70%) of the full beam is passed into a 200-μm-thick BBO crystal to produce the second harmonic, while the remaining portion in sent into the other arm. Waveplates ($\lambda/2$ and $\lambda/4$) are placed in each arm to produce circular driving beams of opposite helicity, while the power in each beam is controlled via waveplate-polarizer pairs. The two beams are then recombined with a dichroic mirror and focused (f=250mm) onto a supersonic expansion of argon or helium gas. A one-to-one Galilean-type telescope[4] is placed in the fundamental arm in order to correct for chromatic aberrations in the single focusing lens. The combined focus is then placed 1mm before the gas jet in order favor phase matching of the short trajectories [232, 233]. The emitted harmonics pass through either 200-nm-thick aluminum (for argon harmonics) or zirconium (for helium harmonics) filters (Luxel Corporation), which serve to block the residual driving beam and as a band-pass filter for the harmonic spectrum in the range of 17-72 eV for aluminum and >50 eV for zirconium. The harmonics are collected via a gold-coated cylindrical grating (Hitachi 001-0266) and the resulting spatiospectral image is recorded with a CCD camera (Andor Newton 940).

3.4 Generation of Chiral Spectra and Polarization Control of the Underlying APTs in BHHG

3.4.1 Generation of Chiral High-Harmonic Spectra with a Bicircular Driver (cBHHG)

As the intensity ratio is varied, either RCP ($3n+\omega_1$) or LCP ($3n+\omega_2$) harmonics are preferentially produced, which imparts a net chirality to the harmonic spectrum (Figure 3.2). Remarkably, this spectral

[4] The use of a Galilean vs. a Keplerian telescope is two-fold. The high intensity at the interstitial focus in a Keplerian telescope introduces significant self-actions on the light pulse (e.g. self-diffraction, self-phase modulation, etc.), while also serving as an optical “bear trap” for distracted fingers.

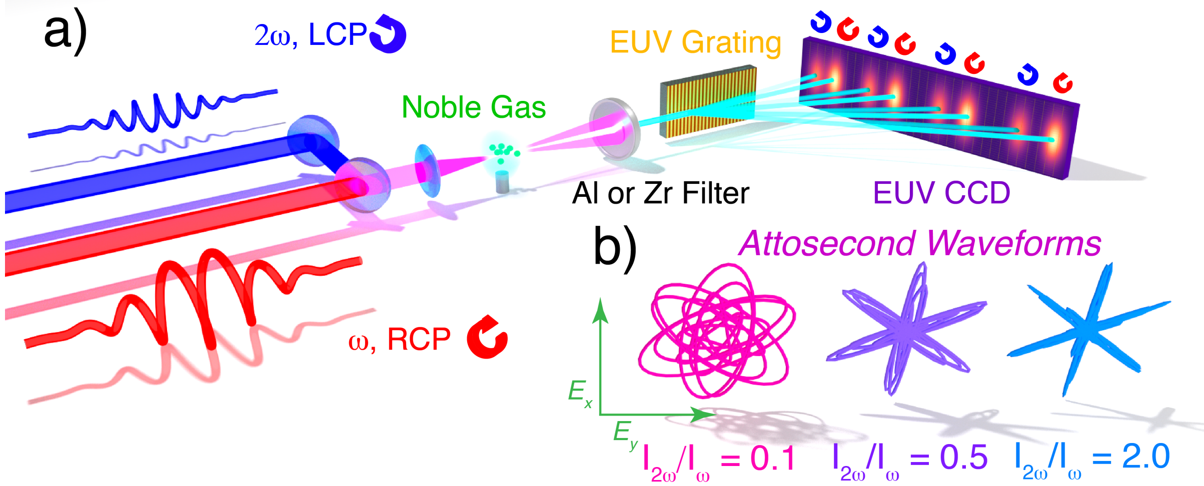

Figure 3.1: **Experimental scheme for bicircular generation of chiral high-harmonic spectra and elliptically polarized APTs.** **a**, Experimental scheme for generating chiral high-harmonic spectra via a bicircular (ω_1, $\omega_2 = 2\omega_1$) driving field (cBHHG). **b**, Polarization plane projections of the temporal structure for the theoretical APTs supported by experimental cBHHG spectra generated at different intensity ratios, $I_{\omega_2}/I_{\omega_1}$, of the driving field, plotted for one cycle of the ω_1 field (i.e., 2.67 fs). Adapted with permission from Ref. 1. ©2017 American Physical Society

chirality can be introduced without significantly altering the bandwidth of the individual harmonic orders or the spectral envelope, indicating that the conversion process is not strongly altered as the intensity ratio is varied. For instance, a strong suppression of the spin-forbidden $3n$ harmonic orders is observed for all intensity ratios, which is a strong indication that effects from dynamical symmetry breaking [222] are minimal. Furthermore, the spectral envelope varies smoothly in amplitude as the intensity ratio is scanned, which is indicative of a near-constant total intensity of the bicircular driver. This suggests that the chirality of the high-harmonic spectrum can be controlled in an energy-independent manner, a crucial necessity for producing high-energy circularly polarized attosecond pulses. Taken together, the smooth variation of the chirality of the HHG spectra indicate a concurrent, smooth variation of the ellipticity of the APTs. However, this comes at the price of a decreased HHG yield, which is a direct result of the intensity-ratio-dependent quantum dynamics of the photoionized electrons in bicircular fields [8–10, 234].

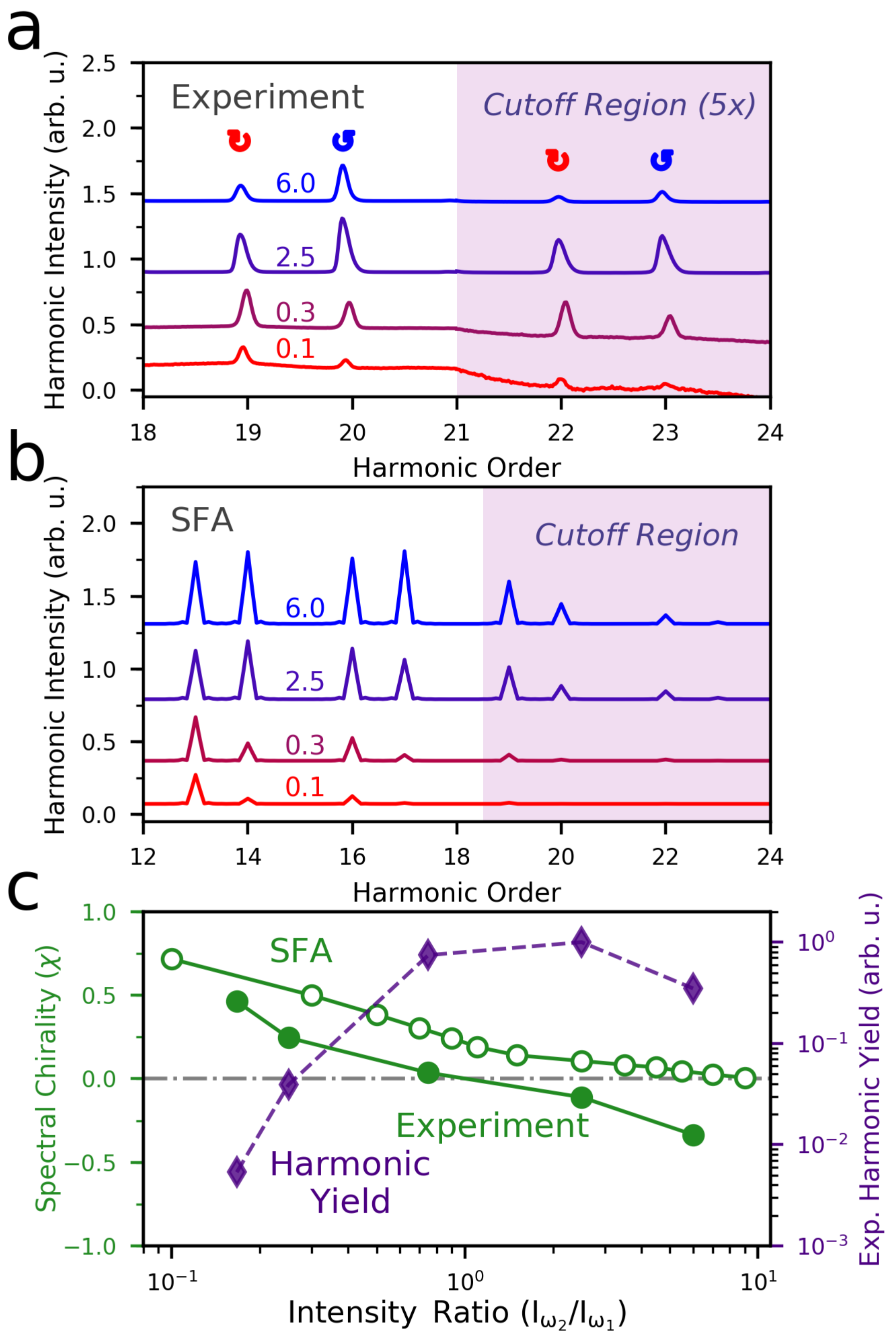

Figure 3.2: **Generation and control of chiral EUV spectra via cBHHG in Ar. a**, Experimental and **b**, theoretical cBHHG spectra recorded at increasing $I_{\omega_2}/I_{\omega_1}$(exact values given next to the spectra) at total intensities of $\approx$ 210^{14} W/cm^2. The harmonics in the cutoff region in **a** have been scaled for clarity. **c**, Experimental and theoretical spectral chirality $\chi = (I_{RCP} - I_{LCP})\,/\,(I_{RCP} + I_{LCP})$ (left axis) and experimental cBHHG yields (right axis) observed in Ar as a function of $I_{\omega_2}/I_{\omega_1}$of the two-color field. Harmonic yields are given as the total integrated signal for all observed harmonic orders in the experimental spectra. Adapted with permission from Ref. 1. ©2017 American Physical Society

3.4.2 Confirmation of Ellipticity Control of APTs via cBHHG

In order to establish the link between the chirality of the cBHHG spectra and the ellipticity of the underlying APTs, we employ numerical simulations—including propagation—of the cBHHG process. To this end, we use the electromagnetic-field-propagator method [155], where the single-atom dipole response is calculated within the SFA. Although phase-matching effects are explicitly included in the simulations, we note that under the experimental conditions of this work phase matching does not play a significant role in the observed chiral control (see Chapter A, Section A.2). Aside from slight differences in cut-off, the theoretical spectra accurately reproduce the experimentally measured variation of the spectral chirality as a function of the intensity ratio of the bicircular driving beam. Interestingly, the simulations suggest that the chirality of the cBHHG spectra may only be controlled in favor of RCP harmonics, which could be the result of helicity-dependent absorption in the generating medium [184, 217], or simply a stronger envelope effect in the theoretical spectra.

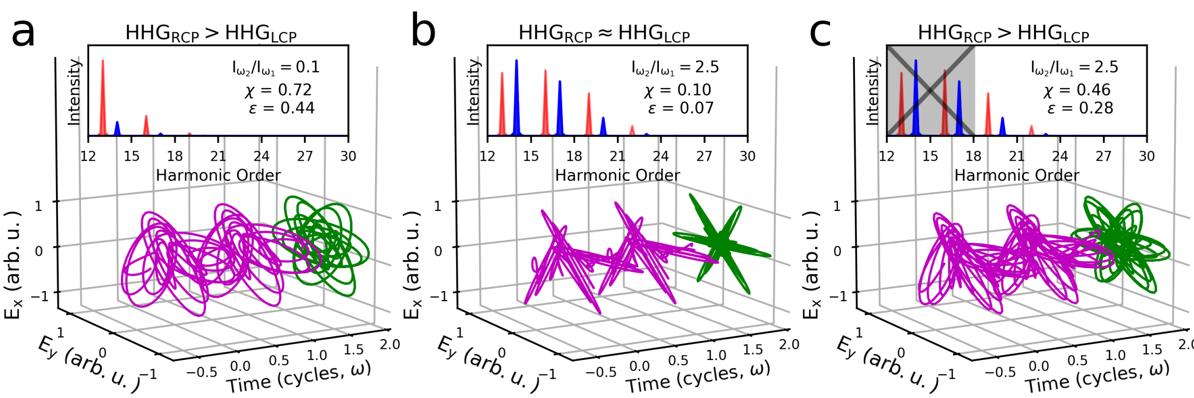

Figure 3.3: **Active control of the polarization of attosecond pulses produced in Ar gas via cBHHG.** Theoretical attosecond pulse trains (APTs) and corresponding spectra in Ar [**a**–**c**] at a total intensity of 2.010^{14} W/cm^2. The temporal profile is obtained via an inverse Fourier transformation of the corresponding cBHHG spectra at the indicated $I_{\omega_2}/I_{\omega_1}$ ratio, spectral chirality (χ) and harmonic field ellipticities (ϵ) [insets]. Here, light-red HHG orders are RCP, while dark-blue orders are LCP. As the cBHHG spectra evolve from being dominated by RCP harmonics to a preference of LCP harmonics, the APTs evolve from elliptical to linear (**a**, **b**). Selecting a small bandwidth near the cutoff (**c**, unshaded region) restores the ellipticity of the APTs, even when $I_{\omega_2}/I_{\omega_1}$ is optimized for the brightest harmonic signal. Adapted with permission from Ref. 1. ©2017 American Physical Society

The theoretical spectra give direct access to the temporal properties of the underlying APTs as the intensity ratio is varied. A Fourier transform yields a picture into the subcycle dynamics of the cBHHG emission process, which reveals a smooth variation of the ellipticity of the individual attosecond bursts. As the intensity ratio is increased, the spectral intensity of LCP harmonics is also increased, which results in the evolution of the polarization state of the APTs from elliptical to near linear. Interestingly, there seems to be a plateau-like effect for large intensity ratios of the driving field. Although this is likely due to the same effects responsible for the lack of negative values for the spectral chirality in the simulated spectra (Figure 3.2), this trend may be circumvented in practice by filtering the near-cutoff high-harmonic orders, which then restores the ellipticity of the APTs. This is particularly attractive for generating high-energy elliptical attosecond pulses, as band-pass filtering of the harmonic spectrum is to date still the most straight-forward way to produce high-energy IAPs [54]. Taken together, the similarly smooth variation in the ellipticity of the APTs and their corresponding spectral chirality confirm the experimentally observed chiral control results in elliptical APTs. As such, the spectral chirality can be used as a real-time parameter in BHHG setups for generating APTs with tailor-made polarization.

3.4.3 Mechanism of Helicity-Selective Enhancement and Chiral Control in cBHHG

The helicity-selective enhancement observed in the BHHG spectra recorded at different intensity ratios of the bicircular driving field is a direct result of the complex quantum dynamics governing the BHHG emission process. For simplicity, we restrict the following discussion to single-emitter effects (i.e., phase-matching effects are minimal in this geometry, see Appendix A, Section A.2) and a constant total intensity of the bicircular field for each intensity ratio[5]. Under these conditions, the observed asymmetry in the intensity of RCP and LCP harmonic peaks can be largely recaptured by considering the propensity rules governing the photoionization and photorecombination steps in BHHG [1, 215, 216, 226, 229–231, 235–238].

First, we consider ionization of spherically (e.g., helium) and non-spherically (e.g., neon and argon) symmetric ground states by a bicircular field. In the strong-field regime, the ionization rates of electronic states that counter-rotate with the bicircular field are higher than those that co-rotate or do not rotate at all[6] [237–239]. Intuitively, this can be understood as the instantaneous electric field vector of the bicircular

[5] For the intensities employed in this work, the ionization rate is largely independent of the intensity ratio of the bicircular field [10, 226].

[6] This is in contrast to the Fano-Bethe-type propensity rules for a pure photoionization process [235, 236], where the electron need not return to the parent ion.

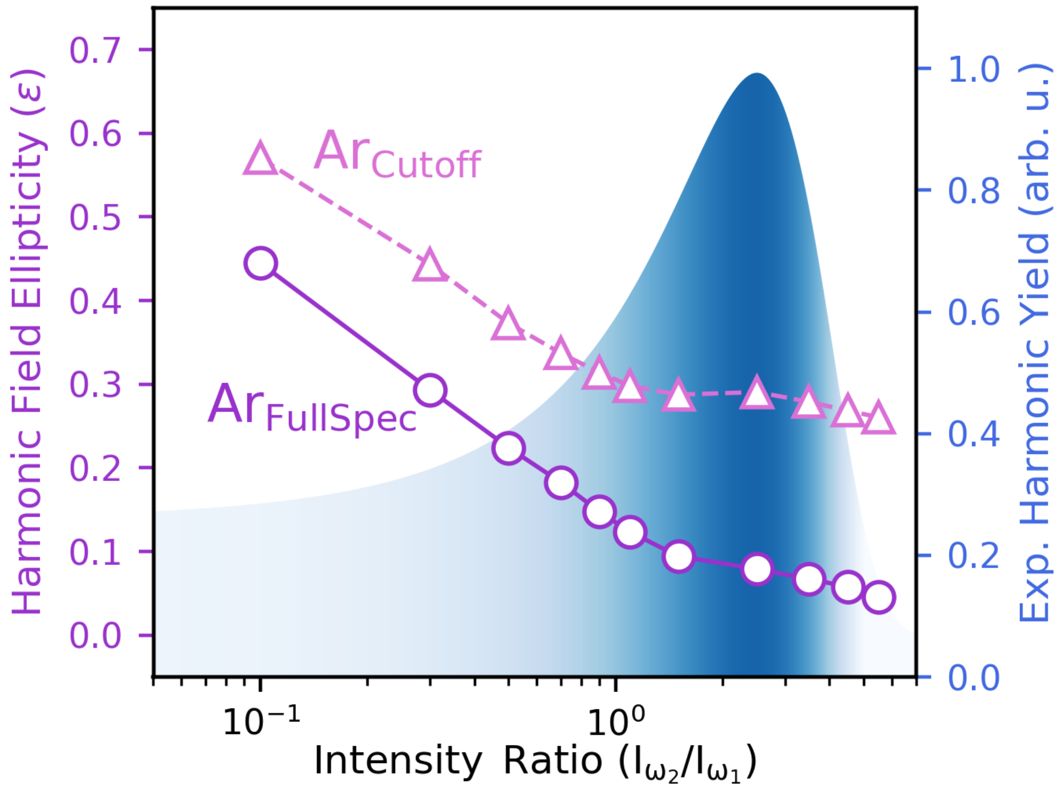

Figure 3.4: **Practical implications of controlling the ellipticity of APTs in Ar.** As the intensity ratio of the two-color field is increased in favor of the ω_2 component, the ellipticity of the attosecond bursts (circle symbols) is quickly reduced, such that near–linearly polarized bursts are obtained when the experimental cBHHG signal is brightest (shown here as a Gaussian fit of the experimental data, blue gradient, right axis). However, spectral filtering of the cBHHG spectra to select the cutoff harmonics can significantly increase the ellipticity of the APTs (triangle symbols), even when the intensity ratio of the driving field is optimized for the cBHHG yield. Adapted with permission from Ref. 1. ©2017 American Physical Society

driver creating a rotating depression in the combined laser-atom potential energy landscape and electrons in counter-rotating (co-rotating) electronic states encounter this depression more (less) often than their co-rotating (counter-rotating) counterparts, thus leading to a higher (lower) ionization rate. As such, when the intensity ratio is large, the bicircular field rotates with the fundamental driver and, combined with an increased recombination probability (see below), the co-polarized RCP harmonics become more intense than their LCP counterparts, as observed in Figure 3.2. The same argument, but inverted, also holds when the ω_2 component is the more intense of the two beams.

Second, we consider the recombination process of the liberated photoelectrons. For s-type ground states, recombination can only happen via p partial waves and there is no preference with regard to the helicity of the emitted photon upon recombination (note this is also true of the propensity rules for ionization from s states as mentioned above). However, for p-type ground states, recombination can occur from either both s and d partial waves, or just solely s waves. Under the current definitions of the field helicities, $p+$ electronic states rotate withe RCP driver, while p- states rotate with the LCP driver. For recombination to the $p+$ state, transitions involving the absorption of an extra ω_1 photon are favored, while channels requiring the absorption of an extra ω_2 photon lead to a higher recombination probability to p- states.

Taking these points together, a unified picture of helicity control in BHHG begins to emerge. For media with p-type ground states (e.g., neon and argon), both ionization and recombination exhibit a helicity-dependence, with the exact dependence spelled out via the relative angular momenta of the light field, the liberated electron, and the electron hole remaining in the parent emitter. For the case of spherically symmetry ground states (i.e., s-type such as helium), there is no helicity preference during the ionization step, so that chiral asymmetry in the BHHG spectra can only result from helicity-dependent effects during recombination. This provides a clean separation of the effects from ionization and recombination in cBHHG, which clearly explains why a larger degree of chiral control can be achieved for emitters who possess a ground state with initial angular momentum. Although we have ignored propagation dynamics in our arguments, we note that the intensity-ratio-dependent propagation dynamics primarily affect the kinetic energy spectrum of the returning photoelectrons [9, 212], which manifests as increases/decreases in BHHG yield and/or a variation in the spectral chirality as a function of photon energy. As a final aside, we note that despite the complexity of the quantum dynamics involved in cBHHG, most of the features regarding chiral asymmetry and control can be accurately recaptured with a simple perturbative photon model (see Appendix A, Section A.3).

3.5 Conclusions and Future Outlook for cBHHG

In conclusion, we have shown that the chirality of high harmonics generated with a bicircular driver can be controlled via the intensity ratio of the two components of the two-color field, which makes it possible to selectively enhance either the left or right circularly polarized harmonic orders. We have shown that the effects of changing the intensity ratio on the BHHG chirality can be understood by considering the propensity rules for photoionization and recombination, which allow access to dynamics occurring in the different regimes by use of an HHG medium with appropriate ground-state symmetry. Moreover, we have provided an intuitive, parametric model that qualitatively recaptures the observed degree of chiral control by treating the individual harmonics as being generated by absorption of photons with a definite spin. Most importantly, we find that the induced chirality in the cBHHG spectra allows for direct control over the attosecond polarization of the underlying APTs. Thus, our results suggest a straightforward route for generating bright, high-energy, elliptically polarized APTs, without extensive modification of existing setups. As such, this method could be exploited to produce polarization-tailored attosecond waveforms and even yield elliptically polarized IAPs. Furthermore, the results presented here do not rely on the choice of frequencies for the bicircular field, thus allowing this method to be applied to BHHG driven by both UV and mid-IR lasers. The results presented here will not only aid development of novel sources of circularly polarized extreme ultraviolet and x-ray radiation, but also extend the applicability of these light sources to studying chiral dynamics on the attosecond time scale.

Chapter 4

Helicity in a Twist: Controlling the polarization, divergence and vortex charge of attosecond high-harmonic beams via Simultaneous Spin-Orbit Momentum Conservation

This chapter is adapted, with permission, from:

- K. M. Dorney, L. Rego, N. J. Brooks, J. San Román, C.-T. Liao, J. L. Ellis, D. Zusin, C. Gentry, Q. L. Nguyen, J. M. Shaw, A. Picón, L. Plaja, H. C. Kapteyn, M. M. Murnane, and C. Hernández-García. Controlling the polarization and vortex charge of attosecond high-harmonic beams via simultaneous spin–orbit momentum conservation. *Nat. Photonics*, 13 (2), **2019**, 123–130. DOI: `10.1038/s41566-018-0304-3`

Figure 4.1: **Illustration of the generation of circularly polarized, extreme ultraviolet, attosecond vortices via SAMOAM HHG.** When high-harmonic generation is driven by a bicircular vortex beam (left), exquisite control over the SAM and OAM of the emitted harmonics is gained, allowing, for example—as shown here—the generation of spatially isolated vortices of opposite, left (purple tubes) and right (cyan tubes) circular polarizations. Artwork and design by Kevin Dorney and Steve Burrows, JILA.

4.1 Chapter Overview

This chapter continues our journey with a “suspiciously chronological” extension of the work detailed in Chapter 3. Here, we add a new free parameter to our familiar bicircular field by introducing a controllable, integer amount of OAM to each beam. By driving the HHG process with a bicircular optical vortex beam (Section 4.3), we generate, for the first time, circularly polarized EUV beams—and attosecond pulses—with an OAM content that is fully controlled by the driving lasers themselves. This exquisite control over the angular momenta of the emitted high-harmonics is manifested from entwined SAM and OAM conservation laws, which enforce restrictions on the allowed quantum channels that lead to the emission of each high-harmonic. We show that this novel, simultaneous coupling regime allows for the generation of a variety of circularly polarized, high-harmonic vortices; high-harmonic doublets with equal OAM but opposite SAM (Section 4.4), spatially isolated APTs of opposite circular polarization (Section 4.5), and EUV vortex beams with low topological charges that are equal to the driving laser (Section 4.6). We further show that these unique light sources are bright and stable enough for spectroscopic applications, by performing spatially resolved measurements of the extreme ultraviolet magnetic circular dichroism (EUV-MCD) response of a uniformly magnetized cobalt film (Section 4.5). Advanced, full, quantum simulations of the OAM HHG emission process, including propagation to the detector, as always, are used to confirm the experimentally generated EUV vortex beams obtained for different configurations of the SAM and OAM of the bicircular field, as well as inform the inherent physics of SAM-OAM HHG (Section 4.3.3). The work described here provides the only experimental realization of the generation of attosecond, EUV beams with designer SAM and OAM, thus opening the door for ultrafast, element-specific spectroscopies of SAM and OAM transfer.

4.2 Introduction

4.2.1 An Attosecond Twist In Time: OAM in High-Harmonic Generation

Interestingly, the first generation of EUV light with a non-zero OAM actually preceded the ”rediscovery” of bicircular-driven HHG by nearly three years, with the first report being that of Zürch et al. in 2012 [97]. In that seminal work, an IR vortex pulse (1 mJ, 30 fs, 800 nm, 1 kHz) was produced by directing the output of a Ti:sapph amplifier onto a spatial light modulator (SLM) with an appropriately imprinted phase mask, then focusing that resulting vortex beam onto a supersonic expansion of Ar gas. The generation of high-harmonics with a spatial mode similar to the driver was not so surprising, but the fact that visible phase fronts could be imprinted into EUV light via HHG was unexpected and generated much excitement in the strong-field and attosecond science community. However, this was equally paralleled by an intense curiosity regarding the results of Ref. [97]; the harmonics were inferred to have a topological charge *equal* to that of the driving laser. This came as quite a surprise, since it was (and is) well-established, both experimentally and theoretically [153, 240, 241], that the microscopic, nonlinear response of the HHG medium would lead to the emission of harmonics with a phase (under the SFA) given by

$$\phi_q = \mathrm{n}\phi_{\omega_0} + \phi_{q,0} - \alpha_q \mathrm{I}. \tag{4.1}$$

Here, ϕ_q is the phase of harmonic q (with an energy of nq, where n is the numbers of photons absorbed from the driving beam), ω_0 is the central frequency of the driving laser, α_q makes an appearance once again a trajectory-dependent constant related to the dipole phase associated with harmonic q, and $\phi_{q,0}$ is an inherent phase that is characteristic of the nonlinear medium. As such, the experimental results did not agree with expectations based on the current knowledge of HHG at the time, which predicted that harmonic q should possess a topological charge of $\ell_q = n\ell_0$.

Despite this initial discrepancy, the prospect of imprinting topological structure onto EUV waveforms—along with all the spooky physics that comes with "singular" light beams [22, 70]—sparked several follow up papers. A detailed theoretical investigation [99] within the SFA+ framework, including propagation of course, showed that the expected phase scaling should indeed apply to OAM-driven HHG, thus providing a feasible route for generating short wavelength, coherent light with an ultrafast topological phase variation (since the phase "wraps" every T_0/Nq seconds). Moreover, the nature of the OAM HHG process was shown to yield helical APTs, naturally, which is the result of the azimuthally-dependent phase delay across the profile of twisted light pulses. Subsequent experimental studies confirmed both the OAM conservation law [98] and the helical structure of the APTs [100], which themselves triggered a surge of theoretical [170–172, 242] and experimental [2, 3, 101, 102, 243] works related to generating and controlling optical OAM in

HHG-based light sources. Until recently; however, the knowledge pipelines of optical SAM or OAM control in HHG processes remained largely separated, despite the similarities describing the dynamic conservation of both types of angular momentum in HHG[1] .

4.2.2 Spin and Orbital Angular Momentum in High-Harmonic Generation: SAM-OAM HHG

Since the pioneering studies of Beth [62] and Allen [69], it has been well known that propagating light waves, under the paraxial approximation, can possess two distinct forms of angular momenta—spin and orbital angular momentum (SAM and OAM, respectively). Although similar in nature, the distinction between the SAM and OAM of light is straightforward when one considers an interaction picture: the SAM of light is mediated through anisotropic interactions, whereas the OAM of light is associated with inhomogeneity in a physical system [70]. This powerful decoupling allows for the independent manipulation and measurement of either the SAM or OAM of a single light field [75, 244, 245], and enables many applications [24], including optical sensing and communication [23], molecular detection [246], kinematic micromanipulation [21], and photonic momentum control [247].

Initially, applications exploiting optical SAM or OAM interactions were largely limited to macroscopic systems using visible light. These limitations stemmed from the challenges in producing and controlling coherent, short-wavelength light beyond the UV. Fortunately, recent advances in HHG have bridged this photonic gap, allowing for the straightforward generation of coherent, sub-femtosecond radiation in the EUV, with controllable SAM or OAM properties [6, 12, 97–102, 158, 161, 163, 165, 171, 172, 248, 249]. These advanced light sources have opened up the possibility of monitoring and manipulating the SAM and OAM of light-matter interactions on the atomic scale, with the potential of extending quantum optical/logical metrologies, optical manipulation, and chiral spectroscopies to the nanometer spatial and sub-femtosecond temporal scales.

Fundamentally, these exciting capabilities are enabled by the quantum physics of the high-harmonic up-conversion process [107, 250]. In HHG, an electron wave-packet in an atomic, molecular, or material

[1] This is in the sense that the angular momenta of high-harmonics can be understood via the absorption of photons of definite SAM and OAM.

system is liberated by an intense laser field, which then accelerates the free electron wave-packet. The oscillatory nature of the laser field can drive the wave-packet back to the parent ion and, upon recollision, the acquired kinetic energy is released in the form of high-order harmonics, which can span deep into the EUV and soft x-ray spectral regions [11, 113, 127, 128]. It is this field-driven nature of HHG that provides an opportunity for mapping the properties of near-infrared laser light, in particular SAM and OAM, to short-wavelength radiation. Indeed, recent experimental demonstrations of independent control of SAM [1, 161, 165, 226] or OAM [98, 101, 251] in the EUV via HHG has propelled the topic of optical angular momentum control and measurement to the forefront of attosecond science.

In this work, we present a significant advance in producing EUV beams with designer angular momenta (i.e., helicity and twist) by generating, for the first time, high-order harmonics——and attosecond pulses——possessing controllable spin and orbital angular momenta. By driving the HHG process with a bichromatic, counter-rotating vortex beam (i.e., a bicircular vortex beam), we uncover and subsequently harness, a new form of simultaneous SAM-OAM momentum conservation. We exploit this simultaneous conservation to produce spatially isolated vortex beams of opposite SAM through proper selection of the angular momenta of the bicircular vortex driver, which allows us to control the polarization state of attosecond EUV vortex beams in the time domain; from linear to purely circularly polarized. This unique SAM-OAM control also makes it possible to generate highly elliptically polarized high-harmonic OAM beams with controllable topological charge. In particular, apart from generating highly charged vortex beams with designer OAM, we generate harmonic beams of highly circular polarization with the same, low, topological charge—equal to the co-rotating component of the bicircular vortex driving laser field. Our work opens a new route to perform ultrafast studies of angular momentum exchange and interactions at EUV/x-ray wavelengths, with the potential for nanometer spatial and sub-femtosecond temporal resolution.

4.3 Experimental

4.3.1 Scheme for the Generation of EUV Vortex Beams with Tunable SAM and OAM (SAM-OAM HHG)

To generate EUV SAM-OAM vortex beams, we utilize a modified version of the collinear, bichromatic scheme typically used in bicircular HHG (see Sections 3.2 and 3.3 of Chapter 3). The full output of a regenerative Ti:sapph amplifier (785 nm, 9 mJ, 1 kHz, KMLabs Wyvern HE [173, 174]) is passed into a Mach-Zhender-type interferometer with a power branching ratio of 70/30. The more intense of the two arms contains a 200-μm-thick β-barium borate (BBO) crystal, which generates the second harmonic field at $\sim$392 nm. Achromatic waveplates ($\lambda/2$ and $\lambda/4$) are placed in each arm to independently control the polarization of each component, resulting in LCP (785 nm, ω_1, σ_1=-1) and RCP (392 nm, ω_2, σ_2=+1) beams. A multi-faceted spiral phase plate (SPP, HoloOr, 16-steps per phase wrap) is placed in each arm of the interferometer to control the topological charge of the visible vortex wavefront, and different SPPs and their orientations are utilized to generate vortex beams with charges of $\ell_1 = \pm 1, \pm 2$ and $\ell_2 = \pm 1$. The purity of the vortex mode and the relative sign of the OAM of each beam is characterized by a combination of a beam profiling camera and a cylindrical lens (see Appendix B Section B.1). The two arms are then recombined via a dichroic mirror and spatiotemporal overlap is achieved via a delay stage and independent convex lenses in each arm; generating a bicircular, vortex driving beam. In the experiment, and also in the theoretical simulations (see Section 4.3.3 below), the input beam parameters are carefully adjusted so that the ring of maximum intensity of each driver is spatially overlapped just before the gas jet (see Appendix B Section B.1). The combined focus of the bicircular driver is placed just before the exit of a supersonic expansion of Ar gas to drive the HHG process. The generated high-harmonics are collected via a 1D+1D (spatio-spectral) spectrometer consisting of a gold-coated cylindrical mirror and a flat grating. The resulting spectrum is recorded with an EUV CCD array (Andor, Newton 940) at either the flat-field focal plane of the spectrometer (spectral measurements), or at a far field, $\approx$8 cm beyond this focal plane (EUV vortex profile measurements), which measure both the spectrum and spatial mode of the SAM-OAM harmonics, respectively.

4.3.2 EUV-MCD Measurements of the Ellipticity of SAM-OAM High-Harmonics

One of the most straightforward ways to determine the helicity of EUV radiation is by exploiting the dichroic absorption of different helicities of light in a suitable chiral material. In this work, we employed EUV-MCD measurements to quantify the relative helicity of high-harmonics in our SAM-OAM HHG spectra. In EUV-MCD, the transmission of RCP and LCP light is slightly different depending on the magnetic moment of a uniformly magnetized film, and the relative (and sometimes absolute) degree of polarization can be determined by measuring the absorption spectrum under different macroscopic magnetizations of the thin magnetic film. In this work, a 20-nm-thick $Fe_{0.75}Co_{0.25}$ alloy film (capped with a double bilayer consisting of 3 nm each of Cu/Ta) was deposited onto a 200 nm Al metal foil and served as the magnetic sample for the EUV-MCD measurements. The MCD asymmetry was measured by applying a moderate magnetic field ($\approx$15 mT) to the film from an external electromagnet. The film was then oriented at 45 degrees with respect to the SAM-OAM beam propagation direction in order to maximize the MCD effect in this geometry. For the spectrally dispersed measurements in Fig. 4.3, the absorption spectrum of the $Fe_{0.75}Co_{0.25}$ film was recorded for 10 s, then the magnetization of the film was flipped 180 degrees via the electromagnet, and another absorption spectrum was recorded for another 10 s. This procedure was repeated for 90 paired measurements, giving a total exposure time of 30 minutes. For the spatially resolved EUV-MCD measurements, a total of 120 absorption spectra were taken for each magnetization direction, yielding a total exposure time of 40 minutes.

4.3.3 Full Quantum Simulations of the SAM-OAM HHG Process; Including Propagation

The bicircular SAM-OAM HHG process is simulated by employing a theoretical method that computes both the full, quantum, single-atom HHG response and subsequent propagation [155]. The propagation is based on the electromagnetic field propagator, in which we discretize the target (i.e., the gas jet) into elementary radiators [155]. The dipole acceleration of each elementary source is computed using a full quantum version of the SFA, instead of solving directly the time-dependent Schrödinger equation, yielding a performance gain in computational time when computing HHG over the entire target [155]. We assume that the harmonic radiation propagates with the vacuum phase velocity, which is a reasonable assumption for the high-order harmonics considered in this work. Propagation effects in the fundamental field, such as the production of free charges, the refractive index of the neutrals, the group velocity walk-off, as well as absorption in the propagation of the harmonics, are taken into account. Note that although we account for the time-dependent nonlinear phase shifts in the driving fields, nonlinear spatial effects are not taken into account.

The spatial structure of the vortex beams considered in our simulations is represented as a Laguerre-Gaussian beam propagating in the z-direction (see Appendix B Section B.1 for further details). The laser pulses are modeled with a trapezoidal envelope with two cycles of linear turn-on, six cycles of constant amplitude—16 fs—, and two cycles of linear turn-off (in cycles of the ω_1 field, of 800 nm in wavelength). The amplitudes (E_0) of the two fields—ω_1 of 800 nm and ω_2 of 400 nm in wavelength—are chosen to obtain the same peak intensity at focus for each driver at the radii of maximum superposition (i.e., the brightest intensity rings overlap spatially), yielding a total intensity of 2.0x10^{14} W/cm^2. The driving beam waists are chosen to overlap at the focal plane and the beam waists for the different cases $\ell = \pm 1$, w_0=30 μm, for $\ell = \pm 2$, w_0= 21.4 μm and for $\ell = \pm 4$, w_0=15 μm (see Appendix B, Section B.4). The gas jet, flowing along the perpendicular direction to the beam propagation is modeled as a Gaussian distribution of 10 μm at FWHM, and with a peak pressure of 667 Pa ($\approx$5 torr). The low thickness of the gas jet is due to computational time limitations; however, based on our previous results of OAM HHG [171], we do not foresee any fundamental deviation when considering thicker gas jets closer to the experimental jet employed in this work (a diameter of 150 μm).

4.4 Generation of High-Harmonic Beams with Spin and Orbital Angular Momentum

The generation of SAM-OAM EUV vortex beams is depicted in Figure 4.2. A bichromatic Mach-Zehnder interferometer is used to produce two collinear, vortex laser beams with opposite helicities derived from the fundamental (frequency ω_1, spin σ_1=-1, LCP, and topological charge ℓ_1) and frequency-doubled ($\omega_2 = 2\omega_1$, $\sigma_2 = +1$, RCP, ℓ_2) output of an ultrafast Ti:sapph amplifier (see Section 4.3). These beams are then combined, spatially and temporally, to yield a bicircular vortex beam that drives HHG in a supersonic

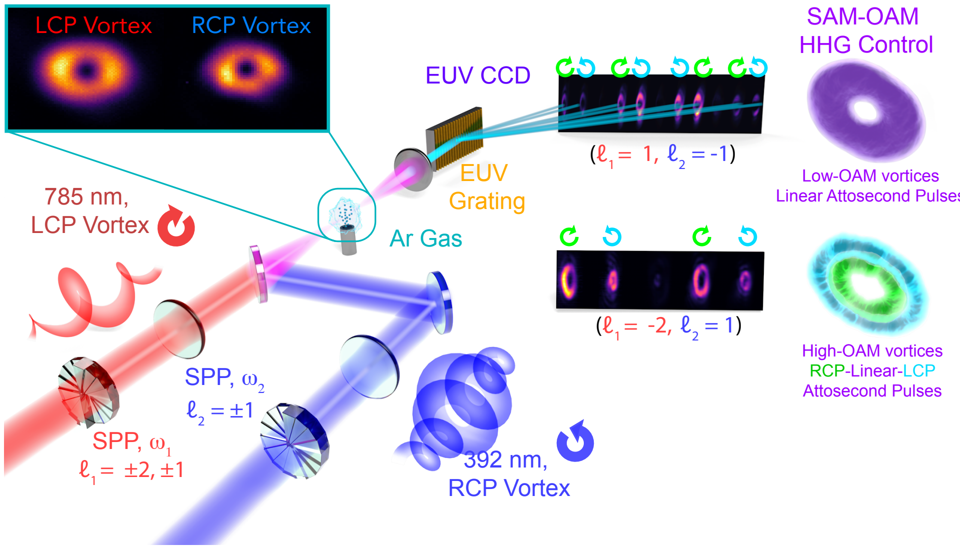

Figure 4.2: **Bicircular high harmonic generation in the presence of simultaneous SAM-OAM conservation (SAM-OAM HHG).** In the experiment, circularly polarized beams of opposite helicity are passed through independent spiral phase plates (SPPs) producing high purity circularly polarized OAM vortex beams (upper-left inset). These beams are spatiotemporally overlapped in a supersonic expansion of Ar gas, yielding a bicircular SAM-OAM vortex beam that drives the HHG process. The SAM-OAM extreme ultraviolet (EUV) beams are collected via a cylindrical mirror-grating pair (cylindrical mirror omitted for clarity) and an EUV camera. The detectors show experimental EUV OAM beam profiles collected in the far field, ≈ 8 cm beyond the flat-field focal plane of the spectrometer. In this scheme, the detectors show experimental SAM-OAM HHG for both complementary ($\ell_1 = 1$, $\ell_2 = -1$) and non-degenerate ($\ell_1 = -2$, $\ell_2 = 1$) configurations of the bicircular vortex driver. When driven with complementary OAM beams, OAM harmonics are generated with a low-OAM charge, equal to the components of the bicircular vortex (upper-right inset). If a non-degenerate vortex driver is employed for the SAM-OAM HHG process, EUV vortices of high-OAM charge and opposite helicity possess significantly different topological charges such that the RCP and LCP harmonics are spatially separated in the far-field (right inset). Adapted with permission from Ref. 2. ©2018 Nature Publishing Group

expansion of Ar gas. The emitted harmonics are collected via an EUV spectrometer consisting of a cylindrical mirror-flat grating spectrometer and an EUV CCD (see Section 4.3). As a reference for these experiments, we have performed full quantum HHG simulations including propagation using the electromagnetic field propagator [155], a method that was used in several previous calculations of HHG involving either SAM [1, 6, 11, 145, 165, 213] or OAM [99, 170–172, 249] (see Section 4.3.3 and Section B.2 of Appendix B).

As a first demonstration of this novel, simultaneous SAM-OAM conservation in HHG, we drive the

SAM-OAM HHG process with a bicircular vortex laser field with $\ell_1 = 1$ and $\ell_2 = 1$. In this configuration, a high-harmonic spectrum consisting of doublets of EUV vortex beams is generated, where the harmonics in each doublet possess the same topological charge, but opposite helicities (Fig. 4.3a-b). Most notably, the strong suppression of every third harmonic order confirms that the same SAM conservation rules are upheld in SAM-OAM HHG as in traditional bicircular HHG [164, 219, 252]. SAM conservation, $\sigma_q = n_1\sigma_1 + n_2\sigma_2$, together with the parity constraints, implies that the number of photons absorbed from each of the drivers (n_1, n_2) to generate the q^{th} order harmonic must differ by one: $n_2 = n_1 - \sigma_q\sigma_1$. Taking into account photon energy conservation, $q\omega_1 = n_1\omega_1 + n_2\omega_2$, the resulting HHG spectrum consists of pairs of adjacent harmonics with opposite circular polarization, and a third, missing harmonic, whose suppression indicates a high circularity of the SAM-OAM EUV beams. This is confirmed by EUV-MCD measurements on an $Fe_{0.75}Co_{0.25}$ film (Fig. 4.3d). Unfortunately, a quantitative value of the harmonic ellipticity cannot be obtained at this time, as MCD-derived ellipticities require a comparison to existing synchrotron data and such experimental data does not exist for this energy range. However, a comparison with extrapolated synchrotron data from resonant MCD measurements of Fe films [12] allows us to confirm the SAM-OAM HHG harmonics are highly elliptically polarized. In short, the strong non-resonant EUV MCD signal, suppression of spin-forbidden harmonic orders, and the excellent agreement with the theoretical simulations verifies the near circular polarization of the SAM-OAM EUV vortex beams (see below). We note that depolarization effects are unlikely in this geometry, as the MCD sample is placed far from the generating region, yet a strong MCD signal is still observed.

The simultaneous conservation of SAM and parity in SAM-OAM HHG also restricts the allowed OAM values for each harmonic [252]. If both beams are linearly polarized, the topological charge of the q^{th} order harmonic driven by a bichromatic laser field is given by a simple OAM conservation rule $\ell_q = n_1\ell_1 + n_2\ell_2$ [171]. Each harmonic can, therefore, exhibit several OAM contributions depending on the number of photons absorbed from each driver [171]. Note that non-perturbative OAM contributions [171] do not appear in our SAM-OAM HHG scheme since the intensity distribution at focus does not vary azimuthally, as also observed in noncollinear bichromatic OAM HHG [101, 102]. On the other hand, when combining the above-mentioned SAM and OAM conservation rules in bicircular SAM-OAM HHG, the topological charge of the q^{th} order harmonic satisfies

$$\ell_q = \frac{q + 2\sigma_q \sigma_1}{3} (\ell_1 + \ell_2) - \sigma_q \sigma_1 \ell_2 \tag{4.2}$$

where SAM conservation restricts ℓ_q to a single value. The products $\sigma_{2,1}\ell_{1,2}$ show that the SAM and OAM of the bicircular vortex driver are inherently entwined via the HHG process, which connects the SAM and OAM of the harmonics to those of the driving beams. This manifests as an entirely new form of simultaneous conservation of SAM and OAM, where the OAM (ℓ_q) and SAM (σ_q) of each harmonic vortex can be controlled via the interplay of the SAM (σ_1, σ_2) and the OAM (ℓ_1, ℓ_2) of the drivers. At this point we would like to remark that the SAM and OAM of the harmonics are controlled via simultaneous conservation of these quantities during the HHG process, and that SAM and OAM are not converted from one another as in more traditional SAM-OAM coupling observed in sub-wavelength and non-paraxial optical regimes [253].

The effects of simultaneous SAM-OAM conservation are readily evident by comparing the theoretical (Fig. 4.3a) and experimental (Fig. 4.3b) SAM-OAM EUV spectra. In such a configuration, ($\ell_1 = \ell_2 = 1$), the OAM conservation rule, Eq. 4.1, reads as $\ell_q = (2q + \sigma_q \sigma_1)/3$. This implies that each pair of adjacent harmonics exhibits the same OAM, as can be seen in Fig. 4.3c, where the OAM is calculated by performing a Fourier transform along the azimuthal coordinate for each frequency component [171]. This method of determining the OAM content is ideally suited for arbitrary, structured beams possessing OAM as it does not rely on decomposition into a particular basis set and is thus more general than methods employing modal decomposition. We note that each harmonic in the SAM-OAM EUV spectrum has a uniform azimuthal intensity profile and little radial mode character, indicating similar modal content between the experimental and theoretical SAM-OAM HHG. Moreover, the excellent agreement of the beam profiles between the experiment and theory also suggest a highly elliptical polarization of the harmonics; if depolarization effects were present, the SAM-dependent OAM selection rules would be relaxed, leading to a superposition of topological charges in each harmonic and consequently nonuniform SAM-OAM HHG beam profiles [171]. Although the OAM of the experimental harmonics was not measured in this work, the points mentioned above strongly suggest a similar modal content as that obtained in the theoretical spectra. Taken together, the generated SAM-OAM EUV vortex beams possess both a high modal purity as well as near circular polarization.

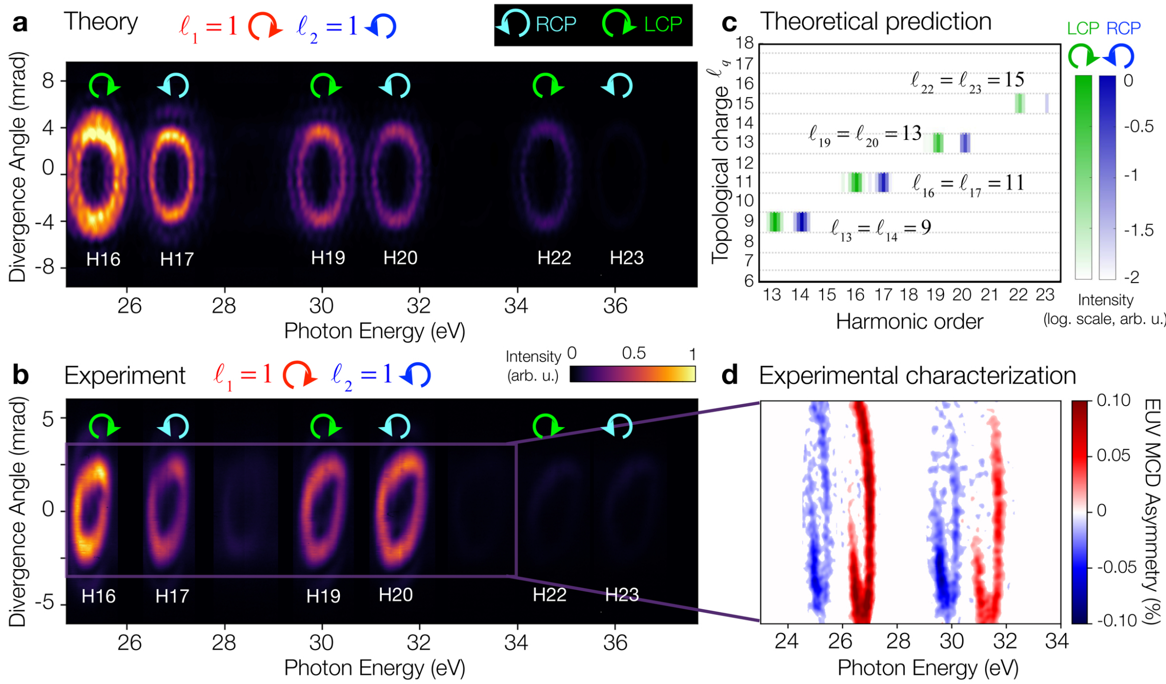

Figure 4.3: **Experimental generation and theoretical confirmation of SAM-OAM EUV vortices in the presence of simultaneous SAM-OAM conservation.** **a**, Full quantum simulation results showing spectrally dispersed SAM-OAM harmonics driven by a bicircular vortex driving beam (σ_1=-1, σ_2=+1, $\ell_1 = +1$, $\ell_2 = +1$). **b**, Spatio-spectral measurement of SAM-OAM EUV vortex beams produced via HHG from the same configuration of the bicircular driver, exhibiting a clean mode with a clear singularity on axis, a single bright intensity ring, and strong suppression of every spin-forbidden (i.e., third) harmonic order. Further calculations (not shown) indicate that the different divergences between the theory, **a**, and experimental, **b**, results are due to slightly different driving beam waists. **c**, Calculated topological charge of the LCP (green) and RCP (blue) harmonic vortices confirms that the presence of simultaneous SAM-OAM conservation results in neighboring harmonics possessing a similar OAM spectrum. The OAM is calculated through a Fourier transform along the azimuthal coordinate for each RCP and LCP frequency component. **d**, EUV-MCD measurement of a 20-nm-thick $Fe_{0.75}Co_{0.25}$ film confirms the near circular polarization of the generated SAM-OAM EUV vortices. Note that inhomogeneity in the EUV MCD signal for each harmonic is the result of slight pointing fluctuations and changes in the sample structure for the different magnetizations of the $Fe_{0.75}Co_{0.25}$ film. Adapted with permission from Ref. 2. ©2018 Nature Publishing Group

4.5 Polarization Control of Attosecond EUV Pulses Through Simultaneous SAM-OAM Conservation

In the past decade, there has been an explosion of interest in controlling the spin polarization of attosecond EUV waveforms, as full polarization control would allow for the possibility of custom-tailored harmonic beams for attosecond, nanometric chiral spectroscopies and metrologies. As such, a wide variety of experimental [1, 6, 11, 12, 158, 161, 163, 165, 213, 226, 248] and theoretical [159, 170, 215, 216] schemes have been investigated to control the SAM of EUV high-harmonics. Here we show that the interplay of SAM-OAM conservation inherent to SAM-OAM HHG opens an entirely new route to control the polarization of attosecond pulses.

In traditional bicircular HHG driven by collinear pulses with a Gaussian spatial profile, RCP and LCP harmonics spatially overlap in the far-field, yielding attosecond bursts with a rotating, linear polarization in the time domain [145, 159, 160, 164, 216]. This is largely the result of the similar propagation properties between RCP and LCP harmonics, as the divergence of a light field does not typically depend upon its SAM. Fortunately, recent advances in BHHG have shown that elliptically polarized APTs [1, 226], spatially isolated APTs [12], and IAPs [165] of opposite helicity can be generated and the ellipticity can be fully tuned by the parameters of the visible driving lasers. Although elegant, these methodologies are only capable of controlling either the SAM or the divergence of the EUV harmonics, instead of both simultaneously. However, the simultaneous conservation of SAM and OAM in bicircular SAM-OAM HHG, together with the OAM-dependent divergence inherent to vortex beams, allow us to circumvent these limitations and simultaneously control the divergence of EUV light and the polarization of the underlying attosecond pulse trains.

To show the power of this concept, we consider HHG performed with a single-mode OAM driver. It is known that the divergence of a harmonic beam decreases with the harmonic order, while the divergence of a vortex beam increases with its topological charge. Therefore, for a single-mode OAM driver, the simple OAM conservation rule, $\ell_q = q\ell_1$, results in an HHG spectrum where all harmonics are emitted with a similar divergence [98–100, 170, 171]. In the case of bicircular SAM-OAM HHG, the restricted selection rules resulting from the mixing of SAM and OAM can be exploited to control the divergence of the harmonics and, for example, to yield spatially isolated vortex beams of pure RCP and LCP polarization, something that is not possible with either linear OAM HHG or collinear, BHHG with Gaussian drivers. This point is illustrated below, where we employ a simple theoretical analysis based on Fraunhofer diffraction that predicts the divergence difference between the RCP and LCP harmonics ($\Delta\beta$) as a function of the OAMs of the bicircular vortex driver (see Appendix B Section B.4) as

$$\Delta\beta \propto (\ell_1 - 2\ell_2)\,\frac{|\ell_1 + \ell_2|}{\ell_1 + \ell_2} \tag{4.3}$$

where $\Delta\beta = 0$ if $\ell_1 + \ell_2 = 0$, and we are assuming $\omega_2/\omega_1 = 2$. In Fig. 4.4a we plot the relative values of $|\Delta\beta|$ as a function of ℓ_1 and ℓ_2. The divergence difference between RCP and LCP harmonics depends strongly on the choice of ℓ_1 and ℓ_2, and as a general trend, the greatest differences in divergence correspond to large differences in the OAMs of the drivers. Thus, it is the OAM-dependent divergence, combined with the simultaneous angular momentum selection rules induced by the bicircular OAM driver, that gives control over the spatial distribution of RCP and LCP harmonics in the EUV vortex beam, and as a consequence, over the polarization of the attosecond pulses.

To further illustrate this point, we return to the case of $\ell_1 = \ell_2 = 1$, presented in Fig. 4.3 (orange dashed circle in Fig. 4.4a). The RCP and LCP vortices exhibit similar divergences and thus spatially overlap, yielding linearly polarized APTs in the time domain. On the other hand, closer inspection of the divergence analysis shows that spatial separation of RCP and LCP components of the EUV beams is achieved when the OAMs of the drivers are complementary, but different in magnitude. To demonstrate this unique capability, we drive the HHG process with a non-degenerate, complementary, bicircular OAM driver ($\ell_1 = -2$, $\ell_2 = 1$, purple-dashed circle in Fig. 4.4a). The theoretical and experimental SAM-OAM HHG spectra (Figs. 4.4b & 4.4c) clearly confirm the ramifications of SAM-OAM conservation on controlling the divergence of the EUV vortices; RCP vortex harmonics are entirely contained by their LCP counterparts, resulting in a double-ring structure in the far-field (Fig. 4.4d, left). The near-circular polarization of the double-ring vortex beam is confirmed by EUV-MCD measurements, which reveal two distinct intensity rings of opposite helicity (Fig. 4.4d, right).

The effects of the OAM-dependent divergence control in SAM-OAM HHG—and thus the OAM-based control over the polarization of the attosecond pulses—can be more clearly demonstrated by performing a spectral integration across the SAM-OAM HHG spectra. Returning to a degenerate configuration of the driving field ($\ell_1 = 1$, $\ell_2 = 1$), the RCP and LCP harmonics both exhibit similar divergences, as well as comparable spectral intensities (Figs. 4.5a and 4.5b). If we define the ellipticity of the attosecond pulses as

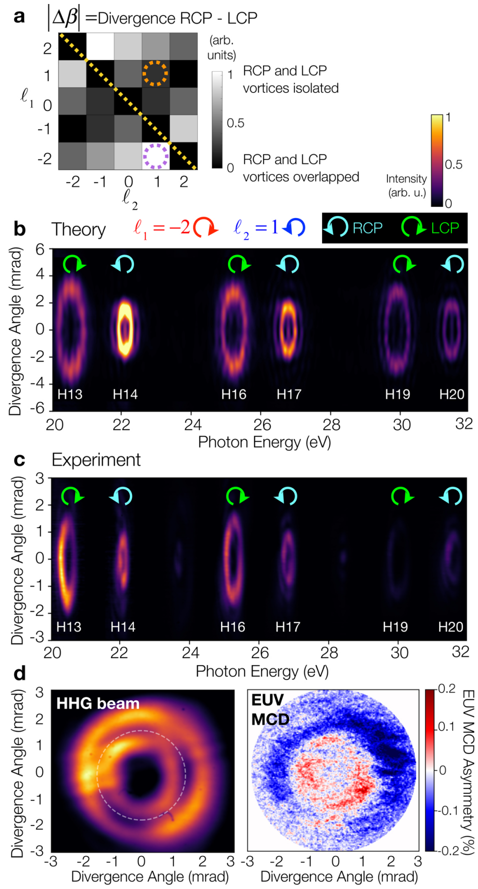

Figure 4.4: **Separation of EUV high-harmonic vortex beams with opposite circularities through the OAM of the bicircular vortex driver.** Theoretical estimation for the divergence difference between the RCP and LCP harmonics ($|\Delta\beta|$) as a function of the OAM of the constituents of the bicircular vortex field. The dashed circles correspond to the configurations of the bicircular vortex driver for experimentally generated SAM-OAM EUV harmonics. Further calculations (not shown) indicate that differences in the theoretical and experimental spectra are due to slightly different driving beam parameters. **b**, A full quantum propagation simulation shows that when SAM-OAM HHG is driven with a bicircular OAM driver of $\ell_1 = -2$, $\ell_2 = 1$, the RCP and LCP vortices exhibit significantly different divergence, resulting in spatially separated RCP and LCP beams in the far field. **c**, A spatio-spectral measurement of SAM-OAM EUV harmonics under the same configuration of the bicircular vortex driver as in **b**, which confirms the OAM-dependent divergence control afforded by SAM-OAM HHG. This control results in a dual intensity ring structure in the far-field of the HHG beams (**d**, left), where the inner, RCP beam is entirely contained by the LCP vortex beam, as confirmed by a spatially resolved EUV-MCD measurement (**d**, right). The inhomogeneity observed in the EUV-MCD-retrieved beam profiles is the result of slight fluctuations in beam pointing, microstructuring of the MCD sample, and attenuation of low-intensity regions of the beam. Adapted with permission from Ref. 2. ©2018 Nature Publishing Group

$\epsilon = (I_{RCP} - I_{LCP})/(I_{RCP} + I_{LCP})$, where I_{RCP} and I_{LCP} are the intensities of the RCP and LCP harmonics, the spatial overlap of the RCP and LCP components of the theoretical SAM-OAM HHG spectrum results in attosecond pulses with predominate linear polarization in the time domain (Figs. 4.5c-e). Given the excellent agreement between the theoretical and experimental spectra and spectrally integrated signals, it is highly likely that the experimental harmonics possess similar ellipticities, and thus we expect a similar polarization of the experimental APTs. However, our experimental and theoretical SAM-OAM HHG spectra show that this symmetry can be broken by employing a complementary, non-degenerate vortex driver (e.g., $\ell_1 = -2$, $\ell_2 = 1$). In this configuration, the oppositely polarized vortex beams experience large enough divergences to be spatially isolated (Figs. 4.5f & 4.5g). As such, the ellipticity of the attosecond pulses evolves all the way from near right circular ($\epsilon 1$), to linear ($\epsilon = 0$), to near left circular ($\epsilon = -1$) across the EUV beam profile (Figs. 4.5h-j). Therefore, by properly modifying the OAM of the driving fields, we can spatially control the ellipticity of the attosecond pulses and this degree of control becomes even greater as the difference in OAM of the bicircular driver increases, where pure circular attosecond pulses ($\epsilon = 1$) can be obtained (see Appendix B Section B.4).

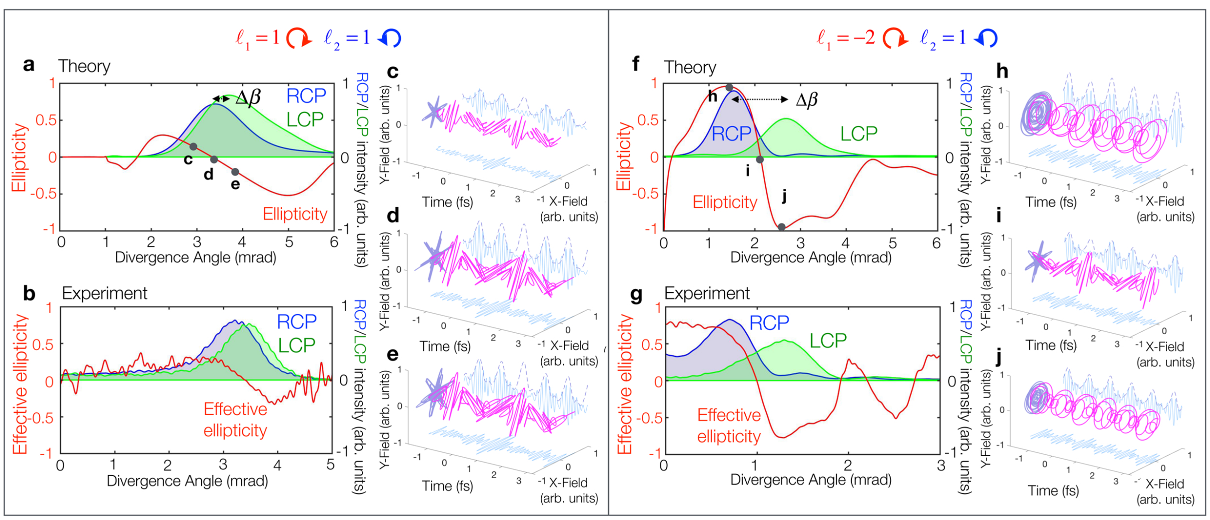

Figure 4.5: **Control over the OAMs of the bicircular driver yields full control of the polarization state of attosecond pulse trains in SAM-OAM HHG.** Spectrally integrated intensities of RCP (blue) and LCP (green) harmonics (from the 13th to the 23rd) for a degenerate bicircular vortex ($\ell_1 = \ell_2 = 1$) confirm that SAM-OAM high harmonics possess similar divergences and thus overlap spatially in the far field (**a**, theory and **b**, experiment), resulting in predominately linearly polarized APTs across the EUV vortex beam profile (as shown in the simulated temporal evolution detected at **c** 2.7, **d** 3.3, and **e** 3.7 mrad). When SAM-OAM HHG is driven with a non-degenerate bicircular vortex beam ($\ell_1 = -2$, $\ell_2 = 1$), the RCP and LCP harmonics exhibit significantly different divergences, which results in the spatial separation of RCP and LCP vortices in the far-field (**f**, theory and **g**, experiment). The combined theoretical and experimental results confirm the degree of divergence control via simultaneous spin-orbit conservation in the HHG process, which results in a spatial evolution of the polarization of the APTs from RCP (**h**, 1.4 mrad), to linear (**i**, 2.1 mrad), to LCP (**j**, 2.6 mrad). Adapted with permission from Ref. 2. ©2018 Nature Publishing Group

4.6 High-Harmonic Vortices with Circular Polarization and Identical, Low-Charge OAM

Since the first experiments of HHG driven by OAM beams [97], there has been significant interest in controlling the OAM content of the high-harmonics, as well as generating harmonic vortices with a low topological charge [101, 102]. Such a desire is rather pragmatic; many OAM light-matter interactions depend upon the topological charge of the optical vortex beam, and lower topological charges inherently lead to less complex interactions and detection geometries. Unfortunately, the simple OAM conservation law governing HHG driven by single OAM beams, $\ell_q = q\ell_1$, implies that high-order harmonic OAM beams emerge with highly-charged OAM [98–100, 170, 171, 254]. Recently, this limitation was overcome by employing a non-collinear scheme [101, 102], resulting in linearly polarized EUV vortex beams with low OAM charge. Here we demonstrate that the simultaneous conservation of SAM and OAM in bicircular SAM-OAM HHG can yield high harmonics not only with high topological charge (as shown in the Sections 4.4 and 4.5), but also with the same OAM as the driving field, without the complications induced by a non-collinear geometry.

When the OAM of the drivers fulfill $\ell_1 = -\ell_2$, Eq. 4.1 transforms into $\ell_q = -\sigma_q\sigma_1\ell_2$, which indicates that all RCP (LCP) harmonics exhibit the same topological charge as the RCP (LCP) driving field (see Appendix B Section B.4). This implies that the divergence decreases linearly with the harmonic order and that RCP and LCP harmonics exhibit similar divergence ($\Delta\beta \approx 0$, yellow dashed line in Fig. 4.4a). As a final demonstration of the control afforded by the conservation rules in SAM-OAM HHG, in Fig. 4.6a and 4.6b we present the theoretical and experimental HHG spectra generated by a bicircular driver of complementary topological charge ($\ell_1 = 1$, $\ell_2 = -1$). Most notably, the divergence decreases with the harmonic order, which is a clear indication of the equal OAM of the harmonics as shorter wavelength harmonics have a lower divergence given the same topological charge. This fact is further corroborated by considering the highly circular polarization of the EUV beams. If the harmonics were not circularly polarized, the lack of SAM conservation would result in the generation of highly divergent, highly charged OAM HHG beams, as implied by the simple OAM conservation rule $\ell_q = n_1\ell_1 + n_2\ell_2$ [171]. However, our SAM-OAM HHG scheme demands SAM conservation, which results in LCP harmonics emitted with $\ell_{LCP} = \ell_1 = 1$, and RCP harmonics with $\ell_{RCP} = \ell_2 = -1$ (Fig. 4.6c). The physical manifestation of this effect is a decrease in the angular diameter of the SAM-OAM harmonics as a function of harmonic energy, which is captured in both experiment and theory (Fig. 4.6d). Although the angular divergence of the experimental harmonics within each doublet show an opposite behavior with respect to the theoretical spectra (a result of slight differences in beam parameters between the experiment and simulations), the general trend is clearly observed. Taken together, our observations demonstrate the power of SAM-OAM HHG for complete control of the angular momentum of attosecond, structured EUV beams carrying OAM.

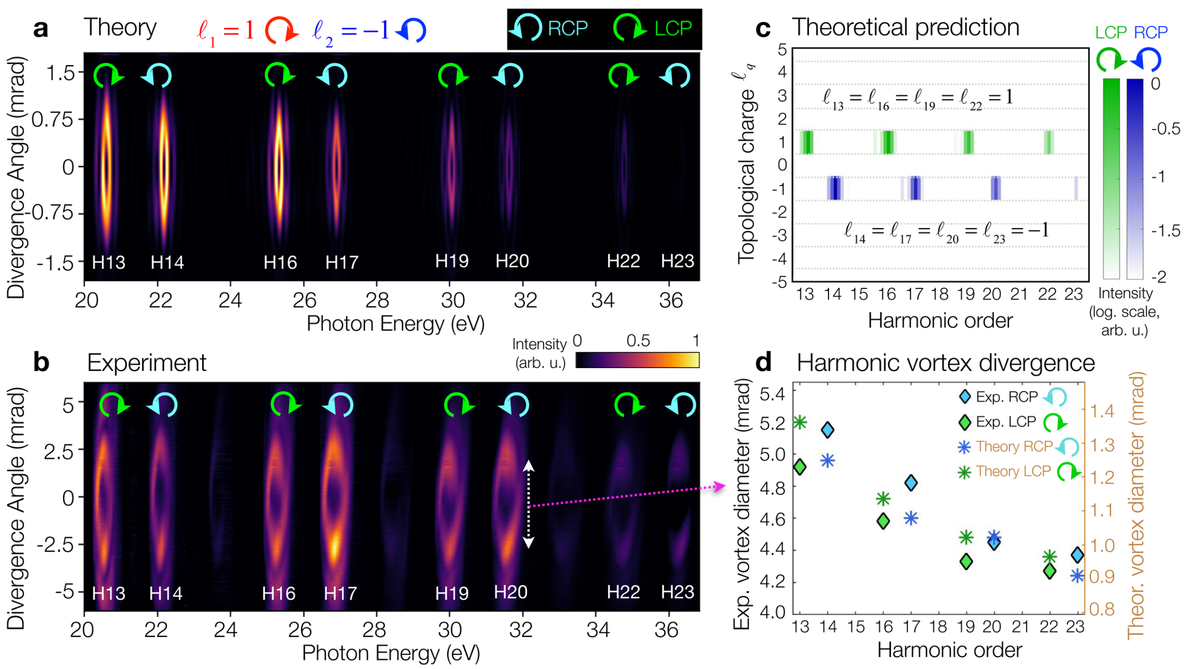

Figure 4.6: **Circularly polarized high-harmonic vortex beams with equal, low-charge OAM.** Simulated **a**, and experimental b, high-harmonic spectra of the EUV OAM beams driven by a degenerate, complementary bicircular field ($\ell_1 = 1$, $\ell_2 = -1$), exhibiting pairs of high harmonics of alternating helicity. The decrease in divergence of the harmonics as a function of energy, combined with the localized singularity indicate that each harmonic has a similar, low topological charge. In panel **c**, we show the theoretical OAM content of the LCP (green) and RCP (blue) HHG projections, which shows that all harmonics with the same SAM present the same OAM as the driver with that SAM. The manifestation of the low topological charge of the EUV harmonics results in decreases in the angular diameter of the beams as a function of energy, as clearly demonstrated in **d** where the experimental (theoretical) results are shown in diamonds (asterisks). Further calculations (not shown) indicate that the different divergences between the theory and experimental results are due to slightly different driving beam parameters (i.e., size of beam waist and the exact location of beam waists), which also results in a low-intensity secondary intensity ring in the experimental spectra. Adapted with permission from Ref. 2. ©2018 Nature Publishing Group

4.7 Conclusions and Further Outlook of SAM-OAM HHG

Despite the fact that many light-matter interactions can possess independent SAM and OAM conservation laws, the simultaneous conservation of both quantities has rarely been utilized to control the light-matter interaction, particularly in HHG. In this work, we have shown that the simultaneous SAM-OAM conservation in highly nonlinear and intense field interactions can be used as a powerful tool for controlling the up-conversion process, and producing HHG beams with designer SAM and OAM. By constructing a bicircular vortex driving beam with varying topological charges of the constituent waveforms, we showed that SAM-OAM HHG entwines the angular momentum conservation rules, yielding unprecedented and exquisite control of the SAM, OAM, and the divergence of extreme ultraviolet light fields.

To demonstrate the potential of the simultaneous SAM-OAM conservation in this regime, we experimentally demonstrated three distinct mixing cases where i) circularly polarized high-harmonic vortex beams are generated with a similar divergence, and thus similar propagation properties regardless of spin polarization or photon energy, ii) spatially isolated harmonic vortex beams are produced, allowing spatial tuning of the polarization of attosecond pulses—linear, elliptical, or pure RCP/LCP—, which enables spatially resolved dichroism measurements or isolation of an EUV vortex beam of pure RCP or LCP polarization, and iii) EUV harmonic vortex beams with topological charge equal to, and thus controlled by, the OAM of the driving lasers. These results significantly extend the degree of the control over short-wavelength radiation via manipulation of visible driving lasers. Perhaps most importantly, our results demonstrate the simultaneous optical spin-orbit angular momentum conservation as a gateway to an entirely new set of applications and fundamental investigations.

These exciting applications are enabled by the short wavelength of high harmonics, which allows these designer SAM-OAM beams to be focused to scale lengths comparable with nanostructured and molecular systems, enabling new nanometric spectroscopies and opportunities for nanoscale optical manipulation. Aside from these capabilities, we also add a new degree of freedom, the OAM, to the recent experiments that uncovered new ultrafast spin/charge dynamics in magnetic materials [33, 37, 255, 256] and the ultrafast study of chiral molecular systems [246, 257]. One could also envision the possibility for skyrmionic spectroscopies [87, 89], or for taking advantage of SAM-OAM selection rules in photoionization/photoemission experiments [79, 258], all of which do not necessarily demand nanometer-scale focusing conditions. Finally, circularly polarized short-wavelength OAM beams also open up new scenarios in spatially resolved circular dichroism spectroscopies (as demonstrated in this work), and even the possibility of performing SAM and/or OAM dichroism x-ray absorption measurements, which allows for decoupling the effects of orbital and spin contributions to energy transport [95].

Chapter 5

Attosecond Optical Rotors: Self-Torqued Extreme Ultraviolet Beams with Time Varying Orbital Angular Momentum

This chapter is adapted, with permission, from:

- L. Rego, K. M. Dorney, N. J. Brooks, Q. Nguyen, C.-T. Liao, J. S. Román, D. E. Couch, A. Liu, E. Pisanty, M. Lewenstein, L. Plaja, H. C. Kapteyn, M. M. Murnane, and C. Hernández-García. Light with a self-torque: extreme-ultraviolet beams with time-varying orbital angular momentum, 1–24. arXiv: `1901.10942`

5.1 Chapter Overview

The previous chapters have detailed how attosecond, EUV waveforms can be generated with controllable amounts of SAM and OAM, thus yielding unique opportunities for time-resolved spectroscopies in our familiar attosecond-nanometer arena. Despite the novelty of these light sources, so far, we have only considered "static" HHG schemes; the components of the bicircular fields were always temporally overlapped at time-zero-ish[1] and their relative time delay remained fixed while we wreaked havoc with the other "knobs". Here we introduce time as a controllable, free parameter of the upconversion process, and in doing so *simultaneously* predict and experimentally validate a new class of light beams, whose unique property is associated with a temporal variation of the OAM along the pulse: the self-torque of light.

[1] The literary uncertainty here is a bit more than just laziness. In a bicircular field, a small offset in temporal overlap between the two drivers simply rotates the trefoil intensity distribution, which—for the long pulses used in these experiments—is negligible.

5.2 Introduction

5.2.1 Application and Generation of Structured Light Beams

Structured light is critical for a host of applications in imaging and spectroscopy, as well as enhancing our ability to optically manipulate macro- to nano-scale objects, such as particles, molecules, atoms and electrons. Particularly in recent years, the novel phase and intensity properties of structured light beams achieved by exploiting the angular momentum of light have garnered renewed interest in optical manipulation and control [26]. Some of the most relevant structured light beams are those carrying OAM, also known as vortex beams, introduced by Allen et al. in 1992 [69]. The OAM of light manifests from a spatially dependent wavefront rotation of the light beam, which is characterized by the phase winding number, or topological charge, ℓ. Such vortex beams have been harnessed for applications in diverse fields [70] such as laser communication [24, 259], phase-contrast [25, 260] and superresolution microscopy [74], kinematic micromanipulation [21], quantum information [23], and lithography [247]. Spurred by these exciting technologies, a paralleled interest in the ability to control and manipulate the OAM of ultrafast light pulses has also emerged, resulting in numerous techniques that can imprint OAM directly onto an arbitrary waveform. Diffractive optics (e.g., q- and spiral-phase plates) [247, 261] and holographic techniques [262] can impart OAM onto waves from radio, to optical, and even x-ray [263] frequencies, while recent advances in HHG have produced attosecond EUV pulses with designer OAM [2, 97–102, 171, 172, 251].

One of the most exciting capabilities enabled by OAM beams is their ability to exert photomechanical torques [69, 71, 264]. Whereas the linear momentum of light can be employed to control and manipulate microscopic objects via the gradient/scattering force associated with its intensity profile, optically-induced torque manifests from angular momentum transfer between an object and a light field. This enables fundamental capabilities in advanced classical and quantum optical control and manipulation techniques, such as optical tweezers, lattices, and centrifuges [21, 265–268], allowing for the realization of molecular and micromechanical rotors, single particle trafficking, and fundamental studies of atomic motion in liquids and Bose-Einstein condensates [77, 78].

5.2.2 Attosecond EUV Waveforms with a Time-Dependent Optical OAM: The Self-Torque of Light

In this work, we theoretically predict and experimentally validate light beams that carry time-dependent OAM, thus, presenting a self-torque. This new property of structured light, the self-torque, $\hbar\xi$, is defined as $\hbar\xi = \hbar d\ell(t)/dt$, where $\hbar\ell(t)$ is the time-dependent OAM content of the light pulse. The term self-torque follows an analogy with other physical systems that possess a self-induced time-variation of the angular momentum—which, for example, results from the radiation reaction of charged particles [269] or from gravitational self-fields [270]. Although OAM is well understood as a spatial property of light beams, to date, temporally-dependent OAM light pulses have not been proposed—nor observed. We demonstrate that the self-torque of light arises as a necessary consequence of angular momentum conservation during the extremely non-linear, non-perturbative optical process of HHG. In HHG, the interaction of an intense field with an atom or molecule leads to the ionization of an electronic wavepacket, which acquires energy from the laser field before being driven back to its parent ion, and emitting a high-frequency photon upon recollision [107, 250]. The emitted harmonic radiation can extend from the EUV to the soft x-ray regime if the emissions from many atoms add together in phase [11, 113, 114, 137]. The resulting comb of fully coherent harmonics of the driving field in turn yields trains of phase-locked attosecond pulses [142, 271].

Self-torqued light beams naturally emerge when HHG is driven by two time-delayed IR pulses that differ by one unit of OAM (see Fig. 5.2). The dynamical process of HHG makes it possible to imprint a "continuous" time-varying OAM, where all OAM components are present—thus creating self-torqued EUV beams. Intuitively, these exotic pulses can be understood as being composed of time-ordered photons carrying consecutively increasing OAM. This self-torque translates to an azimuthal frequency chirp (i.e. a spectral shift along the azimuthal coordinate) on the radiation emission—and vice versa. This important consequence allows us to quantify the self-torque by an experimental measurement of the azimuthal frequency chirp. In addition, the degree of self-torque of EUV harmonic beams can be precisely controlled through the time delay and pulse duration of the IR vortex laser pulses. Our work not only presents and confirms an inherently new property of light beams, but also opens up a route for the investigation of systems with time-varying OAM that spontaneously appear in nature [272], as macroscopic dynamical vortices or—thanks to the high frequency of EUV beams—microscopic ultrafast systems. For example, since short-wavelength light can capture the fastest dynamics in materials [33, 37], self-torqued EUV beams serve as unique tools for imaging magnetic and topological excitations, for launching selective and chiral excitation of quantum matter [79], imprinting OAM centrifuges [266], switching superpositions of adiabatic charge migration in aromatic or biological molecules [273, 274], or for manipulating the OAM dichroism of nanostructures [275] on attosecond timescales.

5.3 Experimental

5.3.1 Scheme for Generation of Self-Torqued Light Beams in the EUV

In order to create light beams with self-torque, we drive the HHG process with two linearly polarized IR pulses exhibiting the same frequency content (centered at, $\omega_0 = 2\pi c/\lambda_0$), but with different OAM, ℓ_1 and ℓ_2, where $|\ell_1 - \ell_2| = 1$ (Figure 5.1). The two laser pulses are synthesized by passing the full output of the same Ti:sapph laser we've encountered before (9 mJ, 40 fs, 1 kHz, KMLabs Wyvern HE [173, 174]) into a frequency-degenerate Mach-Zehnder interferometer. In each spatially separated arm of the interferometer, a combination of half-waveplates, faceted spiral phase plates (HoloOr, 16-steps per phase ramp), and independent focusing lenses result in each beam possessing linear polarization, non-degenerate topological charges, and the same waist size at focus. Independent irises in each beam path allow for fine tuning of the transverse mode size at focus and are utilized to match the size of the maximum intensity ring for each driver. The two beams are recombined at the interferometer exit[2] , and the time delay, t_d, between the two beams is varied using a high-precision linear delay stage (Newport, XPS1160-S). The time delay between the two beams is never varied more than the pulse widths (≈50 fs FWHM, verified by independent FROG measurements of each beam, with the full suite of optics in place), which ensures the combined temporal profile of the dual-vortex driver always maintains a smooth, Gaussian-like envelope. The laser modes for both the individual and combined IR vortex beams are assessed using a modified Gerchberg-

[2] The major downside of a frequency-degenerate Mach-Zehnder interferometer is the nearly 50% loss in available intensity when the beams exit the interferometer. However, this configuration proved ideal for minimizing pulse dispersion, while also allowing for independent control of the polarization and topological charge of the driving beams.

Saxson phase retrevial algorithm, which is capable of fully resolving the complex, spatial amplitude of the IR vortex beams *at focus* with a resolution set only by the camera pixel size (upper-left inset of Fig. 5.2, see Appendix C, Section C.5).

These two collinear IR vortex beams form a dual-vortex HHG driving beam, which is then focused onto our favorite HHG medium; a supersonic expansion of Ar gas. The emitted harmonics, after passing through a 200-nm-thick Al filter (Luxel Corp.), are collected via the same EUV spectrometer we met in Section 4.3 (Hettrick Scientific, ES-XUV) and imaged onto an EUV CCD (Andor, Newton 940). The resulting spatiospectral image contains spectral information on one axis of the detector, while the other axis contains the preserved divergence content—and also the azimuthal angular range—of the dispersed high-harmonic beams.

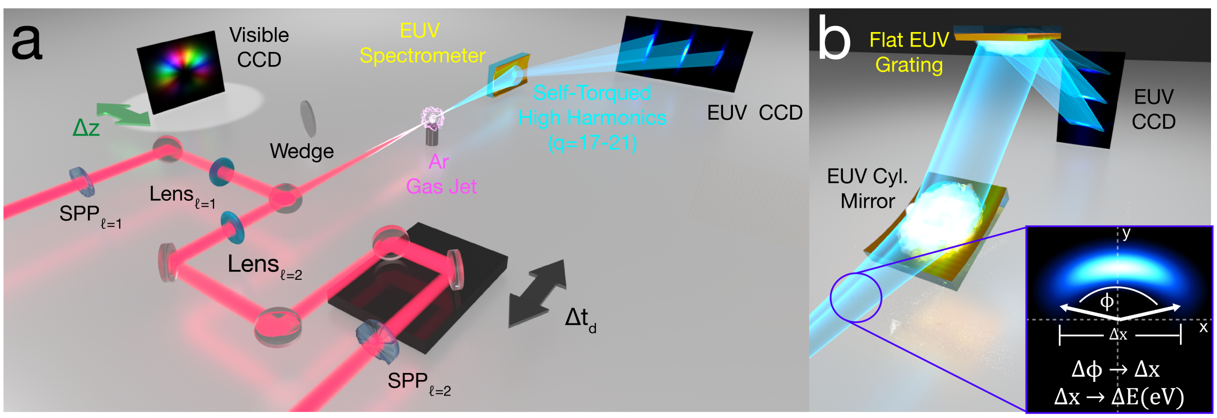

Figure 5.1: **Experimental scheme for the generation and quantification of the self-torque of EUV beams produced via OAM HHG.** The generation of self-torqued EUV beams is achieved by driving the HHG process with an ultrafast beam composed of linearly polarized, collinear OAM beams with topological charges of $\ell_1 = 1$ and $\ell_2 = 2$. **a**, A high-resolution, high-repeatability delay stage is used to control the time delay between the driving pulses with attosecond precision. Upon exiting the HHG medium—an argon gas jet—the residual driving beam is blocked with a 200-nm-thick aluminum filter (Luxel Corp., not shown) and the harmonics are dispersed with a cylindrical-mirror, flat-grating spectrometer (mirror omitted for clarity). **Top-left inset**, A movable wedge may be inserted into the combined (or individual) driving beams to perform beam profiling (e.g., for Gerchberg-Saxton phase retrieval) FROG measurements. **b**, The EUV spectrometer is composed of a cylindrical-mirror and flat-grating pair, which together collapse the HHG beam in the vertical dimension (lab frame y-axis), while preserving spatial information in the transverse dimension (lab frame x-axis). The cylindrical mirror effectively maps the azimuthal frequency chirp into a spatial chirp along the lab frame x-axis, which is then dispersed by the grating (**bottom-right inset**). This is the result of the grating and mirror possessing parallel focusing and dispersion axes, which themselves are orthogonal to the beam propagation. Adapted with permission from Ref. 3.

5.3.2 Quantitative Measurement of the Self-Torque of EUV Light Beams

Quantifying the self-torque of EUV beams in the time-domain would require both a high-resolution spatial measurement of the harmonic phase, coupled with sub-femtosecond time resolution, which is currently unfeasible. In order to circumvent this limitation, we rely upon a frequency domain measurement of the induced azimuthal chirp, and then exploit the fundamental phase relationship between a temporal phase and instantaneous frequency to extract the self-torque of the experimentally generated high harmonics. In order to measure the azimuthal frequency chirp, we harness a unique property of the physics of superposed OAM beams and the optics of our spectrometer system. When two OAM beams with neighboring, but low, topological charges are superposed, a "crescent" shaped intensity distribution is obtained, where the region of maximum intensity is located at an angle that depends upon the time delay between the two beams [70]. As the time delay is scanned, the intensity crescent rotates about the common origin of the two IR vortex drivers (see Section C.6 in Appendix C). By carefully adjusting the time delay, we can align the center-of-mass of the intensity of the driving crescent with the dispersion axis of the EUV spectrometer, which in turn aligns the high-harmonic intensity crescent (since to first order, the harmonics mimic the intensity distribution of the driver) to the spectrometer as well.

Briefly (see Fig. 5.1b and Appendix C Section C.6), the HHG intensity crescent is aligned such that it is directed along the vertical lab-frame coordinate, and when hitting the cylindrical mirror (with its curved axis orthogonal to the propagation direction of the HHG intensity crescent), the HHG beam is collapsed spatially, preserving the divergence and azimuthal angular range of the unfocused HHG beam. The focusing HHG beam then impinges on the grating—which has grooves oriented parallel to the curved axis of the cylindrical mirror—, which disperses the harmonic spectrum along the transverse coordinate of the HHG beam (Figure 5.1b). In such a configuration, the spectrometer naturally disperses the harmonics such that the azimuthal frequency chirp is mapped into the dispersed spectra, yielding spectrally tilted high harmonics. The self-torque for each harmonic order, as a function of time delay, is then extracted from the spectral tilt of the harmonics and a concurrent measurement of the azimuthal extent of the undispersed harmonic beam (see Appendix C, Section C.7), all while keeping the generation chamber and visible beamline undisturbed. Extreme care is taken to ensure that the harmonic beam remains fixed to the dispersion axis of the spectrometer, while potential artifacts from improper imaging conditions and "over driving" of the HHG process are minimized, if not non-existent (see Appendix C, Section C.8). Both long- and short-term drifts in beam pointing are minimized by enclosing the entire beamline from external air currents and vibrations, while any remaining fluctuations and drifts in pointing are actively stabilized via a home-built pointing stabilization system [185].

5.3.3 Full, Quantum SFA Simulations of the Generation of Self-Torqued EUV Beams

In order to calculate the HHG driven by two time-delayed OAM pulses, we employ a theoretical method that computes both the full quantum single-atom HHG response and subsequent propagation [155]. The propagation is based on the electromagnetic field propagator, in which we discretize the target (i.e., gas jet) into elementary radiators [155]. The dipole acceleration of each elementary source is computed using the full, quantum SFA, instead of solving directly the time dependent Schrödinger equation, yielding a performance gain in computational time when computing HHG over the entire target [155]. We assume that the harmonic radiation propagates with the vacuum phase velocity, which is a reasonable assumption for the high-order harmonics considered here. Propagation effects in the fundamental field, such as the production of free charges, the refractive index of the neutrals, the group velocity walk-off, as well as absorption in the propagation of the harmonics, are taken into account. Note that although we account for the time-dependent nonlinear phase shifts in the driving fields, nonlinear spatial effects are not taken into account. We consider two vortex beams with $\ell_1 = 1$ and $\ell_2 = 2$, whose spatial structure is represented by a LG beam (see Eq. C.13 in Appendix C, Section C.5). The laser pulses are modeled with a $\sin^2$ envelope, with a FWHM (in intensity) of τ, and centered at 800 nm in wavelength. The amplitudes of the two fields are chosen to obtain the same peak intensity (1x10^{14} W/cm^2) at focus for each driver at the radii of maximum superposition (i.e., the brightest intensity rings overlap spatially). The driving beam waists are chosen to overlap at the focal plane (being $w_1 = 30.0$ μm for ℓ_1, and $w_2 = w_1/\sqrt{2} = 21.4$ μm for ℓ_2) where a $10-\mu$m-wide Ar gas jet flows along the perpendicular direction to the beam propagation, with a peak pressure of 667 Pa ($\approx$5 torr). The low thickness of the gas jet is due to computational time limitations; however, based on our previous results of OAM-HHG [1, 171], we do not foresee any fundamental deviation when considering thicker gas jets closer to the experimental jet employed in this work (a diameter of 150 μm).

5.4 Theory Underlying the Self-Torque of Light

In order to create light beams with self-torque, we consider driving the HHG process with two linearly polarized IR pulses exhibiting the same frequency content (centered at, $\omega_0 = 2\pi c/\lambda_0$), but with different OAM, ℓ_1 and ℓ_2, where $|\ell_1 - \ell_2| = 1$. The two laser pulses are separated by a variable time delay, t_d, which is on the order of the individual pulse widths (see Section C.4 of Appendix C), as shown in Figure 5.2. These two collinear IR vortex beams are then focused into an atomic gas target, such that the transverse intensity distribution of the two drivers exhibits maximum overlap. We model the HHG process using full quantum simulations within the familiar SFA framework that include propagation via the electromagnetic field propagator [155], a method that was used in several previous calculations of HHG involving structured pulses [1, 11, 99, 170–172, 249]. We consider the driving vortex pulses with $\ell_1 = 1$ and $\ell_2 = 2$, described by a $\sin^2$ envelope with τ=10 fs FWHM in intensity, centered at λ_0=800 nm, and delayed by t_d=τ=10 fs. The inset in Figure 5.2 shows the time-dependent OAM of the 17$^{\text{th}}$ harmonic obtained from our simulations (color background). In order to extract the temporal variation of the OAM, we first select the HHG spectrum in the frequency range $(q-1)\omega_0$ to $(q+1)\omega_0$ where q is the harmonic order to explore, being $q = 17$ in Figure 5.2), and we then perform a Fourier transform along the azimuthal coordinate [171] at each time instant during the HHG process. Remarkably, the temporal variation of the OAM is monotonic and "continuous", spanning over an entire octave of consecutive topological charges—i.e., it includes all OAM components from $q\ell_1 = 17$ to $q\ell_2 = 34$.

The nature of self-torqued beams can be understood through a straightforward theoretical analysis. Previous works in OAM-HHG have demonstrated that an IR vortex beam can be coherently converted into high-frequency vortex beams [2, 97–102, 171, 172, 276]. When HHG is driven by a single, linearly polarized, IR vortex beam with integer topological charge, ℓ_1, the OAM of the q^{th}-order harmonic follows a simple scaling rule, $\ell_q = q\ell_1$ [98, 99]. This scaling reflects the nature of OAM conservation in HHG, where q IR-photons combine to produce the q^{th}-order harmonic. If HHG is driven by the combination of two collinear

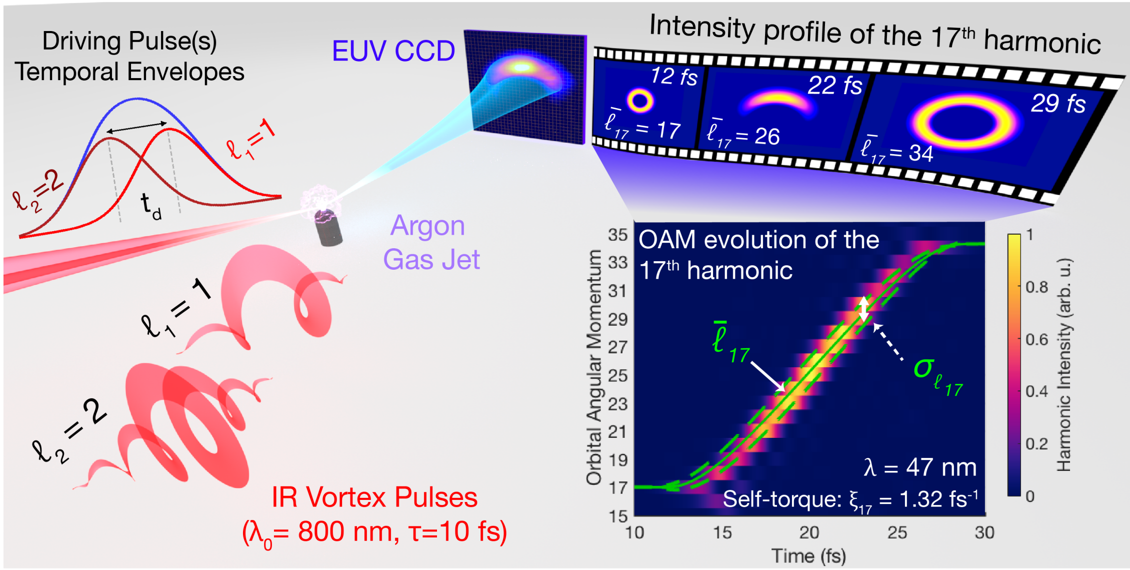

Figure 5.2: **Generation of attosecond, EUV waveforms with self-torque.** Scheme for the creation of EUV beams with self-torque. Two time-delayed, collinear IR pulses with the same wavelength ($\lambda_1 = \lambda_2 = 800$ nm), but different OAM ($\ell_1 = 1$ and $\ell_2 = 2$), are focused into an Ar gas target. The temporal envelopes of each pulse (red), with duration τ and delayed by t_d, and their superposition (blue), are shown on the left. The highly nonlinear process of HHG up-converts the IR pulses into the EUV regime, where harmonic beams with self-torque (i.e., a smooth and continuous time-dependent OAM spectrum) are created. The detector shows the spatial profile of the complete, time-integrated HHG beam from the full quantum SFA simulations, while the film strip shows, schematically, the evolution of the intensity profile of the 17$^{\text{th}}$ harmonic (λ_{17}=47 nm) as a function of time during the emission process. The bottom-right inset represents the temporal evolution of the OAM of the 17$^{\text{th}}$ harmonic, for two driving pulses with the same duration, $\tau = 10$ fs, and a time delay of $t_d = \tau$. The color background shows the results from the full quantum simulations, whereas the mean OAM, $\bar{\ell}_{17}$ (solid green), and the width of the OAM distribution, $\sigma_{\ell_1 7}$ (distance between dashed-green lines), are obtained from Eqs. 5.3 and 5.4. The self-torque associated to this pulse, $\xi = 1.32$ fs^{-1}, is obtained from the slope of the time-dependent OAM. Adapted with permission from Ref. 3.

and temporally overlapped IR vortices with different OAM, ℓ_1 and ℓ_2, each harmonic order will span over a wide OAM spectrum, given by $\ell_q = n_1\ell_1 + n_2\ell_2$ [171], where n_1 and n_2 are the number of photons absorbed from each driver ($n_1 + n_2 = q$, whose total must be odd due to parity restrictions). Each channel, (n_1, n_2), is weighted according to a binomial distribution, associated with the different combinations of absorbing n_1 photons with ℓ_1 and n_2 photons with ℓ_2.[3]

In this work, however, a delay is introduced between the two IR vortex pulses. The superposition of the delayed envelopes introduces a temporal dependence in the relative weights of the driving fields—thus introducing time as an additional parameter. To show how this influences the OAM structure of the EUV

[3] Note that the contribution of the harmonic intrinsic phase to the OAM spectrum, also explored in [171], is a second-order effect, negligible for the results presented here.

harmonics, we consider two time-delayed, collinear, linearly-polarized, IR driving pulses with different OAM, ℓ_1 and ℓ_2. We denote, in cylindrical coordinates (ρ, ϕ, z), the complex amplitudes of the driving fields at the focus position $(z = 0)$ as $U_1\ (\rho, \phi, t)$ and $\mathrm{U}_2\ (\rho, \phi, t)$. For simplicity, we consider the field amplitudes at the ring of maximum intensity at the target—where the HHG efficiency is highest—and the resulting field can be written as

$$U(\phi, t) = U_0(t)\{[1 - \eta(t)]\, e^{i\ell_1\phi} + \eta(t)e^{i\ell_2\phi}\}, \tag{5.1}$$

where $U_0(t) = U_1(t) + U_2(t)$ is the combined amplitude of the LG drivers, and $\eta(t) = U_2(t)/U_0(t)$ is the relative amplitude of the ℓ_2 beam. According to the strong-field description of HHG, the amplitude of the q^{th}-order harmonic, $A_q(\phi, t)$, scales with that of the driving laser with an exponent of $p < q$ ($p \approx 4$ for our laser parameters [171], while the q^{th}-order harmonic phase is considered to be q times that of the driver (see Appendix C, Section C.1 for the complete derivation). As such, we may write the harmonic amplitude at an arbitrary time as

$$A_q(\phi, t) \propto U_0^p(t) \left\{ \sum_{r=0}^{p} \binom{p}{r} [1 - \bar{\eta}(t)]^r e^{ir\ell_1\phi} \bar{\eta}^{(p-r)}(t) e^{i(p-r)\ell_2\phi} \right\} e^{i(q-p)[(1-\eta(t))\ell_1 + \eta(t)\ell_2]\phi}, \tag{5.2}$$

where r is an integer and $\bar{\eta}(t)$ is the average of $\eta(t)$ over the half-cycle that contributes to the generation of a particular harmonic. The summation in Equation 5.2 is carried over p different OAM channels, each weighted by a binomial distribution according with the combinatory nature of the HHG up-conversion process. Remembering again that HHG is an odd-ball and demands parity conservation, the total number of photons absorbed from each driving field, $n_1 + n_2$, must be odd. This in turn implies that in order to generate all intermediate OAM states between $q\ell_1$ and $q\ell_2$, the OAM of the drivers must differ by one unit, i.e. $|\ell_1 - \ell_2| = 1$. The mean OAM of the q^{th}-order harmonic at any instant of time along the harmonic pulse is given by (see Appendix C, Section C.2)

$$\bar{\ell}_q(t) = q\left[(1 - \bar{\eta}(t))\,\ell_1 + \bar{\eta}(t)\ell_2\right], \tag{5.3}$$

and the width of the OAM distribution is

$$\sigma\ell_q = |\ell_2 - \ell_1|\,\sqrt{p\bar{\eta}(t)\,(1 - \bar{\eta}(t))}. \tag{5.4}$$

In analogy with mechanical systems, we characterize the time-varying OAM spectrum of the q^{th}-order harmonic via the self-torque[4]

$$\xi_q = d\bar{\ell}_q(t)/dt. \tag{5.5}$$

In the inset of Figure 5.2, we show the temporal evolution of the mean OAM of the 17^{th} harmonic, $\bar{\ell}_{17}$ (solid-green line), and its OAM width, $\sigma_{\ell_{17}}$ (dashed-green lines). In this case, where $t_d = \tau$, we can approximate the self-torque as constant over the OAM span:

$$\xi_q \sim q\left(\ell_2 - \ell_1\right)/t_d, \tag{5.6}$$

which provides a straightforward route for controlling the self-torque through the OAM of the driving pulses and their temporal properties. The example shown in the inset of Figure 5.2 corresponds to a self-torque of $\xi_{17} = 1.32$ fs^{-1}, which implies an attosecond variation of the OAM. Note that Equation 5.6 is valid only if $t_d \approx \tau$, and if this condition is relaxed, the self-torque must be calculated from the more rigorous definition given in Equation 5.5 (see Appendix C, Section C.2 for OAM spectra obtained at different time delays of the dual-vortex field). Actually, $t_d = \tau$ is a particularly interesting case, as it corresponds to the time delay where the weight of all intermediate OAM states is more uniform over the OAM span[5] .

It is important to stress that even though the mean OAM value at each instant of time may be non-integer, the nature of self-torqued beams is different from that of the well-known fractional OAM beams [172, 277–279]. In particular, the mere superposition of two time-delayed vortex beams—carrying $\ell_i = q\ell_1$ and $\ell_f = q\ell_2$ units of OAM, respectively—does not contain a self-torque. Although it does lead to a temporal variation of the *average OAM* similar as in Equation 5.3, it does not contain physical intermediate OAM states, i.e. photons with OAM other than ℓ_i and ℓ_f. Self-torqued beams, on the other hand, contain all intermediate OAM states, time-ordered along the pulse (see Fig. 5.2 and cf. Figures C.3 and C.4). In addition, the width of the instantaneous OAM distribution of self-torque beams (Equation 5.4) is much narrower than that of the mere superposition of time-delayed OAM beams, in which case—considering a particular high-harmonic, q, $\ell_i = q\ell_1$ and $\ell_f = q\ell_2$—is $\sigma_{\ell_q} = q|\ell_2 - \ell_1|\sqrt{\eta(1-\eta)}$. Moreover, the relative

[4] Note that as the OAM of light is defined by $\hbar\ell$, the self-torque is formally given by $\hbar\xi$. For simplicity—and a dash of ultrafast bias—we factor out $\hbar$ and denote the self-torque by ξ, in units of fs^{-1}.

[5] Conveniently, this is also the maximum time delay at which the combined temporal amplitude of the driving pulses still resembles a Gaussian function.

uncertainty, $\sigma_{l_q}/\bar{\ell}_q(t)$, decreases with the harmonic order, approaching a classical deterministic regime (see Appendix C, Section C.2). This is a direct result of the non-perturbative behavior of HHG, that enables the creation of well-defined intermediate OAM states in a self-torqued beam. Further non-trivial distinctions between these two different kinds of beams, including their temporal evolution of phase and intensity profiles, are highlighted in Appendix C.

The physical nature of the self-torqued beams can be obtained by temporally characterizing the intermediate OAM states, $\ell_q(t_k)$, with $q\ell_1 < \ell_q(t_k) < q\ell_2$. Assuming a beam with constant self-toque ξ_q, the component of the q^{th}-order harmonic carrying an OAM of $\ell_q(t_k)$ will appear at the time $t_k = \frac{\xi_q}{\ell_q(t_k)-q\ell_1}$ after the peak amplitude of the first driving pulse, exhibiting a temporal width of $\Delta\tau_k = \frac{\sigma_{l_q}}{\xi_q} = \tau\frac{\sqrt{p\bar{\eta}(1-\bar{\eta})}}{q} \ll \tau$. Physically, a self-torqued pulse can be thought as a train of time-ordered, overlapping pulses, each one possessing an intermediate OAM, with temporal durations on the attosecond timescale (i.e., much smaller than the width of the driving pulses). This allows us to stress the difference between self-torqued beams and a train of non-overlapping pulses with different OAM [280]. Finally, in analogy to polarization gating techniques [281], self-torqued EUV beams allow the use of subfemtosecond OAM-gating techniques, providing an unprecedented temporal control over laser-matter interactions involving OAM.

5.5 Experimental Confirmation and Quantitative Measurement of the Self-Torque of Light

A direct consequence of self-torque is the presence of an azimuthal frequency chirp in the light beam. As the phase term associated with a time-dependent OAM is given by $\ell_q(t)\phi$, the instantaneous frequency of the q^{th}-order harmonic—given by the temporal variation of the harmonic phase, $\varphi_q(t)$—is shifted by the self-torque as:

$$\omega_q(t,\phi) = \frac{d\varphi_q(t)}{dt} = \omega_q + \frac{d\ell_q(t)}{dt}\phi \approx \omega_q + \xi_q\phi \tag{5.7}$$

Therefore, the harmonics experience an azimuthal frequency chirp whose slope is the self-torque.

In Figures 5.3a and 5.3c, we present the HHG spectrum along the azimuthal coordinate obtained in our full quantum simulations for driving pulses of $\tau = 52$ fs and time delays of $t_d = 50.4$ fs and $t_d = -50.4$ fs, respectively, mimicking the experimental parameters (see Section C.4 of Appendix C). Both spectra reflect the presence of an azimuthal chirp, and thus, a self-torque, whose sign depends on t_d. The full quantum simulations are in perfect agreement with the analytical estimation given by Equation 5.7 (grey-dashed lines). This result shows that the spectral bandwidth of the harmonics can be precisely controlled via the temporal and OAM properties of the driving pulses. Moreover, it provides a direct, experimentally measurable parameter to extract the self-torque, without measuring the OAM of each harmonic at each instant of time with subfemtosecond resolution, which is currently unfeasible. Of course, this reasoning implies that a beam with azimuthal frequency chirp would also exhibit self-torque. Up to now, however, HHG beams have only been driven either by spatially chirped pulses (such as the so-called "attosecond lighthouse" technique [282, 283]), or angularly chirped pulses, which (in theory) yield spatially chirped harmonics [284]. However, to the best of our knowledge, azimuthal chirp—and thus, self-torque—has not been imprinted into EUV harmonics, nor in any other spectral regime.

To experimentally measure the azimuthal frequency chirp of self-torqued EUV beams, we drive the HHG process in Ar gas using two collinear, ~ 52 fs, IR vortex beams with topological charges $\ell_1 = 1$ and $\ell_2 = 2$. The time delay between the two laser pulses is controlled with a high-resolution linear delay stage, with subfemtosecond repeatability and accuracy. The emitted harmonics are collected by a cylindrical-mirror-flat-grating spectrometer and imaged with an EUV CCD camera (see Section 5.3 above). Energy is mapped onto one axis of the camera by spectrally dispersing and focusing along the same dimension, while the other axis preserves spatial information. The measured spatial profile of the HHG beam manifests in a "crescent" shape, also found in our simulations (cf. Figures 5.3g and 5.3h), which already gives a clear indication of the presence of all intermediate OAM contributions from $q\ell_1$ to $q\ell_2$, and thus, of the creation of self-torqued beams (see Section C.2 in Appendix C). To measure the azimuthal frequency chirp, we exploited the spatiospectral mapping of the spectrometer, by aligning the HHG "crescent" (see Section C.6, Figure C.6c in Appendix C) along the spectrometer's dispersion axis, which directly records the azimuthal chirp and yields a tilted harmonic spectrum. Figures 5.3b and 5.3d show the experimental spatial profiles of the HHG spectra along the azimuthal coordinate, for time delays of $t_d = 50.4$ and -50.4 fs, respectively. The different slope of the azimuthal chirp, and the excellent agreement with the analytical theory given by Equation 5.7 (grey-dashed lines), and also the full quantum simulations shown in Figs. 5.3a and 5.3c, confirms the

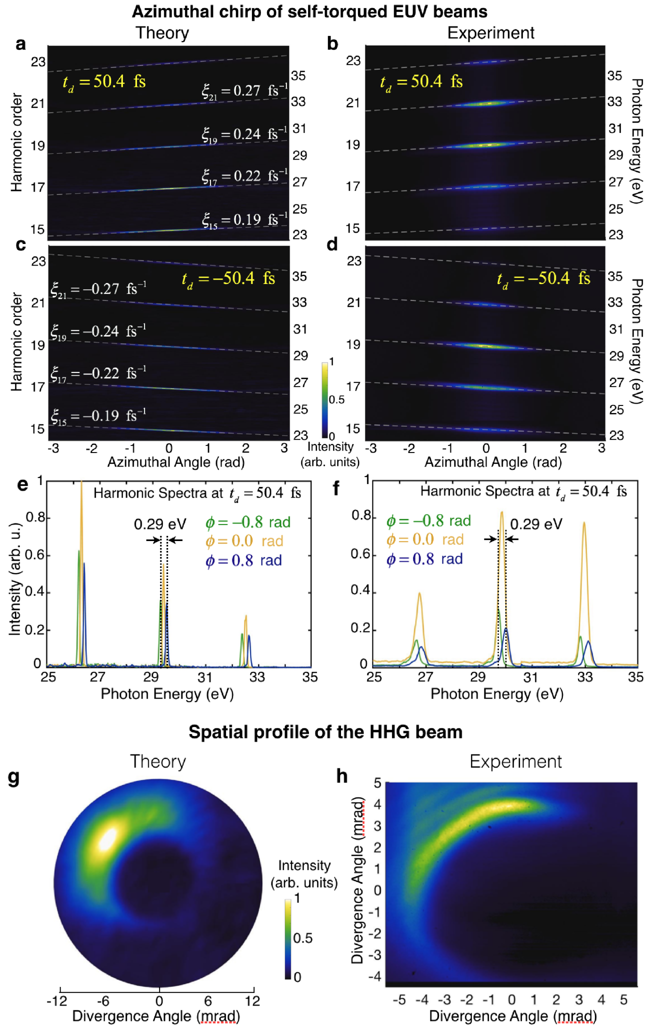

Figure 5.3: **Azimuthal frequency chirp and experimental measurement of the self-torque of EUV beams produced via HHG. a-d** Spatial HHG spectrum along the azimuthal coordinate (ϕ) from quantum simulations (**a,c**) and experiment (**b,d**), when the time delay between the driving pulses is (**a,b**) $t_d = 50.4$ fs and (**c,d**) $t_d = -50.4$ fs. The self-torque of light imprints an azimuthal frequency chirp, which is different for each harmonic, as indicated by the grey-dashed lines (obtained from Equation 5.7). Panels (**e,f**) show the spatially integrated theoretical and experimental harmonic signals obtained at $\phi = -0.8$ rad (green), $\phi = 0$ rad (yellow) and $\phi = 0.8$ rad (blue) for $t_d = 50.4$ fs. The azimuthal frequency chirp serves as a direct measurement of the self-torque of each harmonic beam. Panels (**g,h**) present the theoretical and experimental spatial intensities of the HHG beams, after passing through an Al filter, comprising harmonics $q = 13$-23 ($\sim$ 20-36 eV). Adapted with permission from Ref. 3.

presence of self-torque in the harmonic beams.

In Figure 5.4, we plot the experimental (solid lines) and theoretical (dashed lines) self-torques obtained for the 17$^{\text{th}}$ (a), 19$^{\text{th}}$ (b), 21$^{\text{st}}$ (c) and 23$^{\text{rd}}$ (d) harmonics as a function of the time delay between the IR drivers, for the same parameters as in Fig. 5.3. As the time delay is varied, so too does the degree of azimuthal frequency chirp across the entire harmonic spectrum (according to Equations 5.3 and 5.7], verifying the dynamical build-up of OAM in the self-torqued beams. Note that the self-torque is extracted from the measured azimuthal spectral shift (see Figure 5.3f) and the azimuthal extent of the HHG beam (see Section C.7 in Appendix C for details), using Equation 5.7. The excellent agreement, and most importantly, the overall trend, unequivocally demonstrates the presence of a temporally evolving OAM content and, thus, a self-torque, in all the EUV harmonics generated.

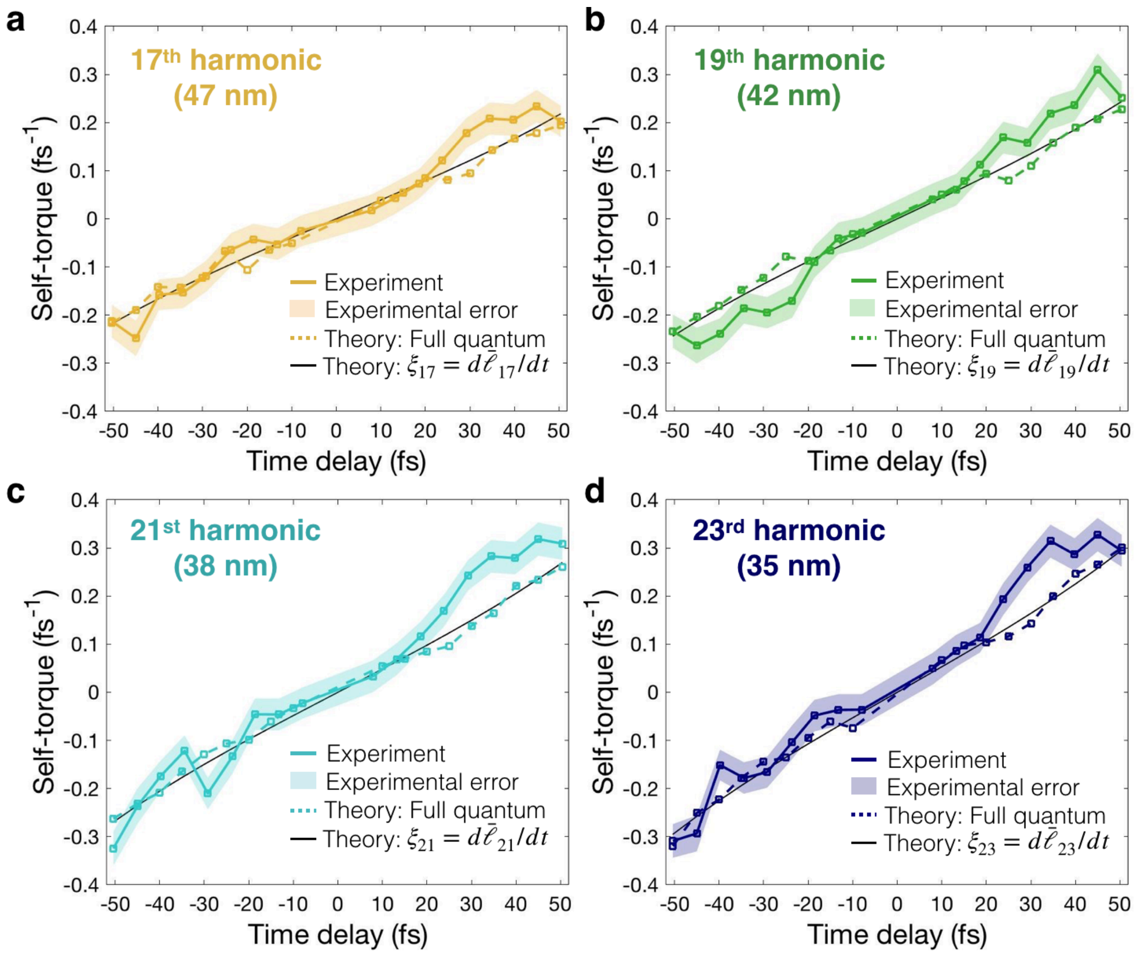

Figure 5.4: **Quantitative measurement of the self-torque of light in attosecond, EUV beams.** Self-torques obtained for the 17$^{\text{th}}$ (**a**), 19$^{\text{th}}$ (**b**), 21$^{\text{st}}$ (**c**) and 23$^{\text{rd}}$ (**d**) harmonics as a function of the time delay between the IR drivers. The experimental data is shown via solid color lines, the results from full quantum simulations in dashed color lines, and the analytical estimation given by Equation 5.3 in solid black lines. The shaded regions depict the experimental uncertainty in the retrieved self-torque for each harmonic order, which themselves comprise the standard “one sigma” deviation of the measured self-torque (i.e., 68% of the measured self-torque values will fall within this uncertainty range). Adapted with permission from Ref. 3.

5.6 Optical Self-Torque vs. Pulse Duration: Generation of EUV Supercontinuua with OAM

Attosecond EUV beams with self-torque can be generated and controlled via the properties of the driving IR vortex beams, with optimal self-torque produced when the laser pulse separation is equal to their duration (i.e., $t_d = \tau$), where all intermediate OAM contributions appear with a similar weight (see Fig. C.1 in the Section C.2 of Appendix C). To illustrate this concept, we present in Figure 5.5a the simulated self-torque obtained for different IR driving pulse durations. In particular, if driven by few-cycle pulses, the self-torque—and thus the azimuthal chirp—is high, with large amounts of OAM building up on an attosecond timescale (Figure 5.5b, where $\tau = 4$ fs). If the torque is high enough, the harmonic frequency comb sweeps along the azimuth, encapsulating all the intermediate frequencies between the teeth of the harmonic comb. Thus, the frequency chirp of time-dependent OAM beams is not only useful to measure the self-torque, but it also represents an approach to obtain an EUV supercontinuum possessing OAM, as shown in the right inset of Figure 5.5b. This allows for the creation of a very precise, azimuthally-tunable frequency comb in the EUV, and a supercontinuum spectrum that is complementary, yet distinct, from other approaches [54, 144, 285].

5.7 Conclusions and Future Outlook of Self-Torqued Attosecond, EUV Beams

We have demonstrated that light beams with time-dependent OAM can be created, thus carrying optical self-torque. This property spans the applications of structured light beams [26] by adding a new degree of freedom, the self-torque, and thus introducing a new route to control light-matter interactions. In particular, ultrafast, short wavelength, high harmonic beams with self-torque can be naturally produced by taking advantage of the conservation laws inherent to extreme non-linear optics. This new capability can deliver optical torque on the natural time and length scales of charge and spin ordering (e.g., femtosecond and nanometer), and can lead to new methods for capturing magnetic and topological excitations, for launching selective excitation of quantum matter, or for manipulating molecules and nanostructures. Finally, the

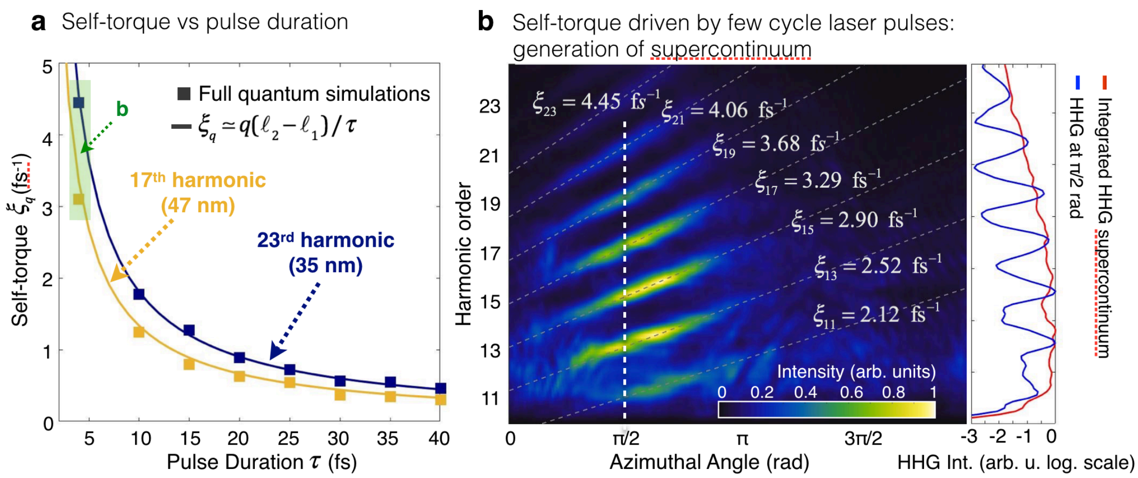

Figure 5.5: **Manifestation of Self-Torque for EUV Supercontinuum Generation.** **a**, Self-torque versus the pulse duration for the 17$^{\text{th}}$ ($\lambda_{17} = 47$ nm) and 23$^{\text{rd}}$ ($\lambda_{23} = 35$ nm) harmonics, where $\tau = t_d$. Solid lines are calculated from Equation 5.3, and the squares correspond to results from our full quantum simulations. **b**, Spatiospectral HHG distribution when driven by two 800 nm, 4 fs pulses with $\ell_1 = 1$ and $\ell_2 = 2$, delayed by 4 fs. The optical self-torque imprints an azimuthal frequency chirp, which is different for each harmonic order, as indicated by the grey dashed lines (obtained from Equation 5.6 and 5.7). The right panel shows the HHG yield at $\pi/2$ rad (blue line) and the spatially integrated supercontinuum (red line). Adapted with permission from Ref. 3.

self-torque of light imprints an azimuthal frequency chirp which allows a way to experimentally measure and control it. Moreover, if the self-torque is high enough, the harmonic frequency comb sweeps smoothly along the azimuth and, if integrated, a high-frequency supercontinuum is obtained, thus presenting exciting perspectives in EUV and ultrafast spectroscopies of angular momentum dynamics.

Appendix A

Appendix: All Optical Control of the Polarization of Attosecond Pulse Trains in Bicircular High-Harmonic Generation

This chapter is adapted, with permission, from:

- K. M. Dorney, J. L. Ellis, C. Hernández-García, D. D. Hickstein, C. A. Mancuso, N. Brooks, T. Fan, G. Fan, D. Zusin, C. Gentry, P. Grychtol, H. C. Kapteyn, and M. M. Murnane. Helicity-Selective Enhancement and Polarization Control of Attosecond High Harmonic Waveforms Driven by Bichromatic Circularly Polarized Laser Fields. *Phys. Rev. Lett.*, 119 (6), **2017**, 45–47. DOI: `10.1103/PhysRevLett.119.063201`

A.1 Overview

This Appendix provides some additional experimental and theoretical tidbits regarding the polarization control of APTs produced via BHHG, as described in Chapter 3. Phase matching effects in cBHHG are considered in Section A.2, while Section A.3 gives the framework for a simple probabilistic photon model that qualitatively recaptures the observed degree of chiral and polarization control on the cBHHG and their underlying APTs. Section A.4 contains extra theoretical details as well as a more detailed look at the results of the simulations by providing a time-frequency analysis of the cBHHG emission process. The effects of ground state symmetry on the observed cBHHG chiral control are investigated in Section A.5 by performing cBHHG in He. Finally, Section A.6 wraps things up with an experimental study of the effects of total intensity on the observed chiral control in cBHHG.

A.2 Phase Matching in High-Harmonic Generation when Driven with a Bicircular Driver

To provide further evidence that our observed control over the attosecond ellipticity of the cBHHG process is not strongly effected by phase matching, we perform phase-matching calculations for our experimental conditions. The phase, or wavevector, mismatch in HHG driven by a bicircular field is given by [184],

$$\Delta k_q = \mathrm{l}k_{\omega_1} + \mathrm{m}k_{\omega_2} - k_q + k_{\mathrm{Gouy}} + k_{\mathrm{dipole}} \tag{A.1}$$

$$\Delta k_q = \mathrm{l}\frac{\omega_1 \Delta \mathrm{n}_1}{c} + \mathrm{m}\frac{\omega_2 \Delta \mathrm{n}_2}{c} + k_{\mathrm{Gouy}} + k_{\mathrm{dipole}} \tag{A.2}$$

Here, $\omega_{i=1,2}$ is the angular frequency of the fundamental (1) or second harmonic (2), l and m are the number of photons absorbed from the ω_1 and ω_2 drivers, respectively, $\Delta \mathrm{n}_{i=1,2}$ is the difference in refractive indices between the two drivers and the harmonics (i.e. $\Delta \mathrm{n}_1 = n_1 - n_q$), which includes effects from neutral atom and plasma dispersion, k_{Gouy} is the phase mismatch resulting from the Gouy phase shift across the laser focus (a positive quantity), and k_{dipole} is the atomic dipole phase mismatch (a positive or negative quantity depending on the focal spot position with respect to the supersonic gas jet). Note that conservation of SAM constrains the allowed values of l and m, such that $l = m \pm 1$. The neutral atom dispersion is found using the measured Semellier equations [286] and the pressure and temperature of the gas in the interaction region. The pressure and temperature are found from the known expressions for continuous supersonic expansion [287] through the gas jet nozzle ($\mathrm{d}_{\mathrm{jet}} = 150\mu\mathrm{m}$). In contrast to one-color HHG, when HHG is driven by a two-color field only one harmonic order can be fully phase matched ($\Delta_k = 0$) at a given set of experimental conditions [184]. However, for all harmonics considered here the coherence length ($1/\Delta_k$) is much larger than the experimental interaction length (Figure A.1) so we can conclude that phase-matching effects do not play a significant role in the measured harmonic yield and observed chiral control in the experimental spectra.

The above analysis was performed considering equal intensities of the two driving lasers, as the phase mismatch of BHHG (Eqs. A.1 and A.2) depends primarily on the total intensity, rather than the particular intensity ratio of the driving fields. However, closer inspection shows that $\mathrm{k}_{\mathrm{dipole}}$ does indeed depend upon

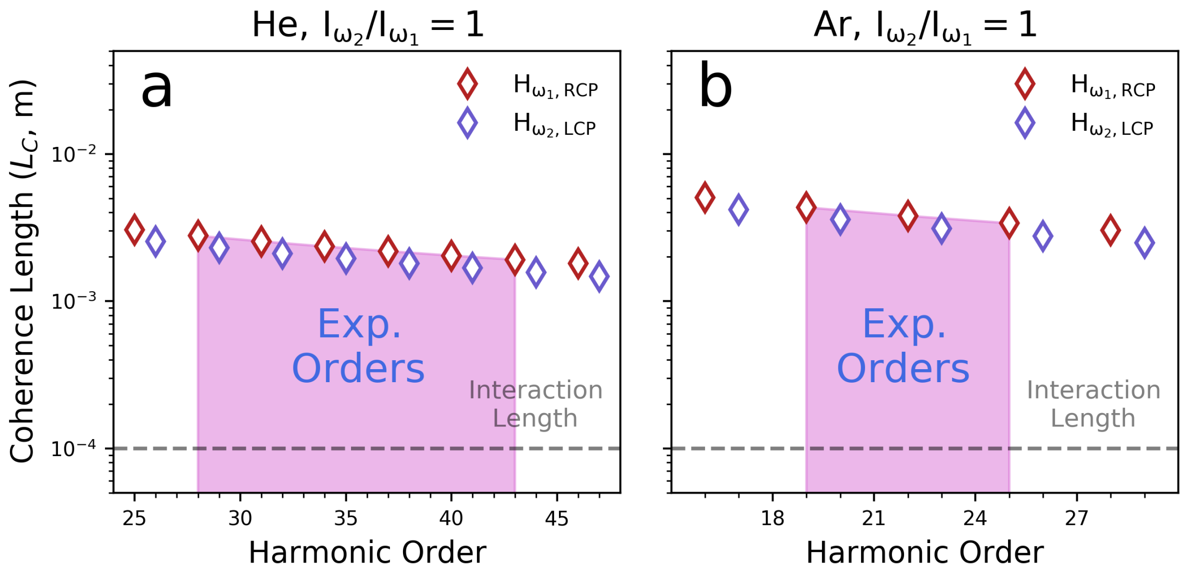

Figure A.1: **Calculated coherence lengths of high-harmonics produced from a bicircular driver.** Coherence lengths for RCP (red diamonds) and LCP (blue diamonds) harmonics generated in **a** He and **b** Ar at $I_{\omega_2}/I_{\omega_1}$= 1 and total intensities of 4.0x10^{14} and 2.0x10^{14} W/cm^2, respectively. The backing pressure of the gas jet was kept the same for each species at 2.76 bar. The plum-shaded region corresponds to the experimentally observed harmonic orders. The interaction length of the BHHG process is indicated with a dashed grey line, which is more than an order of magnitude less than the calculated coherence lengths. Similar results are found for all intensity ratios and all total intensities used in this study. Adapted with permission from Ref. 1. ©2017 American Physical Society

the intensity ratio of the bicircular field.

$$\Delta \mathrm{k_{dipole}} = 8\mathrm{z}\alpha_{\mathrm{q}} \left[\frac{\mathrm{I}_{\omega_1}}{\mathrm{z}^2_{R,\omega_1}\left[1+\left(\frac{2\mathrm{z}}{\mathrm{z}^2_{R,\omega_1}}\right)^2\right]^2} + \frac{\mathrm{I}_{\omega_2}}{\mathrm{z}^2_{R,\omega_2}\left[1+\left(\frac{2\mathrm{z}}{\mathrm{z}^2_{R,\omega_2}}\right)^2\right]^2} \right] \tag{A.3}$$

Here, $I_{i=1,2}$ and $z_{R,\omega_i=1,2}$ are the intensities and Rayleigh lengths of the $\omega_{i=1,2}$ drivers, z is the longitudinal distance from the gas jet (centered at z = 0 mm) and α_q is a coefficient related to the electron trajectory responsible for generating harmonic q ($\alpha_q \approx 1 - 5x10^{14}$ W/cm^2 for the short trajectories). However, this dependence is sufficiently weak such that for all intensity ratios considered here the coherence lengths for all harmonic orders are still much larger than the length of the interaction region (Fig. A.2). Moreover, even if such effects were present, they would affect the phase mismatch of both ω_1 and ω_2 harmonics symmetrically. Therefore, our experimental control of the BHHG chirality across the spectrum is likely not the result of phase-matching effects. This point is of particular importance, as preferential phase matching can be utilized to further increase the degree of chiral control over the harmonic spectrum, resulting in even greater control over the attosecond polarization of the cBHHG process [184].

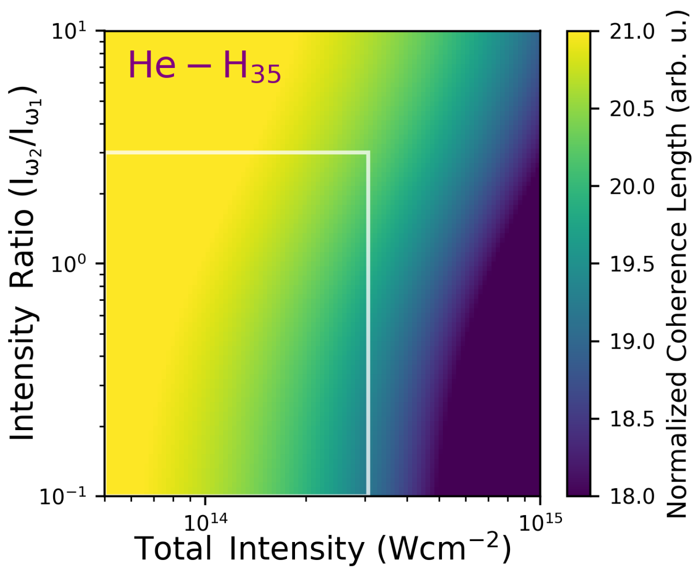

Figure A.2: **Atomic dipole contribution to the phase mismatch of harmonic 35 produced via BHHG in He.** Dependence of the coherence length of the 35$^{\text{th}}$ harmonic in He, normalized to the length of the interaction region as a function of the intensity ratio and total intensity of the bicircular field. Note that the atomic dipole term only significantly contributes to the coherence length at very low intensity ratios and high total intensities, which are well outside the region of experimental intensities and ratios (white box). We note that similar trends are observed for all observed harmonic orders in both He and Ar. Adapted with permission from Ref. 1. ©2017 American Physical Society

A.3 Probabilistic Photon Channel Model for Chiral Control in cBHHG

The effect of the intensity ratio on the chirality of the cBHHG spectra can be intuitively understood by invoking a probabilistic interpretation of the upconversion process [288]. Despite the highly nonlinear nature of HHG, perturbative (or, put another way, multiphoton) models based on the discrete absorption of laser photons have successfully described many qualitative features of HHG-based light sources, such as the allowed emission angles in noncollinear HHG [7, 289, 290], presence of "forbidden" channels [11] and conservation of spin-angular momentum in BHHG [164], and the orbital angular momentum (OAM) spectrum of harmonics produced via OAM-driven HHG [3, 171]. Perturbative models of HHG describe a discrete harmonic spectrum in terms of quantum pathways (i.e. photon channels) involving the absorption of different combinations of photons based on the selection rules governing the particular HHG geometry [288]. In this way, a simple perturbative model provides a qualitative description of chiral control in cBHHG.

In a probabilistic photon-counting picture, we consider all photon channels that result in a given harmonic order, and estimate the contribution of each channel to the total harmonic intensity by computing the probability of absorbing that particular combination of photons. Therefore, the intensity of a given harmonic is determined by the weighted sum of all allowed photon channels,

$$\mathrm{I_q} \propto \mathrm{P}(\Omega) \propto \sum_{i=0}^{\infty} \mathrm{p_1}^{|\mathrm{n}_1^i|} \mathrm{p_2}^{|\mathrm{n}_2^i|}, \tag{A.4}$$

where, $P(\Omega)$ is the total probability of emitting a high harmonic photon at frequency Ω, which is a sum of the probability from each channel i, that are characterized by the total number of photons absorbed from each beam, n_1 and n_2. Here, p_1 and p_2 are the relative probabilities of absorbing a single photon from either beam, which depends on both the total intensity and intensity ratio of the two-color field

$$\mathrm{p}_{\omega_1} = \frac{I_{\omega_1}}{I_{\omega_1} + I_{\omega_2}} = \frac{1}{1 + I_{ratio}} \tag{A.5}$$

$$\mathrm{p}_{\omega_2} = \frac{I_{\omega_2}}{\mathrm{I}_{\omega_1} + I_{\omega_2}} = \frac{1}{1 + 1/\mathrm{I_{ratio}}}. \tag{A.6}$$

The lowest order pathways that contribute to BHHG involve the absorption of equal number of photons from each beam plus an additional ω_1 or ω_2 photon, producing harmonics that rotate with ω_1 or ω_2, respectively. Therefore, the relative probability of producing harmonics that rotate with ω_2 increases as $I_{\omega_2}/I_{\omega_1}$ increases. This enables chiral control over the BHHG process through the control of $I_{\omega_2}/I_{\omega_1}$. We note that this model does not include many of the microscopic (interference, wavepacket diffusion, etc.) and macroscopic effects (phase matching, harmonic re-absorption, etc.) inherent to the BHHG process. Nonetheless, it serves as a simple and intuitive estimate of the degree of chiral control that is possible by varying the intensity ratio in BHHG.

However, the above analysis only considers the lowest order pathway. Higher order pathways are possible, in which additional photon pairs are absorbed (e.g., $n = +1, +2, +3, ...$), followed by simultaneous emission of a necessary amount of ω_1 and ω_2 photons, such that the net absorption of photons is in agreement with the conservation laws. Essentially, these higher order pathways correspond to a combination of high-order sum-frequency generation and difference-frequency generation. Including these higher order pathways results in a general expression for the photon channels that can lead to the emission of RCP and LCP harmonics, for arbitrary driving laser frequencies, ω_1 and ω_2 with $\omega_1 < \omega_2$:

$$\omega_{q,RCP} = (\mathrm{n} + \mathrm{s})(\omega_1 + \omega_2) - [(\mathrm{s} - 1)\omega_1 + \mathrm{s}\omega_2] \tag{A.7}$$

$$\omega_{q,LCP} = (\mathrm{n} + \mathrm{s})(\omega_1 + \omega_2) - [(\mathrm{s} - 1)\omega_2 + \mathrm{s}\omega_1] \tag{A.8}$$

Here n is a positive integer determining the harmonic order and s is a positive integer specifying the number of ω_1 or ω_2 photons emitted during the process. From the above, it is readily evident that for a given harmonic order the $s = 0$ channel obeys a different statistical scaling with respect to the intensity ratio of the bicircular field than the higher order processes. While the probability of the zero-order channel increases with the intensity of the laser that has the same helicity as the emitted harmonic order, the probability of higher s channels increases with the intensity of the pump laser that has the opposite helicity.

Table A.1: Statistical decomposition of spin-allowed photon channels for RCP (q_{19}) and LCP (q_{20}) harmonics in cBHHG.

Channel	$q_{19,RCP}(7\omega_1 + 6\omega_2)$		$q_{20,LCP}(6\omega_1 + 7\omega_2)$	
(n, s)	Photons per Channel	Perturbative Scaling	Photons per Channel	Perturbative Scaling
(6, 0)	$7\omega_1 + 6\omega_2$	p_{ω_1}	$6\omega_1 + 7\omega_2$	p_{ω_2}
(6, 1)	$7\omega_1 + 8\omega_2$	p_{ω_2}	$8\omega_1 + 7\omega_2$	p_{ω_1}
(6, 2)	$9\omega_1 + 10\omega_2$	p_{ω_2}	$10\omega_1 + 9\omega_2$	p_{ω_1}
(6, 3)	$11\omega_1 + 12\omega_2$	p_{ω_2}	$12\omega_1 + 11\omega_2$	p_{ω_1}

As a concrete example, we consider the photon statistics involved in production of the 19$^{\text{th}}$ and 20$^{\text{th}}$ harmonics of cBHHG (Table A.1). Fortunately, as the intensity ratio is altered to favor production of either the 19$^{\text{th}}$ or 20$^{\text{th}}$ harmonic, the $s > 0$ processes become significantly less probable, thus the primary contribution to the overall harmonic signal is the $s = 0$ channel (Fig. A.3a). Thus, for all intensity ratios considered in this study the $s = 0$ channel is the dominant contributor to the harmonic signal. However, the presence of the $s > 0$ channels serves to reduce the degree of chiral control over the BHHG process (Fig. A.3b). A similar behavior occurs when considering multiple harmonics doublets observed in a cBHHG spectrum (Fig. A.3b).

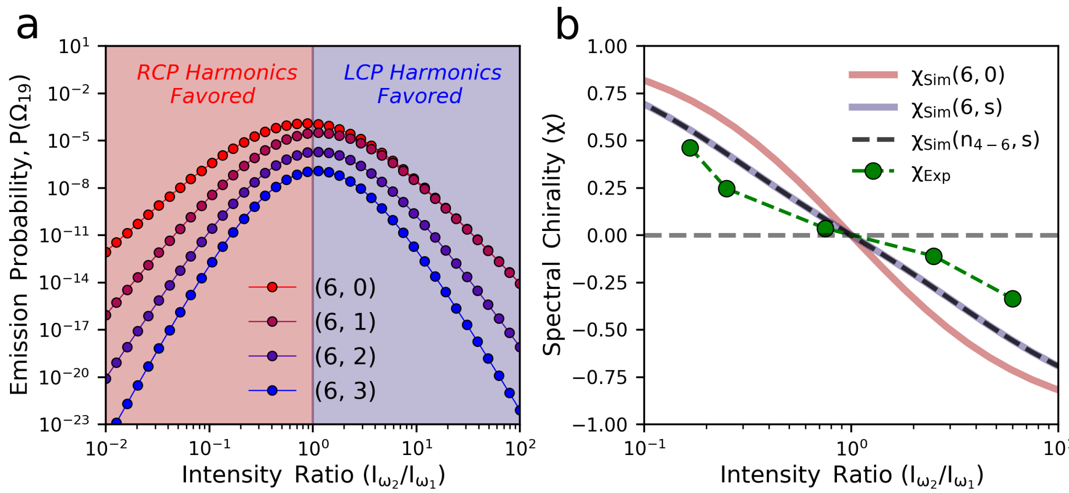

Figure A.3: **Emission probability of the 19$^{\text{th}}$ harmonic within the perturbative photon channel model.** Statistical analysis of photon channel effects on the observed chiral control in BHHG. **a**, Absolute probability of harmonic emission for different photon channels, $(n,\ s)$, that contribute to the intensity of q_{19}, (which is RCP). The shaded regions correspond to intensity ratios that favor either RCP (red) or LCP (blue) harmonic emission across the entire BHHG spectrum. **b**, Simulated spectral chiralities for the $q_{19}q_{20}$ harmonic doublet, calculated for only the (6,0) channel (red solid line), considering all s-type channels (blue solid line), and considering two additional, neighboring harmonic doublets (black dashed line). The $s > 0$ channels serve to slightly reduce the achievable spectral chirality. The experimentally observed spectral chirality in Ar (Fig. 3.2) is given for reference (green circles). Adapted with permission from Ref. 1. ©2017 American Physical Society

A.4 Theoretical Method and Wavelet Analysis of the BHHG Emission Process

The macroscopic BHHG simulations in this work provide valuable insight into the effects of changing the intensity ratio on the attosecond waveform of BHHG. In the simulations, we use the electromagnetic field propagator [155] to compute high-harmonic generation including both the single-atom response (within the SFA) and propagation. To this end, the harmonics emitted at each atom within the target are propagated towards the detector, where the far-field profile is calculated. We assume the harmonic radiation to propagate with the vacuum phase velocity, which is a reasonable assumption for the high-order harmonics observed experimentally. Propagation effects in the fundamental field, such as the production of free charges, the refractive index of the neutrals, the group velocity walkoff [291], as well as absorption in the propagation of the harmonics, are taken into account. Note that although we account for the time-dependent nonlinear phase shifts in the driving fields, nonlinear spatial effects are not taken into account.

In the simulations presented in this work, the laser pulses are modeled with a trapezoidal envelope with three cycles of linear turn-on, six cycles of constant amplitude, and three cycles of linear turn-off (in cycles of the ω_1 field, of 800 nm wavelength). The amplitudes of the two fields—ω_1 of 800 nm and ω_2 of 400 nm wavelengths—are modified in each calculation shown within this work, while maintaining a constant total field intensity. The driving beams are modeled as Gaussian beams, with a beam waist of 40 μm at focus. The gas jet, flowing along the perpendicular direction to the beam propagation is modeled as a Gaussian distribution of 100 μm at FWHM, and with a peak density of 6.67 mbar.

The theoretical BHHG spectra computed in Ar confirm that the BHHG process is robust to the exact choice in intensity ratio of the driving field (Figure A.4). As the intensity ratio is increased, only the harmonic yield is increased while the spectral envelope remains relatively constant. Furthermore, we observe a complete absence of the $3q$, $(q = 1, 2, 3)$, "forbidden" harmonics in the theoretical spectra which is a direct consequence of the three-fold symmetry of the combined ω_1 and ω_2 field [184, 216, 219]. Note that the 2D map of the cBHHG spectra are displayed in log scale in order to emphasize the suppression of forbidden orders, which has the unfortunate effect of masking the degree of chiral control in the computed spectra. The three-fold symmetry of the combined driving field also manifests in the temporal emission of the BHHG process. A time-frequency analysis shows that cBHHG emission occurs three times over the course of an IR cycle (i.e., one complete cycle of the combined field). Figure A.4b shows a typical time-frequency analysis of the cBHHG spectra computed in Ar for $I_{\omega_2}/I_{\omega_1}$=4.0; however, similar results are obtained for all intensity ratios considered in this work. The harmonic bursts also exhibit a positive attochirp, which is indicative of the strong contribution from trajectories that spend a short amount of time in the continuum [240]. These findings are in quantitative agreement with previous theoretical predictions of BHHG, describing the BHHG emission process as the coherent superposition of linearly polarized attosecond bursts that then sum in the far field to yield circularly polarized high harmonics [11, 145, 216].

Although many features of the BHHG emission process are retained as the intensity ratio of the bicircular field is varied, we find that the intensity ratio dramatically alters the ellipticity of the underlying

APTs (Fig. A.4c). The ellipticity of an electric field is given by the following,

$$\epsilon^2 = \frac{|\bar{E}_x|^2 + |\bar{E}_y|^2 - \sqrt{\left(|\bar{E}_x|^2 - |\bar{E}_y|^2\right)^2 + 4|\bar{E}_x|^2|\bar{E}_y|^2\cos^2\left(\phi_y - \phi_x\right)}}{|\bar{E}_x|^2 + |\bar{E}_y|^2 + \sqrt{\left(|\bar{E}_x|^2 - |\bar{E}_y|^2\right)^2 + 4|\bar{E}_x|^2|\bar{E}_y|^2\cos^2\left(\phi_y - \phi_x\right)}} \tag{A.9}$$

where $E_{i=x,y}$ and $\phi_{i=x,y}$ are the amplitude and phase of the $x(y)$-component of the harmonic field. If we consider the case of phase-locked harmonics, the ellipticity of the attosecond bursts depends solely on the relative amplitudes of the dipole oscillation in the polarization plane. Within the three-step model, the strength of this dipole oscillation is, to first order, proportional to the adiabatic ionization rates, which are highly nonlinear on the driving electric field. As such, the amplitude of the cBHHG field is highly sensitive to the strength of the driving field. As the intensity ratio is varied, the x and y components of the driving field corresponding to the brightest cBHHG emission (i.e. near the field maxima) also change, which in turn imparts ellipticity to the harmonic wavetrain. Importantly, this ellipticity is uncoupled from the polarizations of the driving fields, which allows for the production of chiral attosecond pulses while maintaining a high degree of circularity of the emitted harmonics. Moreover, spectral filtering of the cBHHG spectra can be exploited to increase the ellipticity of the attosecond pulse train, even when the process is driven with a large $I_{\omega_2}/I_{\omega_1}$(Figure A.4c).

A.5 Effects of Ground State Symmetry and Harmonic Bandwidth on the Bicircular-Induced Control of Spectral Chirality in cBHHG

Recently, there has been an increased interest in the non-adiabatic nature of strong-field ionization by circularly polarized laser fields, in particular the manifestation of such effects on the BHHG process [229, 230]. Theoretical investigations have predicted [292, 293] and experiments have confirmed [239, 294] that the sense of rotation of an electron in the ground state of an atomic system possessing OAM can significantly influence the strong field ionization rates when driven by a circularly polarized laser field. In short, electrons that rotate against the polarization vector of the driving field are preferentially ionized. Since, to first order, the photorecombination step in HHG can be viewed, with some caveats[1] [226], as the complex conjugate of the photoionization process, increased signals in RCP or LCP harmonics could be the result of selective

[1] The major caveats are given in Chapter 3 Section 3.4.3, but the general tidbit to keep in mind is that the photoionization process restricts the initial momentum and offset angle of photoionized electrons, due to the strong-field nature of the photoionization process.

ionization of counter-rotating orbitals with respect to the stronger component of the combined bicircular field. This fact was exploited recently to theoretically show that in general, the BHHG process yields elliptically polarized attosecond pulse trains at the single-atom level [215].

In order to ensure the generality of controlling the chirality of BHHG via the intensity ratio of the bicircular field, we also performed similar measurements of cBHHG spectra in He, where the ground state of both electrons carries no OAM and thus effects from preferential ionization are not present [226]. Interestingly, we achieve a similar degree of chiral control in He (Fig. A.5), despite the lack of OAM of both electrons. Furthermore, the cBHHG spectra in He possess a much broader envelope, which allows for a more thorough analysis of the energy dependence of the observed chiral control. As the intensity ratio is increased (decreased), the total yield of the harmonics is increased (decreased), while the spectral envelope remains nearly constant. These trends in the experimental data are also confirmed in the numerical simulations of the cBHHG spectra in He. Taken together, these results show that the spectral chirality and, more importantly, the ellipticity of the APTs can be controlled irrespective of the harmonic bandwidth or symmetry of the ground electronic state of the cBHHG medium, as also observed in [226]. This last point is vitally important for generating high-energy elliptical APTs via this method, especially when the individual RCP and LCP harmonics cannot be spectrally isolated. Finally, we observe a lesser degree of chiral control in He as compared to Ar (cf. Figure 3.2c and Figure A.5c], which also corresponds to a lower harmonic field ellipticity (A.6 and A.7) and is the result of a lack of helicity-selective ionization enhancement for spherically symmetric ground states.

A.6 Intensity Dependence of the Chiral Control in Experimental cBHHG Spectra Generated in Helium

The peak intensity of the driving laser field is one of the most influential free parameters affecting the BHHG generation process and thus the subsequent far-field spectra. For instance, the harmonic cutoff energy depends linearly on the peak intensity of the laser field [106, 107, 138, 215, 240]. Additionally, the trajectory dependent phase of the recombining electron wavepacket is particularly sensitive to the peak intensity [138, 216], which can alter the structure of the plateau. The intensity dependence is further complicated in BHHG by the presence of one to three different classes of electron trajectories (i.e., channels) that can contribute to bright BHHG emission [11, 216]. Therefore, changing the peak intensity of the bicircular field could lead to changes in the spectral structure of cBHHG harmonics.

To confirm that the observed chiral control over the BHHG emission process is a result of the intensity ratio and not the peak intensity, we measured cBHHG spectra across a range of intensity ratios and total intensities in both Ar and He (Figure A.8 and Figure A.9, respectively). The two-dimensional analysis in Ar clearly shows that the main contribution to controlling the cBHHG chirality is due to the changing intensity ratio of the driving field, with only a slight dependence on the total intensity for cBHHG in He. However, in either case, as the intensity ratio is increased at a constant total intensity, there is a clear progression of RCP dominated cBHHG spectra to LCP dominated spectra. Moreover, this behavior is retained irrespective of the total intensity of the driving field. These results not only confirm that effects from the harmonic envelope are negligible under our experimental conditions, but also that controlling the spectral chirality, and thus ellipticity of the harmonic field, is independent of the bandwidth of the cBHHG spectra.

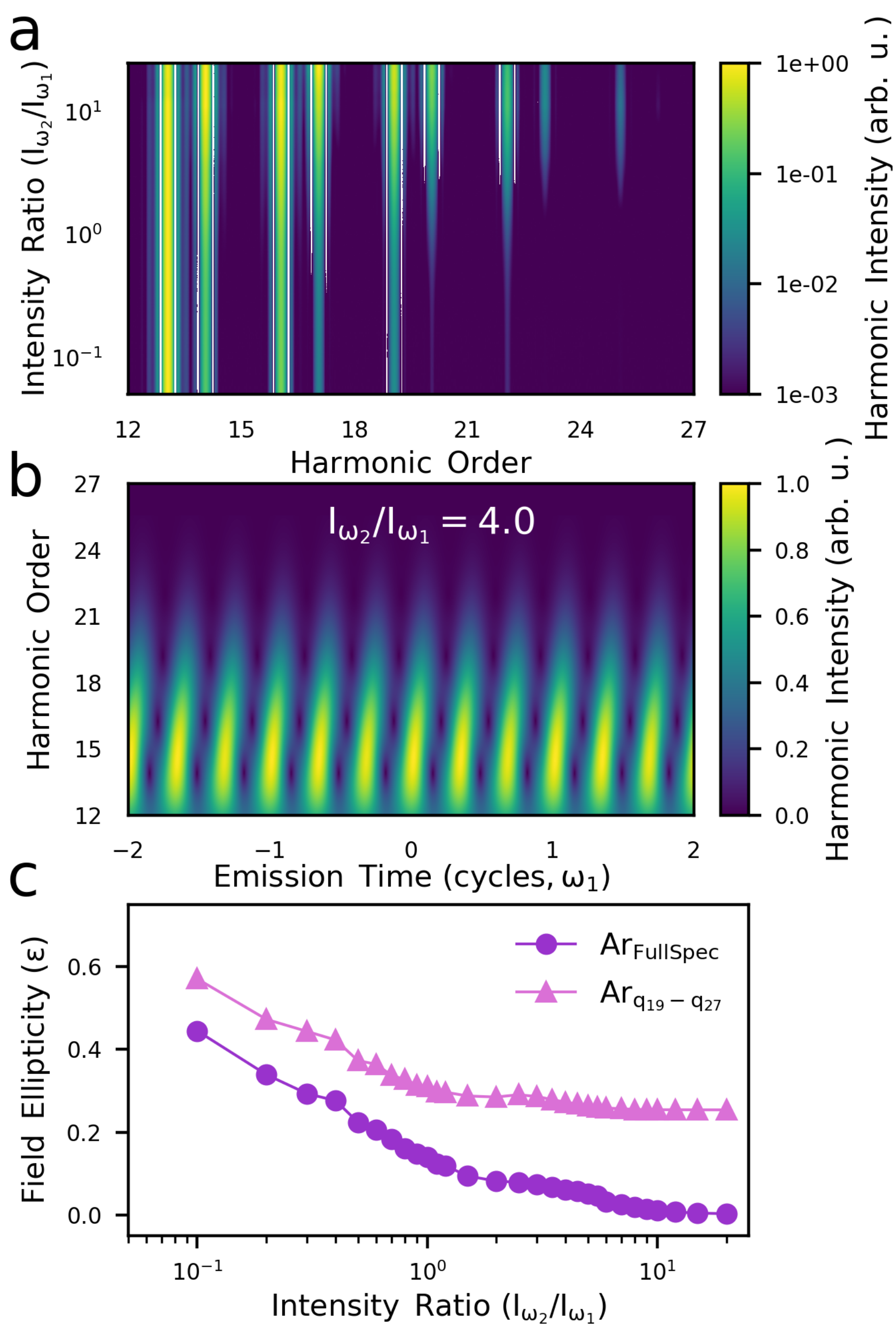

Figure A.4: **Time frequency analysis of cBHHG in Ar.** Full temporal analysis of the macroscopic cBHHG emission process calculated in Ar at a total intensity of $2.0x10^{14}$ W/cm^2 for all intensity ratios of the driving field considered in this work. **a**, cBHHG yields (log scale) computed in Ar as a function of the $I_{\omega_2}/I_{\omega_1}$ ratio of the bircircular field. **b**, Time-frequency analysis of RCP component of the cBHHG spectrum computed in Ar for a $I_{\omega_2}/I_{\omega_1}$=4.0. The individual harmonic bursts exhibit a positive attochirp, where higher energy harmonics are emitted later in time. Similar results are found for the LCP component. **c**, Harmonic field ellipticity as a function of the $I_{\omega_2}/I_{\omega_1}$ ratio of the driving field. As the intensity ratio is further increased to favor the higher frequency component, the polarization of the attosecond pulse train remains linear (circle symbols); however, spectral filtering can be utilized to isolate near cutoff harmonics (triangle symbols), thus increasing the ellipticity. Adapted with permission from Ref. 1. ©2017 American Physical Society

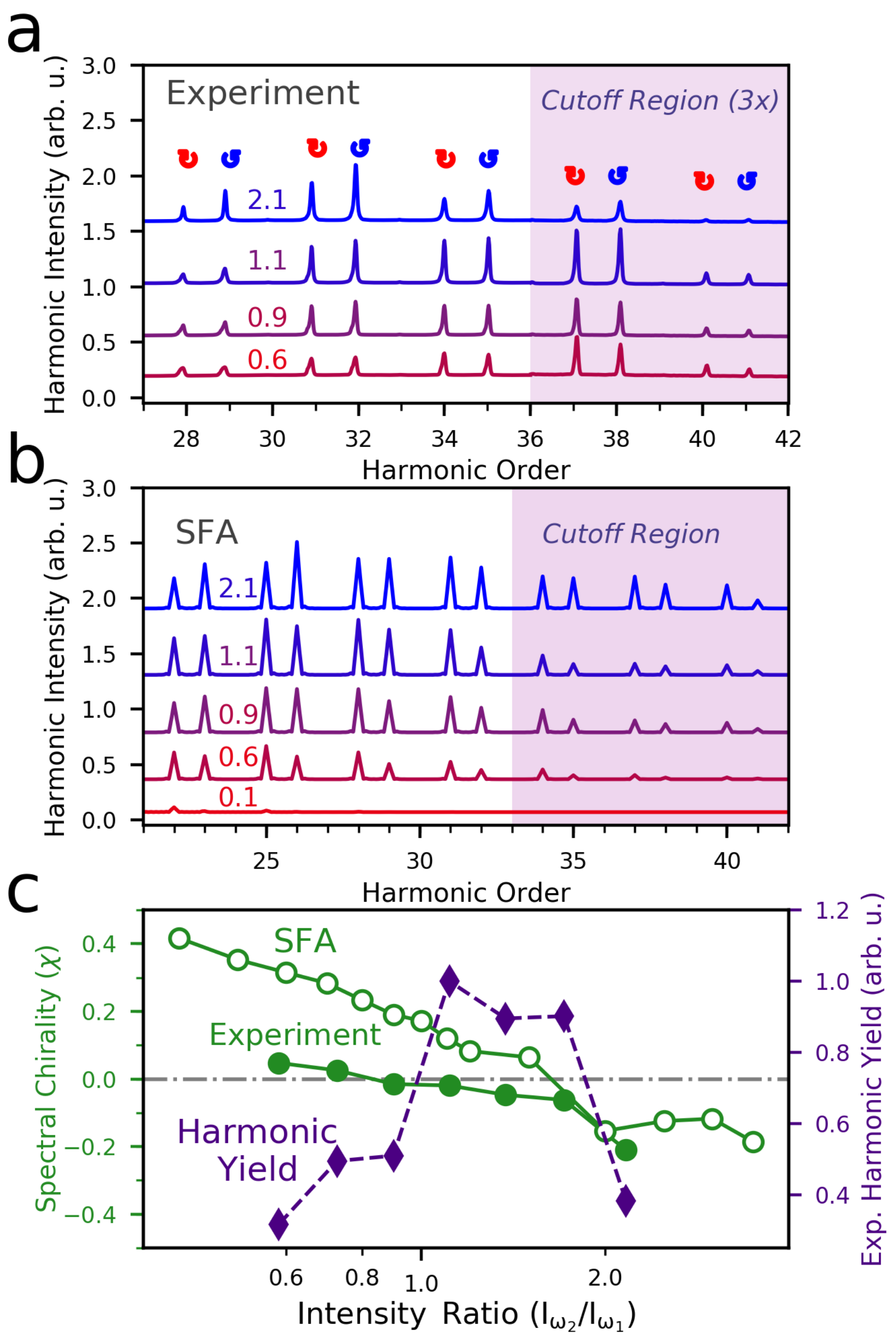

Figure A.5: **Generation and control of chiral BHHG spectra in helium.** Circularly polarized high harmonic spectra in He. **a**, Experimental cBHHG spectra recorded at increasing $I_{\omega_2}/I_{\omega_1}$ ratios ($I_{\omega_2}/I_{\omega_1}$ values given next to the spectra) at a total intensity of $\approx 4x10^{14}$ W/cm^2. *b*, Simulated cBHHG spectra for He at a total intensity of $4.6x10^{14}$ W/cm^2 and the same intensity ratios as the spectra in **a**. The harmonics in the cutoff region in **a** has been scaled for clarity. **c**, Experimental and theoretical spectral chirality, $\chi = (I_{RCP} I_{LCP}) / (I_{RCP} + I_{LCP})$, (left axis) and experimental cBHHG yields (right axis) observed in He as a function of the $I_{\omega_2}/I_{\omega_1}$ ratio of the two-color field. Harmonic yields are obtained as the total integrated signal for all observed harmonics in the experimental spectra. Adapted with permission from Ref. 1. ©2017 American Physical Society

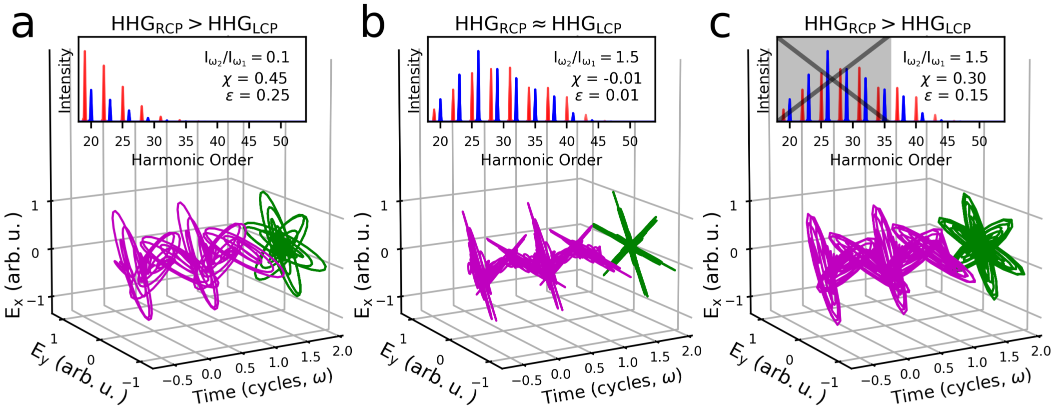

Figure A.6: **Elliptical attosecond pulse trains produced via cBHHG in helium.** Attosecond pulse trains and corresponding theoretical spectra in He (**a**, **b**, **c**) at a total intensity of $4.6x10^{14}$ W/cm^2. The temporal profile is obtained via an inverse Fourier transformation of the corresponding cBHHG spectra at the indicated $I_{\omega_2}/I_{\omega_1}$ ratio, spectral chirality (χ) and harmonic field ellipticity (ϵ) [insets]. Here, light red HHG orders are RCP and rotate with the fundamental, while dark blue orders are LCP and rotate with the second harmonic field. As the cBHHG spectra evolve from being dominated by primarily RCP harmonics to a preference of LCP harmonics, the attosecond pulse trains evolve from elliptical to linear (**a**, **b**). If, however, a small bandwidth near the cutoff is selected (**c**, unshaded region) the ellipticity of the attosecond pulse trains can be restored, especially when the $I_{\omega_2}/I_{\omega_1}$ ratio of the driving field is optimized for the brightest harmonic signal. Adapted with permission from Ref. 1. ©2017 American Physical Society

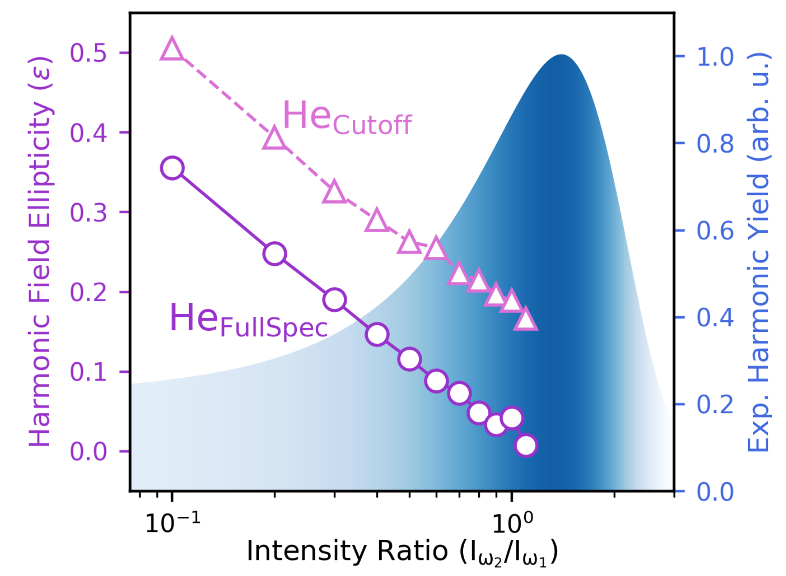

Figure A.7: **Degree of elliptical control over the APTs for cBHHG in helium.** Ellipticity of the underlying attosecond pulse trains for the theoretical cBHHG spectra in He, computed at a total intensity of $4.6x10^{14}$ W/cm^2, as a function of the intensity ratio of the two-color field. By employing a spectral filter to isolate the plateau and near-cutoff harmonics, the ellipticity of the APTs (light orchid triangles) can be increased by a factor of two or more, even in regions where the intensity ratio is set to maximize the experimental cBHHG yield (shown here as a Gaussian fit of the experimental data, blue gradient, right axis). Adapted with permission from Ref. 1. ©2017 American Physical Society

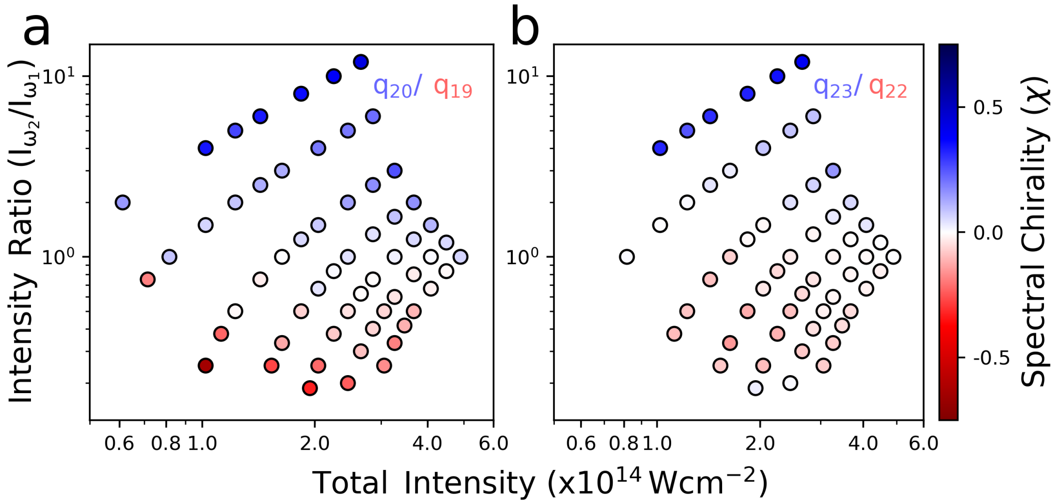

Figure A.8: **2D plots of attosecond ellipticity in cBHHG in argon: dependence on the total intensity and the $I_{\omega_2}/I_{\omega_1}$ of the bicircular field.** Calculated spectral chirality, $\chi = (I_{RCP} - I_{LCP})\,/\,(I_{RCP} + I_{LCP})$, from the cBHHG spectra in Ar over a range of intensity ratios and total intensities of the driving field for **a**, $q = 19$ and $q = 20$ and, **b**, $q = 22$ and $q = 23$. Adapted with permission from Ref. 1. ©2017 American Physical Society

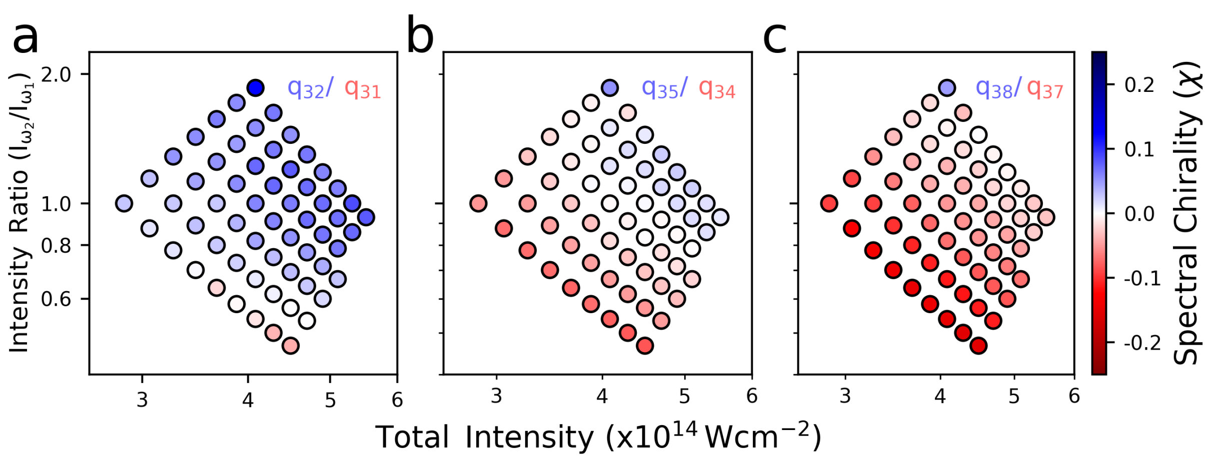

Figure A.9: **2D plots of attosecond ellipticity in cBHHG in helium: dependence on the total intensity and the $I_{\omega_2}/I_{\omega_1}$ of the bicircular field.** Calculated spectral chirality, $\chi = (I_{RCP} - I_{LCP})\,/\,(I_{RCP} + I_{LCP})$, from the cBHHG spectra in He over a range of intensity ratios and total intensities of the driving field for **a**, $q = 31$ and $q = 32$ and, **b**, $q = 34$ and $q = 35$. Adapted with permission from Ref. 1. ©2017 American Physical Society

Appendix B

Appendix: Helicity in a Twist: Controlling the polarization, divergence and vortex charge of attosecond high-harmonic beams via Simultaneous Spin-Orbit Momentum Conservation

This chapter is adapted, with permission, from:

- K. M. Dorney, L. Rego, N. J. Brooks, J. San Román, C.-T. Liao, J. L. Ellis, D. Zusin, C. Gentry, Q. L. Nguyen, J. M. Shaw, A. Picón, L. Plaja, H. C. Kapteyn, M. M. Murnane, and C. Hernández-García. Controlling the polarization and vortex charge of attosecond high-harmonic beams via simultaneous spin–orbit momentum conservation. *Nat. Photonics*, 13 (2), **2019**, 123–130. DOI: `10.1038/s41566-018-0304-3`

B.1 Chapter Overview

This Appendix provides additional information regarding the first realization of EUV waveforms with simultaneously controllable SAM and OAM, as described in Chapter 4. Section B.2 provides additional experimental details as well as the characterization of the driving modes. Sections B.3-B.4 delve deeper in the theoretical aspects of SAM-OAM HHG, setting up and validating a simplified diffraction model (Section B.3), laying down a model for determining the divergence difference between RCP and LCP harmonic vortices (Section B.5), and providing a recipe for generating isolated vortices—and APTs—of pure circular polarization.

B.2 Additional Experimental Details on SAM-OAM HHG

The generation of circularly polarized extreme ultraviolet (EUV) vortices with controllable spin and orbital angular momentum (SAM and OAM) is achieved by driving the HHG process with a bicircular optical vortex field. This driving laser waveform is synthesized from the collinear superposition of a left circularly polarized (LCP) vortex beam (785 nm, $\sigma_1 = -1$, ℓ_1) and its right circularly polarized (RCP) second harmonic (392 nm, $\sigma_2 = 1$, ℓ_2). The topological charge of each beam is controlled via independent spiral phase plates (SPPs, HoloOr, 16-steps per phase ramp) in each arm, which, upon focusing, yields vortex modes (Figure B.1) with a uniform Laguerre-Gaussian (LG) intensity distribution. The spatial structure of an LG beam propagating along the z-direction, with wavelength λ_0, ($k_0 = 2\pi/\lambda_0$), is given by

$$\begin{aligned} LG_\ell^p(\rho,\phi,z;k_0) = E_0 \frac{w_0}{w(z)} \left(\frac{\sqrt{2}\rho}{w(z)}\right)^{|\ell|} L_p^{|\ell|}\left(\frac{2\rho^2}{w^2(z)}\right) \\ \times e^{\frac{\rho^2}{w^2(z)}} e^{i\ell\theta + i\frac{k_0\rho^2}{2R(z)} + i\Phi_G(z)} \end{aligned} \tag{B.1}$$

Here, $w(z) = w_0\sqrt{1+(z/z_0)^2}$ is the beam waist, with w_0 being the beam waist at focus and $z_0 = \pi w_0^2/\lambda_0$ the Rayleigh range, $R(z) = z\left[1+(z_0/z)^2\right]$ is the phase-front radius, $\Phi_G(z) = -(2p+|\ell|+1)\arctan(z/z_0)$ is the Gouy phase, and $L_p^{|\ell|}(x)$ are the associated Laguerre polynomials [70]. The indexes $\ell = 0, \pm1, \pm2, ...$ and $p = 0, 1, 2, ...$ correspond to the topological charge and the number of nonaxial radial nodes of the mode, respectively. For the purposes of this discussion, we refer to these vortex beams as LG beams, but it is important to note that such vortex beams can be accurately described in several different basis sets [295–297].

Contrary to traditional bicircular HHG with Gaussian mode drivers, SAM-OAM HHG with LG drivers places stricter demands on the quality of the bicircular driving field. Unlike their Gaussian counterparts, the modal extent of LG_p^ℓ beams is determined by not only the waist size at the focus, but also the topological charge, ℓ, of the vortex mode (see Equation B.1). Since the waist size and OAM content of each beam is different (and can vary in the experiment), proper mode matching demands independent control over the focusing abilities of each beam. To achieve this, we use separate helical lenses (i.e., an SPP and a converging lens) in each arm of the interferometer, as well as adjustable apertures upstream of the helical lenses. Additionally, the helical lenses employed in this work require the foci of the two beams to be found at the same longitudinal location, as propagation effects from the lens to the focus create radial intensity rings that do not collapse to a well-defined LG_0^ℓ mode until very close to the focal plane [297]. Once the beams pass through the helical lenses, the beams are overlapped such that the ring of maximum intensity of each driver is superposed onto one another, yielding an azimuthally *and* radially uniform focus. We note that this results in a slight mismatch of the Gouy phase for each beam, but under our generating conditions (thin gas target and a relatively long Rayleigh length), these effects are negligible. Finally, the SPPs are placed exactly one focal length behind the converging lens in each arm of the interferometer in order to precisely cancel the propagation phase acquired by the beam on traveling from the SPP to the converging lens. When properly accounting for these parameters, uniform LG_0^ℓ modes are produced at the focus of each beam, which in turn yields a highly pure bicircular vortex beam for driving the HHG process (Fig. B.1a-f).

The degree of OAM-dependent control on the SAM and OAM properties of the EUV vortices depends upon the proper orientation of the SPPs, as this determines the sign and magnitude of the topological charge of the constituents of the bicircular vortex. In order to confirm the relative sign of the OAM of each driver, as well as the quality of the vortex beams, we use a cylindrical lens as a spatial, 1D-Fourier transform element. The cylindrical lens images the focus of the helical lens for each beam, and the secondary focus is imaged with a beam profiling camera. The resulting intensity profile exhibits a characteristic fringe pattern [298], where the number and orientation of the fringe(s) determine the sign and magnitude of the OAM (Fig. B.1g-i). This fringe pattern is utilized to confirm the OAM configuration of the bicircular vortex drivers for controlling the SAM, OAM, and divergence properties of the high-harmonic EUV vortices.

B.3 Additional Details Regarding the Quantum Theoretical Simulations

To predict and inform the SAM-OAM HHG process, we employ full quantum simulations of the up-conversion process, including effects from propagation. The propagation, which is crucial to modeling experimental conditions, is based on the electromagnetic field propagator method [155]. Briefly, the target (i.e., gas jet) is discretized into elementary radiators, and the single-atom response of these emitters to the driving beam is computed within the quantum SFA [299, 300]. The emitted field, $\vec{E}_j(\vec{r}, t)$, is then propagated

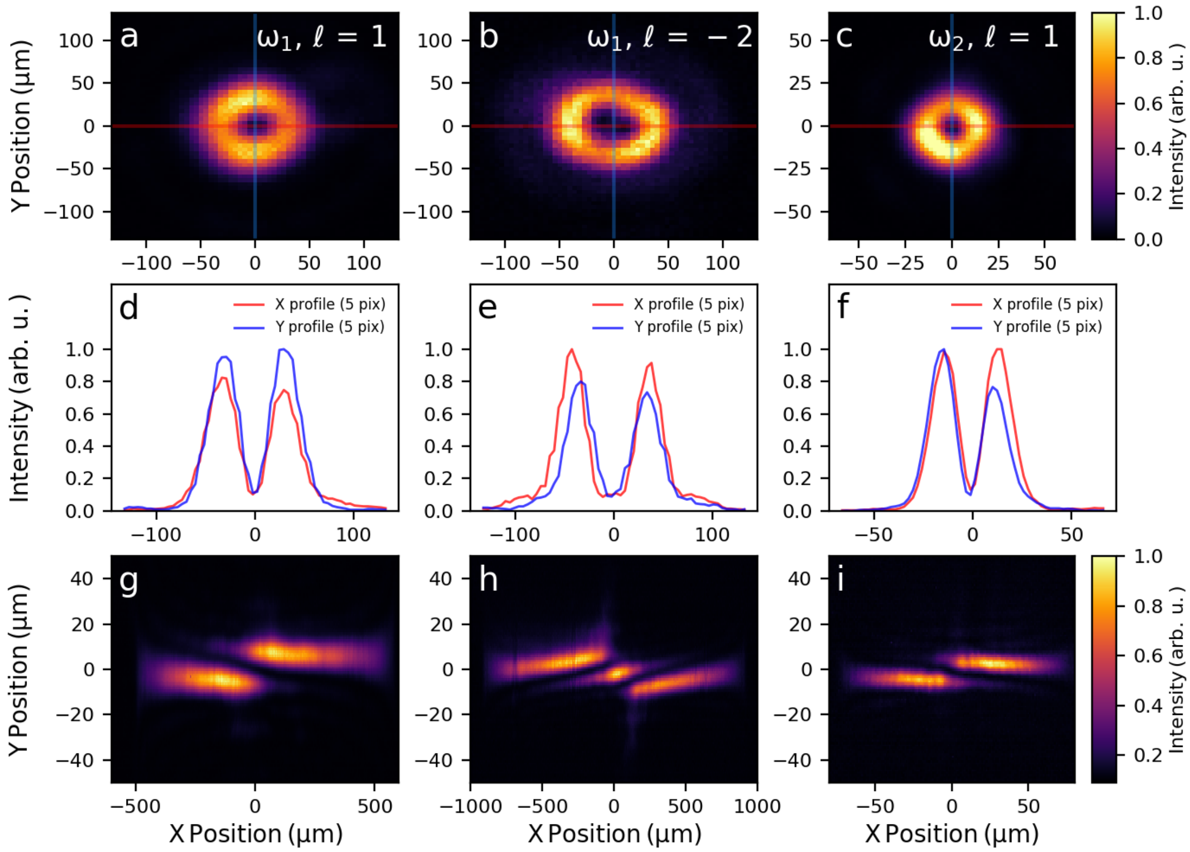

Figure B.1: **Generation and characterization of ultrafast LG beams for constructing a bicircular vortex driver.** When taking into account the stricter demands required of the spatial modes of the driving lasers for bicircular SAM-OAM HHG, vortex beams of a uniform LG_0^ℓ profile are generated for constructing the bicircular vortex field. In panels **a-c** we show the measured intensity profile for **a**, $\omega_1, \ell_1 = 1$, **b**, $\omega_1, \ell_1 = -2$, and **c**, $\omega_2, \ell_2 = 1$. Despite their broadband nature, these beams exhibit a clear singularity on axis, as well as a uniform, single-mode intensity profile **d-f**. The relative sign of the topological charge of each vortex can be determined by reimaging the focus of the helical lens with a cylindrical lens, producing a characteristic intensity interference pattern. The number of fringes, as well as their orientation, readily confirms the sign of the OAM for each driver, **g**, $\ell_1 = 1$ **h**, $\ell_1 = -2$ **i**, $\ell_2 = 1$. Adapted with permission from Ref. 2. ©2018 Nature Publishing Group

to the detector via

$$\vec{E}_j(\vec{r}_d, t) = \frac{q_j}{\vec{s}_d} \times \left[\vec{s}_d \times \vec{a}_j\left(t - \frac{|\vec{r}_d - \vec{r}_j|}{c}\right)\right] \tag{B.2}$$

where q_j is the charge of the electron, $\vec{s}_d$ is the unitary vector pointing to the detector, $\vec{r}_d$ and $\vec{r}_j$ are the position vectors of the detector and of the elementary radiator j, respectively, and c is the speed of light in vacuum. Note that Equation B.2 assumes that the harmonic radiation propagates with the vacuum phase velocity, which is a reasonable assumption for high-order harmonics. Finally, the total field at the detector is computed as the coherent addition of the elementary contributions. We note that one of the advantages of this method is its suitability to compute high-order harmonic propagation in non-symmetric geometries. Therefore, it is especially suited for computing HHG driven by beams carrying orbital angular momentum [99, 170, 171], beams where the polarization varies spatially [172, 249], double gas jet schemes to produce spatially varying polarization harmonics [6], or the SAM-OAM HHG presented in this work.

B.4 Simple Diffraction Model of SAM-OAM HHG to Predict the Polarization of the Underlying APTs

To predict the attosecond pulse polarization in SAM-OAM HHG, we have implemented a simple model based on Fraunhofer diffraction. This model is a simplified version of the so-called thin slab model used in previous works of linearly polarized OAM-HHG [170, 171]. This new method allows us to obtain the far-field profile of the high-order harmonics through some assumptions over their near-field distribution. In this simplified version we mainly consider two assumptions: (i) the main contribution to the high harmonic signal comes from the ring of maximum intensity of the driving vortex field. (ii) the topological charge of each harmonic follows Equation 4.1. Thus, the far-field distribution of the q^{th}-order harmonic, $A_q(\beta)$, with β being the divergence, can be calculated as:

$$A_q(\beta) \propto J_{|\ell_q|}\left(\frac{2\pi}{\lambda_1} q \tan(\beta) r_{max}\right) \tag{B.3}$$

where $J_n(x)$ is the n^{th}-order Bessel function, λ_1 is the wavelength of the ω_1 driver, r_{max} is the radius of maximum intensity of the driving field, and the topological charge ℓ_q is calculated from Equation 4.1 in the main text. Note that the order of the Bessel function is $|\ell_q|$, and its dependence with the divergence is proportional to the harmonic order. The relation between these two quantities unequivocally determines the divergence of the harmonic, as previously reported in [98–100, 170]. In Fig. B.2a we show the far-field profile of the spectrally integrated RCP (blue) and LCP (green) harmonics using the simple diffraction model. We have considered the case analyzed in Fig. 4.3 of Chapter 4 ($\ell_1 = 1$, $\ell_2 = 1$), and spectrally integrating the 10^{th}, 13^{th} and 16^{th} harmonics for RCP, and the 11^{th}, 14^{th} and 17^{th} for LCP. The ellipticity $\epsilon = (I_{RCP} - I_{LCP})\ (I_{RCP} + I_{LCP})$ is presented as the red line.

To validate our simple diffraction model, we have compared it against our quantum simulations including propagation, described in the previous section. Note that the parameters in the quantum simulations are the same as those in the main text. First, we have considered high-order harmonic generation only in the ring of maximum intensity of the driving field (Fig. B.2b). The excellent agreement between Fig. B.2a and B.2b demonstrates the accuracy of the simple diffraction model in the near field. Second, we consider the full quantum simulation results (Fig. B.2c), corresponding to those presented in Fig. 4.3 of Chapter 4. The good agreement between the three approaches shows the suitability of only considering the maximum intensity ring of the driving field. Note that there is some deviation in the divergence angle, that arises from transverse phase-matching [99, 170, 301]. Therefore, the simple diffraction model allows us to accurately predict the intensity distributions of RCP and LCP harmonics, and thus the ellipticity of the attosecond pulses.

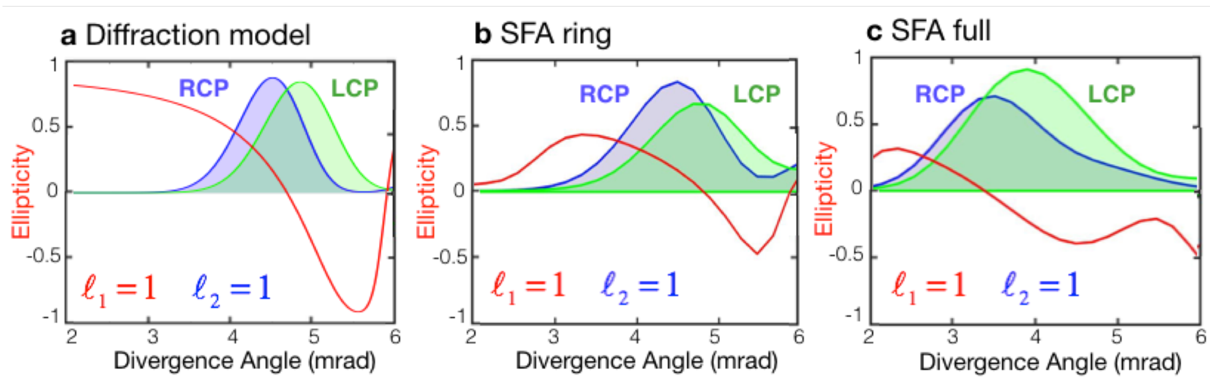

Figure B.2: **Validation of the simple diffraction model.** Far-field profiles of the integrated RCP (blue) and LCP (green) harmonic vortices and the resulting pulse ellipticity, $\epsilon = (I_{RCP} - I_{LCP})\,(I_{RCP} + I_{LCP})$ (red), when using **a**, the simple diffraction model, **b**, the quantum model considering only the ring of maximum intensity of the driving field, and **c**, the full quantum model. The configuration of the driving field is the same as that used in Fig. 4.3 (i.e., $\ell_1 = 1$, $\ell_2 = 1$). Adapted with permission from Ref. 2. ©2018 Nature Publishing Group

B.5 Control of the Attosecond Pulse Polarization Through Different OAM Combinations

In this section, we first derive the simple rule presented in Equation B.3 in the main text to predict the divergence difference between the RCP and LCP harmonics ($\Delta\beta$) as a function of the OAM of the drivers.

Then we show how to take advantage of this simple rule to select the polarization of the attosecond pulses by proper OAM combinations in the driving field.

Based on the simple diffraction model presented in the previous section, the divergence of the high-order harmonics is given by the Bessel function described in Equation B.3. The maximum of that Bessel function depends on the relation between its order, $|\ell_q|$, and its argument. Thus, for given values of r_{max} and λ_1 this dependence is reduced to the ratio $|\ell_q|/q$. Introducing the driving frequencies (ω_1, ω_2) in Equation 4.1, the ratio $|\ell_q|/q$ can be expressed as

$$\frac{|\ell_q|}{q} = \left| \frac{\omega_1}{\omega_1 + \omega_2} (\ell_1 + \ell_2) + \sigma_q \sigma_1 \frac{\ell_1 \omega_2 - \ell_2 \omega_1}{q (\omega_1 + \omega_2)} \right| \tag{B.4}$$

To calculate the divergence difference between RCP and LCP harmonics, we consider a pair of adjacent harmonics $(q-1, q)$. As explained in the main text, each one exhibits opposite circular polarization satisfying $\sigma_{q-1}\sigma_1 = 1$ and $\sigma_q \sigma_1 = -1$. Introducing this into Equation B.4 we obtain:

$$\frac{|\ell_q|}{q} = \left| \frac{\omega_1}{\omega_1 + \omega_2} (\ell_1 + \ell_2) + \frac{\ell_1 \omega_2 - \ell_2 \omega_1}{q (\omega_1 + \omega_2)} \right| \tag{B.5}$$

$$\frac{|\ell_{q-1}|}{q} = \left| \frac{\omega_1}{\omega_1 + \omega_2} (\ell_1 + \ell_2) + \frac{\ell_1 \omega_2 - \ell_2 \omega_1}{(q-1) (\omega_1 + \omega_2)} \right| . \tag{B.6}$$

Then, the divergence difference between the two adjacent harmonics, $\Delta\beta$, is proportional to the difference between these ratios:

$$\begin{aligned} \Delta\beta \propto \frac{|\ell_q|}{q} - \frac{|\ell_{q-1}|}{q-1} &= \left| \frac{\omega_1}{\omega_1 + \omega_2} (\ell_1 + \ell_2) - \frac{\ell_1 \omega_2 - \ell_2 \omega_1}{q(\omega_1 + \omega_2)} \right| - \left| \frac{\omega_1}{\omega_1 + \omega_2} (\ell_1 + \ell_2) + \frac{\ell_1 \omega_2 - \ell_2 \omega_1}{(q-1)(\omega_1 + \omega_2)} \right| \\ &= \frac{\omega_1 |\ell_1 + \ell_2|}{\omega_1 + \omega_2} \left\{ \left| 1 - \frac{\ell_1 \omega_2 - \ell_2 \omega_1}{q\omega_1 (\ell_1 + \ell_2)} \right| - \left| 1 + \frac{\ell_1 \omega_2 - \ell_2 \omega_1}{(q-1)\omega_1 (\ell_1 + \ell_2)} \right| \right\} . \end{aligned} \tag{B.7}$$

For high-order harmonics ($q \gg 1$) we can assume that $\frac{\ell_1 \omega_2 - \ell_2 \omega_1}{q\omega_a(\ell_1+\ell_2)} < 1$ and $\frac{\ell_1 \omega_2 - \ell_2 \omega_1}{(q-1)\omega_1(\ell_1+\ell_2)} > -1$, which allows us to simplify the former expression as

$$\begin{aligned} \Delta\beta \propto \frac{\omega_1 |\ell_1 + \ell_2|}{\omega_1 + \omega_2} &\left(1 - \frac{\ell_1 \omega_2 - \ell_2 \omega_1}{q\omega_1 (\ell_1 + \ell_2)} - 1 - \frac{\ell_1 \omega_2 - \ell_2 \omega_1}{(q-1)\omega_1 (\ell_1 + \ell_2)} \right) \\ &= \frac{1}{\omega_1 + \omega_2} \frac{|\ell_1 + \ell_2|}{\ell_1 + \ell_2} \frac{\ell_2 \omega_1 - \ell_1 \omega_2}{q(q-1)} . \end{aligned} \tag{B.8}$$

Removing the constant factor depending on the harmonic order we obtain the following simplified equation

$$\Delta\beta \propto \frac{\ell_2 \omega_1 - \ell_1 \omega_2}{\omega_1 + \omega_2} \omega_1 + \omega_2 \frac{|\ell_1 + \ell_2|}{\ell_1 + \ell_2} \tag{B.9}$$

which is the generalized version of Equation 4.2 including the explicit dependence on ω_1 and ω_2. This rule allows us to predict the polarization of the harmonics for any combination of OAM and frequency of the drivers in bicircular SAM-OAM HHG.

In Fig. B.3 we show the comparison of Equation B.9 (panel a) against the results obtained with the simple diffraction model (panel b) for a wide range of OAM combinations. We have chosen the nearly the same frequencies used in the main text (λ_1=800 nm, λ_2=400 nm). Although we cannot retrieve a quantitative value of $\Delta\beta$ directly from Equation B.9, its dependence with the OAM is in excellent agreement with that obtained with the diffraction model, allowing us to select the attosecond pulse polarization through the OAM of the drivers. The lighter regions in panels B.3a and B.3b reflect the OAM combinations that provide higher $\Delta\beta$, leading to spatial separation of the EUV vortices, and thus pure circularly polarized attosecond pulses. For example, in panels Fig. B.3cV and B.3cVI with OAM combinations ($\ell_1 = -2$, $\ell_2 = 4$) and ($\ell_1 = -4$, $\ell_2 = 2$) respectively, RCP and LCP harmonics are widely separated and thus the attosecond pulse ellipticity varies from left-circular to right-circular along the divergence dimension. On the other hand, darker regions in panels a and b reflect the OAM combination with lower $|\Delta\beta|$ and thus higher overlap between RCP and LCP harmonics, leading to linearly polarized attosecond pulses. For instance, this can be observed in panel Fig. B.3cIII ($\ell_1 = 1$, $\ell_2 = -1$). The remaining OAM combinations considered in this work are shown in Fig. B.3c.

Regarding the analysis performed in Fig. B.3, we now study separately one of most interesting cases to produce pure circularly polarized attosecond pulses, ($\ell_1 = -2$, $\ell_2 = 4$), for which the simple diffraction model predicts that RCP and LCP harmonics are widely separated (Fig. B.3cV). In Fig. B.4 we present the results obtained through the full quantum SFA simulations. First, we observe an excellent agreement with the simple diffraction model. Note that the secondary orders that are present in the simple diffraction model (Fig. B.3cV) disappear in the full simulation due to the contributions beyond the ring of maximum intensity. In Fig. B.4a we show the divergence of RCP and LCP harmonics and the resulting attosecond ellipticity for this particular case, while in Fig. B.4b-c we present the spatial evolution of the attosecond pulses detected at two different divergence angles (2.7 mrad and 4.7 mrad, respectively). Whereas the combination presented in Fig. 4.6 of the Chapter 4 ($\ell_1 = -2$, $\ell_2 = 1$) resulted in a train of pulses with almost pure circular polarization

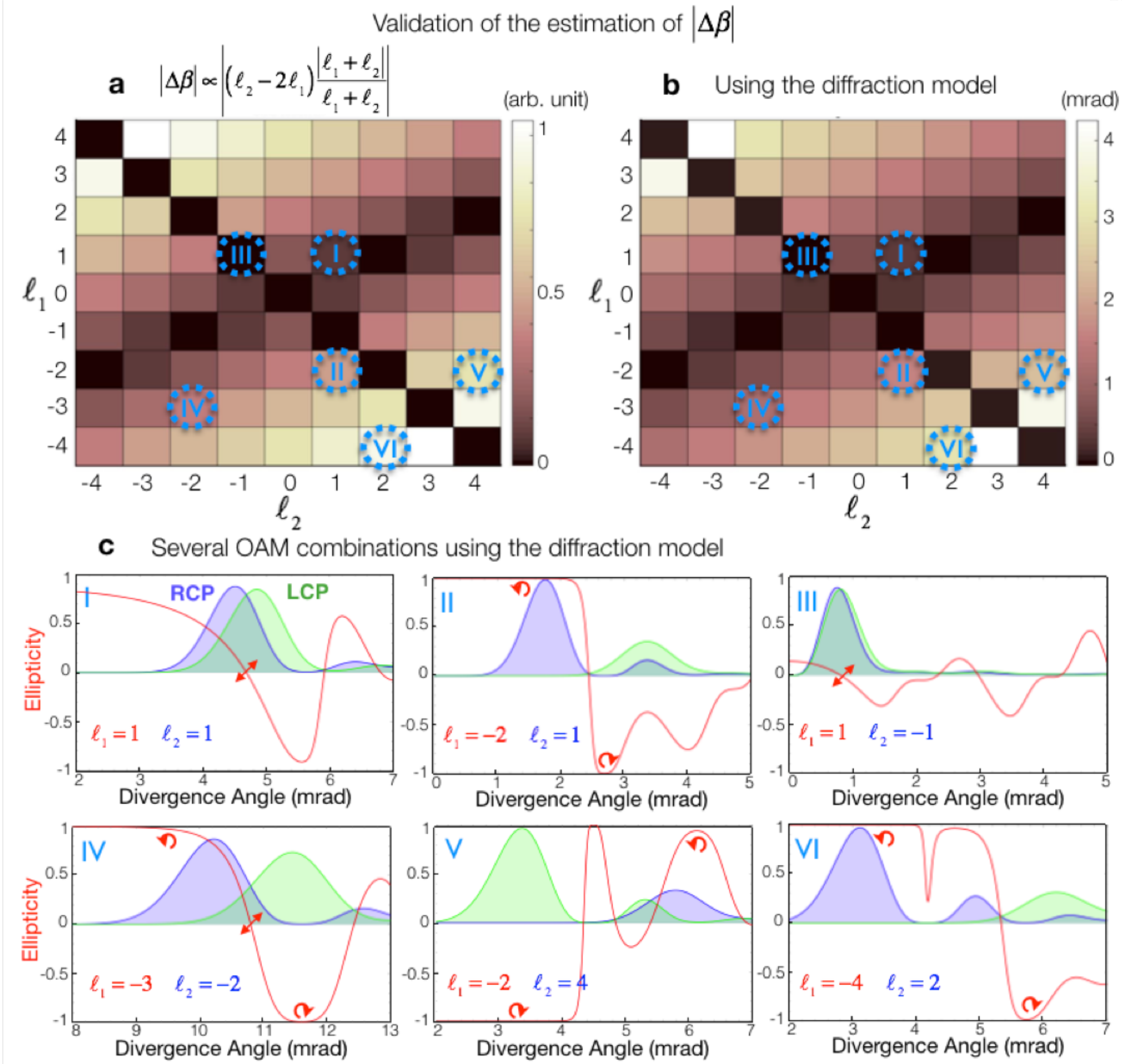

Figure B.3: **Attosecond pulse ellipticity as a function of the divergence difference between RCP and LCP harmonics ($|\Delta\beta|$).** We show the dependence of $|\Delta\beta|$ with the OAM of the drivers resulting from **a**, Equation B.9 and **b**, the simple diffraction model. In **c** we present some examples of different combinations of OAM to illustrate how we can predict the attosecond pulse polarization. We show the far-field profile of the spectrally integrated RCP (blue) and LCP (green) harmonic vortices and the resulting pulse ellipticity, ϵ (red), using the simple diffraction model. Note that panels c*I-III* correspond to the experimental configurations presented in the main text. Adapted with permission from Ref. 2. ©2018 Nature Publishing Group

($\epsilon \approx \pm 0.97$), here we show that it is also possible to obtain a train of purely circularly polarized attosecond pulses ($\epsilon = -1$, Fig. B.4b). Moreover, in this configuration, the ellipticity remains constant along a wider divergence range. As an added bonus, this combination is experimentally more favorable, as the mode sizes of the two beams are nearly perfectly matched with a single focusing lens, owing to the naturally smaller waist size of the ω_2 driver. Finally, we note that the mechanism resulting in the separation of RCP and LCP harmonics works at the single-atom level, thus this scheme is entirely compatible with quasi-phase matching or helicity selective phase matching schemes to increase the brightness and cut-off of the high-harmonics [184, 302].

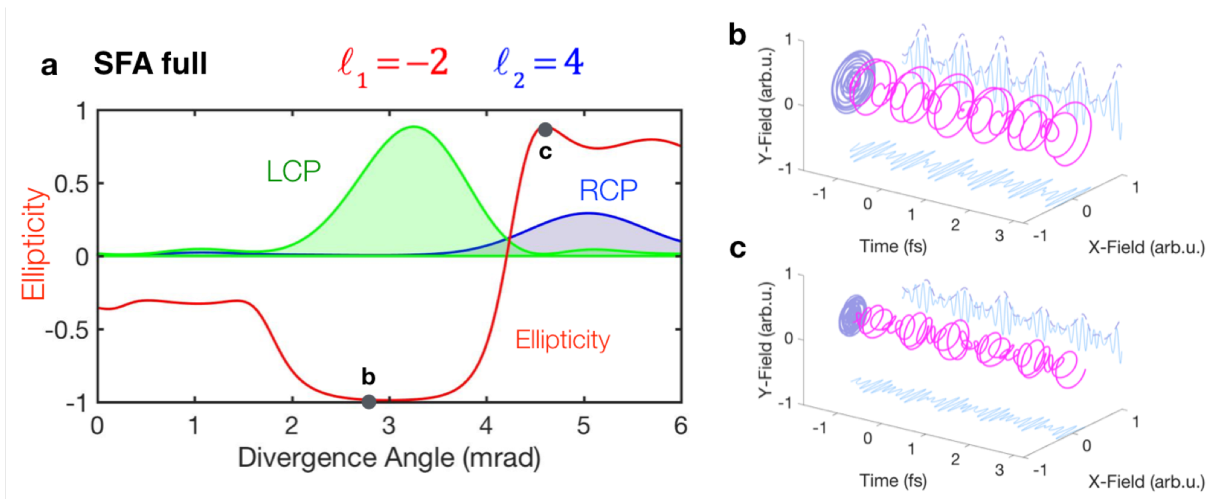

Figure B.4: **Obtaining pure, circularly polarized attosecond pulses via SAM-OAM HHG.** In panel **a**, we show the spectrally integrated harmonic signal along the divergence dimension using the fully quantum SFA simulations for the case of ($\ell_1 = -2$, $\ell_2 = 4$). The wide separation between RCP (blue) and LCP (green) harmonics allows us to obtain attosecond pulses with pure circular polarization, as depicted by the ellipticity (red line). In panels **b**, and **c**, we present the temporal evolution of the attosecond pulses detected at 2.7 mrad and 4.7 mrad, respectively. Adapted with permission from Ref. 2. ©2018 Nature Publishing Group

Appendix C

Appendix: Attosecond Optical Rotors: Self-Torqued Extreme Ultraviolet Beams with Time Varying Orbital Angular Momentum

This chapter is adapted, with permission, from:

- L. Rego, K. M. Dorney, N. J. Brooks, Q. Nguyen, C.-T. Liao, J. S. Román, D. E. Couch, A. Liu, E. Pisanty, M. Lewenstein, L. Plaja, H. C. Kapteyn, M. M. Murnane, and C. Hernández-García. Light with a self-torque: extreme-ultraviolet beams with time-varying orbital angular momentum, 1–24. arXiv: `1901.10942`

C.1 Chapter Overview

This Appendix provides additional information regarding the first realization of optical self-torque, as described in Chapter 5. Section C.2 provides a rigorous theoretical derivation of the self-torque of light, assuming a highly non-linear and non-generation process. It is important to evidence the difference between self-torqued OAM beams and time-delayed OAM beams, and Section C.3 comes to save the day. Additional experimental tidbits are given in Sections C.4-C.8; Section C.4 gives a general layout of the experiment and measurement of optical self-torque in the EUV, while Section C.5 provides a high-resolution characterization of the visible driving beams via a GS phase-retrieval algorithm. The physics of dual-vortex beams is critical to measuring the self-torque, and this is delved into in Section C.6. Some simple geometry to extract the azimuthal extent of the self-torqued high-harmonic beam is presented in Section C.7, and we finally wrap things up with control measurements of HHG spectra with single mode drivers (Section C.8).

C.2 Derivation of the Theoretical Equation for the Self-Torque of Light

The physical nature of the self-torque imprinted into EUV beams can be understood through the conservation of OAM during the HHG process. To begin, we consider HHG driven by two time-delayed, linearly polarized, IR vortex beams with different OAM, ℓ_1 and ℓ_2, such that $|\ell_1 - \ell_2| = 1$. In order to extract the OAM contributions, we follow a similar derivation as performed in the Supplementary Information of Ref. [171]. In contrast to the analysis performed in Ref. [171], in this work the weight of the two drivers is not the same, but instead varies in time.

Let us consider the total driving field as the superposition of two OAM pulses with complex amplitudes $U_1(\rho, \phi, t)$ and $U_2(\rho, \phi, t)$, expressed in cylindrical coordinates (ρ, ϕ, z). For non-zero angular momenta, these fields have a ring-shaped amplitude profile. We consider the beams such that the rings of maximal intensity overlap (i.e., those of the same radius) in the gas target, located at the focus position ($z = 0$). Since the harmonic conversion efficiency is optimal along the intensity ring, we describe the total amplitude in the radius of maximal intensity as

$$U(\phi, t) = U_1(t)e^{i\ell_1\phi} + U_2(t)e^{i\ell_2\phi}. \tag{C.1}$$

Defining $U_0(t) = U_1(t) + U_2(t)$ as the combined amplitude of the two drivers, and the relative amplitude for the second driving pulse is given by $\eta(t) = U_2(t)/U_0(t)$. Therefore, we can write the resulting field at the target as

$$\begin{gathered} U(\phi, t) = U_0(t)\left[(1-\eta)e^{i\ell_1\phi} + \eta e^{i\ell_2\phi}\right] = \\ U_0(t)e^{i(\ell_1-\ell_2)\phi/2}\left[\cos\frac{(\ell_1-\ell_2)\,\phi}{2} + i\left(1 - 2\eta(t)\sin\frac{(\ell_1-\ell_2)\,\phi}{2}\right)\right]. \end{gathered} \tag{C.2}$$

For simplicity in notation, we will drop the time variable in the following derivations. We can now factorize $U(\phi) = |U(\phi)|e^{i\varphi(\phi)}$, where the intensity and phase are given by,

$$|U(\phi)|^2 = |U_0|^2\left\{[1-2\eta]^2 + 4\eta[1-\eta]\cos^2\frac{(\ell_1-\ell_2)\,\phi}{2}\right\} \tag{C.3}$$

$$\varphi(\phi) = \arctan\left\{[1-2\eta]\tan\frac{(\ell_1-\ell_2)\,\phi}{2}\right\} + \frac{(\ell_1-\ell_2)}{2}\phi. \tag{C.4}$$

The phase term in can be approximated via the following,

$$\begin{aligned} \varphi(\phi) &\approx [1-2\eta]\frac{(\ell_1-\ell_2)\,\phi}{2}\phi + \frac{(\ell_1+\ell_2)\,\phi}{2}\phi \\ &= \{[1-\eta]\ell_1 + \eta\ell_2\}\,\phi. \end{aligned} \tag{C.5}$$

In order to calculate the q^{th}-order harmonic field we follow the familiar SFA model [171, 303], where the q^{th}-order harmonic amplitude scales with the amplitude of the driver with an exponent $p < q$ (we take $p = 4$ for the plateau harmonics, driven in Ar by 800 nm laser pulses, as shown in the Supplemental Information of Ref. [171]). On the other hand, the phase of the q^{th}-order harmonic corresponds to q times the phase of the driving field, plus the intrinsic phase [171, 303]. Neglecting the latter—as it gives rise to secondary OAM contributions of nearly an order of magnitude weaker [171]—the q^{th}-order harmonic amplitude, $A_q(\phi)$, can be written as

$$A_q(\phi) \propto |U(\phi)|^p e^{iq\varphi(\rho,\phi)} = \left|U(\phi)e^{i(q-p)\varphi(\phi)}\right|^p e^{i(q-p)\varphi(\phi)} = U^p(\phi)e^{i(q-p)\varphi(\phi)}. \tag{C.6}$$

Inserting the form of the driving field given by Equation C.2, we arrive at the following,

$$\begin{aligned} A_q(\phi) \propto U_0^p \left[(1-\bar{\eta})e^{i\ell_1\phi} + ^{i\ell_2\phi}\right]^p e^{i(q-p)\varphi(\phi)} \\ = U_0^p \left[\sum_{r=0}^{p} \binom{p}{r} (1-\bar{\eta})^r e^{ir\ell_1\phi}\bar{\eta}^{(p-r)}e^{i(p-r)\ell_2\phi}\right] e^{i(q-p)\varphi(\phi)}, \end{aligned} \tag{C.7}$$

where r is an integer. Finally, using Equation C.5 and writing explicitly the temporal dependence, the q^{th}-order harmonic is given by

$$\begin{aligned} A_q(\phi,t) \propto U_0^p(t) \left[\sum_{r=0}^{p} \binom{p}{r} (1-\bar{\eta})^r e^{ir\ell_1\phi}\bar{\eta}^{(p-r)}e^{i(p-r)\ell_2\phi}\right] \\ \times e^{i(q-p)[(1-\eta(t))\ell_1+\eta(t)\ell_2]\phi}, \end{aligned} \tag{C.8}$$

where $\bar{\eta}(t)$ is the average of $\eta(t)$ over the time it takes the ionized electron to complete the rescattering trajectory that contributes to the generation of a particular harmonic. We have considered the so-called short trajectories, whose excursion time can be approximated to a half cycle of the driving laser. On the right side of Equation C.8 we can identify two terms that contain azimuthally dependent phase terms, and thus contribute to the OAM content: the sum over r, and the last exponential term. This latter term has an explicit OAM contribution while the OAM of the sum over r is more involved.

Each term in the sum over r in Equation C.8 has a definite angular momentum $r\ell_1 + (p-r)\ell_2$. Therefore, the sum corresponds to the combination of these angular momentum contributions according to a binomial statistical distribution with probabilities $P_{\ell_1} = 1 - \bar{\eta}(t)$ and $P_{\ell_2} = \bar{\eta}(t)$. The mean angular momentum of the sum over r, thus, corresponds to

$$\begin{aligned}\langle \ell_q(t)\rangle &= \sum_{r=0}^{p} \binom{p}{r} P_{\ell_1}^{r} P_{\ell_2}^{(p-r)} \left[r\ell_1 + (p-r)\ell_2 \right] \\ &= (\ell_1 - \ell_2) \sum_{r=0}^{p} \binom{p}{r} P_{\ell_1}^{r} P_{\ell_2}^{(p-r)r} + p\ell_2 \sum_{r=0}^{p} \binom{p}{r} P_{\ell_1}^{r} P_{\ell_2}^{(p-r)}.\end{aligned} \tag{C.9}$$

Taking into account that $\sum_{r=0}^{p} \binom{p}{r} P_{\ell_1}^{r} P_{\ell_2}^{(p-r)} = 1$, and that $\sum_{r=0}^{p} \binom{p}{r} P_{\ell_1}^{r} P_{\ell_2}^{(p-r)r} = pP_{\ell_1}$, we can extract the mean OAM of this sum as

$$\langle \ell_q(t)\rangle = \sum_{r=0}^{p} \binom{p}{r} P_{\ell_1}^{r} P_{\ell_2}^{(p-r)} \left[r\ell_1 + (p-r)\ell_2 \right] = p \left\{ \left[1 - \bar{\eta}(t)\right] \ell_1 + \bar{\eta}(t)\ell_2 \right\}. \tag{C.10}$$

As a consequence, from Equation C.8, the mean OAM of the q^{th} harmonic is given by

$$\begin{aligned}\bar{\ell}_q(t) &= \langle \ell_q(t)\rangle + (q-p)\{\left[1 - \bar{\eta}(t)\right] \ell_1 + \bar{\eta}(t)\ell_2\} \\ &= q\left[(1 - \bar{\eta}(t))\ell_1 + \bar{\eta}(t)\ell_2\right].\end{aligned} \tag{C.11}$$

The width of the OAM distribution at each instant of time can be calculated as

$$\sigma_{\ell_q} = \sqrt{\langle \ell_q^2(t)\rangle - \left[\langle \ell_q(t)\rangle\right]^2} = |\ell_2 - \ell_1| \sqrt{p\bar{\eta}(t)(1 - \bar{\eta}(t))}. \tag{C.12}$$

Note that σ_{ℓ_q} depends weakly on the harmonic order, as the parameter p remains almost constant along the non-perturbative spectral plateau. The non-perturbative nature of the HHG process reduces the number of available channels to generate the q^{th}-order harmonic from q (perturbative) to $p \approx 4$ (non-perturbative). As typically $p << q$, $\bar{\ell}_q(t)$ appears as a well-defined quantity whose relative error, $\sigma_{\ell_q}/\bar{\ell}_q$, decreases as the harmonic order increases. Thus, $\bar{\ell}_q(t)$ approaches the classical behavior, i.e. its relative uncertainty tends to 0 in the limit of large harmonic orders, resulting in well-defined intermediate OAM states. We stress that this feature results from the non-perturbative behavior of HHG ($p < q$). On the other hand, in the case of perturbative nonlinear optics, the OAM width would be much larger as compared to HHG (Equation C.12, with $p = q$). This, together with the substantially lower values of q and ℓ_q associated with perturbative processes, would yield not only a lower—but also an ill-defined—self-torque.

The inset of Fig. 5.2 in Chapter 5 already shows the excellent agreement between Equations C.11 and C.12 and the full quantum simulations. In order to show how the self-torque is imprinted for different time-delays, we present in Figure C.1 the results of our full quantum simulations for the time-dependent

OAM evolution of the 17$^{\text{th}}$ harmonic when the time-delay between the driving vortex fields ($\ell_1 = 1$ and $\ell_2 = 2$) is (a) $t_d = 2/3\tau = 6.66$ fs, (b) $t_d = 5/6\tau = 8.33$ fs, (c) $t_d = \tau = 10$ fs, and (d) $t_d = 7/6\tau = 11.66$ fs, where $\tau = 10$ fs is the pulse duration (FHWM) and the rest of the parameters are the same as in Fig. 5.2 of the Chapter 5. As indicated by the green lines, the mean OAM, $\bar{\ell}_{17}$ (solid lines) and the OAM width, $\sigma_{\ell_{17}}$ (dashed lines) faithfully follow the prediction given by Equations C.11 and C.12 at each temporal delay.

Two main observations can be obtained when looking at self-torqued beams generated using different time delays. First, the self-torque, ξ_{17}, increases with the time-delay. This is confirmed by our experiments (see Fig. 5.3 of the Chapter 5). Second, we note that although in all cases self-torqued beams are generated, when the time-delay is closer to the pulse duration ($t_d = \tau$, Fig. C.1c), the OAM trace is smoother and extends through a wider range of topological charges exhibiting similar weight, i.e., a time delay similar to the pulse duration is the optimal to generate self-torqued beams.

In Fig. C.2, we present the spatiospectral HHG distribution along the azimuthal coordinate obtained in the full quantum simulations for the same driving pulse configurations as in Figure C.1. We observe that the dependence of the self-torque with the time-delay between the driving fields and with the harmonic order is reflected in the different azimuthal frequency chirps. Moreover, the azimuthal chirp is smoother for the optimal case in which $t_d = \tau$, Fig. C.2c. The full quantum simulations are in excellent agreement with the analytical estimation of the self-torque (grey-dashed lines).

Note that although Equation 5.6 in Chapter 5 states that $\omega_q(t, \phi)$ is a continuous function for all values of ϕ, the physical quantity giving rise to the self-torque—the HHG beam itself—is not continuous over the full range of ϕ and as such the self-torque in the low intensity region is ill-defined. However, further studies on this region of “structured darkness” [279] could be beneficial for a thorough fundamental understanding of the nature of the self-torque of light. Finally, we note that the definition of ϕ, and its orientation with respect to the beam axis, is rather arbitrary, as it can only be defined when a singularity is present (however, the absolute value of ϕ subtended by the HHG beam is not arbitrary).

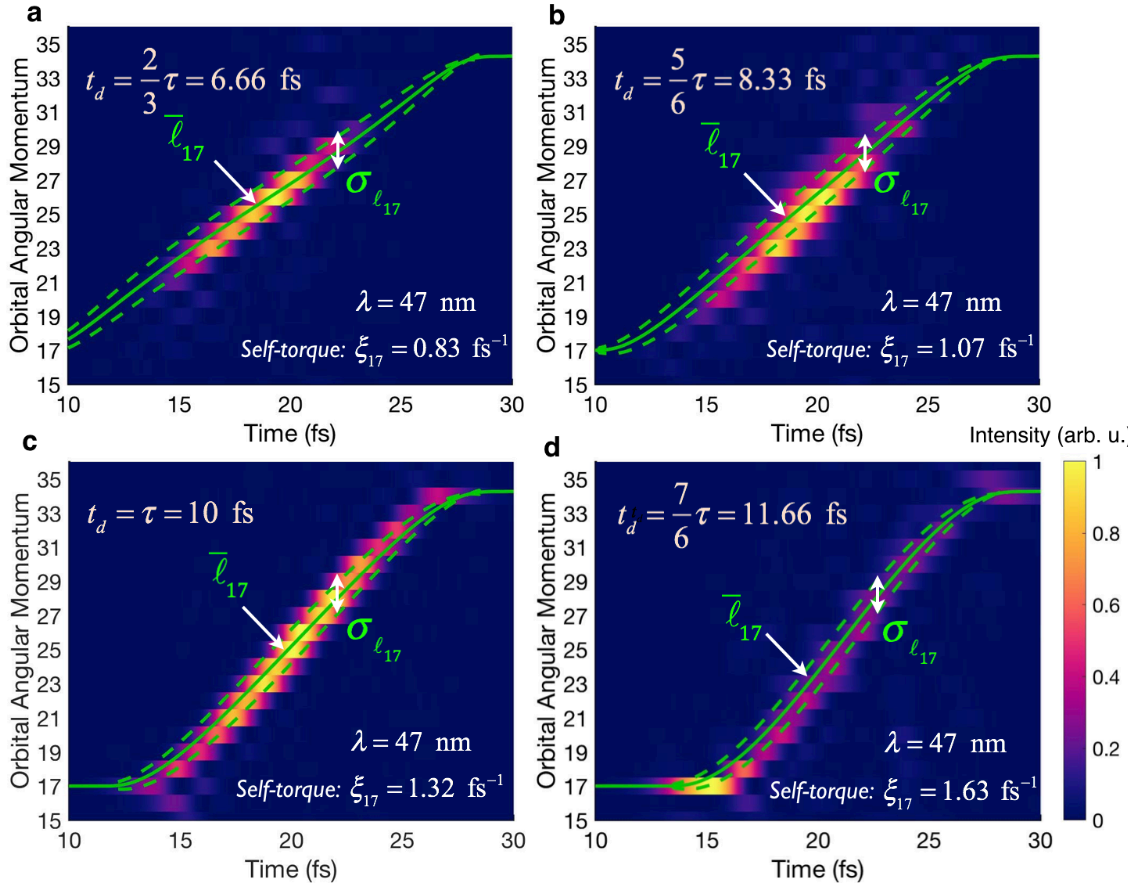

Figure C.1: **Temporal evolution of the OAM for different time delays.** Computed OAM of the 17$^{\text{th}}$ harmonic beam generated by two 800 nm driving pulses ($\ell_1 = 1$ and $\ell_2 = 2$) with duration, $\tau = 10$ fs, for different time delays: **a**, $t_d = 2/3\tau = 6.66$ fs, **b** $t_d = 5/6\tau = 8.33$ fs, **c** $t_d = \tau = 10$ fs, **d** $t_d = 7/6\tau = 11.66$ fs. The color background shows the results from the full quantum simulations, whereas the mean OAM, $\bar{\ell}_{17}$ (solid green), and the width of the OAM distribution, $\sigma_{\ell_{17}}$ (dashed-green line), are obtained from Equations C.11 and C.12. The self-torque, ξ_{17}, is obtained from the slope of the time-dependent OAM. Adapted with permission from Ref. 3.

C.3 Distinction Between Self-Torqued Beams and Time-Delayed, Mixed OAM Beams

In this section, we stress the difference between a self-torqued pulse, with OAM ranging from $q\ell_1$ and $q\ell_2$, and a pulse resulting from the mere superposition of two delayed vortex pulses, the first carrying $q\ell_1$ units of OAM and the second ℓ_2. While in both cases the mean OAM varies in time from $q\ell_1$ to $q\ell_2$, only the self-torqued beams include all the intermediate OAM contributions, thus containing physical photons of all the intermediate OAM states.

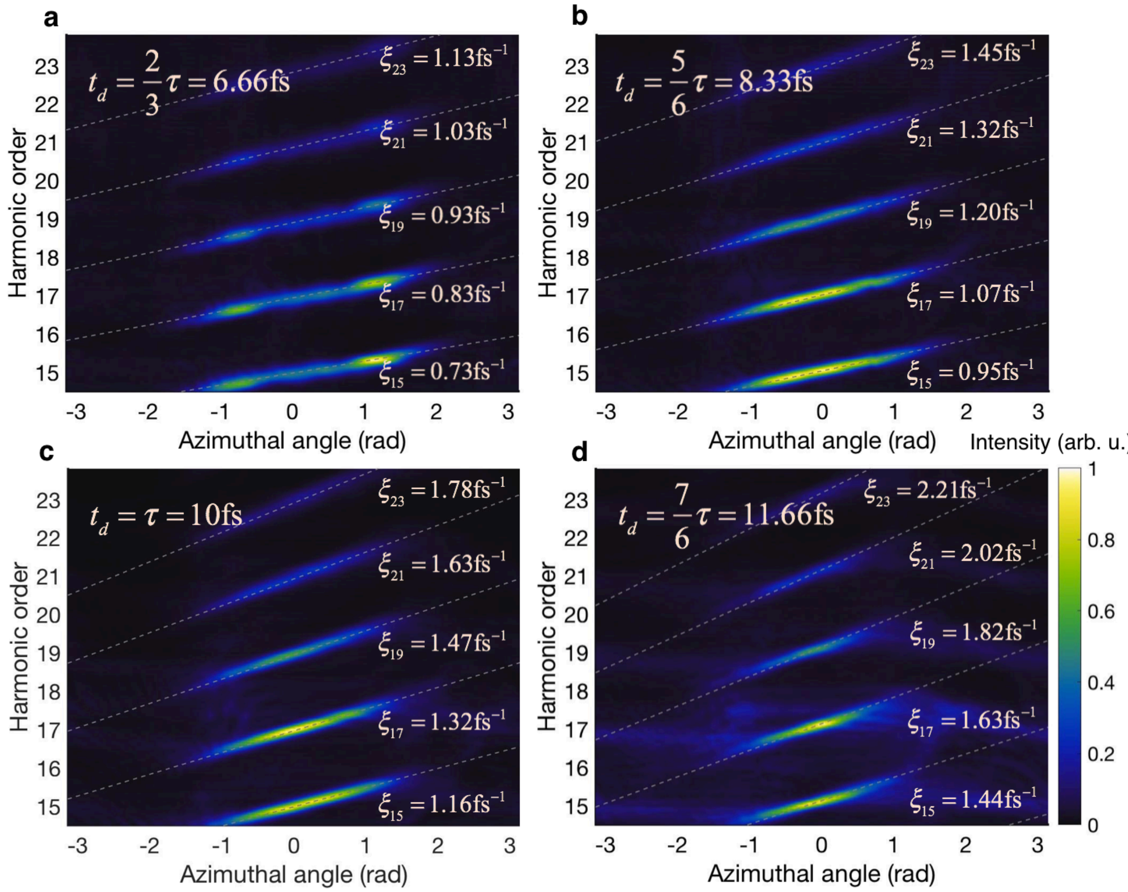

Figure C.2: **Azimuthal chirp of self-torqued beams for different time delays.** Spatial HHG spectrum along the azimuthal coordinate (ϕ) obtained from the full quantum simulations. The driving pulses, centered at 800 nm, with $\ell_1 = 1$ and $\ell_2 = 2$ and pulse duration, $\tau = 10$ fs, for different time delays: **a** $t_d = 2/3\tau = 6.66$ fs, **b** $t_d = 5/6\tau = 8.33$ fs, **c** $t_d = \tau = 10$ fs, **d** $t_d = 7/6\tau = 11.66$ fs. The self-torque of light imprints an azimuthal frequency chirp, which is different for each harmonic order, and each time-delay, as indicated by the grey dashed lines (obtained from Equation 5.6 in Chapter 5). Adapted with permission from Ref. 3.

This distinction—which is evident in the OAM spectrum—also has unequivocal signatures in the temporal evolution of the phase and intensity profiles of the beams. In order to explore this aspect, we have performed high-spatial resolution simulations of the HHG process. For this, the computational load is drastically reduced if a diffraction model is employed, instead of the exact full quantum simulation. The so-called TSM considers the HHG medium as a thin (2D) slab perpendicular to the driving laser propagation. The harmonics are calculated using the analytic SFA representation introduced in Section C.2 and propagated using Fraunhofer diffraction. The model has been proved to successfully reproduce detailed features of HHG driven by vortex beams [2, 99, 170, 171].

In Figures C.3-C.4, we present the temporal evolution of the spatial phase, intensity, and OAM profiles for the two cases under study: (top row) the self-torqued 11$^{\text{th}}$ harmonic—calculated with similar parameters as in Fig. 5.2 in Chapter 5 under the TSM; (bottom row) the mere superposition of two vortex beams carrying $\ell_i = q\ell_1 = 11$ and $\ell_f = q\ell_2 = 22$, delayed by $t_d = \tau = 10$ fs. Three instants of time of both cases are captured in Figs. C.3 and C.4, respectively.

On one hand, the spatial phase distribution of the self-torqued harmonic beam—from which one can extract the OAM content by counting the number of phase branches—shows the continuous appearance of new vortex singularities along a single row, breaking the q-fold symmetry (which resembles the phase structure of the Hilbert's Hotel paradox when applied to OAM beams [304]). This reflects the continuous variation of OAM from $q\ell_1 = 11$ to $q\ell_2 = 22$. In addition, the temporal evolution of the intensity distribution follows the structure of the combination of vortex beams with subsequent OAM charges, $\ell_i + \ell_{i+1}$, canceling out in the spatial region where the phase singularities are born (see for example Fig. C.3e), and presenting a crescent shape. Thus, a self-torqued beam can be understood as a topological structure where new vortices emerge one at a time.

On the other hand, the temporal evolution of the spatial phase and intensity distributions of the two time-delayed vortex beams remains q-fold symmetric, as the OAM content is the superposition of two components $q\ell_1$ and $q\ell_2$, with time-dependent weights. This symmetry is reflected in the spatial phase distribution, where all the new singularities appear simultaneously (see Fig. C.4d). Moreover, the spatial intensity profile exhibits two clear radial rings, instead of the crescent shape (see Fig. C.4e). The intensity profile evolves gradually from the ring shape of the vortex beam with $q\ell_1$ to that with $q\ell_2$, evidencing the absence of intermediate OAM contributions.

Our results show that there is a fundamental distinction between a field carrying ℓ OAM units—as one of the intermediate states in a self-torqued beam—, and the superposition of two modes of different topological charges, but same averaged-OAM, $\bar{\ell} = \ell$. These two kinds of beams have different essential physical properties, not only the OAM content but also the spatial phase and intensity evolutions. Thus, the intensity profile already gives an unambiguous piece of evidence for the presence of self-torque in optical beams. In particular, the crescent intensity shape measured in our experiments (Fig. 5.4h in Chapter 5 and

Figs. C.6-C.7) is a clear signature of the generation of beams with self-torque.

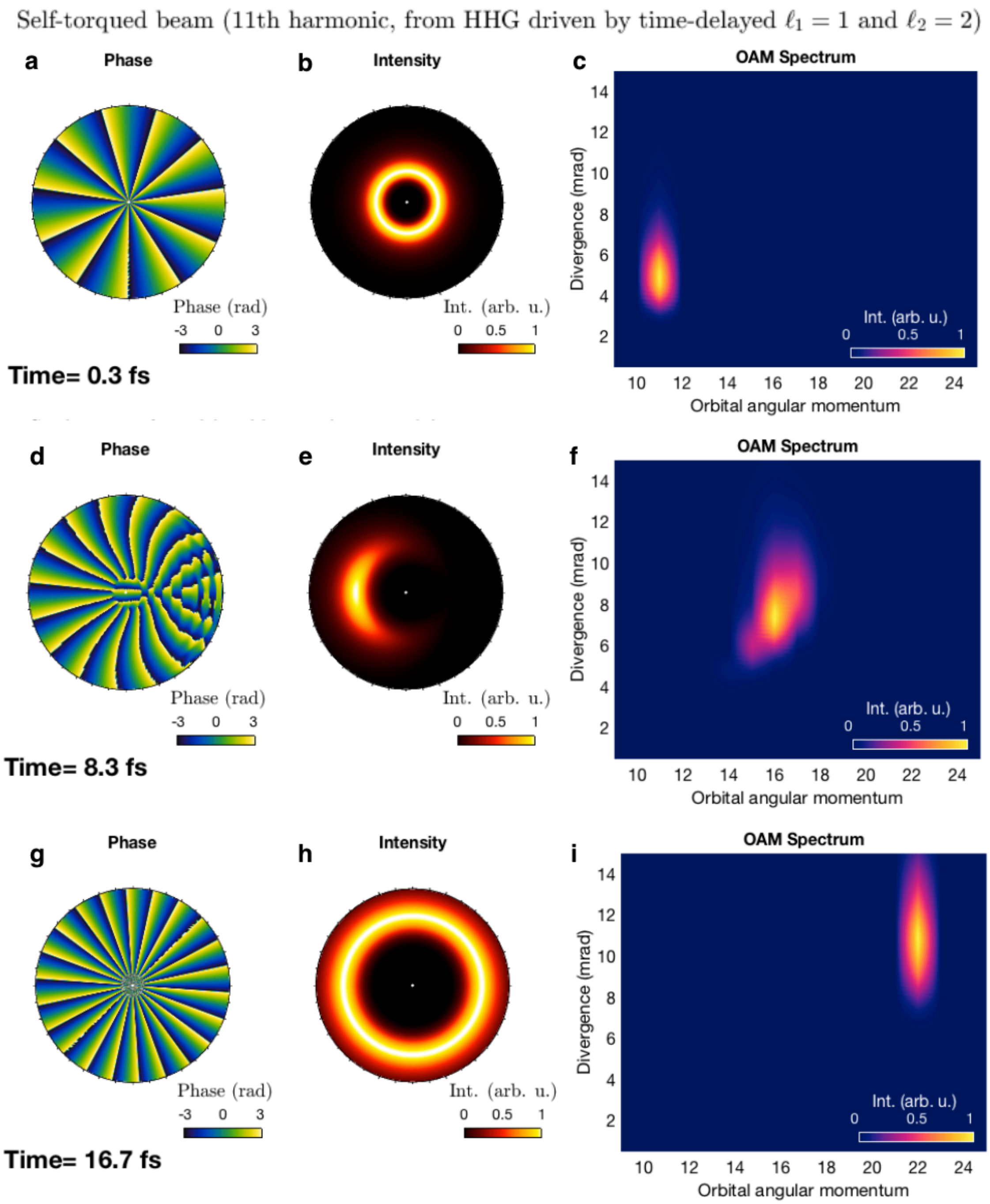

Figure C.3: **Temporal evolution of phase, intensity and OAM content of self-torqued beams.** Phase (**a**, **d**, **g**), intensity (**b**, **e**, **h**), and OAM distribution along the divergence (**c**, **f**, **i**) at three different instants of time: the initial state (**a-c**, $t = 0.3$ fs), an intermediate state (**d-f**, $t = 8.3$ fs) and the final state (**g-i**, $t = 16.7$ fs) for a self-torqued beam generated through HHG ($\ell_1 = 1$, $\ell_2 = 2$, $\tau = 10$ fs, $t_d = 10$ fs, $\lambda_1 = \lambda_2 = 800$ nm). These results have been calculated using the TSM and the panels are snapshots from the Supplemental Movie S1 in Ref. [3]. Adapted with permission from Ref. 3.

Combination of two delayed beams: $\ell_1 = 11$ and $\ell_2 = 22$

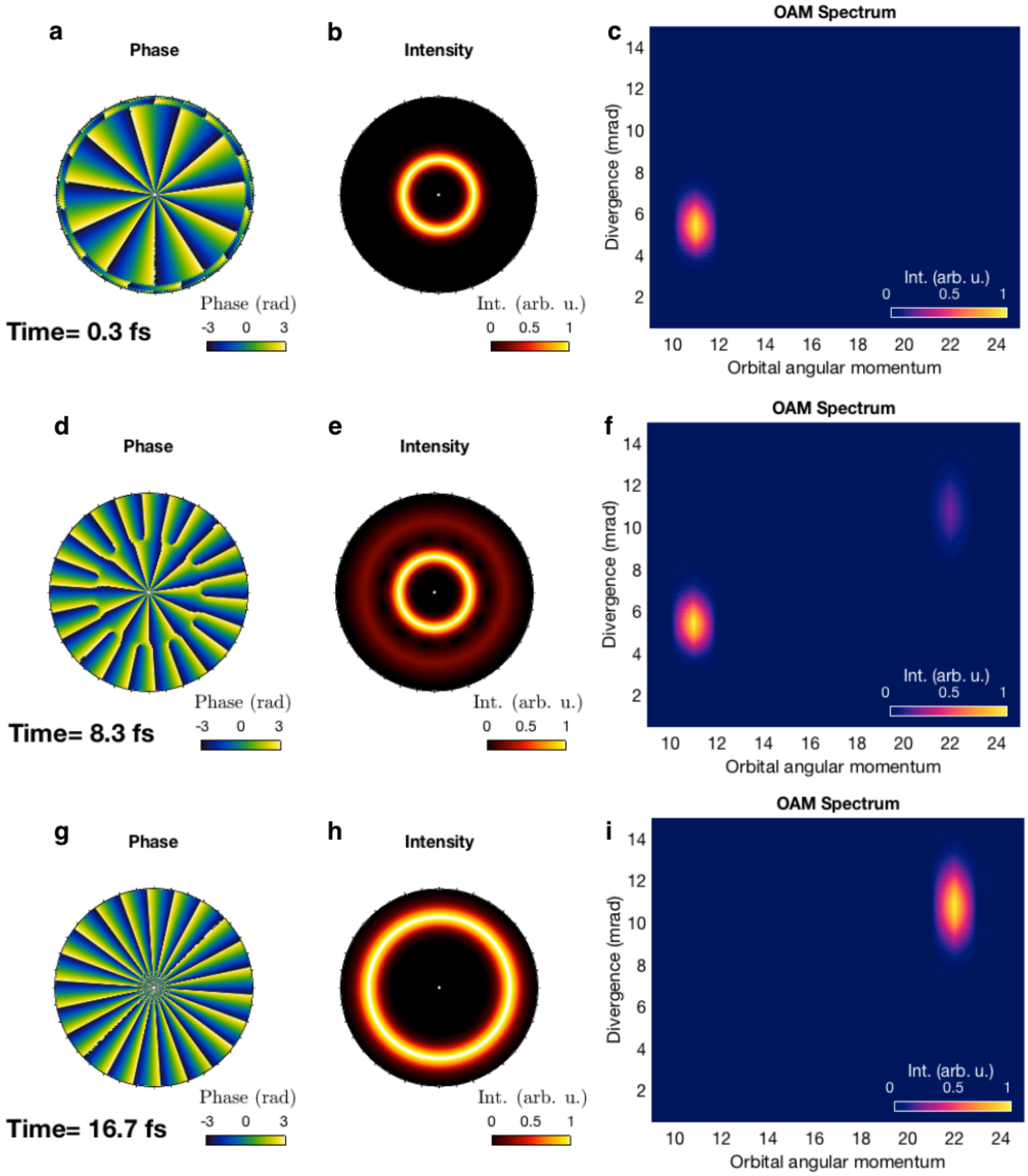

Figure C.4: **Temporal evolution of phase, intensity and OAM content of two time-delayed vortex beams.** Phase (**a**, **d**, **g**), intensity (**b**, **e**, **h**), and OAM distribution along the divergence (**c**, **f**, **i**) at three different instants of time: the initial state (**a-c**, $t = 0.3$ fs), an intermediate state (**d-f**, $t = 8.3$ fs) and the final state (**g-i**, $t = 16.7$ fs) for the combination of two time-delayed vortex beams ($\ell_1 = 11$, $\ell_2 = 22$, $\tau = 10$ fs, $t_d = 10$ fs, $\lambda_1 = \lambda_2 = 800$ nm). These panels are snapshots from the Supplemental Movie S1 in Ref. [3]. Adapted with permission from Ref. 3.

C.4 Additional Details Regarding the Experimental Setup for the Generation and Characterization of Self-Torqued EUV Beams

Self-torqued light beams are generated by driving HHG with an IR vortex driving beam comprised of a superposition of two pure OAM modes (i.e., ℓ is an integer). Essential to both the generation and subsequent detection (see below) of the self-torque of light is the use of highly pure ultrafast vortex pulses, as well as a robust and stable beamline capable of maintaining subfemtosecond timing resolution and repeatability. Moreover, we require few-micron pointing stability over a relatively large range in delay times ($\sim$ 100 fs, see Figure 5.4 in Chapter 5). These demanding criteria are realized by using a setup that employs a high-accuracy and high-precision delay stage (Newport, XPS-160S), a modified, iterative phase-retrieval algorithm to optimize and quantify the dual-vortex driving beam [196, 197], and a home-built beam pointing stabilization system [185], all of which are described in more detail below.

In order to ensure precise overlap of the single-mode OAM driving beams, and thus the synthesis of a high-quality dual-OAM driver—also known in the literature as a "fractional" OAM beam—, independent circular apertures and lenses are placed in each arm of the Mach-Zehnder interferometer (see Figure 5.1 in Chapter 5), which yield highly pure, single-mode OAM drivers with a similar intensity and waist size at focus. The quality of the driving beams, as well as their modal purity, are quantified by directing a small portion of the IR vortex beams onto a visible CCD camera (Mightex, BTE-B050-U) and recording intensity profiles as a function of propagation distance (top-left inset of Fig. 5.1 in Chapter 5). These intensity profiles are then fed into a modified GS phase-retrieval algorithm [196, 197], which reconstructs the complex, spatial amplitude of the beams with a high resolution[1] (see below).

A separate pair of visible CCD cameras is used to monitor fluctuations in beam pointing over the delay range of the experiment, and these fluctuations are minimized using a home-built beam pointing stabilization system [185]. Briefly, the beam pointing stabilization system is comprised of two piezo-actuated mirror mounts (one in the amplifier itself, one at the entrance of the interferometer, $\sim$ 4 m away), the two previously mentioned CCD cameras, and a desktop computer that closes the digital feedback loop. The

[1] This method is ideal for characterizing the wavefronts of tightly focused beams, as the resolution is determined by the camera pixel size, which in our case is 2.2 μm

leak-through of the full, amplified beam upon hitting the last mirror before the interferometer is passed through a lens, and one camera monitors the beam centroid at focus while the other measures the far-field intensity centroid of the beam. The use of two independent feedback loops allows for control of not only the transverse position of the common focus of the OAM beams, but also the propagation angle, which ensures good overlap and collinearity between the two beams. Drifts in beam pointing on the two cameras are then compensated via an active, digital feedback loop that adjusts the tip and tilt of the piezo-actuated mirrors at a rate of $\sim$ 100 Hz, ensuring that the OAM driving beams remain spatially overlapped throughout the duration of the experiment. Such a scheme yields few-micron repeatability and stability of the driving beams, with only small fluctuations occurring due to mechanical noise (e.g., thermal expansion of optomechanics, high-frequency vibrations, etc.) in the beamline.

In addition to stability and timing requirements, the nature of self-torqued EUV beams places strict demands on the quantitative measurement of the self-torque. Since measuring the subfemtosecond variation in OAM with high spatial resolution in the EUV is currently unfeasible, we instead exploit the physics of time-dependent OAM and the optics of the EUV spectrometer to measure and confirm the self-torque of light (see Fig. 5.1b in Chapter 5). Briefly, the intensity "crescent" of the HHG driving beam is aligned to the dispersion axis of the spectrometer by precise control of the phase delay between the two single-mode OAM drivers (see Section C.6 below). When the HHG intensity profile is aligned to the EUV spectrometer (i.e., the crescent is orthogonal to the focusing and dispersion axes of the spectrometer), the azimuthal frequency chirp resulting from the self-torque is naturally mapped to the dispersion axis of the HHG spectra, while preserving the azimuthal angular range in the spatial dimension (Figure 5.1b). This allows us to simultaneously measure both the self-torque-induced frequency chirp of the HHG beams and the azimuthal angular range with a high resolution. In order to preserve the HHG beam pointing, the relative group delay between the pure, IR OAM beams is advanced in steps of two complete cycles (here, $\sim$ 5.270 fs), which ensures the HHG beam profile retains constant alignment to the EUV spectrometer. The self-torque is then computed from the measured frequency shift and the azimuthal extent of the generated EUV high harmonics (see Section C.7 below). We would like to note that the use of two-cycle steps in delay is rather pragmatic; using two-cycle delays steps provides a nice convergence of high enough sampling density in time delays, while also ensuring the experiment can be completed before long term instabilities (e.g., thermal fluctuations from the building, etc.) start to take hold.

C.5 Characterization of IR Vortex Driving Modes via a Modified Gerchberg-Saxton Phase Retrieval Algorithm

Essential to both the generation and subsequent detection (see below) of the self-torque of light is the use of highly pure, ultrafast driving vortex pulses. In order to achieve highly pure OAM driving beams, a frequency-and-power degenerate, Mach-Zehnder-type interferometer is employed to enable independent control of the polarization, intensity, waist size, and OAM in each beam (see Chapter 5 for details). To assess the quality of these beams, as well as their combination, a wedge is translated into and out of the collinear focusing beams just after the exit of the interferometer, and the beam(s) are imaged onto a CCD camera (Mightex, BTE-B050-U) for modal analysis (top-left inset of Fig. 5.1). Beam profile images are recorded as a function of propagation distance, z, and then fed into a modified GS phase retrieval algorithm that is based on previous work in the literature [196, 197].

In our implementation of the GS algorithm, we first record a series of intensity images as a function of propagation distance, sampling from the focal point to at least two Rayleigh lengths, z_R, on both sides of the focus. Since only the intensity is captured by a camera, we use a phase-retrieval algorithm to extract the phase of the beam. The phase retrieval itself is over-constrained, meaning there is an optimal solution as well as additional degrees of freedom that can be used to evaluate and confirm the retrieval. In the first iteration, a uniform (i.e., flat) phase is applied to the square root of the recorded intensity in the first image, which serves as the initial guess for the complex electric field. This initial guess is numerically propagated to the plane of the next recorded image. At this plane, the amplitude of the retrieved beam is replaced by the observed amplitude, while preserving the retrieved phase. The algorithm continues to propagate the beam to each plane where an image was taken, replacing the retrieved amplitude with the observed amplitude at each plane. Once the algorithm has incorporated all the images once, the final retrieved electric field is used as the initial guess for the next iteration. This entire process is repeated for up to 1,000 iterations, until the error between the retrieved and measured amplitudes reaches a global minimum. In order to ensure that the algorithm finds the correct OAM content without stalling in a local minimum, we apply an azimuthal phase perturbation of $\ell = \pm 1/2$ every 10 iterations (alternating the sign for each perturbation), for the first 100 iterations. These perturbations do not affect the retrieval of a Gaussian beam ($\ell = 0$), but greatly reduce the number of iterations needed to converge the retrieval for OAM beams. This algorithm correctly retrieved the phase of simulated data of a variety of superpositions of $\ell = \{0, 1, 2\}$ and the radial index $p = \{0, 1\}$ with and without random noise applied. Using this approach, we can reconstruct the complete complex amplitude of the vortex beams as a function of propagation distance (see Supplemental Movie S2 of Ref. [3]) in under 5 minutes on a personal laptop computer (MacBook Pro, Intel Core i7, 16 GBs RAM), with a resolution limited only by the CCD pixel size (in this case, 2.2 μm).

The intensity recorded by the CCD camera as a function of propagation distance, z, near the focus of each driving beam corresponds to the squared amplitude of an LG laser beam with wavelength λ_0,($k_0 = 2\pi/\lambda_0$),

$$\begin{aligned} LG_{\ell,p}\left(\rho,\phi,z;k_0\right) = E_0 \frac{w_0}{w(z)} \left(\frac{\sqrt{2}\rho}{w(z)}\right)^{|\ell|} L_p^{|\ell|}\left(\frac{2\rho^2}{w^2(z)}\right) \\ \times e^{\left[-\frac{\rho^2}{w^2(z)}\right]} e^{\left[i\ell\phi + i\frac{k_0\rho^2}{2R(z)} + i\Phi_G(z)\right]}. \end{aligned} \tag{C.13}$$

Here, $w(z) = w_0\sqrt{1 + (z/z_R)^2}$ is the beam waist, with w_0 being the beam waist at focus and $z_R = \pi w_0^2/\lambda_0$ is the Rayleigh range with wavelength λ_0,($k_0 = 2\pi/\lambda_0$), $R(z) = z\left[1 + (z_R/z)^2\right]$ is the phase-front radius, $\Phi_G(z) = -(2p + |\ell| + 1)\arctan\left(z/z_R\right)$ is the Gouy phase, and $L_p^{|\ell|}(x)$ are the associated Laguerre polynomials [70]. The indices $\ell = 0, \pm 1, \pm 2, ...$ and $p = 0, 1, 2, ...$ correspond to the topological charge and the number of nonaxial radial nodes of the mode, respectively. In experiments, Equation C.13 does not strictly apply and real LG beams are described by a summation of LG modes with a common waist size, but varying mode indices. As such, the purity of an OAM beam is quantified by the power of the desired topological charge divided the power of the entire OAM spectrum of the beam (note that the same is true of any beam possessing azimuthally varying phase, e.g., hypergeometric gaussian beams [305]). In order to obtain the OAM spectrum, we perform a Fourier transform over the azimuthal coordinate of the reconstructed complex amplitude of the driving beams (Figure C.6a-c), which is more general and efficient than modal decomposition algorithms [171, 306]. The resulting OAM spectra show that highly pure vortex driving modes with little radial mode character are obtained for the ℓ_1 and ℓ_2 drivers, leading to a high quality, dual-OAM vortex beam for driving the HHG process (Figure C.5d-f). Overall, we find that 95% (93%) of the total power in the ℓ_1 (ℓ_2) driver is contained within the $\ell = 1(2)$ mode (Figure C.5g-i). We note that the GS algorithm is ambiguous with respect to the absolute sign of ℓ; however, the relative sign between the two beams not ambiguous. For this work, ℓ_1 and ℓ_2 have the same sign, which is confirmed to be positive via an independent measurement of the OAM sign by using a cylindrical lens as 1D Fourier transform element [298]. Finally, the reconstructed beams can be propagated arbitrarily in space, which allows us to inspect the beam quality both before and after the focus (see Supplemental Movie S2 of Ref. [3]).

C.6 Control of IR and HHG Beam Pointing with a Time-Delayed Combination of Vortex Driving Beams

The quantitative measurement of the self-torque of the experimentally generated EUV beams requires a high precision measurement of either the induced azimuthal frequency chirp, or the ultrafast variation of OAM on the subfemtosecond time scale. Since the latter is currently unfeasible with existing technologies, the azimuthal frequency chirp is instead measured by exploiting both the physics of time-dependent OAM and the optics of the EUV spectrometer system. However, such a scheme demands few-micron spatial control of the HHG beam pointing, which we achieve by exploiting the optics of multicomponent OAM beams.

Vortex beams comprised of the superposition of two (or more) LG beams with differing topological charges exhibit exotic amplitude and phase distributions that can be controlled by either the phase delay between the constituent waveforms, or the topological charge in each beam [70]. In the experiment, the HHG driving vortex beam is synthesized from two ultrafast pulses with topological charges of $\ell_1 = 1$ and $\ell_2 = 2$ —as well as equal amplitudes and waist sizes—, which results in a non-pure vortex beam with a characteristic "crescent" shape to the intensity distribution (see Figure C.6a, also Figure C.5a-c). The angular direction of the center-of-mass (CoM) of the intensity crescent can be controlled via a relative phase delay between the two single-mode OAM drivers, such that a full-cycle phase delay (e.g., 2.635 fs for the 790 nm pulses in the experiment) returns the intensity crescent to its initial position. By carefully adjusting the time delay between the two single-mode IR vortex beams, we can control the alignment of the driving

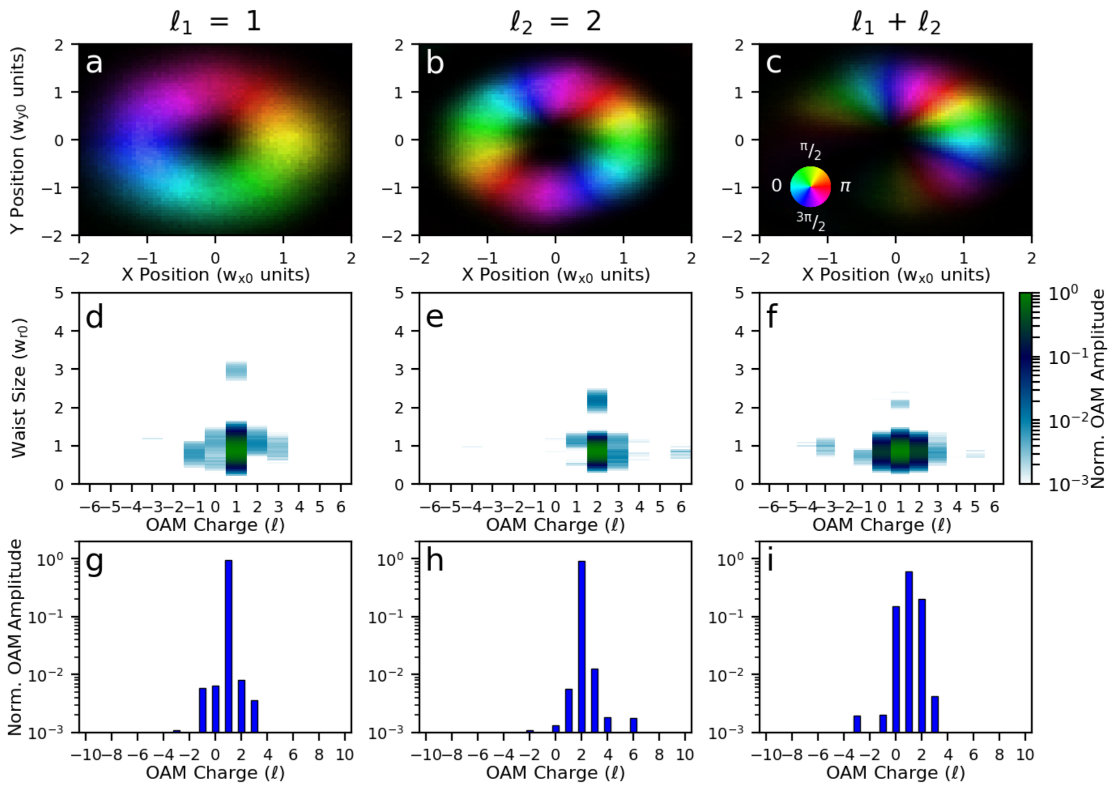

Figure C.5: **Experimental characterization of pure and non-pure IR Vortex Beams.** The GS algorithm reconstructs the complex amplitudes of the ℓ_1 and ℓ_2 driving beams, and the combined HHG driver, with a high resolution and accuracy. **a-c**, The reconstructed wavefronts of the IR vortex beams show that each constituent waveform is comprised of an integer number of phase wraps across a uniform intensity ring, while the OAM-combined HHG driver manifests as an intensity "crescent" with a non-integer number of phase wraps. In **a-c**, amplitude is represented as saturation and value (i.e., brightness), and phase is represented by color (i.e., hue), with the corresponding phase values indicated by the color wheel in **c**. **d-f**, The radial OAM spectrum obtained via an azimuthal Fourier transform of the complex amplitudes in **a-c** show that all beams possess little radial mode character, with nearly all of the OAM content being contained within the primary intensity ring. **g-i**, The radially integrated OAM spectra confirm the high purity of the experimental OAM beams, showing a modal purity of 95% and 93% for the ℓ_1 and ℓ_2 drivers, respectively. Adapted with permission from Ref. 3.

intensity crescent with few-micron precision (Figure C.6b, limited by the 2.2 μm pixel size of the visible CCD camera). Since, to first order, the HHG beam profile mimics the intensity distribution of the driving beams, we can simultaneously and precisely align the HHG intensity crescent (Figure C.6c) to the dispersion axis of the spectrometer, which naturally maps the azimuthal frequency variation to the spectral dimension of the dispersed HHG spectra. This naturally yields a high-resolution measurement of both the azimuthal extent of the beam, as well as the self-torque-induced azimuthal frequency variation, without the need for measuring the subfemtosecond variation of the azimuthal phase in the EUV.

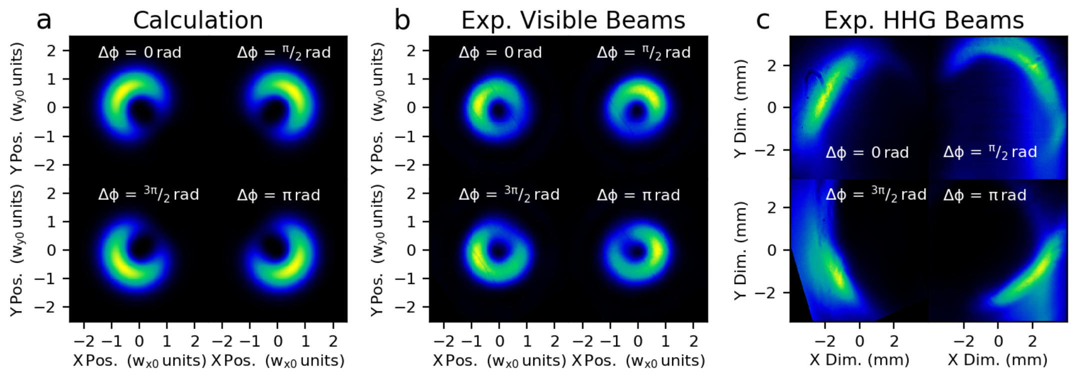

Figure C.6: **Control of IR and HHG beam alignment via the relative phase delay of the single-mode OAM driving beams.** **a**, When single-mode OAM beams with topological charges of $\ell_1 = 1$ and $\ell_2 = 2$ are superposed with the same amplitude and waist size, a "crescent"-shaped intensity distribution is obtained with a directionality determined by the relative phase delay between the two beams. **b**, In the experiment, the relative time delay between the two beams is used to control the phase delay (and thus, the CoM position of the visible beam) with attosecond and few-micron precision. **c**, The control over the visible beams translates directly to the HHG beams, allowing for precise alignment of the HHG crescent to the dispersion axis of the spectrometer. In the lower left of panel **c**, the HHG beam is partially clipped by the filter housing before the EUV CCD camera. Adapted with permission from Ref. 3.

C.7 Extraction of the Azimuthal Angle Subtended by the Self-Torqued EUV HHG Beams

In order to extract the azimuthal angle of the HHG beam, we measure the raw HHG beam profile at the flat-field-image plane of the spectrometer with a high-pixel-density EUV CCD camera (Andor, Newton 940). The HHG intensity crescent subtends a small arc of a uniform circle—the center of which occurs at the common singularity of the OAM harmonics generated by the individual ℓ_1 and ℓ_2 drivers—and we use the properties of a uniform circle to extract the azimuthal angle.

For a uniform circle of radius, r, the chord length, a, between the two extrema of a circular section (i.e., arc) is given by $a = 2r\sin(\phi/2)$, where ϕ is the central angle of the arc and, in this case, the azimuthal angle subtended by the HHG beam (Figure C.7a). By measuring the radius of the inscribed circle and the length of the chord between the e^{-4} intensity points of the beam, we can extract both the chord length and radius of the high-order harmonic beam. Then, using the known relation for the chord length as a function of radius and central (i.e., azimuthal) angle, we can extract the full azimuthal angular range of the high-order harmonics (Figure C.7b).

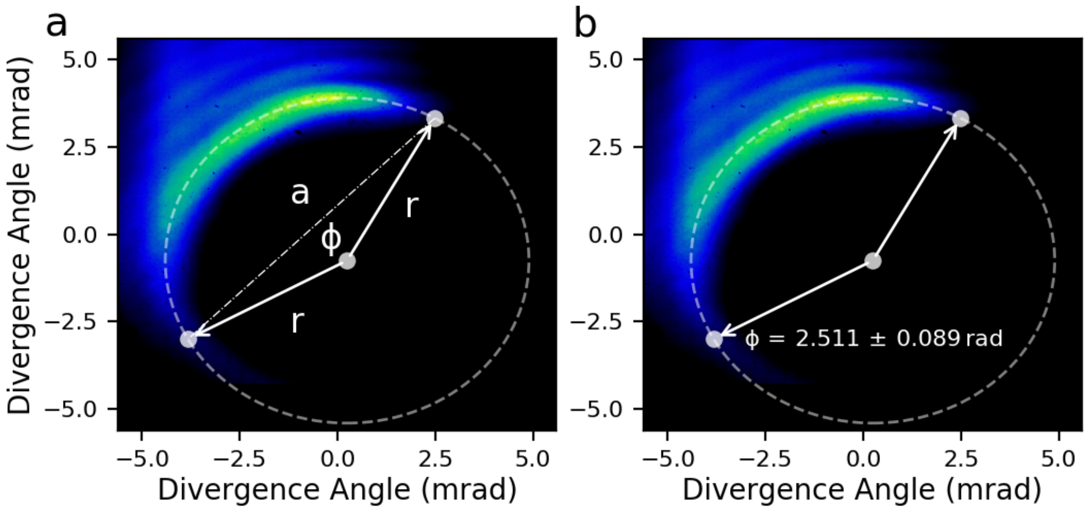

Figure C.7: **Extraction of the azimuthal angular range of self-torque EUV high-order harmonics.** **a**, The HHG beam profile subtends a circular section (i.e., arc) of a uniform circle defined by a central (i.e., azimuthal) angle, ϕ, and the e^{-4} intensity points of this arc define a chord length, a. **b**, Using the equations relating r, a, and ϕ for a uniform circle, we can extract the azimuthal angle of the HHG beam with a high precision. Note that the center of this circle occurs at the common singularity of the OAM harmonics generated from the individual drivers. Adapted with permission from Ref. 3.

C.8 Comparison of HHG Driven with Pure and Non-Pure Driving Beams

Measurement of the self-torque of EUV beams relies on extracting both the azimuthal angle subtended by the HHG beam and the spectral shift of each harmonic in the HHG spectrum, at each time delay. In order to validate that the spectral shift arises from the self-torque and not an artifact of the imaging conditions of EUV spectrometer or dynamics of the HHG up-conversion process, we present in Figures C.8a and C.8b the HHG spectra obtained at a delay where the self-torque is maximized, and at near-zero delay, respectively. Clearly, the azimuthal frequency shift is only observed when the pulses are delayed by a sufficient amount. As a further verification of the self-torque-induced azimuthal frequency chirp, we also drove HHG with the single-mode OAM beams comprising the dual-OAM driving vortex beam. Taken together, the dispersed harmonic spectra (Figures C.8a-d) show that the azimuthal spectral shift of the high-order harmonics is only found when driving the up-conversion process with a time-delayed, dual-vortex mode. Moreover, the single mode spectra (Figs. C.8c-d and Figs. C.8g-h) show that the observed spectral shifts are not the result of over-driving the HHG process, as similar cutoffs and azimuthal ranges are obtained for the self-torqued HHG beams (Figs. C.8a-b).

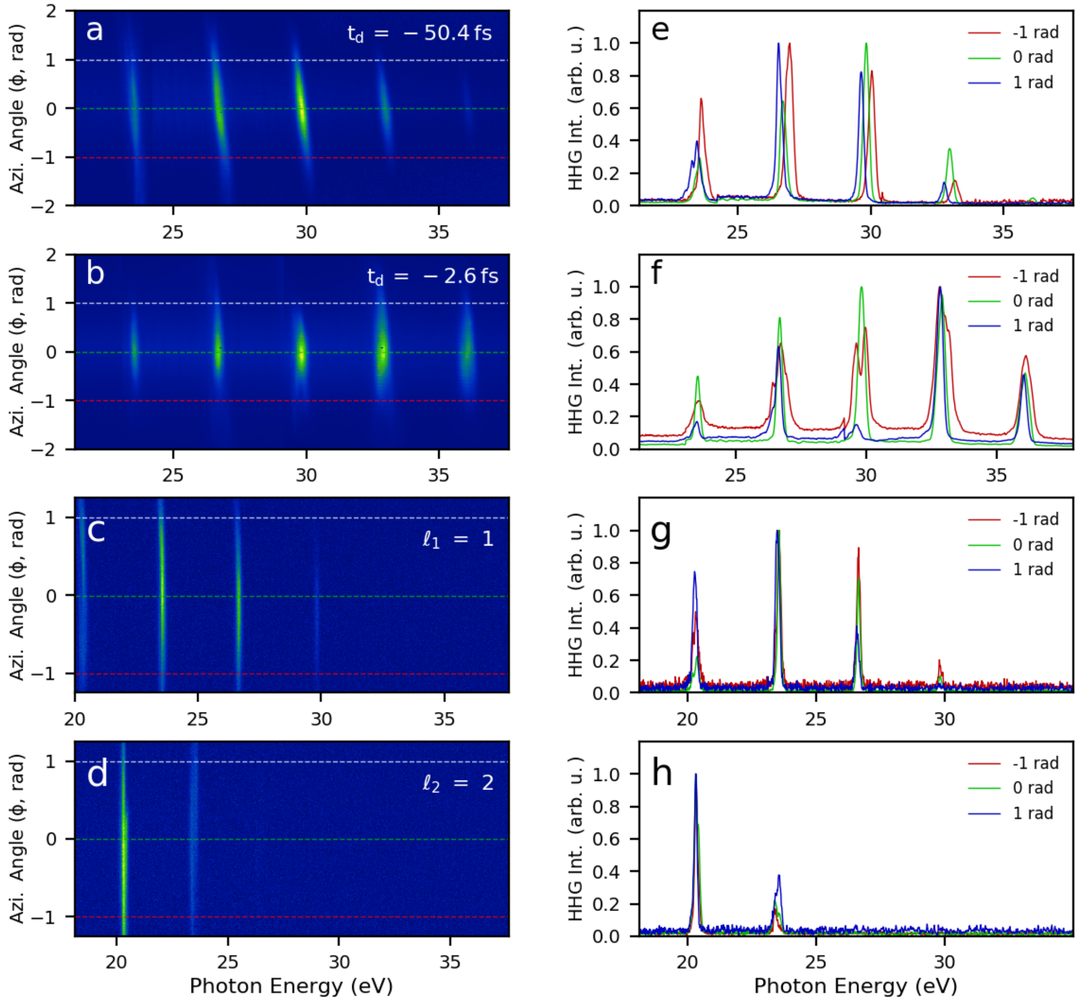

Figure C.8: **Confirmation of the spectral shift induced by the self-torque of light.** An EUV CCD camera records the dispersed OAM HHG spectrum at the flat-field imaging plane of the EUV spectrometer, yielding a spatiospectral image of the emitted harmonics. **a-d**, The HHG spectra for the combined beam at a −50.4 fs and, **b** −2.6 fs, delay and the individual OAM drivers (**c-d**) clearly show that the azimuthal frequency chirp is only present when HHG is driven with a non-pure vortex mode composed of two pulses separated by a time delay comparable to their pulse widths. **e-h**, Azimuthally integrated HHG spectra at different azimuthal angles across the EUV spatial-spectrograms (shown in **a-d**) confirms the spectral shift observed in **a**, while the similar linewidths and cutoffs indicate that the spectral shift does not originate from overdriving the HHG process (e.g., ionization saturation, spatiotemporal reshaping of the driving beam, etc.). Adapted with permission from Ref. 3.

References

[1] K. M. Dorney, J. L. Ellis, C. Hernández-García, D. D. Hickstein, C. A. Mancuso, N. Brooks, T. Fan, G. Fan, D. Zusin, C. Gentry, P. Grychtol, H. C. Kapteyn, and M. M. Murnane. Helicity-Selective Enhancement and Polarization Control of Attosecond High Harmonic Waveforms Driven by Bichromatic Circularly Polarized Laser Fields. *Phys. Rev. Lett.*, 119 (6), **2017**, 45–47. DOI: `10.1103/PhysRevLett.119.063201` (cited on pages iv, 49, 52, 54–58, 66, 70, 73, 74, 89, 99, 101, 102, 105, 110–113).

[2] K. M. Dorney, L. Rego, N. J. Brooks, J. San Román, C.-T. Liao, J. L. Ellis, D. Zusin, C. Gentry, Q. L. Nguyen, J. M. Shaw, A. Picón, L. Plaja, H. C. Kapteyn, M. M. Murnane, and C. Hernández-García. Controlling the polarization and vortex charge of attosecond high-harmonic beams via simultaneous spin–orbit momentum conservation. *Nat. Photonics*, 13 (2), **2019**, 123–130. DOI: `10.1038/s41566-018-0304-3` (cited on pages iv, 18, 61, 64, 70, 73, 76, 77, 79, 83, 89, 114, 117, 119, 122, 123, 130).

[3] L. Rego, K. M. Dorney, N. J. Brooks, Q. Nguyen, C.-T. Liao, J. S. Román, D. E. Couch, A. Liu, E. Pisanty, M. Lewenstein, L. Plaja, H. C. Kapteyn, M. M. Murnane, and C. Hernández-García. Light with a self-torque: extreme-ultraviolet beams with time-varying orbital angular momentum, 1–24. arXiv: `1901.10942` (cited on pages iv, 64, 82, 86, 90, 95, 96, 98, 102, 124, 129, 130, 132, 133, 137–142).

[4] E. Pisanty, L. Rego, J. S. Román, A. Picón, K. M. Dorney, H. C. Kapteyn, M. M. Murnane, L. Plaja, M. Lewenstein, and C. Hernández-García. Conservation of torus-knot angular momentum in high-order harmonic generation, **2018**, 1–6. URL: `http://arxiv.org/abs/1810.06503`. arXiv: `1810.06503` (cited on page v).

[5] Y. Esashi, C.-T. Liao, B. Wang, N. Brooks, K. M. Dorney, C. Hernández-García, H. Kapteyn, D. Adams, and M. Murnane. Ptychographic amplitude and phase reconstruction of bichromatic vortex beams. *Opt. Express*, 26 (26), **2018**, 34007. DOI: `10.1364/OE.26.034007` (cited on page v).

[6] J. L. Ellis, K. M. Dorney, D. D. Hickstein, N. J. Brooks, C. Gentry, C. Hernández-García, D. Zusin, J. M. Shaw, Q. L. Nguyen, C. A. Mancuso, G. S. Matthijs Jansen, S. Witte, H. C. Kapteyn, and M. M. Murnane. High harmonics with spatially varying ellipticity. *Optica*, 5 (4), **2018**, 479. DOI: `10.1364/OPTICA.5.000479` (cited on pages vi, 37, 46, 52, 65, 70, 73, 118).

[7] J. L. Ellis, K. M. Dorney, C. G. Durfee, C. Hernández-García, F. Dollar, C. A. Mancuso, T. Fan, D. Zusin, C. Gentry, P. Grychtol, H. C. Kapteyn, M. M. Murnane, and D. D. Hickstein. Phase matching of noncollinear sum and difference frequency high harmonic generation above and below the critical ionization level. *Opt. Express*, 25 (9), **2017**, 10126. DOI: `10.1364/OE.25.010126` (cited on pages vi, 27, 50, 102).

[8] C. A. Mancuso. Strong Field Ionization of Atoms Irradiated with Two-Color Circularly Polarized Femtosecond Laser Fields : Rescattering in a Whole New Dimension. PhD thesis. University of Colorado Boulder, 2016 (cited on pages vi, 54).

[9] C. A. Mancuso, K. M. Dorney, D. D. Hickstein, J. L. Chaloupka, J. L. Ellis, F. J. Dollar, R. Knut, P. Grychtol, D. Zusin, C. Gentry, M. Gopalakrishnan, H. C. Kapteyn, and M. M. Murnane. Controlling Nonsequential Double Ionization in Two-Color Circularly Polarized Femtosecond Laser Fields. *Phys. Rev. Lett.*, 117 (13), **2016**, 1–6. DOI: `10.1103/PhysRevLett.117.133201` (cited on pages vi, 49, 54, 59).

[10] C. A. Mancuso, K. M. Dorney, D. D. Hickstein, J. L. Chaloupka, X. M. Tong, J. L. Ellis, H. C. Kapteyn, and M. M. Murnane. Observation of ionization enhancement in two-color circularly polarized laser fields. *Phys. Rev. A*, 96 (2), **2017**, 1–10. DOI: `10.1103/PhysRevA.96.023402` (cited on pages vi, 54, 57).

[11] T. Fan, P. Grychtol, R. Knut, C. Hernández-García, D. D. Hickstein, D. Zusin, C. Gentry, F. J. Dollar, C. A. Mancuso, C. W. Hogle, O. Kfir, D. Legut, K. Carva, J. L. Ellis, K. M. Dorney, C. Chen, O. G. Shpyrko, E. E. Fullerton, O. Cohen, P. M. Oppeneer, D. B. Milošević, A. Becker, A. A. Jaroń-Becker, T. Popmintchev, M. M. Murnane, and H. C. Kapteyn. Bright circularly polarized soft X-ray high harmonics for X-ray magnetic circular dichroism. *Proc. Natl. Acad. Sci.*, 112 (46), **2015**, 14206–14211. DOI: `10.1073/pnas.1519666112`. arXiv: `arXiv:1408.1149` (cited on pages vi, 25, 26, 46, 51, 66, 70, 73, 84, 89, 102, 106, 109).

[12] D. D. Hickstein, F. J. Dollar, P. Grychtol, J. L. Ellis, R. Knut, C. Hernandez-Garcia, D. Zusin, C. Gentry, J. M. Shaw, T. Fan, K. M. Dorney, A. Becker, A. Jaron-Becker, H. C. Kapteyn, M. M. Murnane, and C. G. Durfee. Non-collinear generation of angularly isolated circularly polarized high harmonics. *Nat. Photonics*, 9 (11), **2015**, 743–750. DOI: `10.1038/nphoton.2015.181` (cited on pages vii, 27, 50, 52, 65, 71, 73, 74).

[13] S. K. Reinke, S. V. Roth, G. Santoro, S. Heinrich, and S. Palzer. Tracking Structural Changes in Lipid-based Multicomponent Food Materials due to Oil Migration by Microfocus Small-Angle X - ray Scattering. *ACS Appl. Mater. Interfaces*, 7 (18), **2015**, 9929–9936. DOI: `10.1021/acsami.5b02092` (cited on page 1).

[14] E. Hecht. **Optics**. 4th. San Francisco: Pearson Education, 2002. URL: `https://www.pearson.com/us/higher-education/product/Hecht-Optics-4th-Edition/9780805385663.html` (cited on pages 1, 5, 6).

[15] H. Chen, C. T. Chan, and P. Sheng. Transformation optics and metamaterials. *Nat. Mater.*, 9, **2010**, 387. URL: `https://doi.org/10.1038/nmat2743http://10.0.4.14/nmat2743` (cited on page 2).

[16] W. Cai, U. K. Chettiar, A. V. Kildishev, and V. M. Shalaev. Optical cloaking with metamaterials. *Nat. Photonics*, 1, **2007**, 224. URL: `https://doi.org/10.1038/nphoton.2007.28` (cited on page 2).

[17] A Ashkin, J. M. Dziedzic, J. E. Bjorkholm, and S. Chu. Observation of a single-beam gradient force optical trap for dielectric particles. *Opt. Lett.*, 11 (5), **1986**, 288–290. DOI: `10.1364/OL.11.000288` (cited on pages 2, 12).

[18] A Ashkin. History of optical trapping and manipulation of small-neutral particle, atoms, and molecules. *IEEE J. Sel. Top. Quantum Electron.*, 6 (6), **2000**, 841–856. DOI: 10.1109/2944.902132 (cited on page 2).

[19] K Svoboda and S. M. Block. Biological Applications of Optical Forces. *Annu. Rev. Biophys. Biomol. Struct.*, 23 (1), **1994**, 247–285. DOI: 10.1146/annurev.bb.23.060194.001335 (cited on page 2).

[20] A Ashkin, J. M. Dziedzic, and T Yamane. Optical trapping and manipulation of single cells using infrared laser beams. *Nature*, 330 (6150), **1987**, 769–771. DOI: 10.1038/330769a0 (cited on pages 2, 12).

[21] M. Padgett and R. Bowman. Tweezers with a twist. *Nat. Photonics*, 5 (6), **2011**, 343–348. DOI: 10.1038/nphoton.2011.81 (cited on pages 2, 12, 17, 65, 83).

[22] M. J. Padgett. Orbital angular momentum 25 years on [Invited]. *Opt. Express*, 25 (10), **2017**, 11265. DOI: 10.1364/oe.25.011265 (cited on pages 2, 15, 64).

[23] J. P. Torres and L. Torner. **Twisted Photons: Applications of Light with Orbital Angular Momentum**. 1st. Wiley-VCH Verlag GmBH & Co. KGaA, 2011. DOI: 10.1002/9783527635368 (cited on pages 2, 16, 17, 65, 83).

[24] A. E. Willner, H. Huang, Y. Yan, Y. Ren, N. Ahmed, G. Xie, and C. Bao. Optical communications using orbital angular momentum beams. *Adv. Opt. Photonics*, 7 (1), **2015**, 66–98. DOI: 10.1364/AOP. arXiv: 1303.6810 (cited on pages 2, 16, 17, 65, 83).

[25] M. A. Lauterbach, M. Guillon, A. Soltani, and V. Emiliani. STED microscope with Spiral Phase Contrast. *Sci. Rep.*, 3, **2013**. DOI: 10.1038/srep02050 (cited on pages 2, 83).

[26] H. Rubinsztein-Dunlop, A. Forbes, M. V. Berry, C. Alpmann, P. Banzer, T. Bauer, and E. Karimi. Roadmap on structured light. *J. Opt.*, 19 (1), **2017**, 013001. DOI: https://iopscience.iop.org/article/10.1088/2040-8978/19/1/013001/meta (cited on pages 2, 13, 14, 16, 17, 83, 97).

[27] B. Alberts, A. Johnson, J. Lewis, M. Raff, K. Roberts, and J. Watson. **Molecular Biology of the Cell**. Ed. by R. Adams. 1st ed. Yew York, London: Garland Publishing, Inc., 1989. URL: https://books.google.com/books/about/Molecular{_}Biology{_}of{_}the{_}Cell.html?id=FFfW4cH8PdcC{\&}printsec=frontcover{\&}source=kp{_}read{_}button{\#}v=onepage{\&}q{\&}f=false (cited on pages 3, 4).

[28] E. Romero, V. I. Novoderezhkin, and R. van Grondelle. Quantum design of photosynthesis for bio-inspired solar-energy conversion. *Nature*, 543, **2017**, 355. URL: https://doi.org/10.1038/nature22012http://10.0.4.14/nature22012 (cited on page 3).

[29] I. Levine. **Physical Chemistry**. 6th ed. McGraw-Hill Publishing, 2009 (cited on page 3).

[30] C Jacoboni, C Canali, G Otiaviani, and A. A. Quaranta. A REVIEW OF SOME CHARGE TRANSPORT PROPERTIES OF SILICONt. *Solid State Electron.*, 20, **1977**, 77–89 (cited on page 3).

[31] P. H. Bucksbaum. The Future of Attosecond Spectroscopy. *Science (80-.).*, 317 (5839), **2007**, 766–769. DOI: 10.1126/science.1142135 (cited on pages 3, 4).

[32] M. Hase, P. Fons, K. Mitrofanov, A. V. Kolobov, and J. Tominaga. Femtosecond structural transformation of phase-change materials far from equilibrium monitored by coherent phonons. *Nat. Commun.*, 6, **2015**, 8367. URL: `https://doi.org/10.1038/ncomms9367http://10.0.4.14/ncomms9367https://www.nature.com/articles/ncomms9367{\#}supplementary-information` (cited on page 4).

[33] P. Tengdin, W. You, C. Chen, X. Shi, D. Zusin, Y. Zhang, C. Gentry, A. Blonsky, M. Keller, P. M. Oppeneer, H. C. Kapteyn, and M. M. Tao, ZhenshengMurnane. Critical behavior within 20 fs drives the out-of-equilibrium laser-induced magnetic phase transition in nickel. *Sci. Adv.*, 4 (3), **2018**, eaap9744. DOI: `10.1126/sciadv.aap9744` (cited on pages 4, 80, 85).

[34] W. You, P. Tengdin, C. Chen, X. Shi, D. Zusin, Y. Zhang, C. Gentry, A. Blonsky, M. Keller, P. M. Oppeneer, H. Kapteyn, Z. Tao, and M. Murnane. Revealing the Nature of the Ultrafast Magnetic Phase Transition in Ni by Correlating Extreme Ultraviolet Magneto-Optic and Photoemission Spectroscopies. *Phys. Rev. Lett.*, 121 (7), **2018**, 77204. DOI: `10.1103/PhysRevLett.121.077204` (cited on page 4).

[35] T. H. MAIMAN. Stimulated Optical Radiation in Ruby. *Nature*, 187 (4736), **1960**, 493–494. DOI: `10.1038/187493a0` (cited on pages 6, 7).

[36] Z. Tao, C. Chen, T. Szilvási, M. Keller, M. Mavrikakis, H. Kapteyn, and M. Murnane. Direct time-domain observation of attosecond final-state lifetimes in photoemission from solids. *Science (80-.).*, 353, **2016**, 62. URL: `http://dx.doi.org/10.1126/science.aaf6793` (cited on pages 7, 22).

[37] C. Chen, Z. Tao, A. Carr, P. Matyba, T. Szilvási, S. Emmerich, M. Piecuch, M. Keller, D. Zusin, S. Eich, M. Rollinger, W. You, S. Mathias, U. Thumm, M. Mavrikakis, M. Aeschlimann, P. M. Oppeneer, H. Kapteyn, and M. Murnane. Distinguishing attosecond electron–electron scattering and screening in transition metals. *Proc. Natl. Acad. Sci.*, 114 (27), **2017**, E5300–E5307. DOI: `10.1073/pnas.1706466114` (cited on pages 7, 22, 80, 85).

[38] P. W. Smith. Mode-locking of lasers. *Proc. IEEE*, 58 (9), **1970**, 1342–1354 (cited on page 7).

[39] H. A. Haus. Mode-locking of lasers. *IEEE J. Sel. Top. Quantum Electron.*, 6 (6), **2000**, 1173–1185. DOI: `10.1109/2944.902165` (cited on page 7).

[40] J. A. Valdmanis, R. L. Fork, and J. P. Gordon. Generation of optical pulses as short as 27 femtoseconds directly from a laser balancing self-phase modulation, group-velocity dispersion, saturable absorption, and saturable gain. *Opt. Lett.*, 10 (3), **1985**, 131. DOI: `10.1364/ol.10.000131` (cited on page 7).

[41] D. E. Spence, P. N. Kean, and W Sibbett. 60-Femtosecond pulse generation from a self-mode-locked titanium-doped sapphire laser. *Opt. Lett.*, 16 (1), **1991**, 42–44. DOI: `10.1364/OL.16.000042` (cited on pages 8, 32).

[42] M. Asaki, C. Huang, D. Garvey, J. Zhou, H. Kapteyn, and M. Murnane. Generation of 11 femtosecond pulses from a self mode-locked Ti: sapphire laser,' *Opt. Lett.*, 18 (12), **1993**, 977–979 (cited on page 8).

[43] J. Zhou, G. Taft, C.-P. Huang, M. M. Murnane, H. C. Kapteyn, and I. P. Christov. Pulse evolution in a broad-bandwidth Ti:sapphire laser. *Opt. Lett.*, 19 (15), **1994**, 1149. DOI: `10.1364/ol.19.001149` (cited on page 8).

[44] A Stingl, M Lenzner, C. Spielmann, F Krausz, and R. Szipöcs. Sub-10-fs mirror-dispersion-controlled Ti : sapphire laser. *Opt. Lett.*, 20 (6), **1995**, 602–604 (cited on page 8).

[45] W. Li, X. Zhou, R. Lock, S. Patchkovskii, A. Stolow, H. C. Kapteyn, and M. M. Murnane. Time-Resolved Dynamics in N 2 O 4 Probed Using High Harmonic Generation. *Science (80-.).*, 322 (November), **2008**, 1207–1212. DOI: `https://doi.org/10.1126/science.1163077` (cited on page 8).

[46] X Zhou, P Ranitovic, C. W. Hogle, J. H. D. Eland, H. C. Kapteyn, and M. M. Murnane. Probing and controlling non-Born–Oppenheimer dynamics in highly excited molecular ions. *Nat. Phys.*, 8 (3), **2012**, 232–237. DOI: `10.1038/nphys2211` (cited on page 8).

[47] P. M. Kraus, B Mignolet, D Baykusheva, A Rupenyan, L Horný, E. F. Penka, G Grassi, O. I. Tolstikhin, J Schneider, F Jensen, L. B. Madsen, A. D. Bandrauk, F Remacle, and H. J. Wörner. Measurement and laser control of attosecond charge migration in ionized iodoacetylene. *Science (80-.).*, 350 (6262), **2015**, 790–795. DOI: `10.1126/science.aab2160` (cited on page 8).

[48] A Baltuška, T. Udem, M Uiberacker, M Hentschel, E Goulielmakis, C. Gohle, R Holzwarth, V. S. Yakovlev, A Scrinzi, T. W. Hänsch, and F Krausz. Attosecond control of electronic processes by intense light fields. *Nature*, 421, **2003**, 611. URL: `https://doi.org/10.1038/nature01414http://10.0.4.14/nature01414` (cited on page 8).

[49] E Goulielmakis, V. S. Yakovlev, A. L. Cavalieri, M Uiberacker, V Pervak, A Apolonski, R Kienberger, U Kleineberg, and F Krausz. Attosecond Control and Measurement: Lightwave Electronics. *Science (80-.).*, 317 (5839), **2007**, 769–775. DOI: `10.1126/science.1142855` (cited on page 8).

[50] D. M. Villeneuve, P. Hockett, M. J. J. Vrakking, and H. Niikura. Coherent imaging of an attosecond electron wave packet. *Science (80-.).*, 356 (6343), **2017**, 1150–1153. DOI: `10.1126/science.aam8393` (cited on page 8).

[51] M. F. Ciappina, J. A. Perez-Hernandez, A. S. Landsman, W. A. Okell, S Zherebtsov, B Förg, J Schötz, L. Seiffert, T. Fennel, T. Shaaran, T. Zimmerman, A. Chacón, R. Guichard, A. Zaïr, J. W. G. Tisch, J. Marangos, T. Witting, A. Braun, S. A. Maier, L. Roso, M. Krüger, P Hommelhoff, M. F. Kling, F. Krausz, and M. Lewenstein. Attosecond physics at the nanoscale. *Rep. Prog. Phys.*, 80, **2017**, 054401. URL: `https://iopscience.iop.org/article/10.1088/1361-6633/aa574e` (cited on page 8).

[52] R. W. Boyd. Intuitive explanation of the phase anomaly of focused light beams. *J. Opt. Soc. Am.*, 70 (7), **1980**, 877–880. DOI: `10.1364/JOSA.70.000877` (cited on page 9).

[53] G Sansone, E Benedetti, F Calegari, C Vozzi, L Avaldi, R Flammini, L Poletto, P Villoresi, C Altucci, R Velotta, S Stagira, S De Silvestri, and M Nisoli. Isolated Single-Cycle Attosecond Pulses. *Science (80-.).*, 314 (5798), **2006**, 443–446. DOI: `10.1126/science.1132838` (cited on pages 11, 22).

[54] M. Chini, K. Zhao, and Z. Chang. The generation, characterization and applications of broadband isolated attosecond pulses. *Nat. Photonics*, 8 (3), **2014**, 178–186. DOI: `10.1038/nphoton.2013.362`. arXiv: `1312.1679` (cited on pages 11, 57, 97).

[55] D. J. Wineland, R. E. Drullinger, and F. L. Walls. Radiation-pressure cooling of bound resonant absorbers. *Phys. Rev. Lett.*, 40 (25), **1978**, 1639–1642. DOI: `10.1103/PhysRevLett.40.1639` (cited on page 12).

[56] T. W. Hänsch and A. L. Schawlow. Cooling of gases by laser radiation. *Opt. Commun.*, 13 (I), **1975**, 68–69 (cited on page 12).

[57] W. P. Phillips. Laser cooling and trapping of neutral atoms: theory. *Phys. Rep.*, 219 (3-6), **1992**, 153–164. DOI: `10.1016/0370-1573(92)90133-K` (cited on page 12).

[58] P. N. Lebedev. "Experimental examination of light pressure" Translated from Russian by V. Soloviev. *Ann. Phys.*, 6, **1901**, 433–459. URL: `http://web.ihep.su/dbserv/compas/src/lebedev01/eng.pdf` (cited on page 12).

[59] E. F. Nichols and G. F. Hull. The Pressure Due to Radiation. *Phys. Rev.*, 17, **1903**, 26. DOI: `10.2307/20021808` (cited on page 12).

[60] E. F. Nichols and G. F. Hull. A Preliminary Communication on the Pressure of Heat and Light Radiation. *Phys. Rev. (*, 13, **1901**, 307–320. DOI: `10.1103/physrevseriesi.13.307` (cited on page 12).

[61] J. Poynting. The wave motion of a revolving shaft, and a suggestion as to the angular momenutm in a beam of circularly polarised light. *Proc. R. Soc. Lond. A*, 82, **1909**, 560–567. DOI: `10.1098/rspa.1909.0060` (cited on page 12).

[62] R. A. Beth. Mechanical detection and measurement of the angular momentum of light. *Phys. Rev.*, 50 (2), **1936**, 115–125. DOI: `10.1103/PhysRev.50.115` (cited on pages 12, 65).

[63] H. Stapelfeldt and T. Seideman. Colloquium: Aligning molecules with strong laser pulses. *Rev. Mod. Phys.*, 75 (2), **2003**, 543–557. DOI: `10.1103/RevModPhys.75.543` (cited on page 12).

[64] J. F. Nye. Lines of circular polarization in electromagnetic wave fields. *Proc. R. Soc. London. A. Math. Phys. Sci.*, 389 (1797), **1983**, 279–290. DOI: `10.1098/rspa.1983.0109` (cited on pages 13, 15).

[65] J. F. Nye. Polarization effects in the diffraction of electromagnetic waves: the role of disclinations. *Proc. R. Soc. London. A. Math. Phys. Sci.*, 387 (1792), **1983**, 105–132. DOI: `10.1098/rspa.1983.0053` (cited on pages 13, 15).

[66] Q. Zhan. Cylindrical vector beams: from mathematical concepts to applications. *Adv. Opt. Photonics*, 1 (1), **2009**, 1. DOI: `10.1364/aop.1.000001` (cited on page 14).

[67] A. Rubano, F. Cardano, B. Piccirillo, and L. Marrucci. Q-plate technology: a progress review [Invited]. *J. Opt. Soc. Am. B*, 36 (5), **2019**, 70–87 (cited on pages 14, 16).

[68] C. G. Darwin. Notes on the theory of radiation. *Proc. R. Soc. London. Ser. A, Contain. Pap. a Math. Phys. Character*, 136 (829), **1932**, 36–52. DOI: `10.1098/rspa.1932.0065` (cited on page 15).

[69] L. Allen, M. W. Beijersbergen, R. J. Spreeuw, and J. P. Woerdman. Orbital angular momentum of light and the transformation of Laguerre-Gaussian laser modes. *Phys. Rev. A*, 45 (11), **1992**, 8185–8189. DOI: `10.1103/PhysRevA.45.8185`. arXiv: `0703543 [cond-mat]` (cited on pages 15, 16, 28, 65, 83).

[70] A. M. Yao and M. J. Padgett. Orbital angular momentum: origins, behavior and applications. *Adv. Opt. Photonics*, 3 (2), **2011**, 161. DOI: `10.1364/AOP.3.000161` (cited on pages 16, 38, 64, 65, 83, 87, 115, 137, 138).

[71] H. He, M. E. Friese, N. R. Heckenberg, and H. Rubinsztein-Dunlop. Direct Observation of Transfer of Angular Momentum to Absorptive Particles from a Laser Beam with a Phase Singularity. *Phys. Rev. Lett.*, 75 (5), **1995**, 826–829. DOI: 10.1103/PhysRevLett.75.826 (cited on pages 17, 83).

[72] M. Mirhosseini, O. S. Magaña-loaiza, M. N. O. Sullivan, B. Rodenburg, M. Malik, M. P. J. Lavery, M. J. Padgett, D. J. Gauthier, and R. W. Boyd. High-dimensional quantum cryptography with twisted light. *New J. Phys.*, 17, **2015**, 033033. DOI: 10.1088/1367-2630/17/3/033033 (cited on page 17).

[73] J. Wang, J.-y. Yang, I. M. Fazal, N. Ahmed, Y. Yan, H. Huang, Y. Ren, Y. Yue, S. Dolinar, M. Tur, and A. E. Willner. Terabit free-space data transmission employing orbital angular momentum multiplexing. *Nat. Photon.*, 6 (July), **2012**. DOI: 10.1038/NPHOTON.2012.138 (cited on page 17).

[74] G. Vicidomini, P. Bianchini, and A. Diaspro. STED super-resolved microscopy. *Nat. Methods*, 15 (3), **2018**, 173–182. DOI: 10.1038/nmeth.4593 (cited on pages 17, 83).

[75] K. E. Ballantine, J. F. Donegan, and P. R. Eastham. There are many ways to spin a photon: Half-quantization of a total optical angular momentum. *Sci. Adv.*, 2 (4), **2016**, 1–8. DOI: 10.1126/sciadv.1501748 (cited on pages 17, 65).

[76] I. Freund. Cones, spirals, and Möbius strips, in elliptically polarized light. *Opt. Commun.*, 249 (1), **2005**, 7–22. DOI: https://doi.org/10.1016/j.optcom.2004.12.052 (cited on page 17).

[77] E. M. Wright, J. Arlt, and K. Dholakia. Toroidal optical dipole traps for atomic Bose-Einstein condensates using Laguerre-Gaussian beams. *Phys. Rev. A - At. Mol. Opt. Phys.*, 63 (1), **2001**, 1–7. DOI: 10.1103/PhysRevA.63.013608 (cited on pages 17, 83).

[78] A. Turpin, J. Polo, Y. V. Loiko, J. Küber, F. Schmaltz, T. K. Kalkandjiev, V. Ahufinger, G. Birkl, and J. Mompart. Blue-detuned optical ring trap for Bose-Einstein condensates based on conical refraction. *Opt. Express*, 23 (2), **2014**, 1638–1650. DOI: 10.1364/OE.23.001638. arXiv: 1411.1587 (cited on pages 17, 83).

[79] A Picón, A Benseny, J Mompart, J. R. Vázquez de Aldana, L Plaja, G. F. Calvo, and L Roso. Transferring orbital and spin angular momenta of light to atoms. *New J. Phys.*, 12 (8), **2010**, 083053. DOI: 10.1088/1367-2630/12/8/083053 (cited on pages 17, 81, 85).

[80] C. T. Schmiegelow and F Schmidt-Kaler. Light with orbital angular momentum interacting with trapped ions. *Eur. Phys. J. D*, 66 (6), **2012**, 157. DOI: 10.1140/epjd/e2012-20730-4 (cited on page 17).

[81] P. K. Mondal, B. Deb, and S. Majumder. Angular momentum transfer in interaction of Laguerre-Gaussian beams with atoms and molecules. *Phys. Rev. A*, 89 (6), **2014**, 63418. DOI: 10.1103/PhysRevA.89.063418 (cited on page 17).

[82] T Kaneyasu, Y Hikosaka, M Fujimoto, T Konomi, M Katoh, H Iwayama, and E Shigemasa. Limitations in photoionization of helium by an extreme ultraviolet optical vortex. *Phys. Rev. A*, 95, **2017**, 023413. DOI: 10.1103/PhysRevA.95.023413 (cited on page 17).

[83] C. T. Schmiegelow, J. Schulz, H. Kaufmann, T. Ruster, U. G. Poschinger, and F. Schmidt-Kaler. Transfer of optical orbital angular momentum to a bound electron. *Nat. Commun.*, 7, **2016**, 12998. URL: `https://doi.org/10.1038/ncomms12998http://10.0.4.14/ncomms12998https://www.nature.com/articles/ncomms12998{\#}supplementary-information` (cited on pages 17, 18).

[84] A. T. O'Neil, I Macvicar, L Allen, and M. J. Padgett. Intrinsic and Extrinsic Nature of the Orbital Angular Momentum of a Light Beam. *Phys. Rev. Lett.*, 88 (5), **2002**, 5–8. DOI: `10.1103/PhysRevLett.88.053601` (cited on page 17).

[85] M. Babiker, D. L. Andrews, and V. E. Lembessis. Atoms in complex twisted light. *J. Opt.*, 21, **2019**, 013001 (cited on page 17).

[86] F.-A. Sonja. Optical angular momentum and atoms. *Philos. Trans. R. Soc. A Math. Phys. Eng. Sci.*, 375 (2087), **2017**, 20150435. DOI: `10.1098/rsta.2015.0435` (cited on page 17).

[87] M. Van Veenendaal. Interaction between x-ray and magnetic vortices. *Phys. Rev. B - Condens. Matter Mater. Phys.*, 92 (24), **2015**, 1–5. DOI: `10.1103/PhysRevB.92.245116` (cited on pages 18, 81).

[88] H. Fujita and M. Sato. Encoding orbital angular momentum of light in magnets. *Phys. Rev. B*, 96 (6), **2017**, 60407. DOI: `10.1103/PhysRevB.96.060407` (cited on page 18).

[89] H. Fujita and M. Sato. Ultrafast generation of skyrmionic defects with vortex beams: Printing laser profiles on magnets. *Phys. Rev. B*, 95 (5), **2017**, 1–12. DOI: `10.1103/PhysRevB.95.054421` (cited on pages 18, 81).

[90] N. Nagaosa and Y. Tokura. Topological properties and dynamics of magnetic skyrmions. *Nat. Nanotechnol.*, 8, **2013**, 899. URL: `https://doi.org/10.1038/nnano.2013.243http://10.0.4.14/nnano.2013.243` (cited on page 18).

[91] N. Romming, C. Hanneken, M. Menzel, J. E. Bickel, B. Wolter, K. von Bergmann, A. Kubetzka, and R. Wiesendanger. Writing and Deleting Single Magnetic Skyrmions. *Science (80-.).*, 341 (6146), **2013**, 636–639. DOI: `10.1126/science.1240573` (cited on page 18).

[92] G. F. Quinteiro and P. I. Tamborenea. Theory of the optical absorption of light carrying orbital angular momentum by semiconductors Theory of the optical absorption of light carrying orbital angular momentum by semiconductors. *Eur. Phys. Lett.*, 85, **2009**, 47001. DOI: `10.1209/0295-5075/85/47001` (cited on page 18).

[93] G. F. Quinteiro and T Kuhn. Below-bandgap excitation of bulk semiconductors by twisted light Below-bandgap excitation of bulk semiconductors by twisted light. *Eur. Phys. Lett.*, 91, **2010**, 27002. DOI: `10.1209/0295-5075/91/27002` (cited on page 18).

[94] G. F. Quinteiro and T Kuhn. Light-hole transitions in quantum dots: Realizing full control by highly focused optical-vortex beams. *Phys. Rev. B - Condens. Matter Mater. Phys.*, 90 (11), **2014**, 1–9. DOI: `10.1103/PhysRevB.90.115401` (cited on page 18).

[95] M. Van Veenendaal and I. McNulty. Prediction of strong dichroism induced by X rays carrying orbital momentum. *Phys. Rev. Lett.*, 98 (15), **2007**, 1–4. DOI: `10.1103/PhysRevLett.98.157401` (cited on pages 18, 81).

[96] J Wätzel and J Berakdar. Discerning on a sub-optical-wavelength the attosecond time delays in electron emission from magnetic sublevels by optical vortices. *Phys. Rev. A*, 94 (3), **2016**, 33414. DOI: 10.1103/PhysRevA.94.033414 (cited on page 18).

[97] M. Zürch, C. Kern, P. Hansinger, A. Dreischuh, and C. Spielmann. Strong-field physics with singular light beams. *Nat. Phys.*, 8 (10), **2012**, 743–746. DOI: 10.1038/nphys2397 (cited on pages 18, 27, 63–65, 78, 83, 89).

[98] G. Gariepy, J. Leach, K. T. Kim, T. J. Hammond, E. Frumker, R. W. Boyd, and P. B. Corkum. Creating high-harmonic beams with controlled orbital angular momentum. *Phys. Rev. Lett.*, 113 (15), **2014**, 1–5. DOI: 10.1103/PhysRevLett.113.153901 (cited on pages 18, 27, 64–66, 74, 78, 83, 89, 118).

[99] C. Hernández-García, A. Picón, J. San Román, and L. Plaja. Attosecond extreme ultraviolet vortices from high-order harmonic generation. *Phys. Rev. Lett.*, 111 (8), **2013**, 1–5. DOI: 10.1103/PhysRevLett.111.083602. arXiv: 1507.00635 (cited on pages 18, 27, 64, 65, 70, 74, 78, 83, 89, 118, 119, 130).

[100] R. Géneaux, A. Camper, T. Auguste, O. Gobert, J. Caillat, R. Taïeb, and T. Ruchon. Synthesis and characterization of attosecond light vortices in the extreme ultraviolet. *Nat. Commun.*, 7, **2016**. DOI: 10.1038/ncomms12583. arXiv: 1509.07396 (cited on pages 18, 27, 64, 65, 74, 78, 83, 89, 118).

[101] F. Kong, C. Zhang, F. Bouchard, Z. Li, G. G. Brown, D. H. Ko, T. J. Hammond, L. Arissian, R. W. Boyd, E. Karimi, and P. B. Corkum. Controlling the orbital angular momentum of high harmonic vortices. *Nat. Commun.*, 8, **2017**, 6–11. DOI: 10.1038/ncomms14970 (cited on pages 18, 28, 64–66, 71, 78, 83, 89).

[102] D. Gauthier, P. R. Ribic, G. Adhikary, A. Camper, C. Chappuis, R. Cucini, L. F. Dimauro, G. Dovillaire, F. Frassetto, R. Géneaux, P. Miotti, L. Poletto, B. Ressel, C. Spezzani, M. Stupar, T. Ruchon, and G. De Ninno. Tunable orbital angular momentum in high-harmonic generation. *Nat. Commun.*, 8, **2017**, 1–7. DOI: 10.1038/ncomms14971 (cited on pages 18, 28, 64, 65, 71, 78, 83, 89).

[103] D. Gauthier, S. Kaassamani, D. Franz, R. Nicolas, J.-T. Gomes, L. Lavoute, D. Gaponov, S. Février, G. Jargot, M. Hanna, W. Boutu, and H. Merdji. Orbital angular momentum from semiconductor high-order harmonics. *Opt. Lett.*, 44 (3), **2019**, 546–549. DOI: 10.1364/OL.44.000546 (cited on page 18).

[104] P. Rebernik Ribič, B. Rösner, D. Gauthier, E. Allaria, F. Döring, L. Foglia, L. Giannessi, N. Mahne, M. Manfredda, C. Masciovecchio, R. Mincigrucci, N. Mirian, E. Principi, E. Roussel, A. Simoncig, S. Spampinati, C. David, and G. De Ninno. Extreme-Ultraviolet Vortices from a Free-Electron Laser. *Phys. Rev. X*, 7 (3), **2017**, 31036. DOI: 10.1103/PhysRevX.7.031036 (cited on page 19).

[105] Y. Taira and Y. Kohmura. Measuring the topological charge of an x-ray vortex using a triangular aperture. *J. Opt.*, 21 (4), **2019**, 45604. DOI: 10.1088/2040-8986/ab0a51 (cited on page 19).

[106] J. L. Krause, K. J. Schafer, and K. C. Kulander. High-order harmonic generation from atoms and ions in the high intensity regime. *Phys. Rev. Lett.*, 68 (24), **1992**, 3535–3538. DOI: 10.1103/PhysRevLett.68.3535 (cited on pages 19, 21, 108).

[107] P. B. Corkum. Plasma perspective on strong field multiphoton ionization. *Phys. Rev. Lett.*, 71 (13), **1993**, 1994–1997. DOI: `10.1103/PhysRevLett.71.1994` (cited on pages 19, 21, 23, 24, 65, 84, 108).

[108] M. Y. Kuchiev. Atomic antenna. *Sov. Phys. JETP Lett.*, 45 (7), **1987**, 404–406. URL: `http://www.jetpletters.ac.ru/ps/1240/article{\_}18763.pdf` (cited on pages 19, 21).

[109] J Zhou, J. Petross, M. M. Murnane, and H. C. Kapteyn. Enhanced high harmonic generation using 25 femtosecond laser pulses. *Phys. Rev. Lett.*, 76, **1996**, 752. URL: `http://dx.doi.org/10.1103/PhysRevLett.76.752` (cited on page 19).

[110] X. Zhang, A. R. Libertun, A. Paul, E. Gagnon, S. Backus, I. P. Christov, M. M. Murnane, H. C. Kapteyn, R. A. Bartels, Y. Liu, and D. T. Attwood. Highly coherent light at 13 nm generated by use of quasi-phase-matched high-harmonic generation. *Opt. Lett.*, 29 (12), **2004**, 1357. DOI: `10.1364/ol.29.001357` (cited on pages 19, 21).

[111] C. Spielmann, N. H. Burnett, S Sartania, R Koppitsch, M Schnürer, C Kan, M Lenzner, P Wobrauschek, and F Krausz. Generation of Coherent X-rays in the Water Window Using 5-Femtosecond Laser Pulses. *Science (80-.).*, 278 (5338), **1997**, 661 LP –664. DOI: `10.1126/science.278.5338.661` (cited on page 19).

[112] M Schnürer, C. Spielmann, P Wobrauschek, C Streli, N. H. Burnett, C Kan, K Ferencz, R Koppitsch, Z Cheng, T Brabec, and F Krausz. Coherent 0.5-keV X-Ray Emission from Helium Driven by a Sub-10-fs Laser. *Phys. Rev. Lett.*, 80 (15), **1998**, 3236–3239. DOI: `10.1103/PhysRevLett.80.3236` (cited on page 19).

[113] A. Rundquist, C. G. Durfee, Z. Chang, C. Herne, S. Backus, M. M. Murnane, and H. C. Kapteyn. Phase-Matched Generation of Coherent Soft X-rays. *Science (80-.).*, 280 (5368), **1998**, 1412–1415. DOI: `10.1126/science.280.5368.1412` (cited on pages 19, 21, 66, 84).

[114] R. A. Bartels, A. Paul, H. Green, H. C. Kapteyn, S. Backus, M. M. Murnane, I. P. Christov, Y. Liu, D. Attwood, and C. Jacobsen. Generation of Spatially Coherent Light at Extreme Ultraviolet Wavelengths. *Science (80-.).*, 297 (5580), **2002**, 376–378. DOI: `10.1126/science.1071718` (cited on pages 19, 21, 84).

[115] E. A. Gibson, A. Paul, N. Wagner, R. Tobey, D. Gaudiosi, S. Backus, I. P. Christov, A. Aquila, E. M. Gullikson, D. T. Attwood, M. M. Murnane, and H. C. Kapteyn. Coherent soft x-ray generation in the water window with quasi-phase matching. *Science (80-.).*, 302 (5642), **2003**, 95–98. DOI: `10.1126/science.1088654` (cited on page 19).

[116] H. C. Kapteyn, M. M. Murnane, and I. P. Christov. Extreme nonlinear optics: coherent x rays from lasers. *Phys. Today*, 58 (3), **2005**, 39. DOI: `10.1063/1.1897563` (cited on page 19).

[117] L. V. Keldysh. Ionization in the field of a strong electromagnetic wave. *JETP*, 20 (5), **1965**, 1307–1314 (cited on page 20).

[118] A. M. Perelomov, V. S. Popov, and M. V. Terent'ev. Ionization of atoms in an alternating electric field. *J. Exptl. Theor. Phys*, 50 (5), **1966**, 925–934. URL: `http://www.jetp.ac.ru/cgi-bin/e/index/e/23/5/p924?a=list` (cited on page 20).

[119] A. M. Perelomov, V. S. Popov, and M. V. Terent'ev. Ionization of atoms in alternating electric fields: II. *J. Exptl. Theor. Phys*, 24 (1), **1967**, 207–217. URL: `http://www.jetp.ac.ru/cgi-bin/e/index/e/24/1/p207?a=list` (cited on page 20).

[120] A. M. Perelomov and V. S. Popov. Ionization of atoms in an alternating electrical field: II. *J. Exptl. Theor. Phys.*, 25 (2), **1967**, 336–343 (cited on page 20).

[121] F. H. M. Faisal. Multiple absorption of laser photons by atoms. *J. Phys. B At. Mol. Phys.*, 6 (4), **1973**, L89–L92. DOI: `10.1088/0022-3700/6/4/011` (cited on page 20).

[122] P Agostini, F Fabre, G Mainfray, G Petite, and N. K. Rahman. Free-Free Transitions Following Six-Photon Ionization of Xenon Atoms. *Phys. Rev. Lett.*, 42 (17), **1979**, 1127–1130. DOI: `10.1103/PhysRevLett.42.1127` (cited on page 20).

[123] P Agostini and G Petite. Photoelectric effect under strong irradiation. *Contemp. Phys.*, 29 (1), **1988**, 57–77. DOI: `10.1080/00107518808213751` (cited on page 20).

[124] G. Petite, P. Agostini, and F. Yergeau. Intensity, pulse width, and polarization dependence of above-threshold-ionization electron spectra. *J. Opt. Soc. Am. B*, 4 (5), **1987**, 765–769. DOI: `10.1364/JOSAB.4.000765` (cited on page 20).

[125] M. V. Ammosov, N. B. Delone, and V. P. Krainov. Tunnel ionization of complex atoms and of atomic ions in an alternating electromagnetic field. *Zh. Eksp. Teor. Fiz.*, 91, **1986**, 2008–2013 (cited on page 21).

[126] H. R. Reiss. Effect of an intense electromagnetic field on a weakly bound system. *Phys. Rev. A*, 22 (5), **1980**, 1786–1813. DOI: `10.1103/PhysRevA.22.1786` (cited on page 21).

[127] A. McPherson, G. Gibson, H. Jara, U. Johann, T. S. Luk, I. A. McIntyre, K. Boyer, and C. K. Rhodes. Studies of multiphoton production of vacuum-ultraviolet radiation in the rare gases. *J. Opt. Soc. Am. B*, 4 (4), **1987**, 595. DOI: `10.1364/JOSAB.4.000595` (cited on pages 21, 25, 50, 66).

[128] M Ferray, A. L'Huilleier, X. F. Li, L. A. Lompre, G. Mainfray, and C Manus. Multiple-harmonic conversion of 1064 nm radiation in rare gases. *J. Phys. B At. Mol. Opt. Phys.*, 21, **1988**, L31–L35. DOI: `https://doi.org/10.1088/0953-4075/21/3/001` (cited on pages 21, 25, 50, 66).

[129] R Rosman, G Gibson, K Boyer, H Jara, T. S. Luk, I. A. McIntyre, A McPherson, J. C. Solem, and C. K. Rhodes. Fifth-harmonic production in neon and argon with picosecond 248-nm radiation. *J. Opt. Soc. Am. B*, 5 (6), **1988**, 1237–1242. DOI: `10.1364/JOSAB.5.001237` (cited on page 21).

[130] C. G. Durfee, A. R. Rundquist, S. Backus, C. Herne, M. M. Murnane, and H. C. Kapteyn. Phase matching of high-order harmonics in hollow waveguides. *Phys. Rev. Lett.*, 83 (11), **1999**, 2187. URL: `http://dx.doi.org/10.1103/PhysRevLett.83.2187` (cited on page 21).

[131] E. Constant, D. Garzella, P. Breger, E. Mével, C. Dorrer, C. Le Blanc, F. Salin, and P. Agostini. Optimizing high harmonic generation in absorbing gases: Model and experiment. *Phys. Rev. Lett.*, 82 (8), **1999**, 1668–1671. DOI: `10.1103/PhysRevLett.82.1668` (cited on page 21).

[132] A. Rundquist. Phase-Match Generation of Coherent, Ultrafast X-rays using High Harmonics. PhD thesis. University of Colorado Boulder, 1998 (cited on page 21).

[133] T. Popmintchev, M.-c. Chen, O. Cohen, M. E. Grisham, J. J. Rocca, M. M. Murnane, and H. C. Kapteyn. Extended phase matching of high hsarmonics driven by mid-infrared light. *Opt. Lett.*, 33 (18), **2008**, 2128–2130 (cited on page 21).

[134] T. Popmintchev, M.-C. Chen, A. Bahabad, M. Gerrity, P. Sidorenko, O. Cohen, I. P. Christov, M. M. Murnane, and H. C. Kapteyn. Phase matching of high harmonic generation in the soft and hard X-ray regions of the spectrum. *Proc. Natl. Acad. Sci. U.S.A.*, 106 (26), **2009**, 10516–21. URL: `http://www.pnas.org/content/106/26/10516.abstract` (cited on page 21).

[135] M.-C. Chen, P. Arpin, T. Popmintchev, M. Gerrity, B. Zhang, M. Seaberg, D. Popmintchev, M. M. Murnane, and H. C. Kapteyn. Bright, Coherent, Ultrafast Soft X-Ray Harmonics Spanning the Water Window from a Tabletop Light Source. *Phys. Rev. Lett.*, 105 (17), **2010**, 173901. URL: `http://link.aps.org/doi/10.1103/PhysRevLett.105.173901` (cited on page 21).

[136] M.-C. Chen, C. A. Mancuso, C. Hernandez-Garcia, F. Dollar, B. Galloway, D. Popmintchev, P.-C. Huang, B. Walker, L. Plaja, A. A. Jaroń-Becker, A. Becker, M. M. Murnane, H. C. Kapteyn, and T. Popmintchev. Generation of bright isolated attosecond soft X-ray pulses driven by multicycle midinfrared lasers. *Proc. Natl Acad. Sci. USA*, 111, **2014**, E2361. URL: `http://dx.doi.org/10.1073/pnas.1407421111` (cited on page 21).

[137] T. Popmintchev, M.-C. Chen, D. Popmintchev, P. Arpin, S. Brown, S. Alisauskas, G. Andriukaitis, T. Balciunas, O. D. Mucke, A. Pugzlys, A. Baltuska, B. Shim, S. E. Schrauth, A. Gaeta, C. Hernandez-Garcia, L. Plaja, A. Becker, A. Jaron-Becker, M. M. Murnane, and H. C. Kapteyn. Bright Coherent Ultrahigh Harmonics in the keV X-ray Regime from Mid-Infrared Femtosecond Lasers. *Science (80-.).*, 336 (6086), **2012**, 1287–1291. DOI: `10.1126/science.1218497` (cited on pages 21, 84).

[138] M. Lewenstein, P. Balcou, M. Y. Ivanov, A. L'Huillier, and P. B. Corkum. Theory of high-harmonic generation by low-frequency laser fields. *Phys. Rev. A*, 49 (3), **1994**, 2117–2132. DOI: `10.1103/PhysRevA.49.2117`. arXiv: `1106.1603` (cited on pages 21, 23, 108).

[139] A. L'Huillier, M Lewenstein, P Salières, P. Balcou, M. Y. Ivanov, J Larsson, and C. G. Wahlström. High-order Harmonic-generation cutoff. *Phys. Rev. A*, 48 (5), **1993**, R3433–R3436. DOI: `10.1103/PhysRevA.48.R3433` (cited on pages 21, 23).

[140] T. W. Hänsch. A proposed sub-femtosecond pulse synthesizer using separate phase-locked laser oscillators. *Opt. Commun.*, 80 (1), **1990**, 71–75. DOI: `https://doi.org/10.1016/0030-4018(90)90509-R` (cited on page 21).

[141] P. Antoine, A. L'Huillier, and M. Lewenstein. Attosecond Pulse Trains Using High–Order Harmonics. *Phys. Rev. Lett.*, 77 (7), **1996**, 1234–1237. DOI: `10.1103/PhysRevLett.77.1234` (cited on pages 21, 24).

[142] Paul, P M., Toma, E S., Breger, P., Mullot, G., Auge, F., Balcou, Muller, H G., and Agostini. Observation of a Train of Attosecond Pulses from High Harmonic Generation. *Science (80-.).*, 292 (5522), **2001**, 1689–1692. DOI: `10.1126/science.1059413` (cited on pages 22, 84).

[143] M Hentschel, R Kienberger, C. Spielmann, G. A. Reider, N Milosevic, T Brabec, P Corkum, U Heinzmann, M Drescher, and F Krausz. Attosecond metrology. *Nature*, 414, **2001**, 509. URL: `https://doi.org/10.1038/35107000http://10.0.4.14/35107000` (cited on page 22).

[144] I. P. Christov, M. M. Murnane, and H. C. Kapteyn. High-harmonic generation of attosecond pulses in the "single-cycle" regime. *Phys. Rev. Lett.*, 78 (7), **1997**, 1251–1254. DOI: 10.1103/PhysRevLett.78.1251 (cited on pages 22, 97).

[145] C. Chen, Z. Tao, C. Hernández-García, P. Matyba, A. Carr, R. Knut, O. Kfir, D. Zusin, C. Gentry, P. Grychtol, O. Cohen, L. Plaja, A. Becker, A. Jaron-Becker, H. Kapteyn, and M. Murnane. Tomographic reconstruction of circularly polarized high-harmonic fields: 3D attosecond metrology. en. *Sci. Adv.*, 2 (2), **2016**, e1501333. URL: http://advances.sciencemag.org/content/2/2/e1501333.abstract (cited on pages 22, 51, 52, 70, 74, 106).

[146] L. Plaja, R. Torres, and A. Zaïr. **Attosecond Physics**. Ed. by L. Plaja, R. Torres, and A. Zaïr. 1st. Vol. 177. Berlin-Heidelberg, 2013, pp. 3–7. DOI: 10.1007/978-3-642-37623-8 (cited on page 23).

[147] F. Krausz and M. Ivanov. Attosecond physics. *Rev. Mod. Phys.*, 81 (1), **2009**, 163–234. DOI: 10.1103/RevModPhys.81.163 (cited on page 23).

[148] L. Gallmann, C. Cirelli, and U. Keller. Attosecond Science: Recent Highlights and Future Trends. *Annu. Rev. Phys. Chem.*, 63 (1), **2012**, 447–469. DOI: 10.1146/annurev-physchem-032511-143702 (cited on page 23).

[149] G. Sansone, L. Poletto, and M. Nisoli. High-energy attosecond light sources. *Nat. Photonics*, 5, **2011**, 655. URL: https://doi.org/10.1038/nphoton.2011.167http://10.0.4.14/nphoton.2011.167 (cited on page 23).

[150] M. F. Ciappina, J. A. Pérez-Hernández, A. S. Landsman, W. A. Okell, S Zherebtsov, B Förg, J Schötz, L Seiffert, T Fennel, T Shaaran, T Zimmermann, A Chacón, R Guichard, A Zaïr, J. W. G. Tisch, J. P. Marangos, T Witting, A Braun, S. A. Maier, L Roso, M Krüger, P Hommelhoff, M. F. Kling, F Krausz, and M Lewenstein. Attosecond physics at the nanoscale. *Reports Prog. Phys.*, 80 (5), **2017**, 54401. DOI: 10.1088/1361-6633/aa574e (cited on page 23).

[151] L. Young, K. Ueda, M. Gühr, P. H. Bucksbaum, M. Simon, S. Mukamel, N. Rohringer, K. C. Prince, C. Masciovecchio, M. Meyer, A. Rudenko, D. Rolles, C. Bostedt, M. Fuchs, D. A. Reis, R. Santra, H. Kapteyn, M. Murnane, H. Ibrahim, F. Légaré, M. Vrakking, M. Isinger, D. Kroon, M. Gisselbrecht, A. L'Huillier, H. J. Wörner, and S. R. Leone. Roadmap of ultrafast x-ray atomic and molecular physics. *J. Phys. B At. Mol. Opt. Phys.*, 51 (3), **2018**, 32003. DOI: 10.1088/1361-6455/aa9735 (cited on page 23).

[152] S. Ghimire and D. A. Reis. High-harmonic generation from solids. *Nat. Phys.*, 15 (1), **2019**, 10–16. DOI: 10.1038/s41567-018-0315-5 (cited on page 23).

[153] M. Lewenstein, P. Salières, and A. L'Huillier. Phase of the atomic polarization in high-order harmonic generation. *Phys. Rev. A*, 52 (6), **1995**, 4747–4754. DOI: 10.1111/j.1749-6632.1965.tb20242.x (cited on pages 23, 64).

[154] P. Salières, B. Carré, L. L. Déroff, F. Grasbon, G. Paulus, H. Walther, R. Kopold, W. Becker, D. Milošević, A. Sanpera, and M. Lewenstein. Feynman's Path-Integral Approach for Intense-Laser-Atom Interactions. *Science (80-.).*, 292 (5518), **2001**, 902–906. DOI: 10.1126/science.108836 (cited on page 23).

[155] C. Hernández-García, J. A. Pérez-Hernández, J. Ramos, E. C. Jarque, L. Roso, and L. Plaja. High-order harmonic propagation in gases within the discrete dipole approximation. *Phys. Rev. A - At. Mol. Opt. Phys.*, 82 (3), **2010**, 1–11. DOI: 10.1103/PhysRevA.82.033432 (cited on pages 25, 56, 68, 70, 88, 89, 105, 116).

[156] K. S. Budil, P Salières, A. L'Huillier, T Ditmire, and M. D. Perry. Influence of ellipticity on harmonic generation. *Phys. Rev. A*, 48 (5), **1993**, R3437–R3440. DOI: 10.1103/PhysRevA.48.R3437 (cited on page 25).

[157] F. A. Weihe and P. H. Bucksbaum. Measurement of the polarization state of high harmonics generated in gases. *J. Opt. Soc. Am. B*, 13 (1), **1996**, 157–161. DOI: 10.1364/JOSAB.13.000157 (cited on page 25).

[158] H. Eichmann, A. Egbert, S. Nolte, C. Momma, B. Wellegehausen, W. Becker, S. Long, and J. K. McIver. Polarization-dependent high-order two-color mixing. *Phys. Rev. A*, 51 (5), **1995**, R3414(R). URL: http://journals.aps.org/pra/abstract/10.1103/PhysRevA.51.R3414 (cited on pages 25, 50, 65, 73).

[159] D. B. Milosevic, W. Becker, and R. Kopold. Generation of circularly polarized high-order harmonics by two-color coplanar field mixing. *Phys. Rev. A*, 61, **2000**, 063403. URL: http://journals.aps.org/pra/abstract/10.1103/PhysRevA.61.063403 (cited on pages 25, 50, 52, 73, 74).

[160] D. B. Milošević and W. Becker. Attosecond pulse trains with unusual nonlinear polarization. *Phys. Rev. A - At. Mol. Opt. Phys.*, 62 (1), **2000**, 4. DOI: 10.1103/PhysRevA.62.011403 (cited on pages 25, 50, 52, 74).

[161] A. Fleischer, O. Kfir, T. Diskin, P. Sidorenko, and O. Cohen. Spin angular momentum and tunable polarization in high-harmonic generation. *Nat. Photonics*, 8 (7), **2014**, 543–549. URL: http://dx.doi.org/10.1038/nphoton.2014.108 (cited on pages 25, 50, 65, 66, 73).

[162] O. Kfir, P. Grychtol, E. Turgut, R. Knut, D. Zusin, D. Popmintchev, T. Popmintchev, H. Nembach, J. M. Shaw, A. Fleischer, H. Kapteyn, M. Murnane, and O. Cohen. Generation of bright phase-matched circularly-polarized extreme ultraviolet high harmonics. *Nat. Photonics*, 9 (2), **2015**, 99–105. DOI: 10.1038/nphoton.2014.293. arXiv: 1401.4101 (cited on pages 25, 46, 50–52).

[163] A. Ferré, C. Handschin, M. Dumergue, F. Burgy, A. Comby, D. Descamps, B. Fabre, G. A. Garcia, R. Géneaux, L. Merceron, E. Mével, L. Nahon, S. Petit, B. Pons, D. Staedter, S. Weber, T. Ruchon, V. Blanchet, and Y. Mairesse. A table-top ultrashort light source in the extreme ultraviolet for circular dichroism experiments. *Nat. Photonics*, 9 (2), **2015**, 93–98. DOI: 10.1038/nphoton.2014.314 (cited on pages 25, 50, 65, 73).

[164] E. Pisanty, S. Sukiasyan, and M. Ivanov. Spin conservation in high-order-harmonic generation using bicircular fields. *Phys. Rev. A - At. Mol. Opt. Phys.*, 90 (4), **2014**, 1–7. DOI: 10.1103/PhysRevA.90.043829 (cited on pages 25, 51, 52, 71, 74, 102).

[165] P.-C. Huang, C. Hernández-García, J.-T. Huang, P.-Y. Huang, C.-H. Lu, L. Rego, D. D. Hickstein, J. L. Ellis, A. Jaron-Becker, A. Becker, S.-D. Yang, C. G. Durfee, L. Plaja, H. C. Kapteyn, M. M. Murnane, A. H. Kung, and M.-C. Chen. Polarization control of isolated high-harmonic pulses. *Nat. Photonics*, **2018**. DOI: 10.1038/s41566-018-0145-0 (cited on pages 27, 46, 52, 65, 66, 70, 73, 74).

[166] D. Baykusheva, M. S. Ahsan, N. Lin, and H. J. Wörner. Bicircular High-Harmonic Spectroscopy Reveals Dynamical Symmetries of Atoms and Molecules. *Phys. Rev. Lett.*, 116 (12), **2016**, 123001. URL: `https://journals.aps.org/prl/abstract/10.1103/PhysRevLett.116.123001` (cited on pages 27, 52).

[167] D. Baykusheva and H. J. Wörner. Chiral Discrimination through Bielliptical High-Harmonic Spectroscopy. *Phys. Rev. X*, 8 (3), **2018**, 31060. DOI: `10.1103/PhysRevX.8.031060` (cited on pages 27, 52).

[168] F. Mauger, A. D. Bandrauk, and T. Uzer. Circularly polarized molecular high harmonic generation using a bicircular laser. *J. Phys. B At. Mol. Opt. Phys.*, 49 (10), **2016**. DOI: `10.1088/0953-4075/49/10/10LT01`. arXiv: `1501.02557` (cited on pages 27, 52).

[169] S. Patchkovskii and M. Spanner. High harmonics with a twist. *Nat. Phys.*, 8 (10), **2012**, 707–708. DOI: `10.1038/nphys2415` (cited on page 27).

[170] C. Hernández-García, J. S. Román, L. Plaja, and A. Picón. Quantum-path signatures in attosecond helical beams driven by optical vortices. *New J. Phys.*, 17 (9), **2015**. DOI: `10.1088/1367-2630/17/9/093029` (cited on pages 27, 64, 70, 73, 74, 78, 89, 118, 119, 130).

[171] L. Rego, J. S. Román, A. Picón, L. Plaja, and C. Hernández-García. Nonperturbative twist in the generation of extreme-ultraviolet vortex beams. *Phys. Rev. Lett.*, 117 (16), **2016**, 1–6. DOI: `10.1103/PhysRevLett.117.163202` (cited on pages 28, 64, 65, 69–72, 74, 78, 83, 89–91, 102, 118, 125, 126, 130, 137).

[172] A. Turpin, L. Rego, A. Picón, J. San Román, and C. Hernández-García. Extreme Ultraviolet Fractional Orbital Angular Momentum Beams from High Harmonic Generation. *Sci. Rep.*, 7, **2017**, 1–10. DOI: `10.1038/srep43888` (cited on pages 28, 64, 65, 70, 83, 89, 92, 118).

[173] C. Ding, W. Xiong, T. Fan, D. D. Hickstein, T. Popmintchev, X. Zhang, M. Walls, M. M. Murnane, and H. C. Kapteyn. High flux coherent super-continuum soft X-ray source driven by a single-stage, 10mJ, Ti:sapphire amplifier-pumped OPA. *Opt. Express*, 22 (5), **2014**, 6194. DOI: `10.1364/oe.22.006194` (cited on pages 30, 67, 85).

[174] C Ding. Bright Coherent Ultrafast Tabletop Light Sources Development and the Application on EUV to Soft X-Ray Absorption Spectroscopy. PhD Thesis. University of Colorado Boulder, 2014, pp. 596–605. DOI: `10.1107/S010876730001031X` (cited on pages 30, 67, 85).

[175] D. Strickland and G. Mourou. 1-S2.0-0030401885901208-Main.Pdf. *Opt. Commun.*, 56 (3), **1985**, 219–221 (cited on pages 31, 35).

[176] R. M. Wilson. Half of Nobel Prize in Physics honors the inventors of chirped pulse amplification. *Phys. Today*, 71 (12), **2018**, 18–21. DOI: `10.1063/PT.3.4086` (cited on pages 31, 35).

[177] I. Shchatsinin. Free Clusters and Free Molecules in Strong, Shaped Laser Fields. PhD. Freie Universitat Berlin, 2009. URL: `https://refubium.fu-berlin.de/handle/fub188/8219` (cited on page 31).

[178] S. Backus, C. G. Durfee, M. M. Murnane, and H. C. Kapteyn. High power ultrafast lasers. *Rev. Sci. Instrum.*, 69 (3), **1998**, 1207–1223. DOI: `10.1063/1.1148795` (cited on pages 31, 35).

[179] R. Trebino. **Frequency-Resolved Optical Gating: The Measurement of Ultrashort Laser Pulses**. 1st Editio. New York: Springer Science+Business Media, 2002. DOI: 10.1007/978-1-4615-1181-6 (cited on pages 31, 44, 45).

[180] G. Herink, B. Jalali, C. Ropers, and D. R. Solli. Resolving the build-up of femtosecond mode-locking with single-shot spectroscopy at 90 €...MHz frame rate. *Nat. Photonics*, 10 (5), **2016**, 321–326. DOI: 10.1038/nphoton.2016.38 (cited on page 32).

[181] J. K. LL.D. A new relation between electricity and light: Dielectrified media birefringent. *London, Edinburgh, Dublin Philos. Mag. J. Sci.*, 50 (332), **1875**, 337–348. DOI: 10.1080/14786447508641302 (cited on page 32).

[182] S. Backus, J. Peatross, C. P. Huang, M. M. Murnane, and H. C. Kapteyn. Ti:sapphire amplifier producing millijoule-level, 21-fs pulses at 1 kHz. *Opt. Lett.*, 20 (19), **2008**, 2000. DOI: 10.1364/ol.20.002000 (cited on page 35).

[183] J. Zhou, C.-P. Huang, C. Shi, M. M. Murnane, and H. C. Kapteyn. Generation of 21-fs millijoule-energy pulses by use of Ti:sapphire. *Opt. Lett.*, 19 (2), **2008**, 126. DOI: 10.1364/ol.19.000126 (cited on page 35).

[184] O. Kfir, P. Grychtol, E. Turgut, R. Knut, D. Zusin, A. Fleischer, E. Bordo, T. Fan, D. Popmintchev, T. Popmintchev, H. Kapteyn, M. Murnane, and O. Cohen. Helicity-selective phase-matching and quasi-phase matching of circularly polarized high-order harmonics: Towards chiral attosecond pulses. *J. Phys. B At. Mol. Opt. Phys.*, 49 (12), **2016**. DOI: 10.1088/0953-4075/49/12/123501 (cited on pages 37, 51, 52, 56, 100, 102, 106, 123).

[185] M. D. Seaberg. Nanoscale EUV Microscopy on a Tabletop. PhD thesis. University of Colorado Boulder, 2014 (cited on pages 39, 88, 134).

[186] J. Hartmann. Bemerkungen über den bau und die justirung von spektrographen. *Zeitschrift für Instrumentenkd.*, 20, **1900**, 47–58 (cited on page 42).

[187] R. J. Collier. Program of the 1971 Spring Meeting of the Optical Society of America. *J. Opt. Soc. Am.*, 61 (5), **1971**, 648–697. DOI: 10.1364/JOSA.61.000648 (cited on page 42).

[188] B. Platt and R. Shack. History and principles of Shack-Hartmann wavefront sensing. *J. Refract. Surg.*, 17 (5), **2001**, 573–577. URL: http://www.mpia-hd.mpg.de/AO/INSTRUMENTS/FPRAKT/HistoryOfShackHartmann.pdf (cited on page 42).

[189] H. Dacasa, H. Coudert-Alteirac, C. Guo, E. Kueny, F. Campi, J. Lahl, J. Peschel, H. Wikmark, B. Major, E. Malm, D. Alj, K. Varjú, C. L. Arnold, G. Dovillaire, P. Johnsson, A. L'Huillier, S. Maclot, P. Rudawski, and P. Zeitoun. Single-shot extreme-ultraviolet wavefront measurements of high-order harmonics. *Opt. Express*, 27 (3), **2019**, 2656. DOI: 10.1364/oe.27.002656 (cited on page 42).

[190] Y. Wang, T. Guo, J. Li, J. Zhao, Y. Yin, X. Ren, J. Li, Y. Wu, M. Weidman, Z. Chang, M. F. Jager, C. J. Kaplan, R. Geneaux, C. Ott, D. M. Neumark, and S. R. Leone. Enhanced high-order harmonic generation driven by a wavefront corrected high-energy laser. *J. Phys. B At. Mol. Opt. Phys.*, 51 (13), **2018**, 134005. DOI: 10.1088/1361-6455/aac59e (cited on page 42).

[191] D. G. Lee, J. J. Park, J. H. Sung, and C. H. Nam. Wave-front phase measurements of high-order harmonic beams by use of point-diffraction interferometry. *Opt. Lett.*, 28 (6), **2007**, 480. DOI: 10.1364/ol.28.000480 (cited on page 42).

[192] L. Freisem, G. S. M. Jansen, D. Rudolf, K. S. E. Eikema, and S. Witte. Spectrally resolved single-shot wavefront sensing of broadband high-harmonic sources. *Opt. Express*, 26 (6), **2017**, 1317–1320. DOI: 10.1364/OE.26.006860 (cited on page 42).

[193] J. Gautier, P. Zeitoun, C. Hauri, A. S. Morlens, G. Rey, C. Valentin, E. Papalarazou, J. P. Goddet, S. Sebban, F. Burgy, P. Mercère, M. Idir, G. Dovillaire, X. Levecq, S. Bucourt, M. Fajardo, H. Merdji, and J. P. Caumes. Optimization of the wave front of high order harmonics. *Eur. Phys. J. D*, 48 (3), **2008**, 459–463. DOI: 10.1140/epjd/e2008-00123-2 (cited on page 42).

[194] B. R. W. Gerchberg and W. O. Saxton. A Practical Algorithm for the Determination of Phase from Image and Diffraction Plane Pictures. *Optik (Stuttg).*, 35 (2), **1972**, 237–246. DOI: 10.1070/QE2009v039n06ABEH013642 (cited on page 42).

[195] J. R. Fienup. Phase retrieval algorithms: a comparison. *Appl. Opt.*, 21 (15), **2009**, 2758. DOI: 10.1364/ao.21.002758. arXiv: 1403.3316 (cited on page 42).

[196] H. Chang, X.-l. Yin, X.-z. Cui, Z.-c. Zhang, J.-x. Ma, L.-j. Wu, Guo-huaZhang, and X.-j. Xin. Adaptive optics compensation of orbital angular momentum beams with a modified Gerchberg–Saxton-based phase retrieval algorithm. *Opt. Commun.*, 405 (September), **2017**, 271–275. DOI: 10.1016/j.optcom.2017.08.035 (cited on pages 44, 134, 136).

[197] S. Fu, S. Zhang, T. Wang, and C. Gao. Pre-turbulence compensation of orbital angular momentum beams based on a probe and the Gerchberg–Saxton algorithm. *Opt. Lett.*, 41 (14), **2016**, 3185. DOI: 10.1364/ol.41.003185 (cited on pages 44, 134, 136).

[198] R. Trebino and D. J. Kane. Using phase retrieval to measure the intensity and phase of ultrashort pulses: frequency-resolved optical gating. *J. Opt. Soc. Am. A*, 10 (5), **1993**, 1101. DOI: 10.1364/josaa.10.001101 (cited on page 44).

[199] E. Rubino, J. Biegert, L. Tartara, O. Chalus, M. Clerici, P. Di Trapani, D. Faccio, F. Bonaretti, and P. K. Bates. Spatiotemporal amplitude and phase retrieval of space-time coupled ultrashort pulses using the Shackled-FROG technique. *Opt. Lett.*, 34 (24), **2009**, 3854. DOI: 10.1364/ol.34.003854 (cited on page 45).

[200] F. Bonaretti, D. Faccio, M. Clerici, J. Biegert, and P. Di Trapani. Spatiotemporal Amplitude and Phase Retrieval of Bessel-X pulses using a Hartmann-Shack Sensor. *Opt. Express*, 17 (12), **2009**, 9804. DOI: 10.1364/oe.17.009804 (cited on page 45).

[201] S. L. Cousin, J. M. Bueno, N. Forget, D. R. Austin, and J. Biegert. Three-dimensional spatiotemporal pulse characterization with an acousto-optic pulse shaper and a Hartmann–Shack wavefront sensor. *Opt. Lett.*, 37 (15), **2013**, 3291. DOI: 10.1364/ol.37.003291 (cited on page 45).

[202] H. Valtna-Lukner, P. Bowlan, M. Lõhmus, P. Piksarv, R. Trebino, and P. Saari. Direct spatiotemporal measurements of accelerating ultrashort Bessel-type light bullets. *Opt. Express*, 17 (17), **2013**, ThE20. DOI: 10.1364/up.2010.the20. arXiv: 0905.4381 (cited on page 45).

[203] R. Grunwald, T. Elsaesser, and M. Bock. Spatiooral coherence mapping of few-cycle vortex pulses. *Sci. Rep.*, 4, **2014**, 1–7. DOI: 10.1038/srep07148 (cited on page 45).

[204] L. J. Pereira, W. T. Buono, D. S. Tasca, K. Dechoum, and A. Z. Khoury. Orbital-angular-momentum mixing in type-II second-harmonic generation. *Phys. Rev. A*, 96 (5), **2017**, 1–8. DOI: 10.1103/PhysRevA.96.053856 (cited on page 45).

[205] K. Veyrinas, C. Elkharrat, S. Marggi Poullain, N. Saquet, D. Dowek, R. R. Lucchese, G. A. Garcia, and L. Nahon. Complete determination of the state of elliptically polarized light by electron-ion vector correlations. *Phys. Rev. A - At. Mol. Opt. Phys.*, 88 (6), **2013**, 1–5. DOI: 10.1103/PhysRevA.88.063411 (cited on page 46).

[206] Á. Jiménez-Galán, G. Dixit, S. Patchkovskii, O. Smirnova, F. Morales, and M. Ivanov. Attosecond recorder of the polarization state of light. *Nat. Commun.*, 9 (1), **2018**, 1–6. DOI: 10.1038/s41467-018-03167-2 (cited on page 46).

[207] L. Barreau, K. Veyrinas, V. Gruson, S. J. Weber, T. Auguste, J. F. Hergott, F. Lepetit, B. Carré, J. C. Houver, D. Dowek, and P. Salières. Evidence of depolarization and ellipticity of high harmonics driven by ultrashort bichromatic circularly polarized fields. *Nat. Commun.*, 9 (1), **2018**, 1–10. DOI: 10.1038/s41467-018-07151-8 (cited on pages 46, 52).

[208] T. Koide, T. Shidara, M. Yuri, N. Kandaka, K. Yamaguchi, and H. Fukutani. Elliptical-polarization analyses of synchrotron radiation in the 5-80-eV region with a reflection polarimeter. *Nucl. Inst. Methods Phys. Res. A*, 308 (3), **1991**, 635–644. DOI: 10.1016/0168-9002(91)90077-4 (cited on page 46).

[209] S. Valencia, A. Gaupp, W. Gudat, H. C. Mertins, P. M. Oppeneer, D. Abramsohn, and C. M. Schneider. Faraday rotation spectra at shallow core levels: 3p edges of Fe, Co, and Ni. *New J. Phys.*, 8, **2006**. DOI: 10.1088/1367-2630/8/10/254 (cited on pages 46, 47).

[210] P. M. Oppeneer. **Handbook of magnetic materials**. Ed. by K. Buschow. 1st. North Holland, 2001, pp. 229–442. URL: https://www.elsevier.com/books/handbook-of-magnetic-materials/buschow/978-0-444-50666-5 (cited on page 46).

[211] F Willems, S Sharma, J. K. Dewhurst, D Schick, P Hessing, W. D. Engel, and S Eisebitt. Magneto-Optical Functions at the 3 p resonances of Fe, Co, and Ni: Ab-initio description and experiment. *ArXiv*, **2018**, 1–14. URL: https://arxiv.org/abs/1812.06703. arXiv: arXiv:1812.06703v1 (cited on page 47).

[212] C. A. Mancuso, D. D. Hickstein, K. M. Dorney, J. L. Ellis, E. Hasović, R. Knut, P. Grychtol, C. Gentry, M. Gopalakrishnan, D. Zusin, F. J. Dollar, X.-M. Tong, D. B. Milošević, W. Becker, H. C. Kapteyn, and M. M. Murnane. Controlling electron-ion rescattering in two-color circularly polarized femtosecond laser fields. *Phys. Rev. A*, 93, **2016**, 053406 (cited on pages 49, 59).

[213] C. Hernández-García, C. G. Durfee, D. D. Hickstein, T. Popmintchev, A. Meier, M. M. Murnane, H. C. Kapteyn, I. J. Sola, A. Jaron-Becker, and A. Becker. Schemes for generation of isolated attosecond pulses of pure circular polarization. *Phys. Rev. A*, 93 (4), **2016**, 1–8. DOI: 10.1103/PhysRevA.93.043855 (cited on pages 50, 52, 70, 73).

[214] D. B. Miloević and W. Becker. Attosecond pulse generation by bicircular fields: From pulse trains to a single pulse. *J. Mod. Opt.*, 52 (2-3), **2005**, 233–241. DOI: `10.1080/09500340410001731011` (cited on page 51).

[215] L. Medišauskas, J. Wragg, H. Van Der Hart, and M. Y. Ivanov. Generating Isolated Elliptically Polarized Attosecond Pulses Using Bichromatic Counterrotating Circularly Polarized Laser Fields. *Phys. Rev. Lett.*, 115 (15), **2015**, 1–5. DOI: `10.1103/PhysRevLett.115.153001`. arXiv: `1504.06578` (cited on pages 51, 52, 57, 73, 108).

[216] D. B. Milošević. Generation of elliptically polarized attosecond pulse trains. *Opt. Lett.*, 40 (10), **2015**, 2381. DOI: `10.1364/OL.40.002381` (cited on pages 51, 52, 57, 73, 74, 106, 108, 109).

[217] G. Lerner, T. Diskin, O. Neufeld, O. Kfir, and O. Cohen. Selective suppression of high-order harmonics within phase-matched spectral regions. *Opt. Lett.*, 42 (7), **2017**, 1349. DOI: `10.1364/OL.42.001349` (cited on pages 51, 56).

[218] E. A. Pisanty. Electron dynamics in complex time and complex space. PhD thesis. Imperial College London, 2016 (cited on pages 51, 52).

[219] O. E. Alon, V. Averbukh, and N. Moiseyev. Selection Rules for High-Harmonic Generation Spectra. *Phys. Rev. Lett.*, 17 (80), **1998**, 3743–3746 (cited on pages 51, 52, 71, 106).

[220] O. Neufeld, D. Podolsky, and O. Cohen. Floquet group theory and its application to selection rules in harmonic generation. *Nat. Commun.*, 10 (1), **2019**, 405. DOI: `10.1038/s41467-018-07935-y` (cited on page 52).

[221] D. M. Reich and L. B. Madsen. Illuminating Molecular Symmetries with Bicircular High-Order-Harmonic Generation. *Phys. Rev. Lett.*, 117 (13), **2016**, 1–6. DOI: `10.1103/PhysRevLett.117.133902`. arXiv: `1606.05524` (cited on page 52).

[222] Á. Jiménez-Galán, N. Zhavoronkov, M. Schloz, F. Morales, and M. Ivanov. Time-resolved high harmonic spectroscopy of dynamical symmetry breaking in bi-circular laser fields. 25 (19), **2017**, 200–206. DOI: `10.1364/OE.25.022880`. arXiv: `1707.05590` (cited on pages 52, 54).

[223] D. Ayuso, P. Decleva, S. Patchkovskii, and O. Smirnova. Chiral dichroism in bi-elliptical high-order harmonic generation. *J. Phys. B At. Mol. Opt. Phys.*, 51 (6), **2018**. DOI: `10.1088/1361-6455/aaae5e` (cited on page 52).

[224] S. Long, W. Becker, and J. K. McIver. Model calculations of polarization-dependent two-color high-harmonic generation. *Phys. Rev. A*, 52 (3), **1995**, 2262–2278. DOI: `10.1103/PhysRevA.52.2262` (cited on page 52).

[225] O. Neufeld and O. Cohen. Optical Chirality in Nonlinear Optics: Application to High Harmonic Generation. *Phys. Rev. Lett.*, 120 (13), **2018**, 133206. DOI: `10.1016/j.cca.2008.03.021` (cited on page 52).

[226] Jiménez-Galán, N. Zhavoronkov, D. Ayuso, F. Morales, S. Patchkovskii, M. Schloz, E. Pisanty, O. Smirnova, and M. Ivanov. Control of attosecond light polarization in two-color bicircular fields. *Phys. Rev. A*, 97 (2), **2018**, 1–14. DOI: `10.1103/PhysRevA.97.023409`. arXiv: `1805.02250` (cited on pages 52, 57, 66, 73, 74, 107, 108).

[227] N. Zhavoronkov and M. Ivanov. Extended ellipticity control for attosecond pulses by high harmonic generation. *Opt. Lett.*, 42 (22), **2017**, 4720. DOI: 10.1364/OL.42.004720 (cited on page 52).

[228] G. Dixit, Á. Jiménez-Galán, L. Medišauskas, and M. Ivanov. Control of the helicity of high-order harmonic radiation using bichromatic circularly polarized laser fields. *Phys. Rev. A*, 98 (5), **2018**, 1–6. DOI: 10.1103/PhysRevA.98.053402. arXiv: $\backslash$ (cited on page 52).

[229] D. B. Milošević. Control of the helicity of high-order harmonics generated by bicircular laser fields. *Phys. Rev. A*, 98 (3), **2018**, 1–7. DOI: 10.1103/PhysRevA.98.033405. arXiv: 1808.09538 (cited on pages 52, 57, 107).

[230] D. B. Milošević. Quantum-orbit analysis of high-order harmonic generation by bicircular field. *J. Mod. Opt.*, 0340, **2019**. DOI: 10.1080/09500340.2018.1511862 (cited on pages 52, 57, 107).

[231] X. Zhu, P. Lan, K. Liu, Y. Li, X. Liu, Q. Zhang, I. Barth, and P. Lu. Helicity sensitive enhancement of strong-field ionization in circularly polarized laser fields. *Opt. Express*, 24 (4), **2016**, 4196. DOI: 10.1364/OE.24.004196 (cited on pages 52, 57).

[232] P. Salières, A. L'Huillier, and M. Lewenstein. Coherence control of high-order harmonics. *Phys. Rev. Lett.*, 74 (19), **1995**, 3776–3779. DOI: 10.1103/PhysRevLett.74.3776 (cited on page 53).

[233] M. Schnürer, Z. Cheng, M. Hentschel, G. Tempea, P. Kálmán, T. Brabec, and F. Krausz. Absorption-limited generation of coherent ultrashort soft-x-ray pulses. *Phys. Rev. Lett.*, 83 (4), **1999**, 722–725. DOI: 10.1103/PhysRevLett.83.722 (cited on page 53).

[234] S. Eckart, M. Richter, M. Kunitski, A. Hartung, J. Rist, K. Henrichs, N. Schlott, H. Kang, T. Bauer, H. Sann, L. P. H. Schmidt, M. Schöffler, T. Jahnke, and R. Dörner. Nonsequential Double Ionization by Counterrotating Circularly Polarized Two-Color Laser Fields. *Phys. Rev. Lett.*, 117 (13), **2016**, 1–6. DOI: 10.1103/PhysRevLett.117.133202. arXiv: 1606.07303 (cited on page 54).

[235] H Bethe and R Jackiw. **Intermediate Quantum Mechanics**. 3rd. Westview Press, 1997, Chap. 11. URL: https://www.crcpress.com/Intermediate-Quantum-Mechanics-Third-Edition/Jackiw/p/book/9780201328318 (cited on page 57).

[236] U. Fano. Propensity rules: An analytical approach. *Phys. Rev. A*, 32 (1), **1985**, 617–618. DOI: 10.1103/PhysRevA.32.617 (cited on page 57).

[237] I. Barth and O. Smirnova. Nonadiabatic tunneling in circularly polarized laser fields. II. Derivation of formulas. *Phys. Rev. A - At. Mol. Opt. Phys.*, 87 (1), **2013**, 1–16. DOI: 10.1103/PhysRevA.87.013433. arXiv: 1211.5541 (cited on page 57).

[238] I. Barth and O. Smirnova. Nonadiabatic tunneling in circularly polarized laser fields: Physical picture and calculations. *Phys. Rev. A - At. Mol. Opt. Phys.*, 84 (6), **2011**, 1–5. DOI: 10.1103/PhysRevA.84.063415. arXiv: 1304.4875 (cited on page 57).

[239] T. Herath, L. Yan, S. K. Lee, and W. Li. Strong-field ionization rate depends on the sign of the magnetic quantum number. *Phys. Rev. Lett.*, 109 (4), **2012**, 1–5. DOI: 10.1103/PhysRevLett.109.043004 (cited on pages 57, 107).

[240] T. Popmintchev, M. C. Chen, P. Arpin, M. M. Murnane, and H. C. Kapteyn. The attosecond nonlinear optics of bright coherent X-ray generation. *Nat. Photonics*, 4 (12), **2010**, 822–832. DOI: 10.1038/nphoton.2010.256 (cited on pages 64, 106, 108).

[241] K. Varjú, Y. Mairesse, B. Carré, M. B. Gaarde, P. Johnsson, S. Kazamias, R. López-Martens, J. Mauritsson, K. J. Schafer, P. Balcou, A. L'Huillier, and P. Salières. Frequency chirp of harmonic and attosecond pulses. *J. Mod. Opt.*, 52 (2-3), **2005**, 379–394. DOI: 10.1080/09500340412331301542 (cited on page 64).

[242] G. Pariente and F. Quéré. Spatio-temporal light springs: extended encoding of orbital angular momentum in ultrashort pulses. *Opt. Lett.*, 40 (9), **2015**, 2037. DOI: 10.1364/ol.40.002037 (cited on page 64).

[243] A. Denoeud, L. Chopineau, A. Leblanc, and F. Quéré. Interaction of Ultraintense Laser Vortices with Plasma Mirrors. *Phys. Rev. Lett.*, 118 (3), **2017**, 1–5. DOI: 10.1103/PhysRevLett.118.033902 (cited on page 64).

[244] G. F. Calvo, A. Picón, and R. Zambrini. Measuring the complete transverse spatial mode spectrum of a wave field. *Phys. Rev. Lett.*, 100 (17), **2008**, 8–11. DOI: 10.1103/PhysRevLett.100.173902 (cited on page 65).

[245] F. Cardano and L. Marrucci. Spin–orbit photonics. *Nat. Photonics*, 9 (12), **2015**, 776–778. DOI: 10.1038/nphoton.2015.232 (cited on page 65).

[246] S. Beaulieu, A. Comby, D. Descamps, B. Fabre, G. A. Garcia, R. Géneaux, A. G. Harvey, F. Légaré, Z. Mašín, L. Nahon, A. F. Ordonez, S. Petit, B. Pons, Y. Mairesse, O. Smirnova, and V. Blanchet. Photoexcitation circular dichroism in chiral molecules. *Nat. Phys.*, 14 (May), **2018**. DOI: 10.1038/s41567-017-0038-z (cited on pages 65, 80).

[247] L. Marrucci, C. Manzo, and D. Paparo. Optical spin-to-orbital angular momentum conversion in inhomogeneous anisotropic media. *Phys. Rev. Lett.*, 96 (16), **2006**, 1–4. DOI: 10.1103/PhysRevLett.96.163905 (cited on pages 65, 83).

[248] G. Lambert, B. Vodungbo, J. Gautier, B. Mahieu, V. Malka, S. Sebban, P. Zeitoun, J. Luning, J. Perron, A. Andreev, S. Stremoukhov, F. Ardana-Lamas, A. Dax, C. P. Hauri, A. Sardinha, and M. Fajardo. Towards enabling femtosecond helicity-dependent spectroscopy with high-harmonic sources. *Nat. Commun.*, 6, **2015**, 1–6. DOI: 10.1038/ncomms7167 (cited on pages 65, 73).

[249] C. Hernández-García, A. Turpin, J. San Román, A. Picón, R. Drevinskas, A. Cerkauskaite, P. G. Kazansky, C. G. Durfee, and Í. J. Sola. Extreme ultraviolet vector beams driven by infrared lasers. *Optica*, 4 (5), **2017**, 520. DOI: 10.1364/optica.4.000520 (cited on pages 65, 70, 89, 118).

[250] K. J. Schafer, B. Yang, L. F. Dimauro, and K. C. Kulander. Above threshold ionization beyond the high harmonic cutoff. *Phys. Rev. Lett.*, 70 (11), **1993**, 1599–1602. DOI: 10.1103/PhysRevLett.70.1599 (cited on pages 65, 84).

[251] C. Hernández-García. High harmonic generation: A twist in coherent X-rays. *Nat. Phys.*, 13 (4), **2017**, 327–329. DOI: 10.1038/nphys4088 (cited on pages 66, 83).

[252] W. Paufler, B. Böning, and S. Fritzsche. Tailored orbital angular momentum in high-order harmonic generation with bicircular Laguerre-Gaussian beams. *Phys. Rev. A*, 98 (1), **2018**, 1–5. DOI: 10.1103/PhysRevA.98.011401 (cited on page 71).

[253] K. Y. Bliokh, F. J. Rodríguez-Fortuño, F. Nori, and A. V. Zayats. Spin-orbit interactions of light. *Nat. Photonics*, 9 (12), **2015**, 796–808. DOI: 10.1038/nphoton.2015.201. arXiv: 1505.02864 (cited on page 72).

[254] F. Sanson, A. K. Pandey, F. Harms, G. Dovillaire, E. Baynard, J. Demailly, O. Guilbaud, B. Lucas, O. Neveu, M. Pittman, D. Ros, M. Richardson, E. Johnson, W. Li, P. Balcou, and S. Kazamias. Hartmann wavefront sensor characterization of a high charge vortex beam in the extreme ultraviolet spectral range. *Opt. Lett.*, 43 (12), **2018**, 2780. DOI: 10.1364/ol.43.002780 (cited on page 78).

[255] E Beaurepaire, J Merle, A Daunois, and J Bigot. Ultrafast Spin Dynamics in Ferromagnetic Nickel. *Phys. Rev. Lett.*, 76 (22), **1996**, 1–4. DOI: 10.1103/PhysRevLett.76.4250. arXiv: 9709264 [cond-mat] (cited on page 80).

[256] C. Boeglin, E. Beaurepaire, V. Halté, V. López-Flores, C. Stamm, N. Pontius, H. A. Dürr, and J. Y. Bigot. Distinguishing the ultrafast dynamics of spin and orbital moments in solids. *Nature*, 465 (7297), **2010**, 458–461. DOI: 10.1038/nature09070 (cited on page 80).

[257] R. Cireasa, A. E. Boguslavskiy, B. Pons, M. C. Wong, D. Descamps, S. Petit, H. Ruf, N. Thiré, A. Ferré, J. Suarez, J. Higuet, B. E. Schmidt, A. F. Alharbi, F. Légaré, V. Blanchet, B. Fabre, S. Patchkovskii, O. Smirnova, Y. Mairesse, and V. R. Bhardwaj. Probing molecular chirality on a sub-femtosecond timescale. *Nat. Phys.*, 11 (8), **2015**, 654–658. DOI: 10.1038/nphys3369 (cited on page 80).

[258] S. Eckart, M. Kunitski, M. Richter, A. Hartung, J. Rist, F. Trinter, K. Fehre, N. Schlott, K. Henrichs, L. P. H. Schmidt, T. Jahnke, M. Schöffler, K. Liu, I. Barth, J. Kaushal, F. Morales, M. Ivanov, O. Smirnova, and R. Dörner. Ultrafast preparation and detection of ring currents in single atoms. *Nat. Phys.*, 14 (7), **2018**, 701–704. DOI: 10.1038/s41567-018-0080-5 (cited on page 81).

[259] A. Trichili, C. Rosales-Guzmán, A. Dudley, B. Ndagano, A. Ben Salem, M. Zghal, and A. Forbes. Optical communication beyond orbital angular momentum. *Sci. Rep.*, 6, **2016**, 27674. URL: http://dx.doi.org/10.1038/srep27674http://10.0.4.14/srep27674https://www.nature.com/articles/srep27674{\#}supplementary-information (cited on page 83).

[260] S. Fürhapter, A. Jesacher, S. Bernet, and M. Ritsch-Marte. Spiral phase contrast imaging in microscopy. *Opt. Express*, 13 (3), **2005**, 689. DOI: 10.1364/opex.13.000689 (cited on page 83).

[261] M. W. Beijersbergen, R. P. Coerwinkel, M. Kristensen, and J. P. Woerdman. Helical-wavefront laser beams produced with a spiral phaseplate. *Opt. Commun.*, 112 (5-6), **1994**, 321–327. DOI: 10.1016/0030-4018(94)90638-6 (cited on page 83).

[262] J. Atencia, M. Quintanilla, J. Marín-Sáez, Í. J. Sola, and M.-V. Collados. Holographic optical element to generate achromatic vortices. *Opt. Express*, 21 (18), **2013**, 21057. DOI: 10.1364/oe.21.021057 (cited on page 83).

[263] J. C. Lee, S. J. Alexander, S. D. Kevan, S. Roy, and B. J. McMorran. Laguerre–Gauss and Hermite–Gauss soft X-ray states generated using diffractive optics. *Nat. Photonics*, 13 (March), **2019**, 205–210. DOI: 10.1038/s41566-018-0328-8 (cited on page 83).

[264] M. Babiker, W. L. Power, and L. Allen. Light-induced torque on moving atoms. *Phys. Rev. Lett.*, 73 (9), **1994**, 1239–1242. DOI: 10.1103/PhysRevLett.73.1239 (cited on page 83).

[265] A. T. O'Neil and M. J. Padgett. Three-dimensional optical confinement of micron-sized metal particles and the decoupling of the spin and orbital angular momentum within an optical spanner. *Opt. Commun.*, 185 (1-3), **2000**, 139–143. DOI: 10.1016/S0030-4018(00)00989-5 (cited on page 83).

[266] D. M. Villeneuve, S. A. Aseyev, P. Dietrich, M. Spanner, M. Y. Ivanov, and P. B. Corkum. Forced molecular rotation in an optical centrifuge. *Phys. Rev. Lett.*, 85 (3), **2000**, 542–545. DOI: 10.1103/PhysRevLett.85.542 (cited on pages 83, 85).

[267] D. G. Grier. A Revolution in Optical Manipulation. *Nature*, 424 (August), **2003**. DOI: 10.1029/2006WR005733 (cited on page 83).

[268] M. E. J. Friese, H. Rubinsztein-Dunlop, J. Gold, P. Hagberg, and D. Hanstorp. Optically driven micromachine elements. *Appl. Phys. Lett.*, 78 (4), **2002**, 547–549. DOI: 10.1063/1.1339995 (cited on page 83).

[269] A. F. Ranada and L. Vazquez. On the self-torque on an extended classical charged particle. *J. Phys. A Gen. Phys.*, 17 (10), **1984**, 2011–2016. DOI: 10.1088/0305-4470/17/10/013 (cited on page 84).

[270] S. R. Dolan, N. Warburton, A. I. Harte, A. Le Tiec, B. Wardell, and L. Barack. Gravitational self-torque and spin precession in compact binaries. *Phys. Rev. D - Part. Fields, Gravit. Cosmol.*, 89 (6), **2014**, 1–6. DOI: 10.1103/PhysRevD.89.064011 (cited on page 84).

[271] M. Hentschel, R. Kienberger, C. Spielmann, G. A. Reider, N. Milosevic, T. Brabec, P. Corkum, U. Heinzmann, M. Drescher, and F. Krausz. Attosecond metrology. *Nature*, 414 (6863), **2001**, 509–513. DOI: 10.1038/35107000 (cited on page 84).

[272] B. Rodenburg, M. Mirhosseini, M. Padgett, M. N. O'Sullivan, M. Malik, M. P. J. Lavery, D. J. Robertson, and R. W. Boyd. Influence of atmospheric turbulence on states of light carrying orbital angular momentum. *Opt. Lett.*, 37 (17), **2012**, 3735. DOI: 10.1364/ol.37.003735 (cited on page 85).

[273] F. Calegari, A. Trabattoni, A. Palacios, D. Ayuso, M. C. Castrovilli, J. B. Greenwood, P. Decleva, F. Martín, and M. Nisoli. Charge migration induced by attosecond pulses in bio-relevant molecules. *J. Phys. B At. Mol. Opt. Phys.*, 49 (14), **2016**, 142001. DOI: 10.1088/0953-4075/49/14/142001 (cited on page 85).

[274] G. Hermann, C. Liu, J. Manz, B. Paulus, J. F. Pérez-Torres, V. Pohl, and J. C. Tremblay. Multidirectional Angular Electronic Flux during Adiabatic Attosecond Charge Migration in Excited Benzene. *J. Phys. Chem. A*, 120 (27), **2016**, 5360–5369. DOI: 10.1021/acs.jpca.6b01948 (cited on page 85).

[275] R. M. Kerber, J. M. Fitzgerald, S. S. Oh, D. E. Reiter, and O Hess. Orbital angular momentum dichroism in nanoantennas. *Commun. Phys.*, 1 (1), **2018**, 87. DOI: 10.1038/s42005-018-0088-2 (cited on page 85).

[276] C. Hernández-García, J. Vieira, J. Mendonça, L. Rego, J. San Román, L. Plaja, P. Ribic, D. Gauthier, and A. Picón. Generation and Applications of Extreme-Ultraviolet Vortices. *Photonics*, 4 (2), **2017**, 28. DOI: 10.3390/photonics4020028 (cited on page 89).

[277] M. V. Berry. Optical vortices evolving from helicoidal integer and fractional phase steps. *J. Opt. A Pure Appl. Opt.*, 6 (2), **2004**, 259–268. DOI: 10.1088/1464-4258/6/2/018 (cited on page 92).

[278] J. Leach, E. Yao, and M. J. Padgett. Observation of the vortex structure of a non-integer vortex beam. *New J. Phys.*, 6, **2004**, 1–8. DOI: 10.1088/1367-2630/6/1/071 (cited on page 92).

[279] S. N. Alperin and M. E. Siemens. Angular Momentum of Topologically Structured Darkness. *Phys. Rev. Lett.*, 119 (20), **2017**, 1–5. DOI: 10.1103/PhysRevLett.119.203902. arXiv: 1709.09299 (cited on pages 92, 128).

[280] E. Karimi, L. Marrucci, C. de Lisio, and E. Santamato. Time-division multiplexing of the orbital angular momentum of light. *Opt. Lett.*, 37 (2), **2012**, 127. DOI: 10.1364/ol.37.000127 (cited on page 93).

[281] I. J. Sola, E. Mével, L. Elouga, E. Constant, V. Strelkov, L. Poletto, P. Villoresi, E. Benedetti, J.-P. Caumes, S. Stagira, G. Sansone, C. Vozzi, and M. Nisoli. Controlling attosecond electron dynamics by phase-stabilized polarization gating. *Nat. Phys.*, 2 (5), **2006**, 319–322. DOI: 10.1038/nphys281 (cited on page 93).

[282] H. Vincenti and F. Quéré. Attosecond lighthouses: How to use spatiotemporally coupled light fields to generate isolated attosecond pulses. *Phys. Rev. Lett.*, 108 (11), **2012**, 1–5. DOI: 10.1103/PhysRevLett.108.113904 (cited on page 94).

[283] J. A. Wheeler, R. Lopez-Martens, A. Malvache, F. Quéré, S. Monchocé, A. Borot, H. Vincenti, and A. Ricci. Attosecond lighthouses from plasma mirrors. *Nat. Photonics*, 6 (12), **2012**, 829–833. DOI: 10.1038/nphoton.2012.284 (cited on page 94).

[284] C. Hernández-García, A. Jaron-Becker, D. D. Hickstein, A. Becker, and C. G. Durfee. High-order-harmonic generation driven by pulses with angular spatial chirp. *Phys. Rev. A*, 93 (2), **2016**, 1–7. DOI: 10.1103/PhysRevA.93.023825 (cited on page 94).

[285] W. Holgado, C. Hernández-García, B. Alonso, M. Miranda, F. Silva, L. Plaja, H. Crespo, and I. J. Sola. Continuous spectra in high-harmonic generation driven by multicycle laser pulses. *Phys. Rev. A*, 93 (1), **2016**, 1–6. DOI: 10.1103/PhysRevA.93.013816 (cited on page 97).

[286] A. Börzsönyi, M. P. Kalashnikov, A. P. Kovács, K. Osvay, and Z. Heiner. Dispersion measurement of inert gases and gas mixtures at 800 nm. *Appl. Opt.*, 47 (27), **2008**, 4856. DOI: 10.1364/ao.47.004856 (cited on page 100).

[287] M. D. Morse. **Experimental Methods in Physical Sciences**. Ed. by F. Dunning and R. Hulet. Elsevier Inc., 1996, pp. 21–47 (cited on page 100).

[288] L. Li, P. Lan, L. He, X. Zhu, J. Chen, and P. Lu. Scaling Law of High Harmonic Generation in the Framework of Photon Channels. *Phys. Rev. Lett.*, 120 (22), **2018**, 223203. DOI: 10.1103/PhysRevLett.120.223203 (cited on pages 102, 103).

[289] É. Bisson, D. M. Villeneuve, J.-C. Kieffer, P. B. Corkum, H. J. Wörner, J. B. Bertrand, H.-C. Bandulet, and M. Spanner. Ultrahigh-Order Wave Mixing in Noncollinear High Harmonic Generation. *Phys. Rev. Lett.*, 106 (2), **2011**, 1–4. DOI: 10.1103/physrevlett.106.023001 (cited on page 102).

[290] S. N. Bengtsson, A. L'Huillier, F. Brizuela, C. M. Heyl, P. Rudawski, and J. Mauritsson. Macroscopic Effects in Noncollinear High-Order Harmonic Generation. *Phys. Rev. Lett.*, 112 (14), **2014**, 1–5. DOI: 10.1103/physrevlett.112.143902 (cited on page 102).

[291] C Hernández-García, A Becker, L Plaja, A Jaron-Becker, T Popmintchev, M. M. Murnane, and H. C. Kapteyn. Group velocity matching in high-order harmonic generation driven by mid-infrared lasers. *New J. Phys.*, 18 (7), **2016**, 073031. DOI: 10.1088/1367-2630/18/7/073031 (cited on page 105).

[292] I. Barth and O. Smirnova. Nonadiabatic tunneling in circularly polarized laser fields: Physical picture and calculations. *Phys. Rev. A - At. Mol. Opt. Phys.*, 84 (6), **2011**, 63415. DOI: 10.1103/PhysRevA.84.063415 (cited on page 107).

[293] D. B. Milošević. Possibility of introducing spin into attoscience with spin-polarized electrons produced by a bichromatic circularly polarized laser field. *Phys. Rev. A*, 93 (5), **2016**, 1–6. DOI: 10.1103/PhysRevA.93.051402 (cited on page 107).

[294] A. Hartung, M. Richter, A. Kalinin, M. Ivanov, T. Jahnke, M. Schöffler, L. P. H. Schmidt, M. Kunitski, O. Smirnova, F. Morales, K. Henrichs, A. Laucke, and R. Dörner. Electron spin polarization in strong-field ionization of xenon atoms. *Nat. Photonics*, 10 (8), **2016**, 526–528. DOI: 10.1038/nphoton.2016.109 (cited on page 107).

[295] J. M. Knudsen, S. N. Alperin, A. A. Voitiv, W. G. Holtzmann, J. T. Gopinath, and M. E. Siemens. Efficient Modal Decomposition of Vortex Beams via Holographically Reconstructed Phase. 29 (8), **2017**, 1968–1976. URL: http://arxiv.org/abs/1710.02912. arXiv: 1710.02912 (cited on page 115).

[296] A. Longman and R. Fedosejevs. Mode conversion efficiency to Laguerre-Gaussian OAM modes using spiral phase optics. *Opt. Express*, 25 (15), **2017**, 17382. DOI: 10.1364/oe.25.017382 (cited on page 115).

[297] L. Janicijevic and S. Topuzoski. Gaussian laser beam transformation into an optical vortex beam by helical lens. *J. Mod. Opt.*, 63 (2), **2016**, 164–176. DOI: 10.1080/09500340.2015.1085106 (cited on pages 115, 116).

[298] S. N. Alperin, R. D. Niederriter, J. T. Gopinath, and M. E. Siemens. Quantitative measurement of the orbital angular momentum of light with a single, stationary lens. *Opt. Lett.*, 41 (21), **2016**, 5019. DOI: 10.1364/OL.41.005019 (cited on pages 116, 138).

[299] F. H. M. Faisal. Multiple absorption of laser photons by atoms. *J. Phys. B At. Mol. Opt. Phys.*, 6, **1973**, L69. DOI: 10.1088/0953-4075/49/22/220501 (cited on page 116).

[300] W. Becker, A. Lohr, M. Kleber, and M. Lewenstein. A unified theory of high-harmonic generation: Application to polarization properties of the harmonics. *Phys. Rev. A - At. Mol. Opt. Phys.*, 56 (1), **1997**, 645–656. DOI: 10.1103/PhysRevA.56.645 (cited on page 116).

[301] C. Hernández-García, W. Holgado, L. Plaja, B. Alonso, F. Silva, M. Miranda, H. Crespo, and I. J. Sola. Carrier-envelope-phase insensitivity in high-order harmonic generation driven by few-cycle laser pulses. *Opt. Express*, 23 (16), **2015**, 21497. DOI: `10.1364/oe.23.021497` (cited on page 119).

[302] L. Hareli, L. Lobachinsky, G. Shoulga, Y. Eliezer, L. Michaeli, and A. Bahabad. On-the-Fly Control of High-Harmonic Generation Using a Structured Pump Beam. *Phys. Rev. Lett.*, 120 (18), **2018**, 183902. DOI: `10.1103/PhysRevLett.120.183902` (cited on page 123).

[303] A. L'Huillier, P. Balcou, S. Candel, K. Schafer, and K. Kulander. Calculations of high-order harmonic-generation processes in xenon at 1064 nm. *Phys. Rev. A*, 46 (5), **1992** (cited on page 126).

[304] G. Gbur. Fractional vortex Hilbert's Hotel. *Optica*, 3 (3), **2016**, 222–225. DOI: `10.1364/OPTICA.3.000222` (cited on page 131).

[305] E. Karimi, G. Zito, B. Piccirillo, L. Marrucci, and E. Santamato. Hypergeometric-Gaussian modes. *Opt. Lett.*, 32 (21), **2007**, 3053–3055 (cited on page 137).

[306] E. Yao, S. Franke-Arnold, J. Courtial, S. Barnett, and M. Padgett. Fourier relationship between angular position and optical orbital angular momentum. *Opt. Express*, 14 (20), **2006**, 9071–9076. DOI: `10.1364/OE.14.009071` (cited on page 137).